universität wien

DISSERTATION /DOCTORAL THESIS

Titel der Dissertation /Title of the Doctoral Thesis

„Mechanistic Insight into endothelial cell dysfunction linked to cardiovascular disease in progeria“

verfasst von / submitted by

Christina Manakanatas, MSc

angestrebter akademischer Grad / in partial fulfilment of the requirements for the degree of

Doctor of Philosophy (PhD)

Wien, 2022/ Vienna 2022

Studienkennzahl lt. Studienblatt / degree programme code as it appears on the student record sheet:	UA 794 685 490
Dissertationsgebiet lt. Studienblatt / field of study as it appears on the student record sheet:	Molekulare Biologie
Betreut von / Supervisor:	Univ.-Prof. Dipl.-Ing. Dr. Roland Foisner

Ἓν οἶδα ὅτι οὐδὲν οἶδα

Sokrates

Acknoledgments

Θέλω να ευχαριστήσω τους γονείς μου, Νέστορα και Ανδρέα, και την αδερφή μου Αγγελική για την υποστήριξή τους και την αγάπη τους όλα αυτά τα χρόνια. Θέλω επίσης να ευχαριστήσω όλη την υπόλοιπη οικογένεια μου, και τις φίλες μου, Στέλλα, Βιβή και Δήμητρα που όλα αυτά τα χρόνια είναι η δεύτερη οικογένειά μου.

I would like to truly thank my supervisors Roland Foisner and Selma Osmanagic-Myers for giving me the opportunity to develop my Ph.D project in the lab of Roland Foisner. Thank you very much Roland and Selma for your support and your guidance over the last years, for your help, patience, and motivation to keep my head up and for making this stage of my life something to learn from and move forward with enthusiasm.

Thanks to all former and current members of the Foisner lab. You have undoubtedly contributed to my going forward during these years. Thank you also Gerlinde, for your help and your constant smile.

Thank you also to my Ph.D committee members Johannes Grillari, Martin Leeb and Roland Foisner. Thank you to the Max Perutz Labs and the SMICH Ph.D programm, the infrastructure and so many great scientific and social experiences.

Thank you also to all the many friends and amazing people I have met in Vienna.

Contents

1. Abstract

Cardiovascular diseases (CVDs) are among the most frequent deadly diseases worldwide in the aged population. CVDs are also prominent pathologies in patients suffering from Hutchinson Gilford Progeria syndrome (HGPS), a premature aging disease caused by a single point de novo mutation in the *LMNA* gene encoding nuclear lamin A and C. One of the key initiating events in the development of age-linked CVDs is a dysfunctional endothelium, which lines the inside of all blood vessel and the inner walls of the heart chambers. Under physiological conditions, the endothelium is a key regulator of vascular tone and homeostasis, but in pathological conditions and during aging endothelial functions are impaired, leading to downregulation of atheroprotective pathways.

In this thesis I investigated, if and how a dysfunctional endothelium contributes also to HGPS pathologies. We generated a novel transgenic HGPS mouse model (Prog-Tg mice), expressing progerin - the disease-causing lamin A mutant – exclusively in vascular endothelial cells (Prog-Tg ECs). These mice develop many HGPS-related cardiovascular pathologies including premature death, left ventricular hypertrophy, left ventricular diastolic dysfunction and interstitial and perivascular fibrosis. Functionally, we detected an impaired shear stress response to blood flow in the atheroprone aortic endothelium and in primary endothelial cells (ECs) in vitro, and defects in mechanosignalling including impaired nucleocytoskeletal coupling, abnormal localization and /or increased expression of stress response proteins at the nuclear envelope and an increase of F-actin/G-actin ratio. Mechanistically we find that Prog-Tg ECs have an impaired myocardin-related transcription factor A (MRTF-A) signaling pathway leading to reduced levels of endothelial nitric oxide synthase (eNOS) and atheroprotective nitric oxide (NO). Prog-Tg ECs also initiated a paracrine pro-fibrotic effect to surrounding tissues.

In order to get further insight into the cellular phenotype of progerin-expressing ECs we performed genome-wide mRNA and micro-RNA (miR) profiling in primary ECs, EC culture supernatants and in plasma of mice. These analyses revealed upregulation of the p53-linked senescence pathway and initiation of a senescence associated secretory phenotype (SASP), including upregulation of cellular and extracellular senescence-associated miRs. Specifically, pro-inflammatory and pro-fibrotic miR34a-5p and miR31-5p were found upregulated in Prog-Tg ECs as well as in plasma of Prog-Tg mice, and miR133a-3p, miR21a-3p and miR582-5p in EC-secreted extracellular vesicles. Interestingly, increased levels of senescence and SASP markers including miRs were also detected in lung and heart tissues in vivo, and in non-endothelial cells and tissues. Moreover, in vitro co-culture assays revealed that Prog-Tg ECs exert a paracrine senescence and SASP phenotype on co-cultured wildtype fibroblasts. Since miR34a-5p is an established CVD biomarker we tested its functional relevance for CVD by antagomiR-mediated inhibition of miR34a-5p and found reduced senescence markers p53 and p16. RNAi-mediated knockdown of p53 on the other hand reduced senescence marker p21 and miR34a-5p as well as pro-fibrotic signalling.

Altogether, based on our findings we propose a disease mechanism, in which progerin-expression in the endothelium leads to mechanosignalling defects, in turn causing upregulation of-p53 linked senescence signalling and SASP in ECs, including senescence associated miRs (SA-miRs). p53 and miR34a-5p pathways work synergistically to initiate and maintain this complex senescence signalling network, and components of the SASP including secreted miRs in extracellular vesicles mediate a paracrine senescent and pro-fibrotic effect on non-endothelial cells and tissues and initiation of an inflammatory response. Our findings are highly relevant for the identification of novel diagnostic and therapeutic drugs for HGPS- and age-linked CVD.

2. Zusammenfassung

Herz-Kreislauf-Erkrankungen gehören weltweit zu den an den häufigsten auftretenden Todesursachen. Dies gilt insbesondere für alternde Gesellschaften. Bei Patient*innen, die unter dem Hutchinson-Gilford-Progerie-Syndrom (HGPS) – einer Krankheit des vorzeitigen Alterns – leiden, treten Herz-Kreislauf-Erkrankungen schon in sehr jungen Jahren auf. HGPS wird durch eine einzelne De-novo-Punktmutation im LMNA-Gen verursacht, das für A-type Lamine (strukturelle Proteine im Zellkern) kodiert. Die altersbedingten Herz-Kreislauf-Erkrankungen, in gesunden so wie auch HGPS Patient*innen, gehen häufig mit einer Fehlfunktion des Endothels in den Blutgefäßen einher. Unter physiologischen Bedingungen ist das Endothel, das die Innenseite der Blutgefäße und der Herzkammern auskleidet, ein wichtiger Regulator des Gefäßtonus und der Homöostase. Unter pathologischen Bedingungen und im Zuge des Alterns sind die Endothelfunktionen jedoch beeinträchtigt, was oft zu Atherosklerose führt.

In dieser Arbeit habe ich untersucht, ob und wie ein dysfunktionales Endothel auch zu HGPS-Pathologien beiträgt. In Zusammenarbeit mit meinen Kolleg*innen habe ich ein neues transgenes HGPS-Mausmodell entwickelt, das Progerin (die krankheitsverursachende Lamin Mutante) ausschließlich in vaskulären Endothelzellen exprimiert. Die transgenen Mäuse entwickeln viele HGPS-spezifische, kardiovaskuläre Pathologien, darunter linksventrikuläre Hypertrophie, linksventrikuläre diastolische Dysfunktion, interstitielle und perivaskuläre Fibrose, bis hin zum vorzeitigen Tod. Im Gegensatz zu gesunden Mäusen können die Endothelzellen unserer Mäuse nicht angemessen auf den durch den Blutstrom verursachten, mechanischen Stress reagieren, weil durch die Expression von Progerin die Mechanosignalübertragung beeinträchtigt wird. Im Atherosklerose-anfälligen Bereichen des Aortenendothels und in primären Endothelzellen konnten wir zudem einen gestörten Mechanokopplungs-Mechanismus zwischen Zellkern und Zytoskelett zeigen, der durch eine abnormale Lokalisierung und/oder verstärkte Expression von Stressreaktionsproteinen in der Kernhülle und einen Anstieg von fibrillären Actin hervorgerufen wird. Dadurch wird der Signalweg des „Myocardin-Related Transcription Factor A (MRTF-A)“ beeinträchtigt, was zu einer Reduktion von endothelialer Stickstoffmonoxid-Synthase (eNOS) und Atherosklerose-vorbeugenden Stickstoffmonoxid (NO) im Blut führt. Zugleich induzieren die Endothelzellen auch eine parakrine, pro-fibrotische Wirkung im umliegenden Gewebe.

Um weitere molekularen Defekte in Progerin-exprimierenden Endothelzellen zu identifizieren, haben wir genomweite mRNA- und micro-RNA (miR) Expressionsanalysen in primären Endothelzellen und im Plasma von Mäusen durchgeführt. Wir konnten dabei eine Hochregulierung des p53-verknüpften Seneszenz-Signalwegs und den Beginn eines Seneszenz-assoziierten sekretorischen Phänotyps (SASP), einschließlich der Hochregulierung von zellulären und extrazellulären Seneszenz-assoziierten miRs zeigen. Pro-inflammatorische und pro-fibrotische miRs, miR34a-5p und miR31-5p waren sowohl in Endothelzellen, wie im Plasma hochreguliert. Zudem wurden miR133a-3p, miR21a-3p und miR582-5p in extrazellulären Vesikeln von Endothelzellen sekretiert. Erhöhte Werte von Seneszenz- und SASP-Markern, einschließlich miRs, wurden auch in Lungen- und Herzgewebe in vivo sowie in nicht-endothelialen Zellen und Geweben nachgewiesen. Darüber hinaus zeigten In-vitro-Ko-kulturversuche, dass Endothelzellen durch parakrine Effekte Seneszenz und einen SASP-Phänotyp in Wildtyp-Fibroblasten induzieren können. Da miR34a-5p ein etablierter Biomarker für kardiovaskuläre Erkrankungen ist, testeten wir seine funktionelle Bedeutung durch antagomiR-vermittelte Inhibierung von miR34a-5p und stellten dabei eine Reduzierung der Seneszenzmarker p53 und p16 fest. Die RNAi-vermittelte Ausschaltung von p53 reduzierte dagegen den Seneszenzmarker p21 und miR34a-5p sowie die pro-fibrotische Signalübertragung.

Insgesamt schlagen wir auf Grundlage unserer Ergebnisse einen Krankheitsmechanismus vor, bei dem die Progerin-Expression im Endothel zu Defekten bei der Mechanosignalübertragung führt, was schlussendlich zur Induktion einer zellulären Seneszenz und des SASP Phänotyps führt. Ein komplexes Wechselspiel der p53- und miR34a-5p-Signalwege hält dabei den Seneszenz-Phänotyp der Endothelzellen aufrecht, wodurch parakrine Effekte induziert werden, die im umliegenden Gewebe Fibrose und entzündliche Reaktionen auslösen und zur kardiovaskulären Pathologie beitragen. Unsere Erkenntnisse sind von großer Bedeutung für die Identifizierung neuer diagnostischer und therapeutischer Mittel für HGPS und für andere altersbedingte, kardiovaskuläre Erkrankungen.

3. Preamble

Rising living standards in modern societies have led to an increase of life expectancy and concomitantly to an increase of age-related diseases. One of the most prominent group of age-related diseases, leading to a great number of deaths annually, is cardiovascular disease (CVD) (WHO report 2017) [1]. Age related cardiovascular pathologies and atherosclerosis occur due to damage in our arteries and capillaries, which in many cases translates to a damaged and dysfunctional endothelium. The endothelium, or tunica intima, is the innermost of three different cell layers that comprise the walls of all vessels, the other two being the tunica media (mainly comprised of smooth muscle cells (SMC)) and the tunica adventitia (mainly comprised of fibroblasts) [2]. The endothelium is a one-cell-thick layer comprised of endothelial cells (ECs) which line the inside of every blood vessel in the body, as well as the inner walls of the heart chambers and lymphatic vessels. The endothelium has emerged as a key regulator of vascular tone and homeostasis since it does not merely fulfill a role as a barrier between blood and tissues but also acts as a signal transducer for circulating factors that can influence the vessel wall phenotype [3]. Changes in the endothelium occurring during aging include a downregulation of atheroprotective pathways such as reduced endothelial NO synthase (eNOS) levels (an enzyme that produces the atheroprotective nitric oxide (NO)), an insensitive shear stress response, which is the response of ECs to the constant fractional force created by the blood flow, and an upregulation of pro-inflammatory molecules, such as ICAM1 and ICAM2 [4]. Moreover, in aged and dysfunctional arteries structural changes occur in the extracellular matrix (ECM) of the intima, medial and adventitia layers, leading to changes in the actomyosin-mediated cellular contractility and in the shear stress response [5] [6].

One of the main molecular causes of age-linked diseases, such as CVD, is cellular senescence occurring in almost all tissues and leading to aged-linked tissue damage [7] [8]. To this regard it has been proven that endothelial cell senescence is a major initiating event in geriatric CVD and atherosclerosis [4] [9]. Although permanently cell cycle arrested, senescent cells are still metabolically active and can influence their surrounding environment by secretion of pro-inflammatory and pro-fibrotic factors, growth factors and proteases. The specific secretome of senescent cells, through which they establish a ‘’communication network’’ with their surrounding cells and tissues, is termed senescence associated secretory phenotype (SASP) [10] [11]. In addition to the well-established SASP members, microRNAs (miRs) have recently been characterized as a novel member of the SASP [12]. miRs are small 22 nucleotide long RNAs that regulate gene expression at a post-transcriptional level by binding to the 3´ UTR region of target mRNAs leading to either mRNA decay or inhibition of translation [13]. Interestingly, miRs are emerging as key regulators of senescence signaling [14]. To this extend, a novel group of senescence-associated miRs, termed geromiRs, has been established [15].

The canonical miR biogenesis pathway starts with the generation of a pri-miR transcript that is processed inside the nucleus by a multiprocessor complex (Drosha and DiGeorge Syndrome Critical Region 8 (DGCR8)) that cleaves the pri-miR molecule and produces the precursor-miR (pre-miR). The pre-miR is subsequently exported to the cytoplasm by Exportin 5 and is there further processed by the protein complex Dicer to produce the mature miR molecule. As a final step, either the 5p or the 3p strand of the mature miR molecule is loaded into the Argonaute (AGO) protein to form the miR-induced silencing complex (miRISC). Inside this miRISC complex binding of the active miR strand and the 3´ UTR of the target mRNA occurs which results in mRNA degradation or translational inhibition [16]. miRs are produced intracellularly and can influence gene expression inside their cell of origin, but can also participate in intercellular communication through their secretion. Since miRs are highly

susceptible to degradation by extracellular RNases in order for them to be able to communicate signals in between cells they need to be protected. This protection is achieved by small extracellular vesicles (sEV) that enclose secreted miRs, along with other biological cargoes, and allow them to "safely" exit into the extracellular space.

It has extensively been proposed that cell to cell communication over large distances is established by secretion of small extracellular vesicles (sEV) from donor cells and uptake of these sEV by recipient cells [17]. Small extracellular vesicles are composed of a lipid bilayer containing transmembrane proteins and can carry different contents such as cytosolic proteins, RNA, DNA, lipids and metabolites [18] . Different sEV can have different pathways of biogenesis, different sizes, different cell-specific origins and function. According to their biological pathway of biogenesis, typically three major subtypes of EVs are defined. Exosomes (30-150nm in diameter) are generated by inward budding of the endosomal membrane and fusion of the multivesicular body (MVB) with the plasma membrane. Microvesicles are formed by outward budding of the plasma membrane and apoptotic bodies are shedded from cells during apoptosis [18]. The most well studied sEV are exosomes and microvesicles.

Recently, increasing attention has been payed to sEV and their integral role in intercellular communication in the context of age-related diseases, including CVD. Interestingly, a recent study showed that senescent ECs secret a significantly higher number of sEV, in particular exosomes, compared to their quiescent counterparts [19]. Moreover, the composition of those senescent cell-derived exosomes was shown to be different in comparison to the one from exosomes released by young healthy cells [20]. More specifically, it has been shown that the miR content of exosomes released by senescent cells is significantly altered, revealing an enrichment in anti-apoptotic (pro-senescent) miRs [12]. In accordance to that, it was proposed that a major mechanism linking endothelial cell senescence and progression of CVD is the production and release of specific sEV, in particular exosomes, by senescent endothelial cells [20]. Therefore, exosomes and their miR cargo have been proposed to play an integral role in the development of atherosclerosis and CVD.

As a model to study age related CVD and atherosclerosis we utilize a premature aging disease, the Hutchinson-Gilford progeria syndrome (HGPS). HGPS is a severe and very rare premature aging disease with many clinical symptoms including alopecia, loss of subcutaneous fat, aged-looking skin and osteoporosis [21] [22] [23]. The most prominent hallmark of HGPS is severe progressive atherosclerosis in childhood, characterized by left ventricular (LV) diastolic dysfunction and hypertrophy [24] [25], early to late stage collagen rich plaques and severe vascular smooth muscle cell (VSMC) loss in large arteries [24] [26] [27]. Cardiovascular abnormalities in HGPS patients are very similar to those observed in geriatric cardiovascular disease [24] [9] [28] [29] with the difference being that the extrinsic risk factors present in aged individuals like hypertension, hypercholesterolemia, an unhealthy diet and smoking, are not present in HGPS patients. Therefore, HGPS poses a great model for particularly studying CVD and atherosclerosis, strictly in regard to aging.

HGPS is caused by a single point autosomal dominant de novo (GGC>GGT) mutation in the *LMNA* gene. Mammals carry 3 different genes for expression of lamins, *LMNA* gene encoding lamin A and lamin C, *LAMINB1* gene encoding lamin B1 and *LAMINB2* encoding lamin B2. Lamins are part of the nuclear lamina, a mesh-like structure at the nuclear periphery which fulfills many roles inside the cell, with the main ones being providing mechanical stability and regulating chromatin organization and gene expression [30]. Lamin A is expressed as prelamin A which undergoes several steps of post-translational modification including farnesylation and carboxymethylation of the C-terminus and eventually cleavage of the modified C-terminal 15 amino acids, resulting in the mature non-

carboxymethylated and non-farnesylated lamin A molecule [31]. This last cleavage step does not take place in B-type lamins, so that they maintain their C-terminal farnesylation and carboxymethylation. The single point mutation in LMNA causal for HGPS leads to activation of a cryptic splice site and results in the generation of a truncated version of prelamin A, with a 50 amino acid internal deletion, which stays permanently farnesylated and therefore permanently tethered to the nuclear periphery. This mutant version of LMNA is termed progerin [32] [33]. Since lamins fulfill many important functions in the cells, expression of the mutant version of lamin A – progerin - in cells leads to many problems, including mechanical defects, lobulated nuclei and changes in heterochromatin, DNA damage and shortened telomeres strongly resembling age-linked mechanisms.

Although one of the initiating events of geriatric CVD and atherosclerosis is endothelial cell senescence, most of the studies in HGPS until now have focused on delineating the role of VSMC depletion in HGPS patients in regard to CVD [24] [26] [34] [35] [36]. Based on the key initiating role of endothelial cell dysfunction in the development of CVD and atherosclerosis and the importance of progerin accumulation in endothelial cells in the development of a dysfunctional endothelium [37], we generated a transgenic mouse model with ectopic endothelial cell specific expression of progerin (Prog-Tg). As a control we generated a mouse model that expresses the wild type (WT) human LAMIN A specifically in the endothelium (LA-Tg).

In our first publication [38] we analyzed the phenotype of the Prog-Tg mouse model in order to understand how progerin expression, specifically in the endothelium, can contribute to the development of a dysfunctional endothelium and subsequently to the formation of an atherosclerotic prone environment. We showed that on an organismal level endothelial specific Prog-Tg mice died prematurely and developed a CVD phenotype highly similar to the phenotype observed in HGPS patients. Prog-Tg mice develop left ventricular hypertrophy and aging related diastolic dysfunction with preserved ejection fraction. Furthermore, atheroprotective *eNOS* was downregulated in heart tissue and ECs from Prog-Tg mice, which correlated with increased interstitial and perivascular fibrosis [38]. However, Prog-Tg mice did not show VSMC loss and atherosclerosis as reported in patients and VSCMC specific progerin mice [26]. These data indicated that VSMC pathology and atherosclerosis is likely linked to progerin expression in VSMCs, while expression of progerin in ECs leads to cardiac diastolic dysfunction and extensive fibrosis [38], other major CVD pathologies observed in HGPS patients [24]. The control LA-Tg mice and WT mice did either not develop a phenotype at all or showed only a very mild phenotype.

On the cellular level, EC dysfunction in Prog-Tg mice was reflected by misalignment of nuclei and actin fibers in the aortic endothelial layer and an impaired shear stress response [38], consistent with previous reports on an impaired mechano-response in fibroblasts expressing lamin A mutants [39] [40] [41]. In Prog-Tg ECs we found defects in nuclear envelope proteins involved in mechanotransduction, such as SUN1/2 and emerin, which are members of the Linker of Nucleoskeleton and Cytoskeleton Complex (LINC) that mechanically couples cytoskeletal and nuclear components across the nuclear envelope [42]. Moreover, emerin is known to affect F-actin/G-actin (filamentous actin/ global actin) levels [38] and the mechanoresponsive myocardin-related transcription factor-A (MRTF-A) [43]. MRTF-A is a co-transcription factor of the serum response factor (SRF) and is known to mediate a fibrotic effect in response to pro-atherogenic stimuli by activating gene expression of cytoskeletal components and by downregulating atheroprotective *eNOS* [44] [45] [46] [47] [48]. Accordingly, we also found F-actin/G-actin upregulated and MRTF-A deregulation in Prog-Tg ECs [38].

Overall these data led us to our initial working model which suggests that progerin accumulation at the nuclear lamina results in upregulation of SUN1/2, formation of emerin aggregates and an increase of F-actin. These changes lead to the formation of more rigid nucleocytoskeletal links. We could further show that MRTF-A binds to the promoter of the atheroprotective eNOS and MRTF-A activity is required to downregulate eNOS and its secreted product NO in ECs, leading to a paracrine pro-fibrotic effect. Overall, these data showed for the first time that endothelial specific progerin expression leads to profibrotic changes resulting in cardiovascular defects and premature death in mice, involving an impaired MRTF-A/eNOS signaling axis [38].

Our next focus was to find out at mechanistic detail, how endothelial progerin expression can lead to a dysfunctional endothelium and to a HGPS like CVD phenotype. In particular we wanted to address which signaling pathways are affected upon progerin expression in the endothelium in order to delineate specific disease mechanisms. Furthermore, we aimed at addressing the previously observed paracrine effect of Prog-Tg ECs. Given the important role of endothelial cell senescence in the development of CVD we wanted to test whether progerin expression in our Prog-Tg mouse model leads to endothelial cell senescence. Moreover, we investigated whether progerin induced senescent endothelial cells can influence surrounding cells and tissues through secretion of an endothelial specific SASP.

In our second study we performed messenger RNA sequencing (mRNA-seq) and could show that progerin expression in the endothelium leads to a significant deregulation of many genes (Table 4, Table 5). In particular we noticed upregulation of genes involved in pro-inflammatory and pro-fibrotic signaling pathways and in the senescence signaling pathway p53 [49]. p53 is a transcription factor with a pro-apoptotic function upregulated upon various stresses, particularly genotoxic stress. Under normal conditions p53 is expressed at very low levels, upon DNA damage, p53 accumulates in the nucleus mediated through post-translational modifications and increased stability, resulting in cell cycle arrest and either DNA repair or apoptosis, which depends on the extend of DNA damage [50]. Furthermore, our transcriptome analysis revealed an upregulation of immune molecules such as cytokines, chemokines and interleukins, of pro-fibrotic molecules like TGF-beta pathway components and of proteases, indicating initiation of a SASP. Moreover, we confirmed a cell non-autonomous paracrine effect of ECs ex vivo, showing that endothelial cells from different tissues lead to upregulation of senescence and SASP markers in surrounding tissues. An in vitro co-culture model also revealed a senescence- and SASP-specific paracrine effect of Prog-Tg ECs to co-cultured fibroblasts. Again, these results were strictly progerin specific since LA-Tg ECs did not show upregulation of senescence and SASP signaling (Table 6, Table 7).

Since miRs are emerging as key regulators of senescence and bona fide members of the SASP [14] [12] we decided to analyze also the miR EC specific signature by performing miR-sequencing (miR-seq). Prog-Tg ECs showed a significant deregulation of many miRs and revealed a senescence associated miR signature with upregulation of many p53 signaling-pathway associated miRs (Table 8, Table 9). In order to address a systemic effect, we also performed miR-seq of plasma samples originating from Prog-Tg mice (Table 12, Table 13). An overlay of deregulated miRs in Prog-Tg ECs and in plasma samples of Prog-Tg animals showed senescence-associated miR34a-5p and miR31-5p as commonly deregulated miRs. Especially miR34a-5p was a very interesting hit since it is a previously reported senescence associated miR (SA-miR) [15] [51] as well as a well-established cardiovascular disease mediator and biomarker [52] [53] [54]. Moreover, we found miR34a-5p upregulated in lung and heart tissue of Prog-Tg animals. Importantly, miR34a-5p and p21 were both found upregulated in the

atheroprone aortic arch regions of Prog-Tg mice. These findings suggested on the one hand a high relevance of miR34a-5p for cardiovascular pathology in HGPS and geriatric patients and a link between mechanical stress and upregulation of senescence markers and SA-miRs on the other hand.

Mechanistically, inhibition of miR34a-5p led to a reduction of p53 levels and of the late-stage senescence marker p16, leaving p21 unaffected. p53 knockdown led to a reduction of miR34a-5p and p21 levels, while only moderately affecting SASP. These data strongly suggest that miR34a-5p reinforces senescence through two different branches, the p53 and the p16 branches, in progerin expressing endothelial cells maintaining a senescence phenotype synergistically.

Overall our two publications suggest a model in which endothelial specific progerin expression leads to an increased mechanical stress through deregulation of nuclear membrane bound proteins like SUN1, SUN2 and emerin, which in turn leads to an increase of F-actin/G-actin levels and of MRTF-A pro-fibrotic and pro-atherogenic intrinsic and paracrine signaling [38]. A constantly increased mechanical stress leads to the activation of p53 senescence signaling and its target miRs, including miR34a-5p. We observed an intrinsic senescence signaling with an increase of the p53/p21 and the p16 senescence signaling branches and of SA-miRs, like miR34a-5p and miR31-5p. Moreover, we confirmed upregulation of many SASP members in Prog-Tg ECs, including pro-inflammatory and pro-fibrotic mediators. Presumably, through EC-mediated secretion of such SASP members and of SA-miRs, a paracrine senescence signaling network is established via which ECs influence their surrounding cells and tissues. To this end we confirmed immune cells attraction and infiltration in lung and liver tissues and cardiac fibrosis. Collectively, our data propose that Prog-Tg ECs through an increased mechanical stress upregulate senescence and SASP signaling intrinsically and establish a paracrine senescence and SASP signaling network leading to a systemic senescence effect.

As mentioned above, it has recently been shown that endothelium derived sEV can play an important role in the pathogenesis of CVD, but can also serve as prognostic biomarkers [55]. Moreover, it has been demonstrated that ECs can communicate with their surrounding microenvironment through secretion of sEV. In particular, an atheroprotective communication between shear stress responsive endothelial cells and smooth muscle cells (SMCs) was shown to be mediated through secretion of sEV containing atheroprotective miRs by endothelial cells and uptake by SMCs [56]. Moreover, communication between endothelial cells and immune derived cells through secreted sEV are emerging as important regulators of different stages of CVD development [57]. Interestingly, senescent endothelial cells showed an altered sEV secretome which contributed to the formation of CVD [20].

Given the important role that sEV in endothelial play in the communication with other cell types and the novel role of miRs as members of the SASP, we wanted to check the miR content of sEV secreted by Prog-Tg ECs. In our study that is currently still **unpublished data** we isolated specifically the exosome containing fraction of secreted sEV and performed miR-sequencing of the exosome contained miRs. We characterized the isolated exosomes using a nanoparticle track analyzer (NTA) and electron microscopy in order to confirm that the isolated fraction was indeed the exosome containing fraction (unpublished data). Prog-Tg EC secreted exosomes revealed only three miRs significantly upregulated, miR133a-3p, miR21a-3p and miR582-5p. Nevertheless, all three showed a high physiological relevance to out working model [58] [59] [60] [19] [61] [62] and importantly were not found upregulated in exosomes of LA-Tg ECs (unpublished data). Further on, in order to prove that exosome mediated miR transfer can occur in our system we performed an in vitro experiment in which

donor endothelial cells were transfected with a fluorescently labeled miR and then the exosome containing fraction of their secretome was collected and untransfected recipient ECs were incubated with those exosomes. Interestingly, after 24 hours of incubation the recipient ECs showed the fluorescent signal of the labelled miR, indicating an exosome mediated miR transfer between endothelial cells.

Endothelial cell communication with the surrounding microenvironment via miR containing sEV raises interesting aspects for CVD pathology and therapy, but also for the physiological function of the cardiovascular system. In our unpublished data we show that Prog-Tg ECs have a specific miR containing sEV signature and that exosome mediated miR transfer between endothelial cells can occur in our cell system. Further analysis is needed to determine the specific roles of the exosome enclosed secreted miRs in Prog-Tg ECs and to investigate whether endothelial to endothelial cell communication through exosomes occurs also in vivo.

4. First peer reviewed publication

Status of manuscript and submitters contribution

Our first peer reviewed manuscript `` Endothelial progerin expression causes cardiovascular pathology through an impaired mechanoresponse `` was accepted for publication in November 2018 and published online in February 2019 in the medical research article *Journal of Clinical Investigations* (https://www.jci.org/).

My personal contribution to the publication of this manuscript included performing two key experiments and contributing to several other experiments. Moreover, I helped in establishing key experimental procedures for the isolation of endothelial cells, the setup of the in vitro co-culture experiments and the Chip-qPCR with primary cells.

The first experiment that I conducted was the in vitro co-culture experiment of primary ECs with primary fibroblasts (Figure 7E). This experiment was performed in absence as well as in presence of the MRTF-A inhibitor and was therefore crucial for establishing the role of MRTF-A in the paracrine pro-fibrotic effect mediated by Prog-Tg ECs to co-cultured fibroblasts. Further on, the results of this experiment supported the already previously by us proven pro-fibrotic in vivo effect in Prog-Tg mice, by confirming a paracrine pro-fibrotic effect also in an in vitro co-culture setup.

The second experiment that I conducted was the Chip-qPCR for MRTF-A (Figure7D). This experiment was also very important since it proved that MRTF-A binds to the promoter of eNOS and downregulates its expression in Prog-Tg ECs. Therefore, it helped us getting a better mechanistic insight into the deregulated signaling pathways in Prog-Tg ECs.

Moreover, I contributed in conducting the in vivo measurements depicted in Figure 2 D-G and the gene expression experiments in Figure 3D.

Publication: Endothelial progerin expression causes cardiovascular pathology through an impaired mechanoresponse

The Journal of Clinical Investigation RESEARCH ARTICLE

Endothelial progerin expression causes cardiovascular pathology through an impaired mechanoresponse

Selma Osmanagic-Myers,[1,2] Attila Kiss,[3] Christina Manakanatas,[1,2] Ouafa Hamza,[3] Franziska Sedlmayer,[1] Petra L. Szabo,[3] Irmgard Fischer,[1] Petra Fichtinger,[1] Bruno K. Podesser,[3] Maria Eriksson,[4] and Roland Foisner[1]

[1]Max F. Perutz Laboratories (MFPL), Department of Medical Biochemistry, Medical University of Vienna and University of Vienna, Vienna Biocenter (VBC), Vienna, Austria. [2]Department of Biotechnology, University of Natural Resources and Life Sciences (BOKU), Vienna, Austria. [3]Ludwig Boltzmann Cluster for Cardiovascular Research at the Center for Biomedical Research, Medical University of Vienna, Vienna, Austria. [4]Department of Biosciences and Nutrition, Karolinska Institutet, NEO, Huddinge, Sweden.

Hutchinson-Gilford progeria syndrome (HGPS) is a premature aging disorder characterized by accelerated cardiovascular disease with extensive fibrosis. It is caused by a mutation in *LMNA* leading to expression of truncated prelamin A (progerin) in the nucleus. To investigate the contribution of the endothelium to cardiovascular HGPS pathology, we generated an endothelium-specific HGPS mouse model with selective endothelial progerin expression. Transgenic mice develop interstitial myocardial and perivascular fibrosis and left ventricular hypertrophy associated with diastolic dysfunction and premature death. Endothelial cells show impaired shear stress response and reduced levels of endothelial nitric oxide synthase (eNOS) and NO. On the molecular level, progerin impairs nucleocytoskeletal coupling in endothelial cells through changes in mechanoresponsive components at the nuclear envelope, increased F-actin/G-actin ratios, and deregulation of mechanoresponsive myocardin-related transcription factor-A (MRTFA). MRTFA binds to the *Nos3* promoter and reduces eNOS expression, thereby mediating a profibrotic paracrine response in fibroblasts. MRTFA inhibition rescues eNOS levels and ameliorates the profibrotic effect of endothelial cells in vitro. Although this murine model lacks the key anatomical feature of vascular smooth muscle cell loss seen in HGPS patients, our data show that progerin-induced impairment of mechanosignaling in endothelial cells contributes to excessive fibrosis and cardiovascular disease in HGPS patients.

Introduction

Hutchinson-Gilford progeria syndrome (HGPS) is a rare, progressive, premature aging disease characterized by growth retardation, alopecia, loss of subcutaneous fat, aged-looking skin, bone abnormalities, and osteoporosis (1–3). A hallmark of HGPS is severe atherosclerosis in childhood characterized by left ventricular (LV) diastolic dysfunction associated with LV hypertrophy (4, 5). Cardiovascular features in HGPS include a spectrum of early- to late-stage collagen-rich plaques with a primary vascular pathology of severe vascular smooth muscle cell (VSMC) loss in large arteries (4, 6, 7) and massive fibrosis in the adventitial layer (4), hyaluronan accumulation, and calcification of blood vessels (8). These changes increase aortic stiffness and cardiac afterload, presumably causing LV hypertrophy and myocardial infarction in patients at a mean age of 14.6 years (9).

HGPS is caused by mutations in *LMNA*, encoding lamin A and C. Lamins are major components of the nuclear lamina, a complex protein meshwork underlying the inner nuclear membrane that provides shape and mechanical stability to the nucleus and interacts with heterochromatin (10). Lamin A is expressed as prelamin A and posttranslationally processed in a multistep pathway, including C-terminal farnesylation and carboxymethylation, followed by proteolytic cleavage of the modified C-terminal 15 amino acids, yielding nonfarnesylated and noncarboxymethylated mature lamin A (10). HGPS is predominantly caused by a dominant 1824C>T mutation in *LMNA* that activates a cryptic splice donor site leading to the formation of an incompletely processed and stably farnesylated prelamin A with a 50–amino acid internal deletion, termed progerin (11, 12).

HGPS-linked cardiovascular features resemble in many aspects those of geriatric cardiovascular disease (CVD) (4, 13–16). Despite the fact that endothelial senescence is a major initiating event in geriatric CVD and atherosclerosis (13, 17), research on CVD in HGPS has mainly focused on VSMCs based on the reports on VSMC depletion in HGPS patients and some murine models (4, 6, 8, 18, 19). The relevance of progerin expression in the endothelium and its contribution to cardiovascular pathologies in HGPS is still unknown. Aging-related changes in the endothelium involve downregulation of atheroprotective pathways such as reduced endothelial NO synthase (eNOS) levels, shear stress insensitivity (20), and activation of proinflammatory molecules ICAM1 and ICAM2 (17) increasing atherosclerosis susceptibility (21, 22). Other key features of aged, dysfunctional arteries include increased stiffening due to structural changes in the extracellular matrix

▶ Related Commentary: p. 492

Conflict of interest: The authors have declared that no conflict of interest exists.

Submitted: March 27, 2018; **Accepted:** November 6, 2018.
Reference information: *J Clin Invest.* 2019;129(2):531–545.
https://doi.org/10.1172/JCI121297.

(ECM) within intimal, medial, and adventitial layers (23), which in turn affect actomyosin-mediated cellular contractility and shear stress response (20, 23).

Only a few studies provide potential mechanistic links between progerin expression and CVD (24, 25). Gene expression profiling in HGPS patient fibroblasts revealed prominent misregulation of ECM genes (26, 27). In addition, progerin expression in cultured cells disturbed nucleocytoskeletal connections and affected the linker of nucleoskeleton and cytoskeleton (LINC) complex (28, 29), suggesting that defective mechanotransduction may play a role in HGPS. Various HGPS mouse models were generated, which show phenotypes that range from severe, leading to premature death (18, 30), to relatively mild (19), and several conditional HGPS mouse models have reported various tissue-specific effects of progerin expression (31–33). In regard to CVD, a recently reported mouse model with specific vascular smooth muscle expression of progerin presented VSMC loss and accelerated atherosclerosis (6), but hitherto endothelium-specific HGPS mice have not been reported. Based on the importance of age-related changes of the endothelium in CVD we generated a transgenic mouse model with progerin expression selectively in the endothelium (*Prog-Tg*). *Prog-Tg* mice develop LV hypertrophy and diastolic dysfunction, and myocardial interstitial and perivascular fibrosis, phenocopying many aspects of the HGPS cardiovascular pathology. Our data suggest that progerin expression in endothelial cells (ECs) causes severe cardiovascular pathology through deregulated antifibrotic pathways but does not cause VSMC loss. Mechanistically, progerin expression impaired nucleocytoskeletal coupling and shear stress response in ECs leading to impaired mechanoresponsive myocardin-related transcription factor A (MRTFA) signaling.

Results

Endothelium-specific expression of progerin leads to cardiovascular pathology. To determine the impact of progerin expression in the endothelium on cardiovascular pathology in HGPS, we established mice expressing progerin exclusively in ECs by crossing transgenic mice carrying tet operon–driven wild-type or HGPS mutant (1824C>T; G608G) lamin A minigenes (32), with transgenic mice expressing a tetracycline-responsive transcriptional activator under the control of the endothelium-specific *Cdh5* promoter (34). Bitransgenic mice expressing human progerin and wild-type lamin A in endothelial tissue are referred to as *Prog-Tg* and *LA-Tg* mice, respectively, and their corresponding single-transgenic *tetop-LA*^{WT} and *tetop-LA*^{G608G} littermates as *Wt*. To verify endothelium-specific expression, we performed immunoblot analyses of EC and non-EC extracts (see Methods) using human lamin A–specific antibodies that do not detect endogenous mouse lamin A. As previously shown (32), the HGPS minigene in *Prog-Tg* mice expressed both the ectopic wild-type human lamin A and progerin in ECs but not in non-ECs, while the wild-type lamin A minigene in *LA-Tg* mice expressed only wild-type lamin A (Figure 1A). *Wt* mice did not express human ectopic lamin A proteins in ECs, confirming a tight regulation from the tet operon. Immunoblots using an antibody detecting both endogenous and ectopic lamin A indicated a 4- and 4.4-fold increase in total lamin A levels in *Prog-Tg* and *LA-Tg* versus *Wt* animals, respectively. Immunofluorescence staining of a *Prog-Tg* lung–derived cell mixture using human lamin A antibodies confirmed exclusive expression of transgenes in endothelial, vascular endothelial cadherin–positive (VE-cadherin–positive) cells (Supplemental Figure 1A; supplemental material available online with this article; https://doi.org/10.1172/JCI121297DS1). Mean fluorescence intensity measurement of progerin signals revealed heterogeneous expression levels among individual cells, as reported in HGPS patients (35), with over 75% of nuclei showing clearly detectable progerin staining (Figure 1B). Furthermore, in cardiac coronary vessels, progerin staining was specifically detected in the intimal but not medial and adventitial layers of the artery (Figure 1C and Supplemental Figure 1B, arrowheads). In cardiac tissue, progerin is only expressed in the PECAM1-positive microvasculature (Figure 1D, arrowheads), but not in cardiomyocytes (arrows). Overall, these data confirmed a tightly controlled, endothelium-specific expression of the transgenes in bitransgenic mice.

Next we analyzed the phenotype of bitransgenic mice. We observed reduced growth of male and female *Prog-Tg* but not *LA-Tg* mice (Figure 1E) compared with *Wt* littermates, and in approximately 40% of *Prog-Tg* but not *LA-Tg* mice sudden death occurred at the age approaching 25 weeks (Figure 1F). Since myocardial infarction is the most common cause of death in HGPS patients (4), we examined the hearts of bitransgenic mice. Increased heart weight to body weight ratios in *Prog-Tg* versus *Wt* littermates and *LA-Tg* animals as well as increased heart weight to tibia length ratios in *Prog-Tg* versus *Wt* mice (Figure 2, A and B) indicated cardiac hypertrophy in *Prog-Tg* mice. Histological examination of heart sections showed thickened left ventricles in *Prog-Tg* versus *Wt* littermates (Figure 2A) and an increased mean cross-sectional area of cardiomyocytes (Figure 2, A and C). Unlike *NppA*, expression of hypertrophy marker *NppB* (36, 37) showed a tendential increase in heart and a significant increase in isolated primary *Prog-Tg* ECs and lung (Supplemental Figure 2A). We next performed transthoracic cardiac echocardiography and subsequent LV pressure characterization to examine cardiac functional parameters in vivo in *Prog-Tg* and *LA-Tg* animals in comparison to *Wt* littermate controls. Assessment of echocardiographic and hemodynamic parameters revealed increased end-diastolic septal wall width (EDSW) and end-diastolic posterior wall width normalized to body weight (EDPW), confirming cardiac hypertrophy (Figure 2, D and E, and Supplemental Figure 2, B and C). Cardiac hypertrophy was accompanied by an increase in LV end-diastolic pressure (LVEDP) and a mild increase in LV systolic pressure (LVSP) (Figure 2, F and G) with preserved ejection fraction (Supplemental Table 1). Furthermore, an increased diastolic wall stress, a trend toward increased dP/dt, and a reduced isovolumic relaxation time (IVRT) (Supplemental Table 1 and Supplemental Figure 2, D and E) in *Prog-Tg* mice implicated restrictive filling consistent with a restrictive diastolic function in *Prog-Tg* mice (38). Altogether, our data point toward LV diastolic dysfunction in *Prog-Tg* mice, which is the most prevalent cardiac abnormality observed in HGPS patients (5).

Since increased LV stiffness is a detrimental factor for LV diastolic function (38), we tested for accumulation of fibrous tissue in the hypertrophic myocardium, using picrosirius red and Masson's trichrome blue staining in heart sections. *Prog-Tg* animals showed significantly increased myocardial interstitial and perivascular fibrosis in comparison with both *Wt* and *LA-Tg* controls (Figure 3A), which is known to impair coronary blood flow and

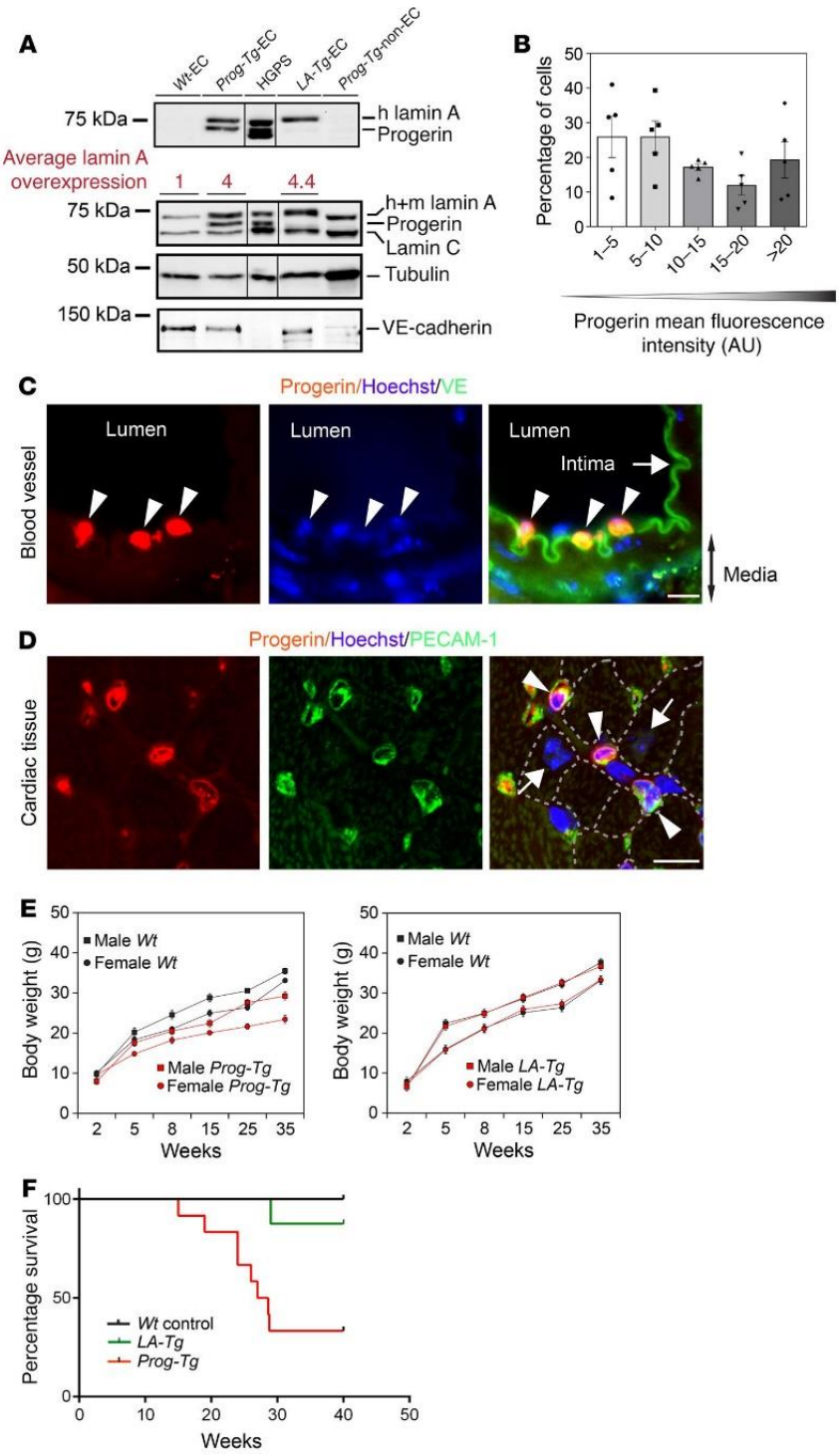

Figure 1. Characterization of *Prog-Tg* mice. (**A**) Immunoblots of indicated lysates using anti–human lamin A/C (detecting transgenes, upper panel), anti–lamin A/C (recognizing human and mouse lamin A/C, lower panel), and anti-tubulin and anti–VE-cadherin as loading controls. Numbers show ratio of total lamin A levels in transgenic over *Wt* animals. Endothelial cells (ECs) from *Wt* (*Wt*-EC), *Prog-Tg* (*Prog-Tg*-EC) and *LA-Tg* (*LA-Tg*-EC) animals; EC-depleted cell mixture from *Prog-Tg* animals (*Prog-Tg*-non-EC); and HGPS patient fibroblasts (HGPS) were analyzed. (**B**) Histogram of mean progerin fluorescence intensities in immunofluorescence images of *Prog-Tg* ECs (see Figure 5C) ($n = 5$ *Prog-Tg* mice, 462 cells in total). (**C** and **D**) Immunofluorescence images of coronary artery (**C**) and cardiac tissue (**D**) from *Prog-Tg* animals stained with antibodies against progerin, VE-cadherin (note green autofluorescence of elastic lamina), and PECAM1, and Hoechst (representative of $n = 3$ *Prog-Tg* animals). Progerin expression is confined to the intimal layer (**C**, arrowheads) and PECAM1-positive cardiac microvasculature (**D**, arrowheads). Dashed lines, cardiomyocyte boundaries; arrows, intima (**C**) and progerin-negative cardiomyocytes (**D**). Scale bars: 10 μm. (**E**) Body weight over time for male and female *Prog-Tg* and *LA-Tg* versus *Wt* littermates. Two-way repeated-measures ANOVA revealed a significant impact for the *Prog-Tg* genotype (females $F = 72.6$, $P < 0.001$, males $F = 65.3$, $P < 0.001$, $n = 6$ littermate pairs), but not for the *LA-Tg* genotype (females $F = 0.517$, $P = 0.493$; males $F = 0.221$, $P = 0.651$, $n = 5$ littermate pairs). Comparison of *Prog-Tg* versus *Wt* revealed at least $P < 0.01$ (Holm-Sidak method) for females and males at more than 5 and 8 weeks, respectively. (**F**) Kaplan-Meier survival plot showing significantly reduced life span of *Prog-Tg* mice ($n = 12$) versus *Wt* littermate controls ($n = 20$) and *LA-Tg* mice ($n = 8$). $P < 0.0001$, log-rank (Mantel-Cox) test; pairwise comparison with Bonferroni's correction of threshold showed significant difference in survival of *Prog-Tg* compared with control, *Prog-Tg* with *LA-Tg*, but not *LA-Tg* with control mice. Data presented as mean ± SEM.

cardiac function (39). Consistent with perivascular fibrosis, we observed an increased adventitial to medial thickness ratio (Figure 3B), indicating adventitial thickening in *Prog-Tg* mice similar to that in HGPS patients (4). In contrast to reports on HGPS patients and mice expressing progerin in all tissues or VSMCs (4, 6), we did not observe loss of VSMCs in *Prog-Tg* mice. Quantification of VSMCs by counting nuclei or by measuring smooth muscle actin–positive (SMA-positive) area in the media showed even a trend toward higher numbers of VSMCs (Figure 3C). Van Gieson staining revealed only subtle elastic tissue distortions, and calcium deposits were absent as tested by von Kossa staining (Figure 3B). Thus, *Prog-Tg* mice did not present severe pathologies in VSMCs, indicating that VSMC loss in HGPS patients is not caused by a dysfunctional endothelium but may be an intrinsic

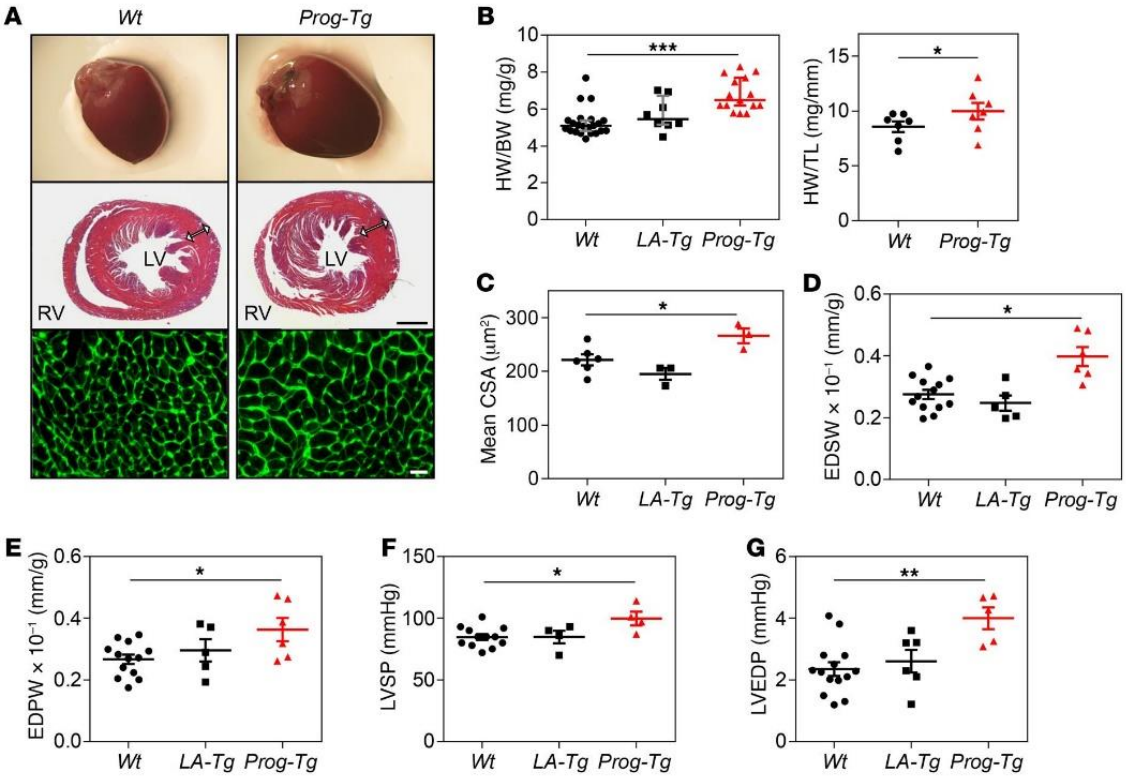

Figure 2. Cardiac hypertrophy and diastolic dysfunction in *Prog-Tg* mice. (**A**) Representative heart images (upper panel) and H&E-stained thin slices of cardiac ventricle cross sections of *Wt* and *Prog-Tg* mice at 6 months (n = 3 per genotype). Arrows indicate thickness of left ventricular free wall. Scale bar: 1,000 μm. High-power view of left ventricular wall area (lower panel) using cell membrane staining with wheat germ agglutinin–fluorescein conjugate for cardiomyocyte area analysis (n = 3 per genotype). Scale bar: 20 μm. (**B**) Diagrams depict heart weight to body weight (HW/BW) ratio in *Wt*, *LA-Tg*, and *Prog-Tg* mice (age >25 weeks, n = 22, 8, and 15 mice, respectively, Kruskal-Wallis 1-way ANOVA). Multiple comparisons (Dunn's method) versus *Wt* control group reveal $^{***}P < 0.001$ for *Prog-Tg* and not significant for *LA-Tg* mice. Data presented as values (dots), median (middle line), and whiskers (25th and 75th percentile). Right panel shows HW to tibia length (TL) ratio in *Wt* and *Prog-Tg* mice (n = 7 littermates; age >27 weeks). $^{*}P < 0.05$ by paired Student's t test. Data presented as mean ± SEM. (**C**) Mean cardiomyocyte cross-sectional area (CSA), n = 6 for *Wt* and n = 3 mice for *LA-Tg* and *Prog-Tg* genotypes, >2,000 cells per genotype. (**D**) End-diastolic septal wall width to body weight ratio (EDSW). (**E**) End-diastolic posterior wall width to body weight ratio (EDPW). (**F**) Left ventricular systolic pressure (LVSP). (**G**) Left ventricular end-diastolic pressure (LVEDP). For **D**–**G**, age >27 weeks, n = 11 *Wt*, n = 5 *LA-Tg*, n = 6 *Prog-Tg*. For **C**–**G**, 1-way ANOVA, pairwise comparisons versus *Wt* control group, $^{*}P < 0.05$ or $^{**}P < 0.01$ for *Prog-Tg* and not significant for *LA-Tg* mice (Holm-Sidak method). Data presented as mean ± SEM.

defect of progerin-expressing VSMCs. The impaired, progerin-expressing endothelium, however, causes a strong profibrotic phenotype in *Prog-Tg* mice. To further assess the progerin-mediated fibrotic pathology we analyzed collagen expression patterns in cardiac tissue and ECs. Fibroblast-derived collagen 3 (*Col3a1*) (40) but not endothelium-derived collagen 4 (*Col4a5*) transcript levels were increased in hearts of *Prog-Tg* versus *Wt* littermates (Figure 3D). In ECs, *Col1a1* and *Col4a5* levels were unaltered and *Col3a1* levels were even decreased, indicating that excessive collagen was not primarily derived from the endothelium. Thus, progerin-expressing ECs may mediate a profibrotic response in surrounding tissue. Collectively, transthoracic cardiac echocardiography, histological analyses, and assessment of collagen levels revealed LV hypertrophy and fibrosis of cardiac tissue in *Prog-Tg* mice, similar to the strong fibrotic phenotype in HGPS patients (4) and during vascular aging (14). These findings suggest that the profibrotic CVD pathology in HGPS may be mediated by progerin-expressing endothelium. Importantly, cardiac fibrosis was observed in *Prog-Tg*, but absent in *LA-Tg* mice, suggesting a progerin-specific pathology.

Downregulation of the antifibrotic eNOS pathway in Prog-Tg ECs. To obtain insight into potential mechanisms underlying how progerin expression in the endothelium contributes to the profibrotic phenotype, we analyzed endothelium-linked pro- and antifibrotic pathways, such as expression of antifibrotic *Nos3* and profibrotic *Icam1* and *Icam2* genes that have been used as prognostic markers for EC dysfunction (21, 22). The antifibrotic effect of endothelium-specific eNOS is mediated through production and secretion of NO that exerts antifibrotic paracrine effects causing downregulation of collagen 3 in surrounding cells (41). *Prog-Tg* mice had significantly reduced levels of *Nos3* transcript in both lung and heart tissue, and eNOS mRNA and protein levels were reduced in *Prog-Tg* ECs, although EC numbers were unaltered (as judged by endothelial marker *Cdh5*; Figure 4, A and B). Accordingly, the total NO metabolite level was significantly reduced in *Prog-Tg* versus *Wt* EC extracts (Figure 4C). To test whether reduced levels of eNOS and

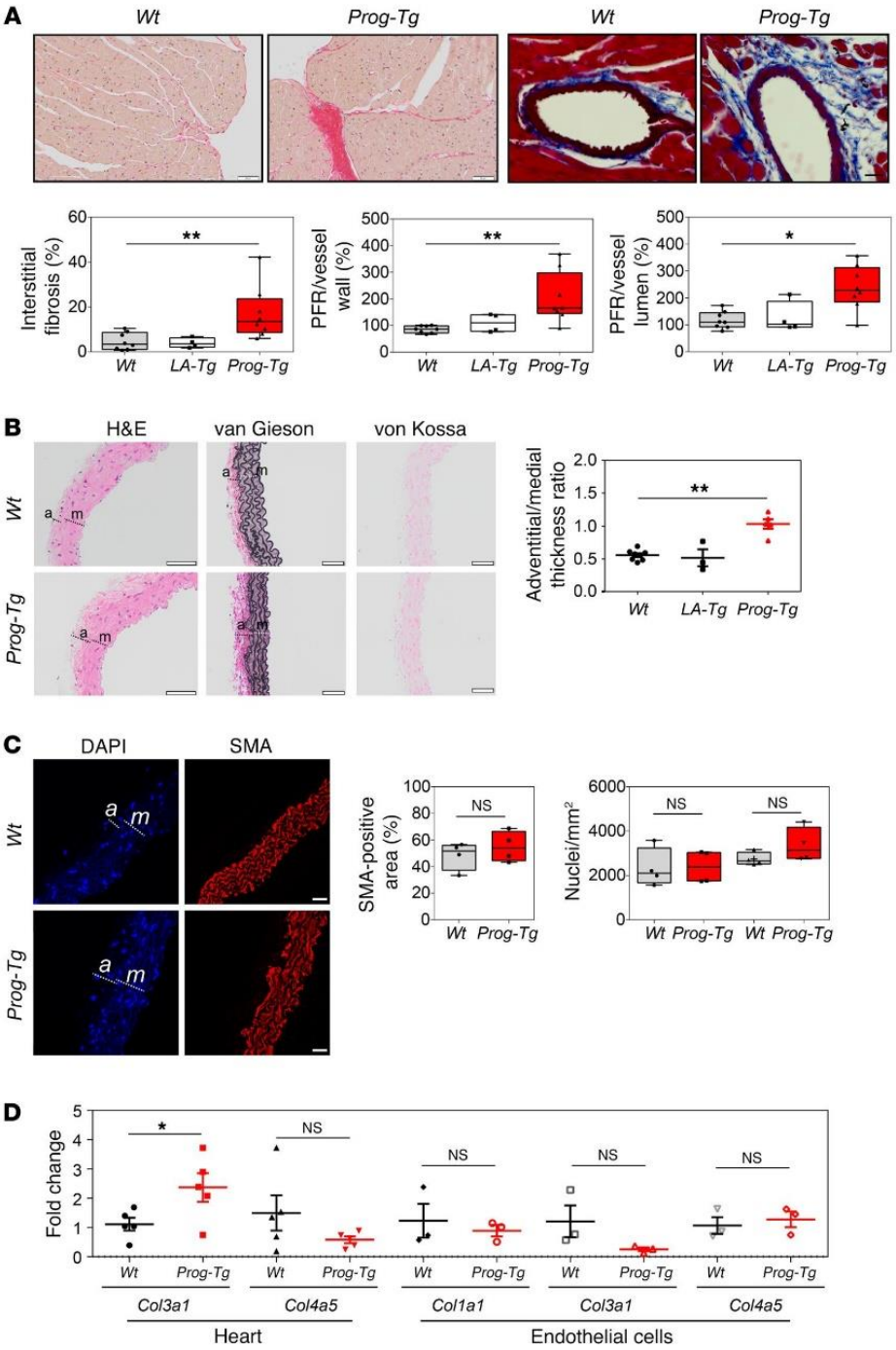

Figure 3. Cardiac fibrosis and adventitial thickening. (**A**) Representative cardiac cross sections stained with picrosirius red (left) and coronary artery sections stained with Masson's trichrome (right) in *Wt* and *Prog-Tg* mice (representative of littermate pairs analyzed below). Scale bars: 50 μm (left panels) and 20 μm (right panels). Left ventricular myocardial interstitial fibrosis and perivascular fibrosis were evaluated (n = 8 *Wt* and *Prog-Tg*, n = 4 *LA-Tg*, age >27 weeks). Perivascular fibrosis ratio (PFR) expressed as the ratio of perivascular collagen area to vessel wall area (PFR, vessel wall) and perivascular collagen area to vessel lumen area (PFR, lumen) is shown. Kruskal-Wallis 1-way ANOVA, multiple comparisons versus *Wt* control group reveal $^*P < 0.05$ or $^{**}P < 0.01$ for *Prog-Tg* and not significant for *LA-Tg* mice (Dunn's method). (**B**) Representative aorta sections stained with H&E, van Gieson, and von Kossa. Graph shows adventitia (a) to media (m) thickness ratio (n = 8 *Wt*, n = 3 *LA-Tg*, n = 5 *Prog-Tg*; age >30 weeks). Note, only mild elastic distortions and no calcification (von Kossa) in *Prog-Tg* aortas. One-way ANOVA, multiple comparisons versus *Wt* control group reveal $^{**}P < 0.01$ for *Prog-Tg* and not significant for *LA-Tg* mice (Dunn's method). (**C**) Representative immunofluorescence images of aortas stained with anti–smooth muscle actin (anti-SMA) and DAPI. Scale bars: 20 μm. Graphs show percentage of SMA-positive area or number of nuclei in adventitia or media (n = 4 per genotype; NS, not significant). Mann-Whitney U test. (**A** and **C**) Data presented as median (middle line) with boxes encompassing 25th to 75th percentile, and whiskers, minimum to maximum values. (**D**) *Col3a1* (n = 5 littermate pairs) and *Col4a5* (n = 6 littermate pairs) mRNA levels in heart tissue (age ~25 weeks), and *Col1a1*, *Col3a1*, and *Col4a5* in ECs (n = 3, three independent experiments using ECs from 3 littermate pairs). Values were normalized to hypoxanthine phosphoribosyltransferase 1 (*Hprt*) and compared to *Wt* littermate (fold change). $^*P < 0.05$ by paired (littermate tissues) and unpaired (cells) Student's t test. NS, not significant. Data presented as mean ± SEM.

NO in *Prog-Tg* ECs affect endothelium-dependent vessel relaxation, we assessed vascular reactivity in isolated aortic segments following administration of endothelium-dependent NO-donor acetylcholine (Ach) or endothelium-independent NO-donor sodium nitroprusside (SNP). Arteries from *Prog-Tg* animals showed a trend toward delayed response to Ach at lower Ach concentration, but not to SNP, with slightly reduced pEC_{50} values (Supplemental Figure 3), indicating a prolonged lag phase in endothelium-dependent vessel relaxation in *Prog-Tg* animals. Therefore, we concluded that the reduced eNOS and NO levels in *Prog-Tg* ECs may be one of the primary causes for the profibrotic response in surrounding tissue but may not be sufficient to significantly impair vascular reactivity. In addition, expression of proinflammatory markers *Icam1* and *Icam2* was not significantly increased in *Prog-Tg* animals (Supplemental Figure 2F).

ECs in Prog-Tg mice show impaired flow-induced shear stress response and aberrant nucleocytoskeletal connections. Next, we investigated potential mechanisms leading to reduced eNOS lev-

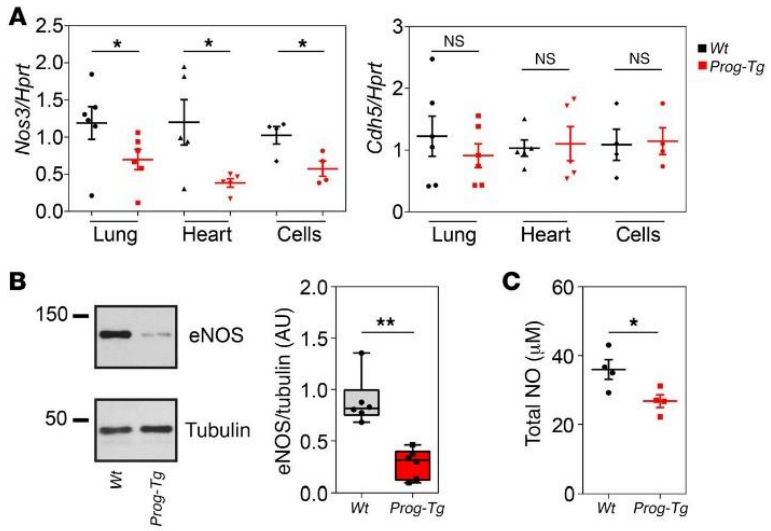

Figure 4. Downregulation of antifibrotic eNOS. (**A**) Expression of *Nos3* and *Cdh5* mRNA in lung, heart, and ECs (n = 6, 5, and 4 littermate pairs, respectively; age ~25 weeks). Values were normalized to *Hprt* and compared to those from *Wt* littermate (fold change). $^*P < 0.05$ by paired (littermate tissues) and unpaired (cells) Student's t test. NS, not significant. (**B**) Quantitative immunoblot analysis of lysates from *Wt* and *Prog-Tg* ECs using eNOS antibodies (n = 6). $^{**}P < 0.01$ by Mann-Whitney U test. Data presented as median (middle line) with boxes encompassing 25th to 75th percentile, and whiskers, minimum to maximum values. (**C**) Reduction in total nitric oxide in *Prog-Tg* and *Wt* cell extracts. Data are presented in micromolar values of total NOx (nitrite and nitrate) per 2×10^5 cells (n = 4 independent experiments). $^*P < 0.05$ by unpaired Student's t test. Data presented as mean ± SEM.

els and activation of profibrotic pathways in *Prog-Tg* mice. The endothelium of blood vessels is constantly exposed to blood flow–mediated shear stress, upon which the cells undergo a complex set of cytoskeletal rearrangements and activate antifibrotic, shear stress–responsive molecules such as eNOS (42). We investigated cell alignment in endothelial sheets of descending aorta by immunofluorescence analysis to test potential defects in shear stress response. Progerin-expressing ECs in endothelial sheets were frequently misaligned, as normally observed at curvatures and branches of vessels (43), in contrast to cells in *Wt* aortas that were well aligned in the direction of flow (Figure 5A, arrows). To quantify cell alignment we measured cell aspect ratios and the alignment angle, the angle between the major cell axis and the axis perpendicular to the flow direction (0°, no alignment; 90°, complete alignment) (44). Both, aspect ratios and alignment angles, were significantly lower in *Prog-Tg* versus *Wt* aortic sheets (Figure 5B), confirming misalignment of mutant cells. To test whether the misalignment of ECs in situ was caused by the inability of progerin-expressing cells to respond to flow, primary ECs were exposed to flow shear stress grown in flow channels. Whereas 3-hour flow shear stress exposure induced cell alignment with parallel bundling of actin stress fibers in *Wt* cells, this effect was much less evident in *Prog-Tg* cells, where merely cortical actin increased and nuclei failed to elongate (Figure 5C). A significantly higher proportion of *Wt* cells showed actin alignment (direction of actin stress fibers within 0°–30° to the cell long axis as described in ref. 45) compared with *Prog-Tg* cells after exposure to flow (Figure 5D). Similarly, cell aspect ratios significantly increased in *Wt* but not in *Prog-Tg* ECs after exposure to flow (Figure 5D), indicating a severe impairment in flow shear stress response of progerin-expressing ECs. As direct connections of the actin cytoskeleton to the nuclear envelope play a central role in force transmission upon shear stress (46), we tested the localization and expression levels of SUN1 and -2, members of the LINC complex. Immunofluorescence microscopy and fluorescence intensity measurements (Figure 6A), and immunoblotting (Figure 6B) revealed SUN1 upregulation and accumulation at the nuclear rim of *Prog-Tg* versus *Wt* ECs, as reported also in HGPS fibroblasts (47). Double immunofluorescence staining and quantification revealed that SUN1 protein levels directly correlated with progerin levels (Figure 6A). A similar accumulation was observed for SUN2 (Supplemental Figure 4). Emerin, a nuclear membrane protein involved in nucleocytoskeletal connections (48) and nuclear mechanoresponse (49), was mislocalized in conspicuous patches in *Prog-Tg* but not *Wt* ECs, while emerin protein levels were unaffected (Figure 6C). As emerin promotes actin polymerization (50, 51), we reasoned that changes in emerin may affect actin organization in *Prog-Tg* ECs. Immunofluorescence microscopy of phalloidin-stained cells revealed abundant actin stress fibers in *Prog-Tg* ECs with frequent actin "knots," suggesting disturbances in actin connections (Figure 6D, arrow). We also found increased F-actin to G-actin ratios in *Prog-Tg* versus *Wt* cells as determined by fluorophore-labeled phalloidin and DNase I staining (Figure 6D). In addition, actin (*Actb*) transcript levels were increased in heart tissue as well as in isolated ECs of *Prog-Tg* animals (Figure 6D). Thus, progerin expression affects the expression and structural organization of actin and impairs nuclear envelope proteins involved in shear stress force transmission.

Impaired MRTFA mechanosignaling leads to reduction of eNOS levels and activation of profibrotic pathways. Given the observed defects in shear stress mechanosensing in *Prog-Tg* ECs, we sought to identify affected mechanosensitive factors that mediate eNOS expression. The *Nos3* promoter harbors a shear stress–responsive element regulated by mechanosensitive transcription factors such as NF-κB, KLF2, and MRTFA (42, 52). In view of the observed changes in actin and emerin in *Prog-Tg* cells and based on previous reports that MRTFA is regulated by F-actin/G-actin ratios in an emerin- and lamin A–dependent fashion (50), we tested MRTFA localization. MRTFA accumulated at the nuclear periphery of *Prog-Tg* cells, in contrast to the relatively even nuclear and cytosolic distribution in *Wt* cells (Figure 7A). Importantly, MRTFA accumulation at the nuclear periphery was not observed in *LA-Tg* ECs (Supplemental Figure 5). MRTFA redistribution was also found in situ in the endothelial lining of *Prog-Tg* aorta in comparison with the relatively uniform MRTFA distribution in *Wt* aorta (Figure 7B). MRTFA is a transcriptional coactivator promoting cardiac hypertrophy and fibrosis (52–54) and acts as a transcriptional suppressor

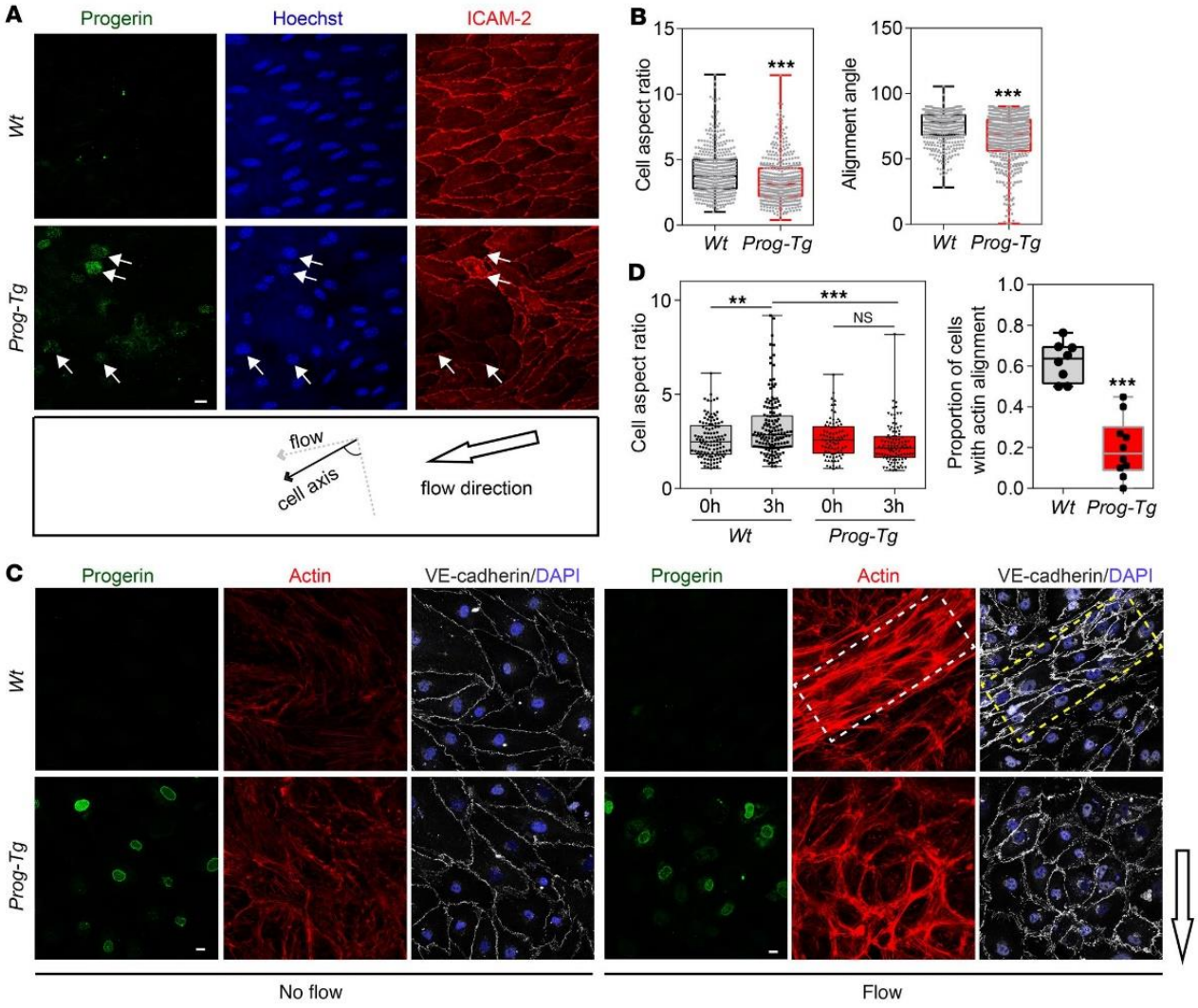

Figure 5. Impaired mechanical response in *Prog-Tg* mice. (**A**) En face view of the endothelial layer in the area of descending aorta isolated from *Wt* and *Prog-Tg* mice and stained with indicated antibodies and Hoechst (DNA) dye. Arrows indicate cells with high progerin levels showing misalignment within aortic sheet (images are representative of $n = 4$ *Wt* and *Prog-Tg* littermate pairs). Scale bar: 10 μm. (**B**) Box plots showing cell aspect ratio and alignment angle (angle between cell major axis and line perpendicular to flow direction) analyzed in equivalent descending aorta regions of *Wt* and *Prog-Tg* littermate pairs ($n > 400$ cells per genotype). $^{***}P < 0.001$ by Mann-Whitney *U* test. (**C**) ECs cultured in flow channels before and after exposure to flow of medium (12 dyn/cm^2) for 3 hours were processed for immunofluorescence microscopy using antibodies and DAPI dye as indicated (images are representative of $n = 3$ independent experiments). Arrow indicates flow direction. Scale bars: 10 μm. (**D**) Box plots showing cell aspect ratios analyzed in *Wt* and *Prog-Tg* ECs after 0-hour (0h) and 3-hour (3h) flow exposure ($n > 150$ cells per condition and per genotype). One-way ANOVA with Dunn's multiple comparisons test revealed $^{**}P < 0.01$ (*Wt* 0h versus *Wt* 3h), $^{***}P < 0.001$ (*Wt* 3h versus *Prog-Tg* 3h), and not significant (NS, *Prog-Tg* 0h versus 3h and all other comparisons). Right panel, proportion of cells with aligned actin stress fibers in ECs after 3 hours of shear stress exposure. Stress fibers were considered aligned if their direction was parallel to or within 30° to the cell major axis, and misaligned if not ($n = 4$; >250 cells per genotype). $^{***}P < 0.001$ by Mann-Whitney *U* test. (**B** and **D**) Data presented as median (middle line) with boxes encompassing 25th to 75th percentile, and whiskers, minimum to maximum values.

of *Nos3* (52, 55). To test whether reduced eNOS levels in *Prog-Tg* mice were caused by MRTFA deregulation, we applied MRTFA inhibitor CCG-203971 to *Wt* and *Prog-Tg* ECs for 24 hours. Administration of MRTFA inhibitor rescued eNOS mRNA levels in *Prog-Tg* ECs, while treatment with the vehicle control (DMSO) had no significant effect, indicating that MRTFA is involved in transcriptional repression of eNOS in *Prog-Tg* ECs (Figure 7C). To test if MRTFA downregulates eNOS expression directly by binding to the *Nos3* promoter as previously shown in aortic ECs (56), we performed chromatin immunoprecipitation (ChIP) using an MRTFA antibody and corresponding IgG control followed by quantitative PCR (qPCR) analyses. MRTFA binding to the *Nos3* promoter was significantly increased in *Prog-Tg* versus *Wt* ECs, while MRTFA binding to a region in the *Nos3* gene body was close to background levels (Figure 7D). Thus, MRTFA directly targets the *Nos3* promoter, suppressing eNOS expression in *Prog-Tg* ECs. To test whether the deregulated MRTFA activity also mediates the paracrine profibrotic signaling of *Prog-Tg* ECs, we set up cocultures of ECs with

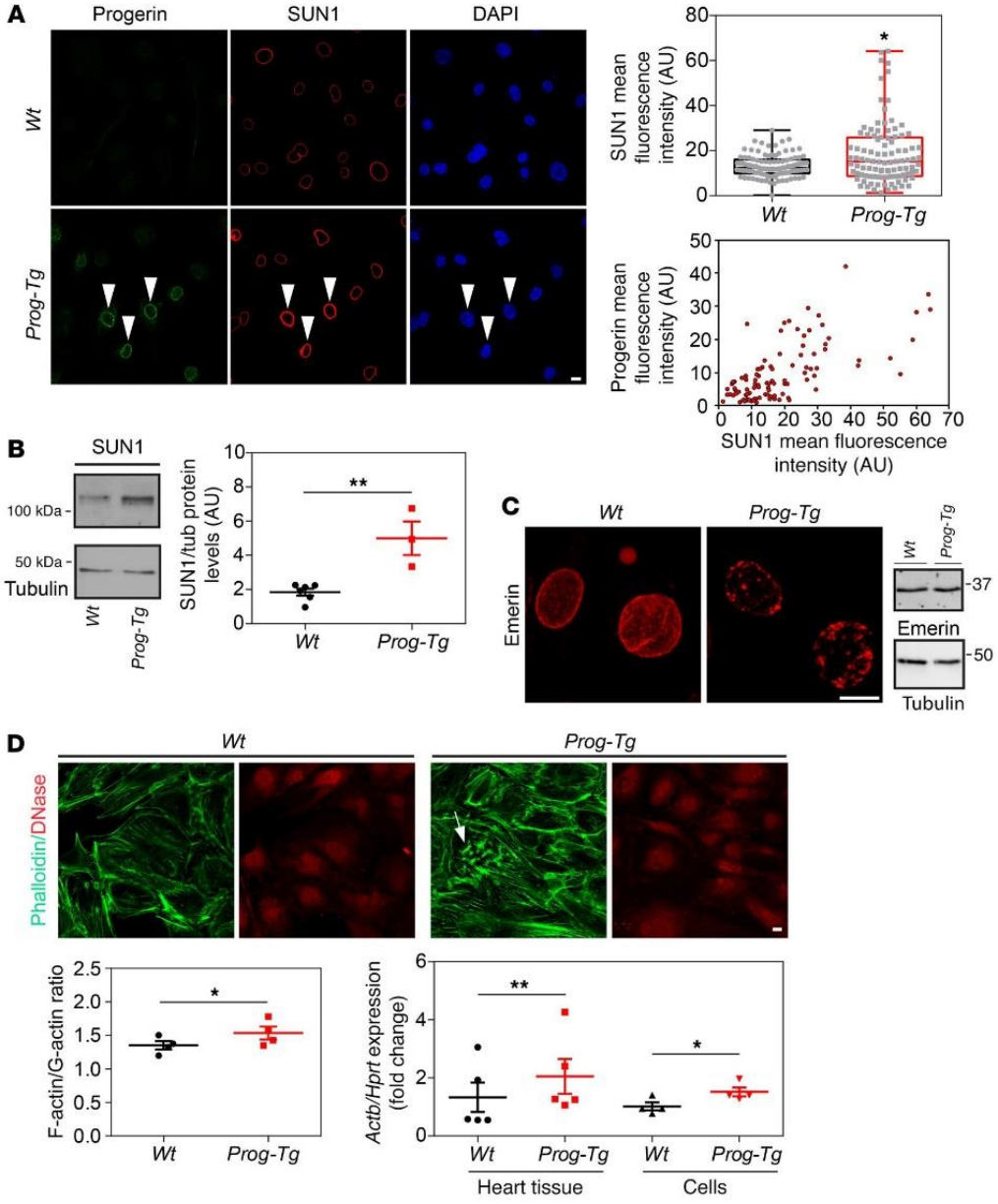

Figure 6. Defective nucleocytoskeletal connections in *Prog-Tg* cells. (**A**) ECs from *Wt* and *Prog-Tg* mice were immunostained with progerin and SUN1 antibodies and DNA dye (DAPI). Arrowheads, cells with high progerin levels show stronger SUN1 staining (images are representative of $n = 3$ independent experiments). Scale bar: 10 μm. Box plots show the distribution of SUN1 mean fluorescence intensities in *Prog-Tg* versus *Wt* ECs ($n = 100$ cells per genotype). Data presented as median (middle line) with boxes encompassing 25th to 75th percentile, and whiskers, minimum to maximum values. $^*P < 0.05$ by Mann-Whitney *U* test. Lower panel, mean progerin fluorescence intensities plotted over mean SUN1 fluorescence intensities in *Prog-Tg* cells. Arbitrary units (AU) of fluorescence, $n = 101$ cells. (**B**) Quantitative immunoblot analysis of *Wt* and *Prog-Tg* endothelial cell lysates ($n = 6$ for *Wt* and $n = 3$ for *Prog-Tg* independent experiments). $^{**}P < 0.01$. (**C**) Projections of confocal *Z* stacks of *Wt* and *Prog-Tg* ECs stained for emerin. Scale bar: 10 μm. Right panel, immunoblot for emerin and tubulin (loading control, images representative of $n = 3$ independent experiments). (**D**) *Wt* and *Prog-Tg* ECs processed for immunofluorescence microscopy using Atto 488–labeled phalloidin and Texas Red–labeled DNase I, quantitatively evaluated to obtain the F-actin/G-actin ratio ($n = 4$ independent experiments). Arrow, actin "knots" in *Prog-Tg* cells. Scale bar: 10 μm. Lower right, expression levels of actin (*Actb*) in heart tissue (age ~24 weeks, $n = 5$ littermate pairs) and ECs ($n = 4$ independent experiments) from *Prog-Tg* and *Wt* littermates. Values were normalized to *Hprt*. $^*P < 0.05$, $^{**}P < 0.01$ by paired (littermate tissue) and unpaired (cells) Student's *t* test (**B** and **D**). Data presented as mean ± SEM.

fibroblasts. Primary *Wt* fibroblasts were cultured in the presence of either *Wt* or *Prog-Tg* ECs that were seeded on top in transwell inserts allowing no direct contact except through secretion of extrinsic factors. Profibrotic effects in fibroblasts were tested by assessing expression of SMA (*Acta2*) and collagen 1 (*Col1*) known to be associated with a myofibroblast switch (57). More than 3-fold higher levels of *Acta2* transcripts were found in fibroblasts cocultured in the presence of *Prog-Tg* ECs compared with those cocul-

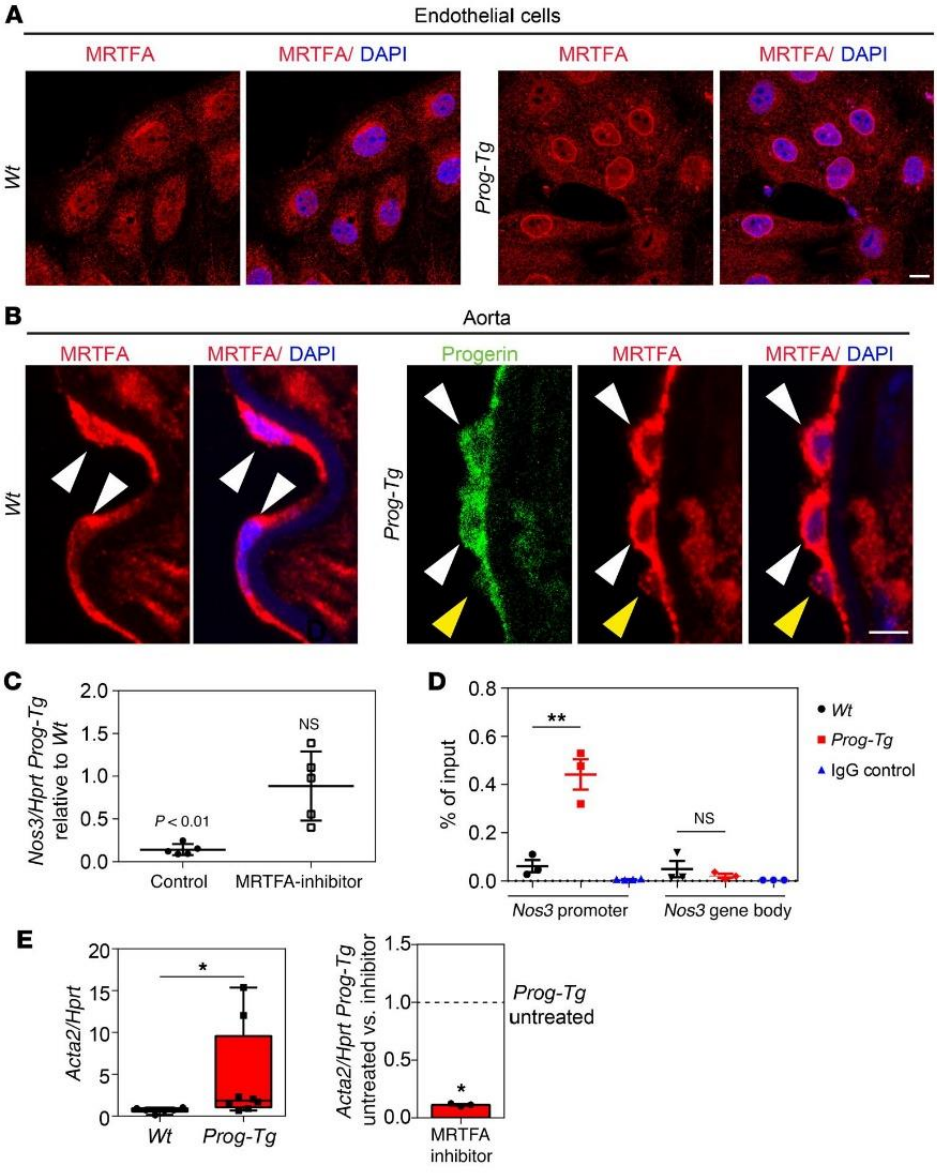

Figure 7. Impaired MRTFA signaling in *Prog-Tg* ECs affects eNOS and profibrotic signaling. (**A**) Immunofluorescence of *Wt* and *Prog-Tg* ECs using MRTFA antibody and DAPI (images are representative of $n = 3$ independent experiments). Scale bar: 10 μm. (**B**) Representative confocal average intensity projections of *Z* stacks from mouse aorta of *Wt* and *Prog-Tg* animals stained with DAPI and MRTFA and progerin antibodies. EC nuclei (arrowheads) lie on internal elastic membrane that displays blue autofluorescence. Arrowheads, MRTFA-positive ECs. Note that MRTFA accumulates at the nuclear periphery of progerin-positive (white arrowheads) but not progerin-negative (yellow arrowheads) ECs ($n = 3$ *Wt* and *Prog-Tg* littermate pairs). Scale bar: 10 μm. (**C**) *Nos3* mRNA in *Wt* and *Prog-Tg* ECs after 24-hour treatment with 15 μM CCG-203971 MRTFA inhibitor or DMSO vehicle control. Values are normalized to *Hprt* and *Nos3*/*Hprt* values in *Prog-Tg* cells are shown relative to values in *Wt* cells after MRTFA-inhibitor and control treatment. *Nos3*/*Hprt* levels in *Wt* cells were arbitrary and set to 1 in both control and CCG-203971 conditions ($n = 5$ independent experiments). *Nos3*/*Hprt* levels in *Prog-Tg* cells relative to *Wt* are not significantly different (NS) after drug treatment, in contrast to control conditions ($P < 0.01$). (**D**) Chromatin immunoprecipitation using anti-MRTFA or goat IgG control. Precipitated DNA was amplified by qPCR with primers spanning *Nos3* promoter or gene body ($n = 3$ independent experiments). $^{**}P < 0.01$ by unpaired Student's *t* test (**C** and **D**). Data presented as mean ± SEM. (**E**) *Acta2* levels normalized to *Hprt* in fibroblasts after 3 days of coculture with *Wt* and *Prog-Tg* ECs either left untreated (left) or treated with 25 μM MRTFA inhibitor CCG-203971 (right). Values were subtracted from those obtained in untreated or CCG-203971–treated fibroblast single cultures ($n = 6$ *Wt*, $n = 8$ *Prog-Tg*, and $n = 3$ inhibitor-treated *Prog-Tg* samples). $^{*}P < 0.05$ by Mann-Whitney *U* test. Data presented as median (middle line) with boxes encompassing 25th to 75th percentile, and whiskers, minimum to maximum values.

tured with *Wt* ECs (Figure 7E). Importantly, the profibrotic effect of *Prog-Tg* ECs on fibroblasts was nearly completely abolished in the presence of MRTFA inhibitor (Figure 7E). A similar MRTFA-dependent increase was observed for *Col1* expression, although it did not reach statistical significance (data not shown).

Overall, our results show that progerin expression in ECs leads to defects in nucleocytoskeletal coupling, in flow stress response, and in MRTFA/eNOS signaling, which in turn induce profibrotic changes, cardiovascular stiffening, and cardiac hypertrophy.

Discussion

Age-related endothelial dysfunction is a prominent initiating event in geriatric CVD and atherosclerosis (13, 17) and is promoted by external insults such as fatty diet, smoking, hypertension, hypercholesterolemia, and increased serum high-sensitivity C-reactive protein, of which only a few are present in patients with HGPS (4, 58). The fact that CVD in HGPS occurs in the absence of most of the classical risk factors suggests that progerin expression directly affects intrinsic properties of the endothelium. So far, vascular pathology in HGPS has been reported to include prominent loss of VSMCs (4, 6, 7), but the contribution of the endothelium to HGPS cardiovascular pathology has not been tested. To address this question we generated a HGPS mouse model with endothelium-restricted progerin expression. Here we show profibrotic changes in the endothelium-specific progerin mice, such as adventitial thickening and increased collagen deposition around coronary arteries, and cardiac interstitial fibrosis, associated with LV hypertrophy and LV diastolic dysfunction. Our data demonstrate that *Prog-Tg* mice phenocopy many aspects of the clinical cardiovascular aberra-

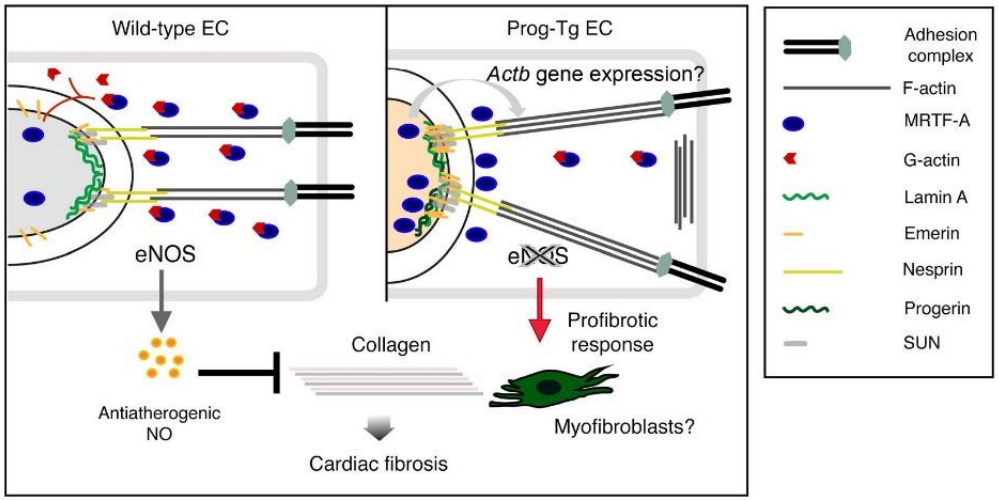

Figure 8. Working model. Progerin accumulation at the nuclear lamina leads to perturbations in F-actin level and actin organization and defects in components involved in nucleocytoskeletal coupling (SUN1/2 and emerin). The defective rigid nucleocytoskeletal links show impaired mechanoresponse and cause MRTFA accumulation at the nuclear periphery. MRTFA or associated complexes exert presumably a positive feedback loop on *Actb* expression (looped arrow). These changes set off the profibrotic signaling cascade (indicated by pale orange color of the nucleus), such as downregulation of eNOS and reduced secretion of NO. Absence of endothelium-derived atheroprotective NO and presumably other unidentified factors leads to increased collagen production in other cell types as shown for fibroblasts through a switch to myofibroblasts, leading to collagen deposition and cardiac fibrosis.

tions in HGPS patients, including the severe profibrotic response and cardiac functional impairment, but they do not present pathologies in the vascular tunica media, such as VSMC loss. Since progerin expression is restricted to the endothelium in *Prog-Tg* mice, the profibrotic cardiovascular pathology in HGPS may be rooted in EC dysfunction, while loss of VSMCs in HGPS is likely caused by intrinsic defects of progerin-expressing VSMCs.

A hallmark of aging-related changes in the endothelium is the reduced secretion of NO, produced by eNOS (20, 59). Endothelium-derived NO is known to mediate endothelium-dependent vasodilation (21) and to exert an antifibrotic paracrine effect on surrounding tissues (41). eNOS and NO levels were significantly reduced in *Prog-Tg* mice and ECs, but *Prog-Tg* aorta showed only a subtle delay in endothelium-dependent relaxation ex vivo. However, other downstream pathways of eNOS/NO, such as the initiation of profibrotic pathways, were clearly affected in *Prog-Tg* mice, as demonstrated by the strong profibrotic response of *Prog-Tg* mice and the profibrotic paracrine signaling of *Prog-Tg* ECs to fibroblasts in cocultures in vitro.

A key feature of healthy atheroprotective blood vessels is their adequate response to shear stress exerted by the blood flow. Thereby a complex set of cytoskeletal rearrangements and nucleocytoskeletal coupling activate atheroprotective and antifibrotic shear stress–responsive pathways such as eNOS (42). Disturbances in flow sensing, which often occurs at branching parts of the arterial tree, impair proper cytoskeletal rearrangements and induce proatherogenic and profibrotic changes including a proinflammatory response, eNOS downregulation, and collagen accumulation. In the present study, we demonstrate a defective cytoskeletal alignment response to shear stress of aortic endothelium and ECs of *Prog-Tg* mice correlating with eNOS downregulation. Our findings are in line with previous reports in other cell systems, showing impaired response of progerin-expressing cells to mechanical stress (60, 61), but, demonstrated for the first time to our knowledge in ECs in vitro and in vivo, our results provide physiological relevance of these defects in HGPS-linked cardiovascular impairment.

Cytoskeletal connections to the nucleus play a central role in the transmission of mechanical forces such as those mediated by shear stress (46, 62) and thus, mutations or impairments in any of the connector molecules, including LINC family members nesprin and SUN1/2 and emerin, were shown to perturb this process (49, 63, 64). We show here severe emerin aggregation and upregulation of SUN1/2 in progerin-expressing ECs, providing a mechanistic explanation for shear stress defects in these cells through aberrant nucleocytoskeletal coupling. In addition, the observed elevated F-actin/G-actin ratio in *Prog-Tg* ECs in conjunction with increased *Actb* transcript levels in tissues and isolated ECs implicates increased cytoskeleton stiffening, expected to hamper the shear stress response. We suggest that actin changes in progerin-expressing cells are rooted in severe aggregation and mislocalization of emerin, which is a key nuclear envelope protein regulating actin polymerization. In line with our hypothesis, recent reports showed that mechanical strain–induced enrichment of emerin at the outer nuclear envelope leads to increased actin polymerization and has a wide range of effects on gene transcription (65). Accordingly, we show aberrant localization of mechanosensitive, F-actin–sensitive, and emerin-regulated transcription factor MRTFA in *Prog-Tg* cells. Importantly, we show that MRTFA inhibition ameliorated the EC-mediated profibrotic paracrine signaling in cocultures, demonstrating a direct involvement of a deregulated MRTFA pathway in the profibrotic effect of progerin-expressing ECs. At a mechanistic level we show that MRTFA binds to the *Nos3* promoter and pharmacological inhibition of MRTFA rescues eNOS levels, suggesting that *Nos3* is a direct MRTFA target gene repressed by MRTFA.

We propose a model (Figure 8) in which progerin accumulation at the nuclear lamina causes upregulation of SUN1/2, emerin aggregation, and F-actin increase, leading to the formation of more rigid nucleocytoskeletal links. Since MRTFA is involved in transcriptional regulation of many cytoskeletal genes (66), including SMA (*Acta2*), it is conceivable that it also exerts a positive feed-back regulation on actin expression. In addition, the MRTFA-mediated downregulation of atheroprotective eNOS results in a decrease of NO secretion by ECs, promoting fibrosis in other, non-endothelial, cell types. In conclusion, we show for the first time to our knowledge that progerin expression in endothelial tissue drives profibrotic changes leading to cardiovascular defects and premature death in mice. Mechanistically, we provide the MRTFA/eNOS axis–rooted mechanosensing defects as the basis for profibrotic changes and vascular insults in HGPS. Our results open new possible intervention strategies for the treatment of progeria and, in view of shear stress insensitivity occurring during normal endothelial aging (20, 23, 67) and of progerin accumulation in arteries of aged individuals (4), our study will also help to elucidate molecular processes of CVD in normal aging and find ways to unwrinkle the aged arteries.

Methods

Generation of bitransgenic mice. Bitransgenic *Prog-Tg* and *LA-Tg* mice were generated by crossing tet operon–driven transgenic mice (C57BL/6J background) carrying either the wild-type (*tetop-LA^{Wt}*) or HGPS mutant (1824C>T; G608G; *tetop-LA^{G608G}*) lamin A minigene (32) with transgenic mice expressing a tetracycline-responsive (TA-responsive) transcriptional activator under the control of the EC-specific VE-cadherin promoter (*Cdh5-tTA* mice, Jackson Laboratories MGI:4437711, *FVB* background, originally generated as described in ref. 34). All experiments were performed with bitransgenic mice backcrossed onto the C57BL/6J background for 4 generations and their corresponding single-transgenic *tetop-LA^{wt}* and *tetop-LA^{G608G}* littermate mice (N4 generation; ~94%). Mice were kept in the absence of doxycycline, allowing constitutive expression of the corresponding transgenes in bitransgenic animals. For genotyping, DNA was extracted from mouse distal phalanx. The following primers were used: DNA lamin A minigene, forward 5′-GCAACAAGTCCAATGAGGACCA-3′ and reverse 5′-GTCCCAGATTACATGATGC-3′; DNA *Cdh5*-tTA, forward 5′-CGCTGTGGGGCATTTTACTTTAG-3′ and reverse 5′-CATGTC-CAGATCGAAATCGTC-3′. For weight and survival curve analysis the indicated number of littermate pairs was monitored for 35 or 40 weeks.

Cells. In all experiments ECs refer to primary ECs isolated from lung (see below), used at a maximum passage number of 3. Primary HGPS patient–derived dermal fibroblast cell line HGADFN003 (2 yr, 10 population doublings [PDs]) was obtained from the Progeria Research Foundation. For assessing EC-specific progerin expression in Figure 1A, a mixed cell population isolated from lungs of *Prog-Tg* mice was depleted of ECs (non-EC) by magnetic bead separation (68). Primary fibroblasts were isolated from lungs of newborn *Wt* (C57BL/6J background) mice by collagenase I treatment (69).

EC isolation and culture. Primary ECs were prepared from lungs of *Wt*, *LA-Tg*, and *Prog-Tg* newborn mice following a protocol adapted from Dong et al. (70). Minced lungs were treated with 200 U/ml collagenase I (MilliporeSigma) for 45 minutes at 37°C and passed through a 19-gauge syringe and a 70-μm cell strainer. After centrifugation, cells were seeded on gelatin-coated (1% w/v) and fibronectin-coated (1 μg/ml) plates in DMEM supplemented with 20% FCS, EC growth supplement (Alfa Aesar, BT-203), 25 mM HEPES, 50 U/ml penicillin, 50 μg/ml streptomycin, 2 mM L-glutamine, 1 mM nonessential amino acids, 1 mM sodium pyruvate, and 139 μg/ml heparin (complete culture medium). ECs were grown to confluence for 3 or 4 days, detached with trypsin, and isolated by magnetic bead sorting using rat anti-ICAM2 antibodies (BD Biosciences Pharmigen, clone 3C4 [mIC2/4], 553326) coupled to sheep anti–rat IgG paramagnetic Dyna-beads (Invitrogen, 11035). For some experiments, sorting was repeated after 3 or 4 days. For collecting EC-depleted cell populations, supernatants of the first magnetic bead separation were seeded on plastic dishes (non-ECs).

Cocultures. ECs (maximum passage number 3) were plated in the inserts, and primary fibroblasts (maximum passage 2) at the bottom of 12-well Transwell plates (Costar Corning Incorporated, 3460; pore size 0.4 μm) separately at a density of 3.6×10^4 cells/cm^2 and 2.4×10^4 cells/cm^2, respectively, and allowed to adhere overnight. After 24 hours, the 2 cell types were placed in coculture by transferring the inserts covered with ECs into wells containing the fibroblasts. On the second day, fibroblasts were either mock treated with DMSO or treated with the MRTFA inhibitor CCG-203971 (Tocris Bioscience). After 3 days of coculture, fibroblast RNA was isolated and qPCR performed. Profibrotic effects were tested by expression of SMA (*Acta2*) and collagen 1 (*Col1a1*). Obtained values were subtracted from values for untreated or CCG-203971 inhibitor-treated fibroblast-only cultures.

Immunoblotting and antibodies. For direct lysis, confluent EC cultures were washed twice with PBS, and overlaid with 50 mM Tris-HCl, pH 6.8, 100 mM DTT, 2% SDS, 0.1% bromphenol blue, and 10% glycerol. Lysates were separated by SDS-PAGE and transferred onto nitrocellulose membranes. Membranes were blocked and incubated with primary antibodies as described previously (69). For protein detection, membranes were incubated with peroxidase-coupled secondary antibodies (Jackson Laboratories) for 1 hour and processed using the Amersham ECL Prime Western Blotting Detection Reagent. Protein bands were quantified using ChemiDoc MP Imaging System with Image Lab Software. The following primary antibodies were used: mouse monoclonal antibody (mAb) against lamin A/C (Santa Cruz Biotechnology, clone E-1, sc-376248), mAb against human lamin A+C (Chemicon, clone JoL2, mab3211, Abcam), goat anti-MRTFA (Santa Cruz Biotechnology, sc-21558), mAb against progerin (Alexis Biochemicals, clone 13A4, provided by Egon Ogris, Medical University Vienna, Vienna, Austria), mAb against α-tubulin (MilliporeSigma, clone B-5-1-2, T5168), mAb against emerin (Leica Biosystems, clone 4G5, NCL-emerin), rabbit anti-emerin (for immunoblotting, Atlas Antibodies, HPA000609), goat anti–VE-cadherin antibodies (Santa Cruz Biotechnology, sc-6458), rabbit anti-PECAM1 (LSBio, LS-B4737), mAb against eNOS (BD Biosciences, 610297), rabbit affinity-purified antibodies against actin (MilliporeSigma, A2066), guinea pig anti-SUN1 and -SUN2 antibodies (a gift from Manfred Alsheimer, University of Würzburg, Würzburg, Germany). See complete unedited blots in the supplemental material.

Histology. Mice (6–8 months old) were euthanized with isoflurane. Tissues were fixed in 4% paraformaldehyde (PFA), embedded in paraffin, and sectioned with a microtome (Leica) at 5 μm. For aortic tissue, PFA-fixed samples were incubated overnight in 20% sucrose in PBS, embedded in OCT (Tissue-Tek), rapidly frozen, and cryosectioned (1 μm thick). Coronal sections at the equator were processed for H&E

and fluorescein-labeled wheat germ agglutinin (Vector Laboratories, FL-1021) staining, and Masson's trichrome/or picrosirius red staining (71) to assess cardiomyocyte cross-sectional area (CSA) and cardiac fibrosis, respectively. For CSA assessment, only round-to-ovoid cells with visible round nuclei from randomly chosen images were analyzed. Samples were examined using a Zeiss Axiophot microscope equipped with an AxioCam camera. For assessment of interstitial fibrosis, the picrosirius red–positive area was determined using the color thresholding method in ImageJ software (NIH). LV interstitial fibrosis was calculated as the sum of all picrosirius red–positive areas divided by the total section surface, in at least 6 images per mouse. Perivascular fibrosis was evaluated as the ratio of perivascular collagen area to vessel lumen area (72) or to vessel wall area (39). Ratios were averaged from images of arteries of more than 10 sections per mouse. All histological evaluations were performed in a blinded manner.

Immunofluorescence microscopy and image analysis. Cells grown in ibidi chambers were fixed in 4% PFA for 10 minutes, permeabilized in 0.5% Triton X-100 in PBS for 5 minutes, and blocked in 3% BSA in PBS. Cells were incubated with primary antibodies (see above) in blocking buffer for 1 hour at room temperature, or in the case of goat antibodies against MRTFA at 4°C overnight. Cells were washed 3 times with PBS and probed with fluorescently labeled secondary antibodies (Thermo Fisher Scientific, DyLight Fluor secondary antibodies) in PBS for 1 hour at room temperature. All samples were counterstained with Hoechst or DAPI (1:10,000 in PBS) for 5 minutes at room temperature and mounted in ibidi Mounting Medium (catalog 50001). For immunofluorescence staining on paraffin-embedded tissue sections, antigen retrieval using a pressure cooker was performed (32) with subsequent staining using the MOM Basic Kit (Vector Laboratories). Images were acquired on a confocal laser scanning microscope (LSM 710, Carl Zeiss) using 100×/1.46 alpha, 63×/1.4, and 40×/1.4 Plan-Apochromat oil immersion objectives. Images were processed in ImageJ and Adobe Photoshop CS4 software. For characterization of cell alignment, the cell aspect ratio, alignment angle, and actin stress fiber alignment were calculated as described (44, 45). Briefly, aspect ratio was determined by dividing the cell long axis by the cell short axis, and alignment angle was measured as the angle between the major cell axis and the axis perpendicular to flow direction using ImageJ software. For actin stress fiber alignment, the proportion of cells with aligned stress fibers after exposure to 3-hour shear stress was determined from analysis of 10 different images obtained from 4 biological replicates of *Wt* and *Prog-Tg* ECs. Stress fibers were considered aligned if their direction was within 0°–30° between the major cell and flow axis. For quantification of Atto 488–phalloidin and Texas Red–DNase fluorescence intensities, images were captured using identical exposure times for *Wt* and *Prog-Tg* cells and unprocessed raw data were used. Digital images for production of printable figures were adjusted for brightness and contrast equally for *Wt* and *Prog-Tg* cells and exported to Adobe Illustrator.

F-actin/G-actin assay. Cells were processed as for immunofluorescence except that 4% PFA was prepared in cytoskeleton buffer (10 mM MES, 3 mM $MgCl_2$, 138 mM KCl, 2 mM EGTA, 320 mM sucrose, pH 6.1) (73). For G-actin staining we used Alexa Fluor 594 Deoxyribonuclease I conjugate (Molecular Probes) and for F-actin phalloidin–Atto 488 (MilliporeSigma).

Shear stress assay and en face aortic preparations. Cells (1.5×10^4) were grown on 0.2% gelatin– and 1 μg/ml fibronectin–coated flow chambers (80601, ibidi) and left to adhere for approximately 24 hours. Cells were exposed for 3 hours to flow generating a shear stress of 12 dynes/cm^2 (equivalent to flow in human arteries) (74). En face aorta preparations were performed as described previously (68). Briefly, animals were sacrificed via isoflurane inhalation, the chest cavity was cut open, the aorta exposed and washed free of blood by perfusing in situ with 2 mM EDTA in PBS, with the right atrium open to allow free flow. The aorta was dissected free from surrounding tissue and slit opened longitudinally. The aorta was pinned flat (with the intima surface up) on a silicone cell culture dish and processed for immunofluorescence staining.

RNA isolation and gene expression analysis. Heart and lung tissues were disrupted and homogenized using ceramic beads in RLT buffer (Qiagen Mini Kit) in a Precellys 24 tissue homogenizer according to the manufacturer's protocols (Bertin Instruments). RNA from tissues and cells was isolated using the RNeasy Mini Kit (Qiagen), and total RNA was quantified by a spectrophotometer (NanoDrop Technologies, ND-1000). cDNA was generated using RevertAid reverse transcriptase (Thermo Fisher Scientific). qPCR was performed using the primers listed in Supplemental Table 2. All reactions were done in triplicate on an Eppendorf RealPlex 2 Mastercycler with KAPA SYBR Green PCR master mix (Peqlab) according to the manufacturer's instructions. Results were normalized to expression of *Hprt* and presented as fold increase relative to *Wt* littermate animals based on the ΔΔCt method.

NO measurement. Cells plated in 12-well plates were lysed in lysis buffer (0.5% Triton X-100, 20 mM Tris-HCl, pH 7.2, 137 mM NaCl, 10% glycerol, 5 mM EDTA) supplemented with a protease inhibitor cocktail tablet (Roche), sheared with a 27-gauge needle, and cleared at 16,000 *g* for 15 minutes. Total NO content was determined by measuring nitrite with Griess reagent (Arbor Assays). Briefly, samples were diluted 1:3 in assay buffer (Arbor Assays) and filtered through spin filters (10 kDa cutoff; Corning Spin-X UF 500, 431478) to remove protein. In order to assay for total NO, nitrate was first converted to nitrite with NADH reductase followed by addition of color reagents, sulfanilamide, and *n*-(1-naphthyl)ethylenediamine. Absorbance was measured at 550 nm using a microplate reader. Nitrite concentration was determined using nitrite standards provided by the manufacturer.

ChIP. ChIP was performed as previously described (75) with slight modifications. Briefly, chromatin was cross-linked with 1% formaldehyde, cells were incubated in lysis buffer (1% SDS, 0.01 M EDTA, 0.05 M Tris pH 8.1, 0.1 mM PMSF in isopropanol) and DNA was fragmented into approximately 500-bp fragments using a Bioruptor (Diagenode Pico Bioruptor). Aliquots of lysates containing 13 μg chromatin were used for immunoprecipitation using anti-MRTFA (Santa Cruz Biotechnology, sc-21558) or goat IgG (76). Cross-links were reversed by heating at 65°C in the presence of 0.2 M NaCl and DNA fragments were recovered using the ChIP DNA Clean and Concentration Kit from Zymo Research (catalog D5205). Primers for the promoter region (Supplemental Table 2) were located within 400 bp upstream of the transcription start site (52).

Transthoracic echocardiography. Echocardiography was performed using a Vevo 2100 Imaging System with a 40-MHz linear probe (Visualsonics). The animals were anesthetized by 1%–1.5% isoflurane. ECG monitoring was obtained via limb electrodes. For the LV function and dimension analysis, parasternal long-axis view and short-axis view were obtained. For each parameter, a mean of 3 cardiac cycles in each view was used. Doppler mitral flow profiles were acquired using pulsed-wave Doppler in the apical 4-chamber view. Attention

was paid to place the sample volume at the mitral leaflets tip parallel to the blood to record the maximal flow velocities. Isovolumic relaxation time (IVRT) measurement was performed by simultaneously recording pulsed-wave Doppler of the mitral and aortic flow. IVRT was measured as the time interval between aortic valve closure and mitral valve opening. E′ was obtained by tissue Doppler in a 4-chamber view by placing the velocity sample at the septal mitral annulus. E′ indicated the peak mitral annular velocity during early filling.

Assessment of LV hemodynamic function in vivo. Mice were anesthetized with a mixture of ketamine and xylazine and analgesic therapy was applied subcutaneously with buprenorphine 0.12 mg/kg body weight. The thorax was opened and a microtip catheter (SPR-1000, Millar Instruments) was inserted into LV chamber. Hemodynamic parameters such as LVSP, LVEDP, heart rate (HR), and LV contractility performance (dP/dt) were continuously registered in a Powerlab 8/30 system with LabChart (v7.3.2) software (both ADInstruments). Systolic and diastolic wall stress were computed accordingly: LVP × LV radius/(2 × wall thickness) (77). The LV radius and LV wall thickness were assessed by echocardiography.

Assessment of vascular reactivity in isolated aortic rings. The thoracic aorta was dissected and placed in cold physiological buffer: 119 mM NaCl, 4.7 mM KCl, 2.5 mM $CaCl_2 \times 2H_2O$, 1.17 mM $MgSO_4 \times 7H_2O$, 20 mM $NaHCO_3$, 1.18 mM KH_2PO_4, 0.027 mM EDTA, 10.5 mM glucose; bubbled with a mixture of 95% O_2 and 5% CO_2, resulting in pH 7.4. Aortic rings (2–3 mm) were mounted onto a multichamber isometric myograph system (Model 620M, Danish Myo Technology) and equilibrated at 37°C. The resting tension was reached by the normalization process using the ADInstuments Normalization module, where the segments of aorta were normalized to their length and diameter. At the beginning of each experiment, the ability of the preparation to develop a contraction was assessed by exposing the aorta segments to a high KCl solution (124 mM). Endothelium-dependent relaxations were determined by administration of cumulatively increasing concentrations of acetylcholine (10^{-9} to 10^{-5} M, MilliporeSigma) to aortas precontracted with phenylephrine (10^{-10} to 10^{-6} M, MilliporeSigma). The aorta segments were then washed 3 times every 10 minutes for 30 minutes. The endothelium-independent relaxation was tested by sodium nitroprusside (SNP, 0.1 nM to 10 μM, Merck), following precontraction with phenylephrine (10 μM, MilliporeSigma). Data were recorded and analyzed with the LabChart Pro evaluation program (ADInstruments).

Statistics. Data are presented as the mean ± SEM or median with minimum and maximum values (whiskers). All experiments using *Wt* and *Prog-Tg* ECs were performed at least 3 times using different primary cells isolated from corresponding littermate pairs. Statistical analyses were performed using either SigmaPlot software or GraphPad Prism statistical software. Comparisons of longitudinal data for growth curve analysis were done with 2-way repeated-measures analysis of variance (ANOVA) with subsequent Holm-Sidak post hoc test. If 3 independent groups were evaluated, data were analyzed using 1-way ANOVA. Comparison of 2 groups was made by unpaired Student's 2-tailed *t* test. A paired *t* test was used in cases of experiments with littermate pairs. For evaluations of non-normally distributed data, a nonparametric Mann-Whitney rank-sum test was used. Data were considered statistically significantly different if $P < 0.05$. For comparisons among multiple groups, we used a 1-way ANOVA with Dunn's multiple comparisons test, except where indicated otherwise. Curves in Supplemental Figure 3 were generated using a nonlinear fit model in GraphPad Prism.

Study approval. All mouse experiments were approved by the regional Ethics Committee for Laboratory Animal Experiments at the Medical University of Vienna and the Austrian Ministry of Science Research and Economy (66.009/0321-WF/V/3b/2016), according to Austrian Law BGBI. I Nr.114/2012 (TVG2012) and in accordance with the Guide for the Care and Use of Laboratory Animals published by the US National Institutes of Health (NIH Publication No. 85-23, revised 1996).

Author contributions

SOM conceived of, performed, and analyzed experiments, prepared figures, and cowrote the manuscript. RF conceived of experiments and cowrote the manuscript. OH, AK, and BKP provided advice on in vivo cardiac data. OH and AK performed and evaluated transthoracic echocardiography and left ventricular pressure characterization, and PLS and AK performed ex vivo vessel reactivity assays, within the group of BKP. All above listed authors edited the manuscript. CM, FS, IF, and PF performed experiments. ME generated and tested mice carrying lamin A minigenes.

Acknowledgments

We acknowledge Johannes Grillari (BOKU) and Laura Isabelle Meszar for providing expertise and assistance, respectively, in the establishment of coculture experiments. We thank Azra Agic, Sabrina Waitz, Nana Naetar-Kerenyi, Philipp Ausserhofer, and Milat Inci for assistance in several experiments. We acknowledge grant support from the Austrian Science Fund (FWF, T 584-B23, P 29668-B28) to SOM and (P 26492-B20) to RF, Herzfelder'sche Familienstiftung (AP00678OFF/KP00678OFF) to SOM, and from the Progeria Research Foundation (PRF 2016-64) and Carly Cares (http://teamcarlyq.com/) to RF.

Address correspondence to: Roland Foisner, Medical University Vienna, Max F. Perutz Laboratories, Dr. Bohr-Gasse 9, A-1030 Vienna, Austria, Phone: 43.1.4277.61680; Email: roland.foisner@meduniwien.ac.at. Or to: Selma Osmanagic-Myers, Department of Biotechnology, University of Natural Resources and Life Sciences (BOKU), Muthgasse 18, A-1190 Vienna, Austria. Phone: 43.1.4277.61671; Email: selma.osmanagic-myers@boku.ac.at.

1. DeBusk FL. The Hutchinson-Gilford progeria syndrome. Report of 4 cases and review of the literature. *J Pediatr*. 1972;80(4):697–724.
2. Gordon LB, Brown WT, and Collins FS. Hutchinson-Gilford Progeria Syndrome. In: Pagon RA, et al., eds. *GeneReviews*. Seattle ,WA; 1993–2018. https://www.ncbi.nlm.nih.gov/pubmed/20301300.
3. Gordon LB, Cao K, Collins FS. Progeria: translational insights from cell biology. *J Cell Biol*. 2012;199(1):9–13.
4. Olive M, et al. Cardiovascular pathology in Hutchinson-Gilford progeria: correlation with the vascular pathology of aging. *Arterioscler Thromb Vasc Biol*. 2010;30(11):2301–2309.
5. Prakash A, et al. Cardiac abnormalities in patients with Hutchinson-Gilford progeria syndrome. *JAMA Cardiol*. 2018;3(4):326–334.
6. Hamczyk MR, et al. Vascular smooth muscle-specific progerin expression accelerates atherosclerosis and death in a mouse model of Hutchinson-Gilford progeria syndrome. *Circulation*. 2018;138(3):266–282.
7. Stehbens WE, Delahunt B, Shozawa T, Gilbert-Barness E. Smooth muscle cell depletion and

collagen types in progeric arteries. *Cardiovasc Pathol*. 2001;10(3):133–136.
8. Stehbens WE, Wakefield SJ, Gilbert-Barness E, Olson RE, Ackerman J. Histological and ultrastructural features of atherosclerosis in progeria. *Cardiovasc Pathol*. 1999;8(1):29–39.
9. Hennekam RC. Hutchinson-Gilford progeria syndrome: review of the phenotype. *Am J Med Genet A*. 2006;140(23):2603–2624.
10. Gruenbaum Y, Foisner R. Lamins: nuclear intermediate filament proteins with fundamental functions in nuclear mechanics and genome regulation. *Annu Rev Biochem*. 2015;84:131–164.
11. De Sandre-Giovannoli A, et al. Lamin A truncation in Hutchinson-Gilford progeria. *Science*. 2003;300(5628):2055.
12. Eriksson M, et al. Recurrent de novo point mutations in lamin A cause Hutchinson-Gilford progeria syndrome. *Nature*. 2003;423(6937):293–298.
13. Gevaert AB, et al. Endothelial senescence contributes to heart failure with preserved ejection fraction in an aging mouse model. *Circ Heart Fail*. 2017;10(6):e003806.
14. Harvey A, Montezano AC, Lopes RA, Rios F, Touyz RM. Vascular fibrosis in aging and hypertension: molecular mechanisms and clinical implications. *Can J Cardiol*. 2016;32(5):659–668.
15. Kudlow BA, Kennedy BK. Aging: progeria and the lamin connection. *Curr Biol*. 2006;16(16):R652–R654.
16. Scaffidi P, Gordon L, Misteli T. The cell nucleus and aging: tantalizing clues and hopeful promises. *PLoS Biol*. 2005;3(11):e395.
17. Wang JC, Bennett M. Aging and atherosclerosis: mechanisms, functional consequences, and potential therapeutics for cellular senescence. *Circ Res*. 2012;111(2):245–259.
18. Osorio FG, et al. Splicing-directed therapy in a new mouse model of human accelerated aging. *Sci Transl Med*. 2011;3(106):106ra107.
19. Varga R, et al. Progressive vascular smooth muscle cell defects in a mouse model of Hutchinson-Gilford progeria syndrome. *Proc Natl Acad Sci U S A*. 2006;103(9):3250–3255.
20. Collins C, Tzima E. Hemodynamic forces in endothelial dysfunction and vascular aging. *Exp Gerontol*. 2011;46(2–3):185–188.
21. Davignon J, Ganz P. Role of endothelial dysfunction in atherosclerosis. *Circulation*. 2004; 109(23 Suppl 1):III27–III32.
22. Rathouska J, et al. Cell adhesion molecules and eNOS expression in aorta of normocholesterolemic mice with different predispositions to atherosclerosis. *Heart Vessels*. 2015;30(2):241–248.
23. Kohn JC, Lampi MC, Reinhart-King CA. Age-related vascular stiffening: causes and consequences. *Front Genet*. 2015;6:112.
24. Villa-Bellosta R, et al. Defective extracellular pyrophosphate metabolism promotes vascular calcification in a mouse model of Hutchinson-Gilford progeria syndrome that is ameliorated on pyrophosphate treatment. *Circulation*. 2013;127(24):2442–2451.
25. Zhang H, Xiong ZM, Cao K. Mechanisms controlling the smooth muscle cell death in progeria via down-regulation of poly(ADP-ribose) polymerase 1. *Proc Natl Acad Sci U S A*. 2014;111(22):E2261–E2270.
26. Csoka AB, et al. Genome-scale expression profiling of Hutchinson-Gilford progeria syndrome reveals widespread transcriptional misregulation leading to mesodermal/mesenchymal defects and accelerated atherosclerosis. *Aging Cell*. 2004;3(4):235–243.
27. Hernandez L, et al. Functional coupling between the extracellular matrix and nuclear lamina by Wnt signaling in progeria. *Dev Cell*. 2010;19(3):413–425.
28. Dahl KN, Ribeiro AJ, Lammerding J. Nuclear shape, mechanics, and mechanotransduction. *Circ Res*. 2008;102(11):1307–1318.
29. Lammerding J, et al. Lamin A/C deficiency causes defective nuclear mechanics and mechanotransduction. *J Clin Invest*. 2004;113(3):370–378.
30. Yang SH, et al. A farnesyltransferase inhibitor improves disease phenotypes in mice with a Hutchinson-Gilford progeria syndrome mutation. *J Clin Invest*. 2006;116(8):2115–2121.
31. Baek JH, et al. Expression of progerin in aging mouse brains reveals structural nuclear abnormalities without detectible significant alterations in gene expression, hippocampal stem cells or behavior. *Hum Mol Genet*. 2015;24(5):1305–1321.
32. Sagelius H, et al. Targeted transgenic expression of the mutation causing Hutchinson-Gilford progeria syndrome leads to proliferative and degenerative epidermal disease. *J Cell Sci*. 2008;121(Pt 7):969–978.
33. Schmidt E, et al. Expression of the Hutchinson-Gilford progeria mutation during osteoblast development results in loss of osteocytes, irregular mineralization, and poor biomechanical properties. *J Biol Chem*. 2012;287(40):33512–33522.
34. Sun JF, et al. Microvascular patterning is controlled by fine-tuning the Akt signal. *Proc Natl Acad Sci U S A*. 2005;102(1):128–133.
35. McClintock D, Gordon LB, Djabali K. Hutchinson-Gilford progeria mutant lamin A primarily targets human vascular cells as detected by an anti-Lamin A G608G antibody. *Proc Natl Acad Sci U S A*. 2006;103(7):2154–2159.
36. Bruggink AH, et al. Brain natriuretic peptide is produced both by cardiomyocytes and cells infiltrating the heart in patients with severe heart failure supported by a left ventricular assist device. *J Heart Lung Transplant*. 2006;25(2):174–180.
37. Kuhn M. Endothelial actions of atrial and B-type natriuretic peptides. *Br J Pharmacol*. 2012;166(2):522–531.
38. Schnelle M, et al. Echocardiographic evaluation of diastolic function in mouse models of heart disease. *J Mol Cell Cardiol*. 2018;114:20–28.
39. Dai Z, Aoki T, Fukumoto Y, Shimokawa H. Coronary perivascular fibrosis is associated with impairment of coronary blood flow in patients with non-ischemic heart failure. *J Cardiol*. 2012;60(5):416–421.
40. Olsen DR, Peltonen J, Jaakkola S, Chu ML, Uitto J. Collagen gene expression by cultured human skin fibroblasts. Abundant steady-state levels of type VI procollagen messenger RNAs. *J Clin Invest*. 1989;83(3):791–795.
41. El Accaoui RN, et al. Aortic valve sclerosis in mice deficient in endothelial nitric oxide synthase. *Am J Physiol Heart Circ Physiol*. 2014;306(9):H1302–H1313.
42. Balligand JL, Feron O, Dessy C. eNOS activation by physical forces: from short-term regulation of contraction to chronic remodeling of cardiovascular tissues. *Physiol Rev*. 2009;89(2):481–534.
43. Al-Musawi SL, Bishton J, Dean J, Williams S, Cremers SG, Weinberg PD. Evidence for a reversal with age in the pattern of near-wall blood flow around aortic branches. *Atherosclerosis*. 2004;172(1):79–84.
44. Lopez-Quintero SV, Cancel LM, Pierides A, Antonetti D, Spray DC, Tarbell JM. High glucose attenuates shear-induced changes in endothelial hydraulic conductivity by degrading the glycocalyx. *PLoS ONE*. 2013;8(11):e78954.
45. Baeyens N, et al. Syndecan 4 is required for endothelial alignment in flow and atheroprotective signaling. *Proc Natl Acad Sci U S A*. 2014;111(48):17308–17313.
46. Davies PF. Hemodynamic shear stress and the endothelium in cardiovascular pathophysiology. *Nat Clin Pract Cardiovasc Med*. 2009;6(1):16–26.
47. Chen ZJ, et al. Dysregulated interactions between lamin A and SUN1 induce abnormalities in the nuclear envelope and endoplasmic reticulum in progeric laminopathies. *J Cell Sci*. 2014; 127(Pt 8):1792–1804.
48. Hale CM, et al. Dysfunctional connections between the nucleus and the actin and microtubule networks in laminopathic models. *Biophys J*. 2008;95(11):5462–5475.
49. Guilluy C, et al. Isolated nuclei adapt to force and reveal a mechanotransduction pathway in the nucleus. *Nat Cell Biol*. 2014;16(4):376–381.
50. Ho CY, Jaalouk DE, Vartiainen MK, Lammerding J. Lamin A/C and emerin regulate MKL1-SRF activity by modulating actin dynamics. *Nature*. 2013;497(7450):507–511.
51. Holaska JM, Kowalski AK, Wilson KL. Emerin caps the pointed end of actin filaments: evidence for an actin cortical network at the nuclear inner membrane. *PLoS Biol*. 2004;2(9):E231.
52. Fang F, et al. Myocardin-related transcription factor A mediates OxLDL-induced endothelial injury. *Circ Res*. 2011;108(7):797–807.
53. Minami T, et al. Reciprocal expression of MRTF-A and myocardin is crucial for pathological vascular remodelling in mice. *EMBO J*. 2012;31(23):4428–4440.
54. Weng X, et al. Endothelial MRTF-A mediates angiotensin II induced cardiac hypertrophy. *J Mol Cell Cardiol*. 2015;80:23–33.
55. Weng X, et al. A crosstalk between chromatin remodeling and histone H3K4 methyltransferase complexes in endothelial cells regulates angiotensin II-induced cardiac hypertrophy. *J Mol Cell Cardiol*. 2015;82:48–58.
56. Fang F, et al. Myocardin-related transcription factor A mediates OxLDL-induced endothelial injury. *Circ Res*. 2011;108(7):797–807.
57. Lee SW, et al. Snail as a potential target molecule in cardiac fibrosis: paracrine action of endothelial cells on fibroblasts through snail and CTGF axis. *Mol Ther*. 2013;21(9):1767–1777.
58. Gerhard-Herman M, et al. Mechanisms of premature vascular aging in children with Hutchinson-Gilford progeria syndrome. *Hypertension*. 2012;59(1):92–97.
59. Harvey A, Montezano AC, Touyz RM. Vascular

biology of ageing-Implications in hypertension. *J Mol Cell Cardiol*. 2015;83:112–121.
60. Booth EA, Spagnol ST, Alcoser TA, Dahl KN. Nuclear stiffening and chromatin softening with progerin expression leads to an attenuated nuclear response to force. *Soft Matter*. 2015;11(32):6412–6418.
61. Philip JT, Dahl KN. Nuclear mechanotransduction: response of the lamina to extracellular stress with implications in aging. *J Biomech*. 2008;41(15):3164–3170.
62. Dahl KN, Kalinowski A, Pekkan K. Mechanobiology and the microcirculation: cellular, nuclear and fluid mechanics. *Microcirculation*. 2010;17(3):179–191.
63. Chambliss AB, et al. The LINC-anchored actin cap connects the extracellular milieu to the nucleus for ultrafast mechanotransduction. *Sci Rep*. 2013;3:1087.
64. Lombardi ML, Jaalouk DE, Shanahan CM, Burke B, Roux KJ, Lammerding J. The interaction between nesprins and sun proteins at the nuclear envelope is critical for force transmission between the nucleus and cytoskeleton. *J Biol Chem*. 2011;286(30):26743–26753.
65. Le HQ, et al. Mechanical regulation of transcription controls Polycomb-mediated gene silencing during lineage commitment. *Nat Cell Biol*. 2016;18(8):864–875.
66. Esnault C, et al. Rho-actin signaling to the MRTF coactivators dominates the immediate transcriptional response to serum in fibroblasts. *Genes Dev*. 2014;28(9):943–958.
67. Schulze C, et al. Stiffening of human skin fibroblasts with age. *Biophys J*. 2010;99(8):2434–2442.
68. Osmanagic-Myers S, et al. Plectin reinforces vascular integrity by mediating crosstalk between the vimentin and the actin networks. *J Cell Sci*. 2015;128(22):4138–4150.
69. Gregor M, et al. Mechanosensing through focal adhesion-anchored intermediate filaments. *FASEB J*. 2014;28(2):715–729.
70. Dong QG, et al. A general strategy for isolation of endothelial cells from murine tissues. Characterization of two endothelial cell lines from the murine lung and subcutaneous sponge implants. *Arterioscler Thromb Vasc Biol*. 1997;17(8):1599–1604.
71. Cingolani HE, Rebolledo OR, Portiansky EL, Pérez NG, Camilión de Hurtado MC. Regression of hypertensive myocardial fibrosis by Na(+)/H(+) exchange inhibition. *Hypertension*. 2003;41(2):373–377.
72. Villari B, et al. Influence of collagen network on left ventricular systolic and diastolic function in aortic valve disease. *J Am Coll Cardiol*. 1993;22(5):1477–1484.
73. Cramer LP, Briggs LJ, Dawe HR. Use of fluorescently labelled deoxyribonuclease I to spatially measure G-actin levels in migrating and non-migrating cells. *Cell Motil Cytoskeleton*. 2002;51(1):27–38.
74. DePaola N, Davies PF, Pritchard WF, Florez L, Harbeck N, Polacek DC. Spatial and temporal regulation of gap junction connexin43 in vascular endothelial cells exposed to controlled disturbed flows in vitro. *Proc Natl Acad Sci U S A*. 1999;96(6):3154–3159.
75. Gesson K, Rescheneder P, Skoruppa MP, von Haeseler A, Dechat T, Foisner R. A-type lamins bind both hetero- and euchromatin, the latter being regulated by lamina-associated polypeptide 2 alpha. *Genome Res*. 2016;26(4):462–473.
76. Esnault C, et al. Rho-actin signaling to the MRTF coactivators dominates the immediate transcriptional response to serum in fibroblasts. *Genes Dev*. 2014;28(9):943–958.
77. Santer D, et al. In vivo and ex vivo functional characterization of left ventricular remodelling after myocardial infarction in mice. *ESC Heart Fail*. 2015;2(3):171–177.

SUPPLEMENTAL DATA, Osmanagic-Myers et al.

1. Supplemental Figures and Figure Legends

2. Supplemental Tables

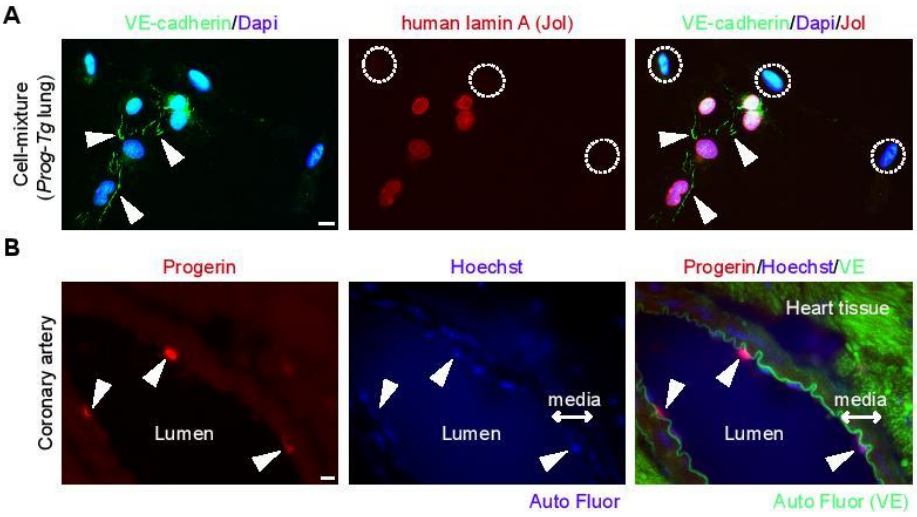

Supplemental Figure 1. Endothelium-specific expression of human lamin A and progerin in *Prog-Tg* mice. (A) Immunofluorescence microscopy of a mixture of cell types obtained from lung tissue using antibodies to human lamin A (Jol) and to endothelial marker VE-cadherin. Arrowheads, VE-cadherin marked endothelial-specific cell-cell junctions. Encircled cells, non-endothelial cells (absence of VE-cadherin cell-cell junctions). Note that only cells positively stained for VE-cadherin junction marker were detected positive for human lamin A. Scale bar, 10 µm.
(B) Immunofluorescence image of larger area from coronary artery (compared to Figure 1C) showing surrounding cardiac tissue from *Prog-Tg* animals stained with progerin antibody, VE-cadherin antibody and DNA dye Hoechst. Progerin expression is confined to intimal layer (arrowheads) and absent in surrounding area. Hoechst and green autofluorescence signals are used to identify internal- and external elastic lamina (IEL) to mark boundaries of the medial layer (media, double arrow). Note, that the VE-cadherin marked intimal layer signal merges with the IEL autofluorescence signal. Scale bar, 10 µm. (A and B, representative of n=3 independent experiments).

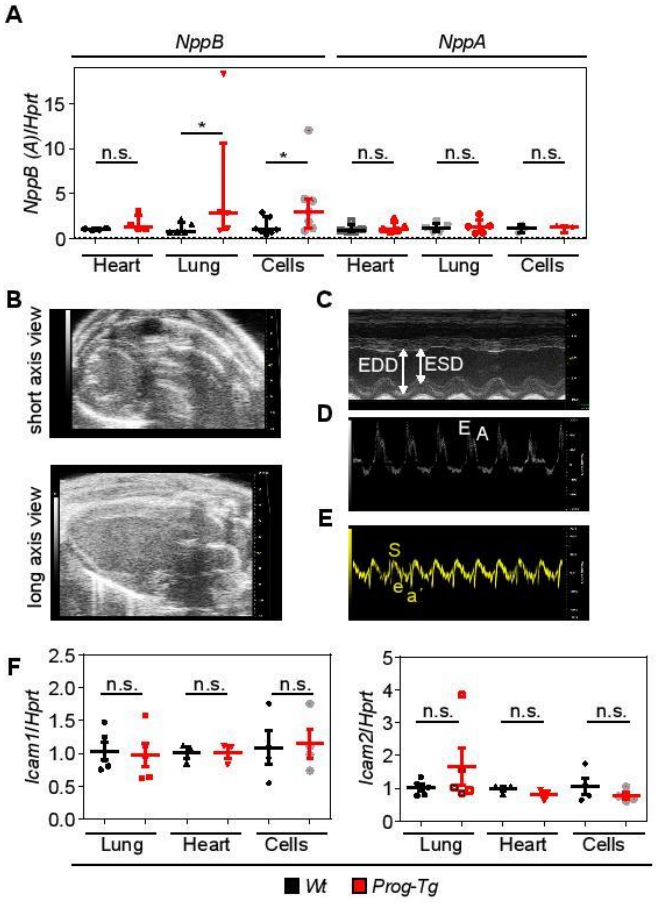

Supplemental Figure 2. Analysis of hypertrophy and inflammatory markers and representative echocardiography measurements in the heart. (A) Expression of *NppB* and *NppA* in heart and lung tissue of *Prog-Tg* animals at ~25 weeks (n=5 littermate pairs) and in *Prog-Tg* ECs (n=7) normalized to hypoxanthine phosphoribosyl-transferase 1 (*Hprt*) and compared to those from *Wt* littermates (fold change) and *Wt* ECs, respectively. n.s. not significant, *p<0.05. Wilcoxon signed rank test (littermate tissues) and Mann-Whitney U test (cells). Median (middle line) and whiskers, 25th and 75th percentile. **(B)** Representative echocardiography 2D mode with a short and long axis view of the left ventricle allowing to obtain a M Mode tracing of the left ventricle in **(C)** in order to evaluate the left ventricle EF, diameters and wall thickness. **(D)** Representative mitral Doppler flow profile for measurement of IVRT and the combined parameter E/e'. **(E)** Representative tissue Doppler tracing of the septum at the mitral annulus level. (B-E) representative of n=5 littermate pairs. **(F)** Gene expression of *Icam1* and *Icam2* in lung, heart and isolated lung endothelial cell cultures (n= 5 and 3 littermate pairs, n=4 independent experiments for cells). All mice were at the age of ~25 weeks. Values normalized to *Hprt* were compared to those from *Wt* littermate or *Wt* cells (fold change). n.s. not significant. Paired (littermate tissues) and unpaired (cells) Student's t-test. Mean and error bars indicate SEM.

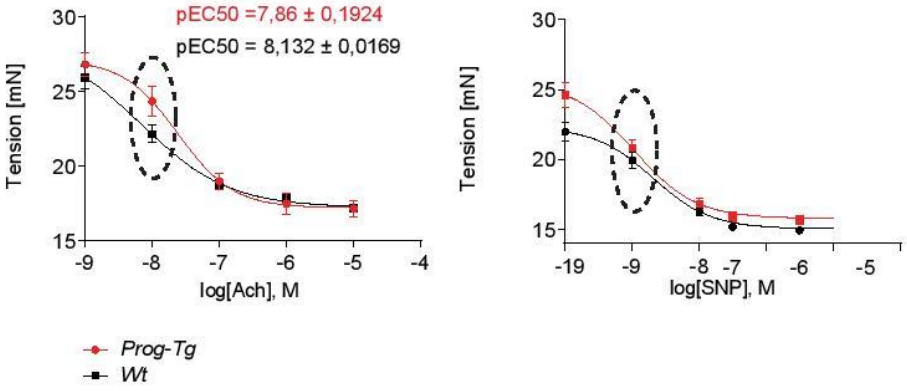

Supplemental Figure 3. Vascular reactivity in isolated aortic segments of *Prog-Tg* mice. Aortic segments were isolated from mice and were mounted onto a Multi Wire Myograph System (DMT 620 M) for determination of endothelium-dependent relaxation and endothelium-independent relaxation by cumulatively increasing concentrations of acetylcholine (Ach, 10^{-9} to 10^{-5} mol/l) and sodium nitroprusside (SNP, 10^{-10} to 10^{-6} mol/l), respectively. Tension in (mN) and log (concentration) in (mol/l) is shown (n=4 animals per genotype; age>30 weeks). Note that in *Prog-Tg* versus *Wt* aortic segments a tendentiously prolonged lag phase and reduced pEC50 values (p=0.2) were observed only for endothelium-dependent relaxation. Error bars denote mean ± SEM.

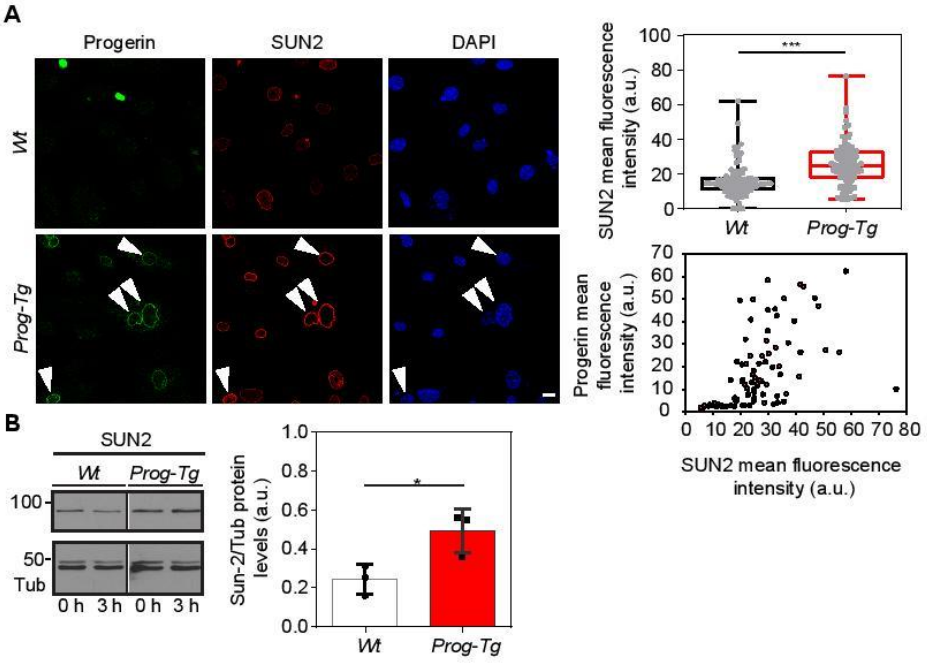

Supplemental Figure 4. Accumulation of SUN2 in *Prog-Tg* endothelial cells. (A) Representative image of endothelial cells from *Wt* and *Prog-Tg* mice immunostained with SUN2 antibody (representative of n=3 independent experiments). Scale bar, 10 µm. Box plots show the distribution of SUN2 mean fluorescence intensities in *Prog-Tg* and *Wt* endothelial cells (n=100 cells per genotype). *** p<0.001, Mann-Whitney U test. Median (middle line) with boxes encompassing 25th to 75th percentile and whiskers, minimum to maximum values Lower panel, mean progerin fluorescence intensities plotted over mean SUN2 fluorescence intensities in *Prog-Tg* cells (n=87 cells). Arbitrary units (a.u.) of fluorescence are shown. (B) Quantitative immunoblot analysis of lysates (0 h, untreated) from *Wt* and *Prog-Tg* endothelial cells (*Wt* and *Prog-Tg* samples from different parts of the same gel; n=3), * p<0.05, unpaired Student's t-test. Mean and error bars indicate SEM. 3h, flow exposed samples.

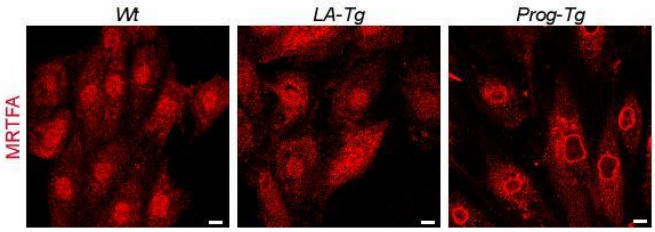

Supplemental Figure 5. MRTFA localization is unaltered in *LA-Tg* endothelial cells. Endothelial cells isolated from *Wt*, *LA-Tg* and *Prog-Tg* mice were processed for immunofluorescence microscopy using MRTFA antibody (representative of n=3 independent experiments). Scale bars, 10 µm.

Supplemental Table 1. Hemodynamic and echocardiographic parameters.

Hemodynamic parameters	**LM_*Prog-Tg***	***Prog-Tg***	**LM_*LA-Tg***	***LA-Tg***
Heart rate [beats/min]	410 ± 24	441 ± 20	445 ± 39	420 ± 21
LVEDP [mmHg]	2.12 ± 0.20	3.99 ± 0.35**	2.52 ± 0.36	2.60 ± 0.36
LVSP [mmHg]	85.2 ± 2.3	99.8 ± 4.9*	84.2 ± 4.4	84.75 ± 4.18
LV +dP/dt [mmHg/s]	5368 ± 348	6009 ±514‡	5857 ± 618	4871 ±417
LV -dP/dt [mmHg/s]	-5465 ± 428	-5177 ± 605	-5355 ± 650	-4573 ± 384
WS_dias_posterior [mm Hg]	5.8 ± 0.5	7.7 ± 0.4*	6.7 ± 0.95	6.3 ± 1.41
WS_diastolic_septum [mm Hg]	5.1 ± 0.6	7.5 ± 0.5*	5.8 ± 0.6	7.16 ± 1.32
WS_systolic_posterior [mm Hg]	92.5 ± 9.8	96.8 ± 15.4	113 ± 7.7	108 ± 10.8
WS_systolic_septum [mm Hg]	77.8 ± 6.4	91.5 ± 7.5	106.5 ± 8.9	102 ± 10.6
Echocardiographic parameters	**LM_*Prog-Tg***	***Prog-Tg***	**LM_*LA-Tg***	***LA-Tg***
Ejection fraction [%]	62.8 ± 2	65.1 ± 2	60.6± 1.28	61.2± 4.01
EDD/BW [mm/g]	0.149 ± 0.033	0.155 ± 0.031	0.138 ± 0.013	0.142 ± 0.023
ESD/BW [mm/g]	0.094 ± 0.018	0.101 ± 0.026	0.089 ± 0.02	0.086 ± 0.03
EDSW/BW [mm/mg]	0.298 ± 0.020	0.397 ± 0.030*	0.247 ± 0.024	0.254 ± 0.048
EDPW/BW [mm/mg]	0.276 ± 0.025	0.363 ± 0.037*	0.258 ± 0.019	0.296 ± 0.036
ESSW/BW [mm/g]	0.051 ± 0.013	0.05 ± 0.008	0.038 ± 0.01	0.04 ± 0.01
ESPW/BW [mm/g]	0.036 ± 0.009	0.053 ± 0.009	0.037 ± 0.01	0.038 ± 0.01
E/e´ ratio	3.03 ± 0.10	2.92 ± 0.16	2.67 ± 0.08	2.77 ±0.07
IVRT [ms]	19.45 ± 0.5	17.7 ± 0.56*	18.33 ± 0.71	19.05 ± 0.7
MGTA [mmHg]	4.2 ± 0.21	4.7 ± 0.28	4.4 ± 0.26	4.5 ± 0.27

Supplemental Table 1. Hemodynamic and echocardiographic parameters. *Prog-Tg* and *LA-Tg* and corresponding littermates were analyzed (age >27 weeks; n=11 Wt, n=5 *LA-Tg*, n=6 *Prog-Tg*;). LVEDP, left ventricular end-diastolic pressure; LVSP, left ventricular systolic pressure; LV +dP/dt, maximal value of the first derivative of LV pressure; LV -dP/dt, minimal value of the first derivative of LV pressure; WS, wall stress; EDD, end-diastolic diameter; ESD, end-systolic diameter; EDSW, end-diastolic septal wall width; EDPW, end-diastolic posterior wall width; ESSW, end-systolic septal wall width, ESPW, end-systolic posterior wall width; E/e´, Ratio of E to e'; IVRT, isovolumic relaxation time; MGTA, mean gradient of transverse aorta. ‡ trend $p<0.08$, *$p<0.05$ and **$p<0.01$ Tg vs LM,. Unpaired Student´s *t*-test. Mean and error bars indicate SEM.

Supplemental Table 2. Primers used for quantitative real-time PCR analysis

Gene	Genbank accession number	Primer Sequences
Cdh5	NC_000074.6	Forward: 5'-CTGCTCACGGACAAGATCAGC-3' Reverse: 5'-CTCTTTTGGCGATGGTGGGC-3'
Hprt	NM_013556.2	Forward: 5'-GCAGTCCCAGCGTCGTGATTA-3' Reverse: 5'-TGATGGCCTCCCATCTCCTTCA-3'
Nos3	NM_008713.4	Forward: 5'-GCATGGGCAACTTGAAGAGTG-3' Reverse: 5'-GCTGCCCACTTCCCAATTCT-3'
Col1a1	NM_007742.3	Forward: 5'-CTGACGCATGGCCAAGAAGA-3' Reverse: 5'-ATACCTCGGGTTTCCACGTC-3'
Col3a1	NC_000067.6	Forward: 5'-TCCGGGAATAACGTCAGTC-3' Reverse: 5'-GGAAGCCCATTTGCACCAGG-3'
Col4a5	NM_001163155.1	Forward: 5'-CCCAAGTGCACCAGCATAAC-3' Reverse: 5'-AGAAGAACACCCATGGCAGG-3'
Actb	NM_007393.3	Forward: 5'-ACAGCTTCTTTGCAGCTCCT-3' Reverse: 5'-TTGTCGACGACCAGCGCA-3'
Nppb	NM_008726.5	Forward: 5'-GGGCACAAGATAGACCGGAT-3' Reverse: 5'-GCCAGGAGGTCTTCCTACAA-3'
Icam1	NC_000075.6	Forward: 5'-CAGATGCCGACCCAGGAGAG-3' Reverse: 5'-CCGCTAGCTCCAAAACGCAG-3'
Icam2	NC_000077.6	Forward: 5'-GCTCACCGGCACAGAGGAGA-3' Reverse: 5'-TATGGGCTTCAGGGGCACAG-3'
Acta2	NP_031418.1	Forward: 5'-GTACCACCATGTACCCAGGC-3' Reverse: 5'-GAAGGTAGACAGCGAAGCCA-3'
Nos3 (promoter, ChIP)	NP_032739.3	Forward: 5'-CCCTCTAGCAGACAACCCAC-3' Reverse: 5'-CTCTCAGATGCTGGCCTTCG-3'
Nos3 (gene body, ChIP)	NP_032739.3	Forward: 5'-AAGTGGGCAGCATCACCTAC-3' Reverse: 5'-GGGACCAGGCCTAGAAACAC-3'

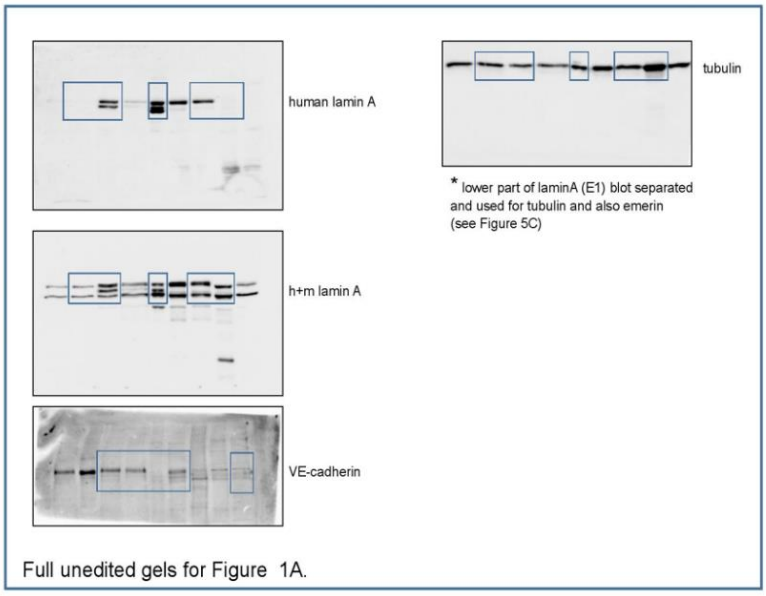

Full unedited gels for Figure 1A.

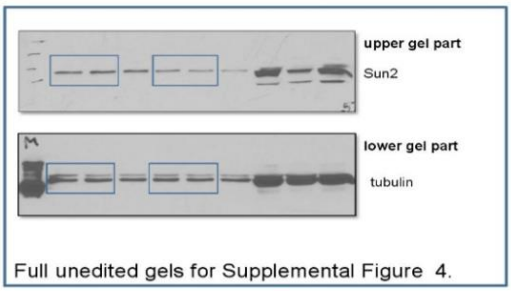

Full unedited gels for Supplemental Figure 4.

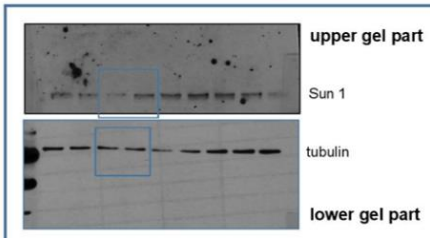

Full unedited gels for Figure 6B.

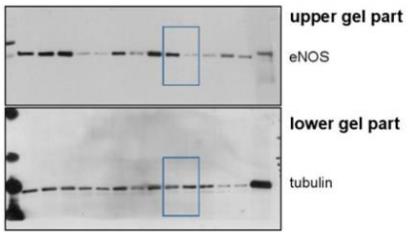

Full unedited gels for Figure 4B.

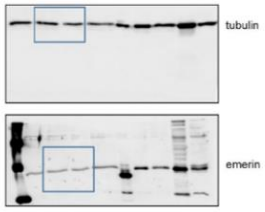

Full unedited gels for Figure 6C.

5. Second peer reviewed publication

Status of manuscript and submitters contribution

Our second peer reviewed manuscript `` Endothelial and systemic upregulation of miR-34a-5p fine tunes senescence in progeria`` was accepted for publication in December 2021 and published online in January 2022 in the research article *Aging* (https://www.aging-us.com/).

As first author of this publication my personal contribution was to conduct most of the experimental procedures and to establish new techniques needed for doing so. Moreover, I assembled the main and supplementary figures presented in this manuscript and contributing to the writing of this research article.

In particular, I performed the experiments and assembled the figures depicted in Figure 1 A-H, Figure 2 A-C, Figure 4 A-D, Figure 5 A, B, D-G, Figure 6 A, B, E, F and Figure 7 A-D. For the supplementary material I performed the experiments and assembled the figures for Supplementary Figure 1, 2, 3, 5 and 6.

I further on wrote the draft of the paper and the materials and methods part of the paper. I also contributed to the writing and in proof reading of our second published manuscript.

Publication: Endothelial and systemic upregulation of miR-34a-5p fine-tunes senescence in progeria

www.aging-us.com AGING 2022, Vol. 14, No. 1

Research Paper

Endothelial and systemic upregulation of miR-34a-5p fine-tunes senescence in progeria

Christina Manakanatas[1], Santhosh Kumar Ghadge[1], Azra Agic[1], Fatih Sarigol[1], Petra Fichtinger[1], Irmgard Fischer[1], Roland Foisner[1], Selma Osmanagic-Myers[1,2]

[1]Max Perutz Labs, Center for Medical Biochemistry, Medical University of Vienna, Vienna Biocenter Campus (VBC), Vienna A-1030, Austria
[2]Institute of Medical Chemistry, Center for Pathobiochemistry and Genetics, Medical University of Vienna, Vienna A-1090, Austria

Correspondence to: Roland Foisner, Selma Osmanagic-Myers; **email:** roland.foisner@meduniwien.ac.at, selma.osmanagic-myers@meduniwien.ac.at
Keywords: Hutchinson-Gilford progeria syndrome, cardiovascular disease, endothelial senescence, senescence-associated micro RNAs
Received: September 25, 2021 **Accepted:** December 25, 2021 **Published:** January 12, 2022

ABSTRACT

Endothelial defects significantly contribute to cardiovascular pathology in the premature aging disease Hutchinson-Gilford progeria syndrome (HGPS). Using an endothelium-specific progeria mouse model, we identify a novel, endothelium-specific microRNA (miR) signature linked to the p53-senescence pathway and a senescence-associated secretory phenotype (SASP). Progerin-expressing endothelial cells exert profound cell-non-autonomous effects initiating senescence in non-endothelial cell populations and causing immune cell infiltrates around blood vessels. Comparative miR expression analyses revealed unique upregulation of senescence-associated miR34a-5p in endothelial cells with strong accumulation at atheroprone aortic arch regions but also, in whole cardiac- and lung tissues as well as in the circulation of progeria mice. Mechanistically, miR34a-5p knockdown reduced not only p53 levels but also late-stage senescence regulator p16 with no effect on p21 levels, while p53 knockdown reduced miR34a-5p and partially rescued p21-mediated cell cycle inhibition with a moderate effect on SASP. These data demonstrate that miR34a-5p reinforces two separate senescence regulating branches in progerin-expressing endothelial cells, the p53- and p16-associated pathways, which synergistically maintain a senescence phenotype that contributes to cardiovascular pathology. Thus, the key function of circulatory miR34a-5p in endothelial dysfunction-linked cardiovascular pathology offers novel routes for diagnosis, prognosis and treatment for cardiovascular aging in HGPS and potentially geriatric patients.

INTRODUCTION

Life expectancy has significantly risen in modern societies but this has been accompanied by an increase in age-related diseases such as cardiovascular diseases (CVDs), which are the leading cause of deaths globally (WHO report 2017) [1]. One of the key initiating events in age-related cardiovascular pathologies is endothelial dysfunction characterized by increased oxidative stress, reduced response to shear stress and consequently decline in atheroprotective endothelial nitric oxide synthase (eNOS). Increasing evidence also highlights the importance of deregulated microRNAs (miRs) in the development of endothelial dysfunction. Several studies demonstrated the involvement of circulating miRs in various age-related pathologies with a remarkable success of miR neutralizing antimiR agents in the treatment of age-related CVD [2, 3]. However, the tissue specific

origins of age-related circulating miRs, particularly in regard to endothelial tissue *in vivo* and their mode and extent of action still remain widely unclear.

Age-linked tissue damage is often associated with cellular senescence occurring in almost all tissues [4, 5]. Cellular senescence occurs upon different cellular stressors such as DNA damage, mechanical damage or telomere erosion [6]. Cell cycle arrested, senescent cells can have deleterious effects on the surrounding cells through their metabolic activities, thereby playing a pivotal role in pathophysiological processes [7]. Senescent cells establish a "communication network" with their environment via secretion of pro-inflammatory and pro-fibrotic factors, growth factors and proteases, known as senescence-associated secretory phenotype (SASP) [8]. Moreover, pro-senescent effects can be mediated through paracrine transmission [9]. At the molecular level, the p53/p21 axis is a key pathway regulating senescence development [10]. p21 (*Cdkn1*) is a cyclin-dependent kinase inhibitor (CDKi) that acts in the early reversible stages of cell cycle arrest, whereas prolonged cell cycle arrest leads to the expression of another CDKi, p16 (*Cdkn2*) [10]. Persistent and high levels of p16 lead to irreversible permanent cell cycle arrest [11]. miRs are also emerging as key regulators of senescence and *bona fide* members of the SASP [12, 13]. miRs regulate gene expression at the post-transcriptional level through base pairing mainly to the 3' untranslated regions of target messenger RNAs (mRNAs), leading to either mRNA decay or translational repression [14]. miRs that downregulate tumor suppressors act as oncogenes, those that downregulate oncogenes as tumor suppressors [15]. Consequently, deregulation of miRs is commonly found in cancer but also in aging and age-related diseases [15–18]. Several senescence-associated miRs, termed geromiRs, were proposed to be key components regulating senescence [19]. Among those, miR34a-5p was one of the first identified p53 targets and plays a key role within the p53-network [20]. From the clinical perspective, a large number of preclinical and clinical studies demonstrated elevated levels of miR34 in heart failure and therapeutic inhibition of the miR-34 family (miR-34a, -34b, -34c) attenuated the cardiac remodeling, left ventricular dysfunction and promoted human heart progenitor proliferation [21–23]. However, not much is known regarding the cell type specific impact of miR34 particularly at the organismal level which is an essential prerequisite for treating cardiovascular disease.

Given the potential importance of senescence-associated miRs and the involvement of a dysfunctional endothelium in age-related CVD pathology, we sought to explore whether an endothelial specific miR signature and alterations of circulating miRs may contribute to cardiovascular aging and pathology. To assess the potential effects of endothelium-specific senescence pathways and senescence-associated miRs on CVD pathology, we used an endothelium-specific mouse model of the premature aging disease Hutchinson Gilford progeria syndrome (HGPS), which develops many age-related CVD pathologies [24]. HGPS is caused by an autosomal dominant *de novo* (GGC>GGT) mutation in the *LMNA* gene that leads to activation of a cryptic splice site and generation of truncated and permanently farnesylated prelamin A, termed progerin [25, 26]. *LMNA* codes for A type lamins that together with lamin B form a mesh-like structure at the nuclear periphery providing mechanical stability to the nucleus and regulating chromatin organization and gene expression [27]. Progerin expression in cells leads to mechanical defects, lobulated nuclei and changes in heterochromatin, DNA damage and shortened telomeres, similar to aging-linked mechanisms [28]. Accordingly, HGPS patients develop many age-related features such as alopecia, skin scleroderma, lipodystrophy, bone abnormalities and prominent CVD within the first one to two decades of life [26]. Vascular smooth muscle cell (VSMC) loss in VSMC-specific progerin mice contributes to severe atherosclerosis, but recent studies in endothelium-specific progeria mice by us and others have also underpinned the importance of endothelial dysfunction in the development of age-related cardiovascular pathology in HGPS [24, 29, 30]. Dysfunctional endothelial cells show deregulation of the mechano-responsive myocardin-related transcription factor A (MRTFA) and Sirt7 activity and exert pro-fibrotic and pro-inflammatory effects. In addition, several key endothelial-specific functions were also impaired in HGPS endothelial cells derived from induced pluripotent stem cells [31, 32]. However, the underlying mechanism and the potential involvement of senescence-associated miRs in endothelial cell dysfunction and its contribution to CVD are unknown.

Here, using the endothelium-specific progeria mouse model [24], we identify a novel endothelial-specific senescence-associated miR signature linked to a senescence-associated p53-signaling and systemic pro-senescent and pro-inflammatory SASP. Senescence-associated miR34a-5p that putatively affects 50% of downregulated mRNA targets in progerin-expressing endothelial cells was also elevated in plasma and significantly upregulated in lung and heart tissues and also in non-endothelial cell populations indicating systemic effects. Importantly, antimiR-mediated inhibition of miR34a-5p reduced the expression of p53 and late-stage senescence marker p16, highlighting the key role of miR34a-5p in sustaining senescence in endothelial cells and presumably through an unknown

paracrine mechanism, also in neighboring non-endothelial populations. Thus, the current study identifies novel potential SA-miR mediated control mechanisms involved in senescence regulation and in vascular induced systemic aging effects in HGPS.

RESULTS

Progerin expression in endothelial cells activates p53-linked senescence and SASP

In order to investigate molecular pathways underlying endothelial dysfunction in HGPS we used an endothelium-specific progeria mouse model (Prog-Tg) [24]. Prog-Tg mice were generated by crossing transgenic mice carrying a tet Operon (TetOp) driven human HGPS mutant lamin A minigene (TetOp-G608G) [33] with transgenic mice expressing a tetracycline-responsive trans-activator (tTA) under the control of the endothelium-specific VE-cadherin (*Cdh5*) promoter [34]. Prog-Tg mice were shown to express both human wildtype lamin A and mutant progerin from the transgene at similar levels [24, 33] (Supplementary Figure 1). As a control, we generated transgenic mice expressing the wildtype human lamin A (LA-Tg) using the same strategy (Supplementary Figure 1). We then performed transcriptome analysis of freshly prepared progerin-expressing endothelial cells (ECs) derived from these mice, and of control ECs derived from mice with transgenic expression of wildtype lamin A (LA-Tg) together with the corresponding littermate controls (WT) [24]. Differential expression analysis between Prog-Tg versus WT and LA-Tg versus WT ECs revealed 131 transcripts significantly up- and 87 downregulated in Prog-Tg versus WT, and evidently much less change in LA-Tg versus WT samples (25 up- and 63 downregulated) with only 14 shared differentially expressed (DE) genes (Figure 1A and Supplementary Table 1). The direct comparison of deregulated genes in Prog-Tg versus LA-Tg ECs showed 147 genes significantly up- and 44 downregulated (Supplementary Figure 2A and Supplementary Table 1) and a 3-way Venn diagram analysis revealed only a weak overlap between these sets of differentially expressed genes (Supplementary Figure 2B). This clearly indicates a unique effect of progerin expression on the EC transcriptome rather than lamin A overexpression per se. Heatmap clustering showed a high degree of correlation between the three biological replicates per genotype (Supplementary Figure 2C). Prog-Tg/WT transcriptome ranked-list enrichment analysis revealed a strong enrichment of the terms "cell-cell adhesion" (124 genes) and "extracellular matrix organization" (172 genes) consistent with previous reports [35]. Furthermore, the terms "leukocyte chemotaxis" (144 genes) and "regulation of leukocyte migration" (141 genes) indicate an inflammatory response, whereas "mesenchymal cell differentiation" (169 genes) and "connective tissue development" (199 genes) point to a pro-fibrotic response (Figure 1B and Supplementary Figure 3A, 3B). Lessened enrichment was observed for these pathways in the control LA-Tg/WT transcriptome (Figure 1B and Supplementary Figure 3A). Importantly, gene ontology (GO) analysis for significantly differentially expressed (DE) genes (FC>1,5 and < -1.5; p>0.05) in the Prog-Tg/WT transcriptome revealed among the top terms "immune response category" with 20 significantly deregulated genes including interleukin (*Il1a*) and many chemokines (Figure 1C). This term was not found in LA-Tg ECs. We confirmed the top upregulated inflammatory factors, CC chemokine ligand 20 (*Ccl20*) and interleukin 1a (*Il1a*), and key pro-fibrotic factors such as connective tissue growth factor *(Ctgf)* and endothelin *(Edn1)* in ECs derived from lung and heart tissues by quantitative real time PCR (qPCR). *Ccl20*, *Il1a*, *Edn1* and *Ctgf* were upregulated in Prog-Tg/WT lung ECs and *Ccl20* in Prog-Tg heart ECs (Figure 1D and Supplementary Figure 4A). However, no significant changes in the expression of these factors were detected in LA-Tg ECs (Supplementary Figure 4B, 4C). Since upregulation of pro-fibrotic and pro-inflammatory factors pointed towards the initiation of a senescence-associated secretory pathway (SASP) in Prog-Tg ECs, we checked for senescence-mediating signaling pathways by functional enrichment analysis against KEGG (Kyoto Encyclopedia of Genes and Genomes). This analysis identified significant enrichment of the p53-pathway comprising many direct p53 targets and senescence-associated genes (Figure 1E). qPCR analysis confirmed significant upregulation of *Trp53* (p53) and validated senescence-linked genes, cyclin-dependent kinase inhibitors *Cdkn1a* ($p21^{Cip1/Waf1}$) and *Cdkn2a* ($p16^{Ink4a}$) (Figure 1F). Accordingly, Prog-Tg primary lung ECs at passage 2 in culture showed an inflated cell phenotype, a distinctive characteristic of senescent cells (Figure 1G). Furthermore, the number of cycling cells was dramatically reduced in Prog-Tg EC vs WT EC cultures, as revealed by bromodeoxyuridine (BrdU) incorporation assay (Figure 1H). Thus, our data suggest that progerin expression in ECs activates p53-linked senescence and SASP with endothelial-specific immunomodulatory function and pro-fibrotic signaling. These data are in line with our previous study revealing perivascular and interstitial cardiac fibrosis in Prog-Tg mice [24].

Cellular senescence and SASP *in vivo* in Prog-Tg mice

To examine senescence and SASP *in vivo* we first performed gene expression analysis in lung and heart tissues derived from Prog-Tg mice and corresponding WT littermates. Both senescence markers, *Cdkn1a* and

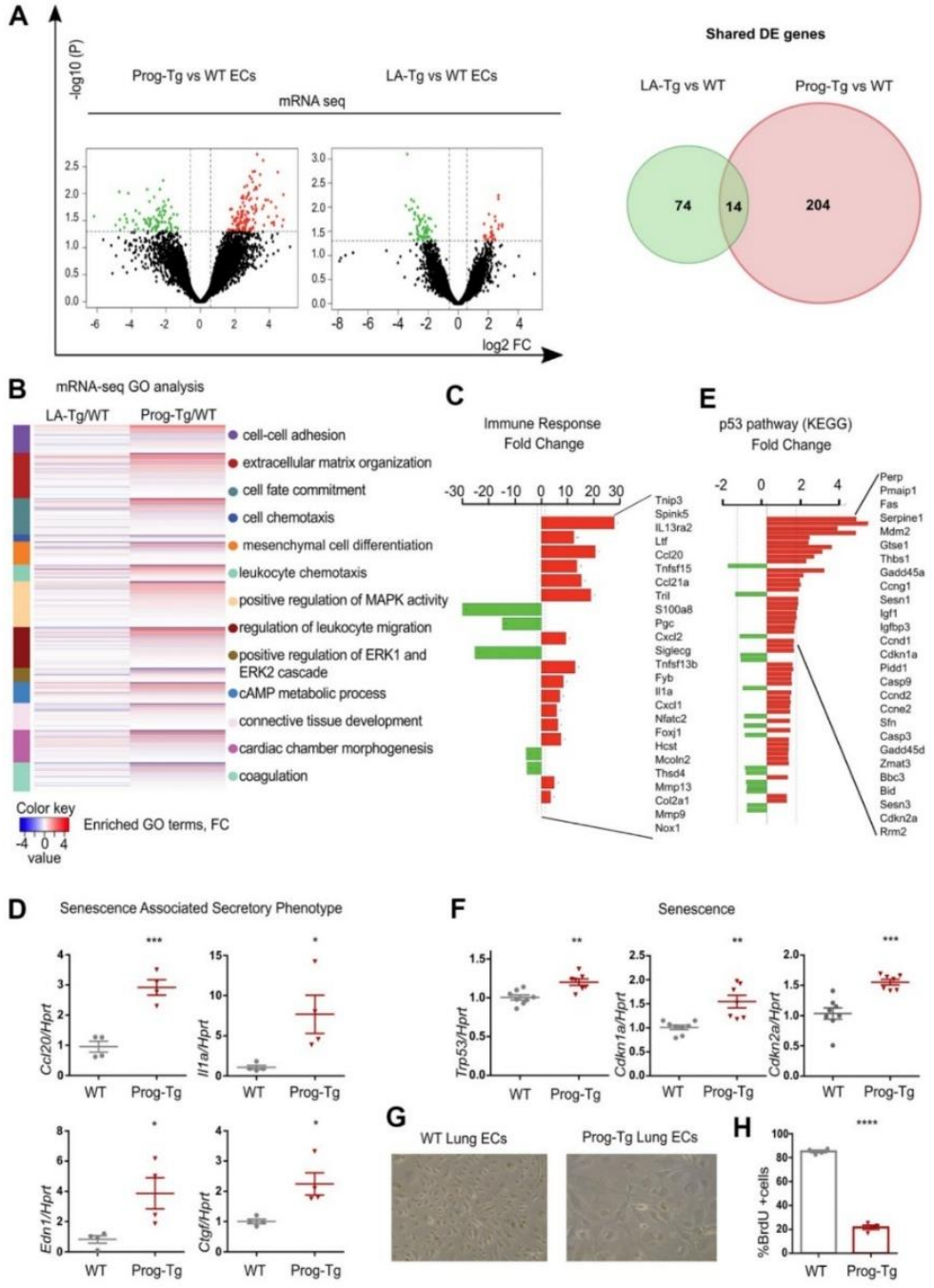

Figure 1. Progerin expression in endothelial cells activates senescence and SASP. (**A**) Volcano plots depicting differential expression (DE) analysis of genes in Prog-Tg/WT and LA-Tg/WT lung endothelial cells (ECs, left panel). Red, upregulated-, green, downregulated genes; X-axis, log_2 values of fold change (FC>1,5 and <-1.5) and y-axis, $-log_{10}$ values of p-value (p<0.05, n=3) (left panel). Analysis of shared DE genes between Prog-Tg/WT and LA-Tg/WT depicted by Venn diagrams (right panel). (**B**) Heatmap displaying enriched Gene Ontology (GO) terms of the whole ranked list of DE genes in Prog-Tg/WT and control group LA-Tg/WT using topGO and GOstats packages in R/Bioconductor. (**C**) Enriched GO term "Immune response" exhibiting significantly DE genes in Prog-Tg/WT lung ECs. (**D**) qPCR analysis of *Ccl20*, *Il1a*, *Edn1* and *Ctgf* in Prog-Tg/WT lung ECs using *Hprt* as reference gene. (**E**) KEGG pathway analysis of the "p53 pathway" enriched term showing DE genes in Prog-Tg/WT ECs. (**F**) qPCR analysis of *Trp53*, *Cdkn1a* and *Cdkn2a* in Prog-Tg/WT lung ECs using *Hprt* as reference gene. (**G**) Representative images from WT and Prog-Tg lung ECs at passage 2. (**H**) Bromodeoxyuridine incorporation assay (BrdU) performed for 40 h using Prog-Tg and WT lung ECs (n=4). For qPCR and BrdU assay, comparisons were performed between Prog-Tg and WT. For qPCRs n=4-8. Statistics were performed using unpaired two-tailed Students *t* test, *p<0.05, **p<0.01, ***p<0.001, ****p<0.0001.

Cdkn2a, were significantly upregulated in lung and heart tissues of Prog-Tg animals (Figure 2A). Concomitantly, inflammatory paracrine mediators *Ccl20* and *Il1a* were significantly increased in the lung and heart of Prog-Tg animals (Figure 2A).

Senescent cells upregulate $p19^{Arf}$ (*Cdkn2d*), an upstream activator of p53 signaling and a valid senescence marker for histological analyses [36]. Immunofluorescence staining of lung tissues from ~25-week-old Prog-Tg animals showed a marked accumulation of $p19^{+}$ cells compared to their WT littermates (Figure 2B). Quantitative analysis revealed an over six-fold increase in $p19^{+}$ cells in Prog-Tg lung specimens, supporting upregulation of senescence *in vivo* (Figure 2C).

Senescent cells mediate pro-inflammatory effects through secretion of SASP factors such as Ccl20 and Il1a [9]. We therefore tested the levels of these proteins in conditioned media and plasma of Prog-Tg mice. Prog-Tg ECs secreted significantly higher levels of Ccl20 compared to WT ECs with even more dramatic effects in plasma samples showing a ~seven-fold elevation (Figure 3A). Importantly, the conditioned medium from control LA-Tg ECs and plasma samples from LA-Tg animals did not show an increase in Ccl20 levels (Supplementary Figure 4D). In contrast to the increase in Ccl20 levels in Prog-Tg plasma, we did not find detectable levels of Il1a, neither in conditioned media nor in plasma samples (data not shown). As Ccl20 is known to recruit immune cells, we were prompted to test immune cell infiltration in the lung of Prog-Tg mice and also liver tissue, which is a key site of immunological defense [9, 36]. Indeed, we found an accumulation of CD3+ immune rosettes surrounding PECAM-positive blood vessels in tissues of Prog-Tg mice (Figure 3B). Quantification of randomly chosen areas in the proximity of blood vessels in lung and liver tissue sections of Prog-Tg vs littermate controls revealed a ~two-fold increase in immune cell infiltration (Figure 3C). In liver tissue, the effect was even more pronounced with a ~three-fold increase in CD3+ infiltrates in the vicinity of blood vessels but also interstitially (Figure 3B, 3C). Altogether, these data suggest that progerin-expressing endothelial cells exert systemic effects on surrounding tissues through SASP.

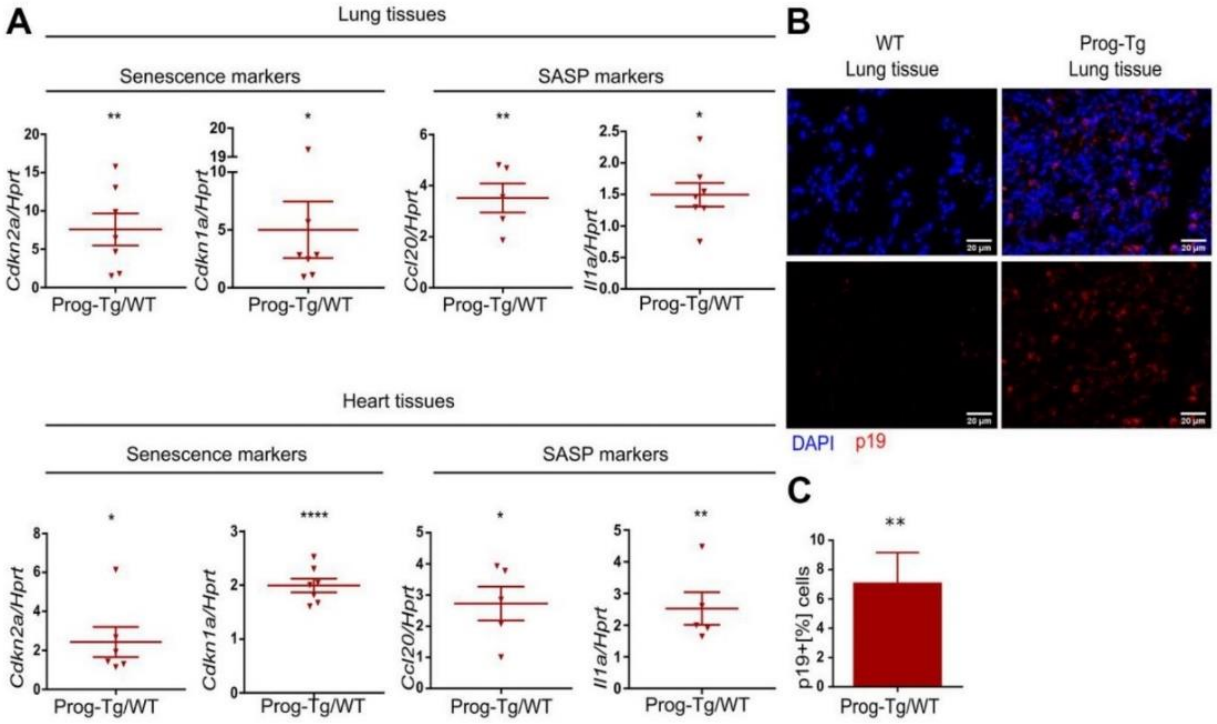

Figure 2. Senescence and SASP are detected *in vivo* in Prog-Tg mice. (**A**) qPCR analysis of depicted genes using RNA extracts from lung and heart tissues of Prog-Tg versus WT littermate mice (>25 weeks), n=5-7. (**B**) Representative immunofluorescence Z-stack projections from lung histological tissues sections of Prog-Tg and WT littermate mice at >25 weeks stained with anti-p19 antibodies and DAPI, Scale bar=20 μm. (**C**) Quantification of the percentage of p19-positive cells compared to DAPI-positive cells in lung tissues of Prog-Tg vs WT littermates on areas selected in a blinded manner (n=3). For qPCRs, a paired two-tailed Students *t* test was used and for statistic evaluation of histological staining a Mann-Whitney test. *p<0.05,**p<0.01, ****p<0.0001.

Progerin-expressing ECs exert paracrine senescence

Senescent hepatocytes were shown to induce inflammation and senescence in surrounding tissues in a paracrine fashion [9]. To examine the specific paracrine effect of progerin-expressing endothelial cells, we tested senescence and key SASP markers in non-endothelial cell populations obtained from lung tissues

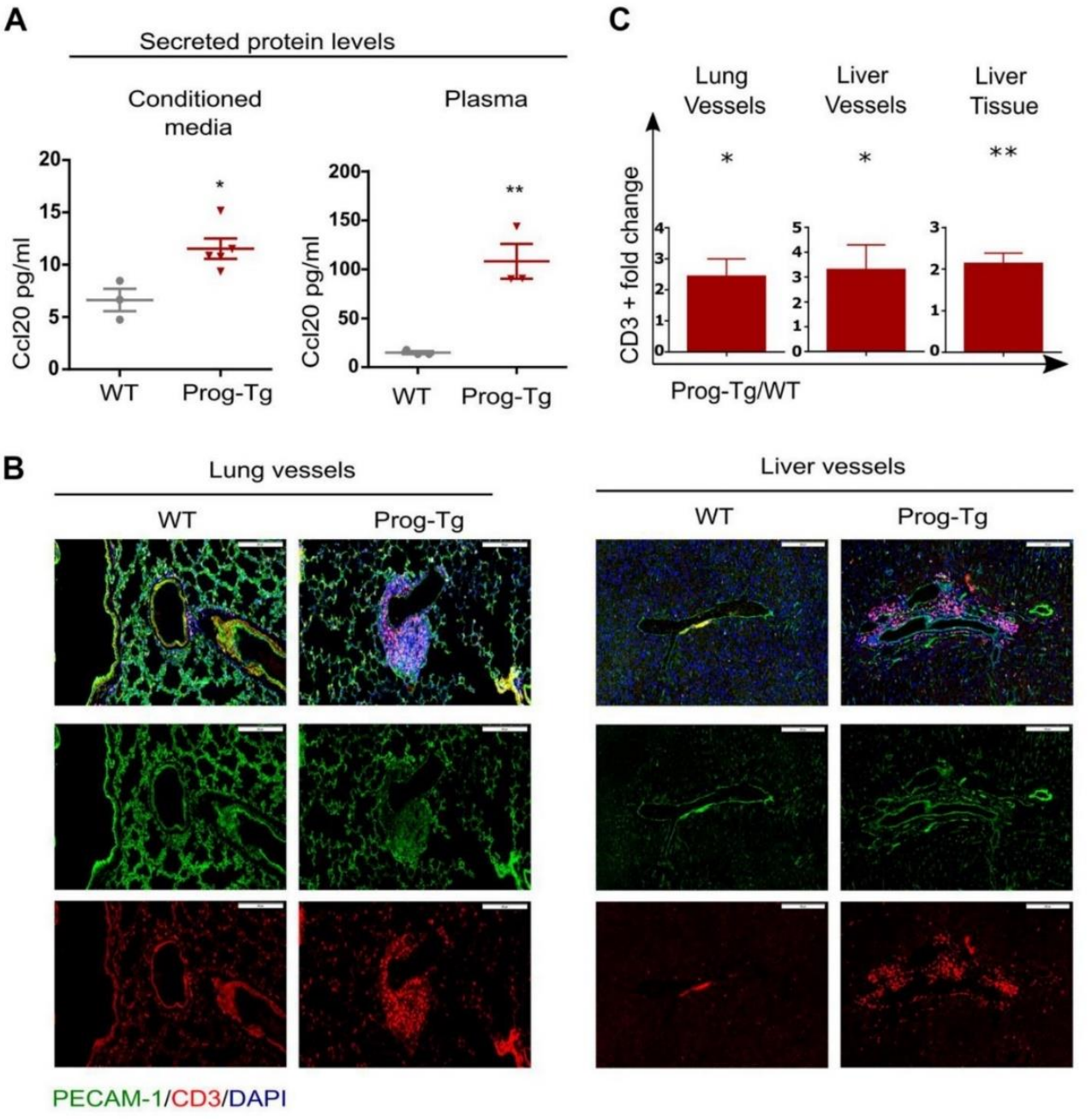

Figure 3. Pro-inflammatory effects in Prog-Tg mice. (**A**) ELISA was used to detect Ccl20 in cell culture supernatant samples of lung ECs and in plasma of ~30-week-old Prog-Tg and WT mice (n=3-4). (**B**) Representative immunofluorescence Z-stack projections of lung and liver sections from Prog-Tg and WT littermates (>25 weeks) stained with anti-PECAM and anti-CD3 antibodies and DAPI. (**C**) Quantification of CD3-positive cells in the vicinity of lung and liver vessels and in liver tissues counted in 10-15 independently selected areas in 4 pairs of Prog-Tg vs WT littermates. Scale bar=200 μm. For ELISA, an unpaired two-tailed Students *t* test was used. For statistic evaluation of histological stainings, a paired students two-tailed *t* test. *p<0.05, **p<0.01.

of Prog-Tg mice mostly depleted of endothelial cells (Figure 4A and Supplementary Figure 5A, 5B). Gene expression analysis revealed significant upregulation of key markers of senescence (*Cdkn2a* and *Cdkn1a)*, inflammation (*Ccl20)* and fibrosis (*Ctgf* and a trend for *Acta2)* in non-endothelial cell populations from Prog-Tg lung tissue (Figure 4B). These data strongly support the notion that progerin-expressing ECs induce senescence and elevate pro-inflammatory and pro-fibrotic effects in non-endothelial cell populations in a paracrine fashion in surrounding tissues.

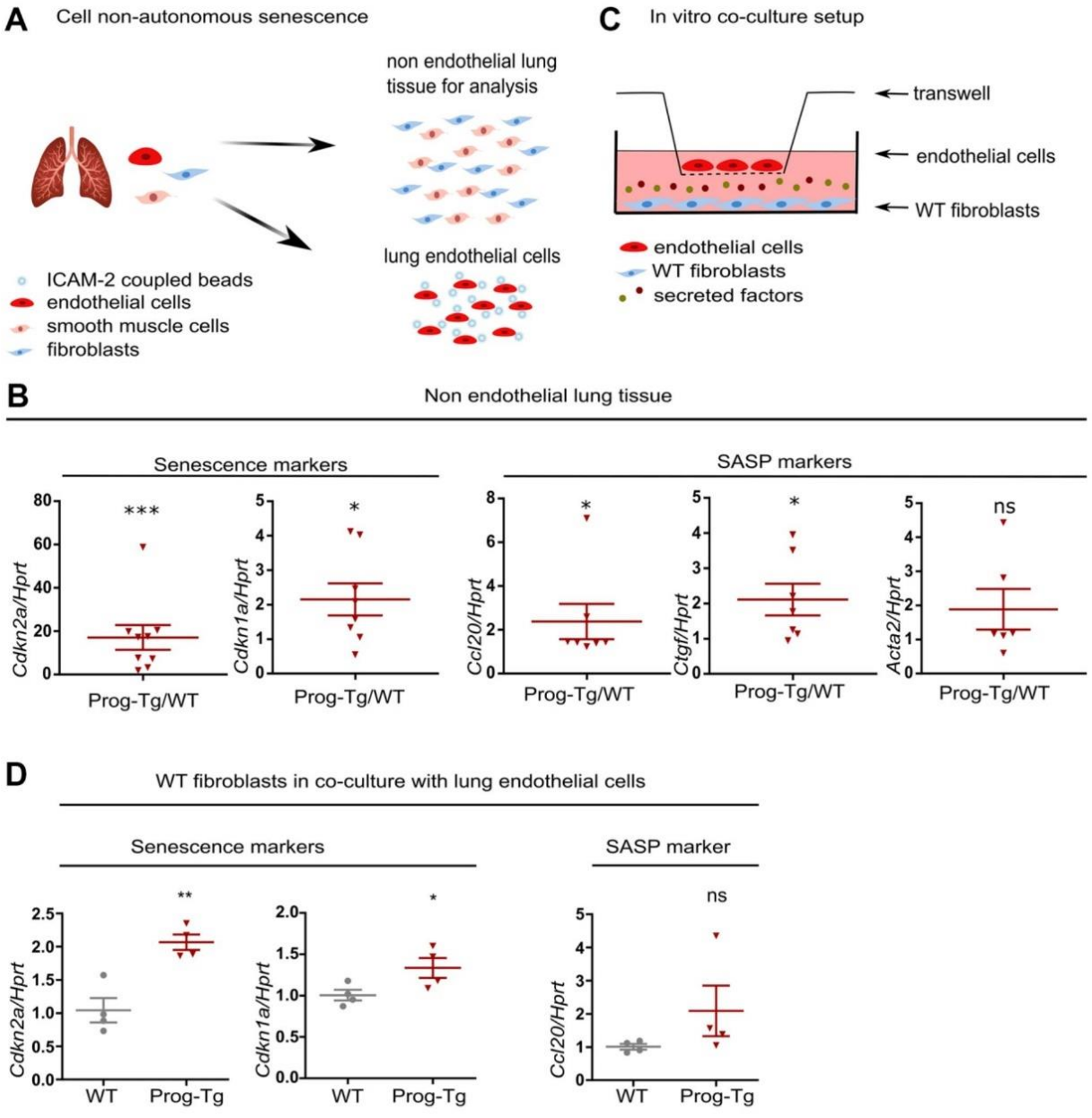

Figure 4. Progerin expressing ECs exert paracrine senescence. (**A**) Schematic representation depicting the separation of EC- from non-EC populations in lung tissue. (**B**) qPCR analysis of senescence and SASP marker genes in non-EC populations of WT vs Prog-Tg mice (>25 weeks). (**C**) Schematic representation of the *in vitro* co-culture setup. (**D**) qPCR analysis of senescence and SASP marker genes in WT fibroblasts co-cultured in the presence of WT or Prog-Tg ECs (n=4-9). Paired two-tailed Students *t* test was applied for *in vivo* experiments with littermate pairs and unpaired two-tailed Students *t* test for *in vitro* co-culture experiments. ns=non-significant, *p<0.05, **p<0.01, ***p<0.001.

Previously, we showed that Prog-Tg ECs exert pro-fibrotic paracrine effects on surrounding fibroblasts in an *in vitro* co-culture model system. The fibroblasts switched to *Acta2* expressing myofibroblasts in the co-culture with progerin-expressing ECs [24]. To directly assess if Prog-Tg ECs were also able to induce senescence and inflammation in a cell non-autonomous manner, we utilized the same set up with ECs seeded on transwell inserts placed on top of wells with cultured WT fibroblasts, allowing no physical contact between these cell types except through secretion of soluble factors (Figure 4C). In the presence of lung Prog-Tg ECs, fibroblasts express significantly higher levels of senescence markers *Cdkn1a* and *Cdkn2a* with a trend towards a pro-inflammatory phenotype as assessed by the expression of *Ccl20* (Figure 4D). Importantly, Prog-Tg ECs derived from heart tissues exert paracrine senescence and promote a myofibroblast switch in the co-culture system as assessed by an increase in *Cdkn2a* and *Acta2* levels compared to fibroblasts co-cultured with WT ECs (Supplementary Figure 5C). Altogether, these results demonstrate that progerin expression in endothelial tissue acts on different vascular beds such as lung and heart through paracrine senescence, fibrosis and inflammation, indicating systemic effects.

Senescent progerin-expressing ECs display a specific senescence-associated miR signature

Growing evidence from recent reports highlights the importance of circulating microRNAs (miRs) in plasma of elderly individuals that pose a high risk for cardiovascular incidents, however, with only a few reports on their cell type-specific origin and functions studied in *in vivo* animal models [2, 3, 12]. Thus, we explored the endothelial-specific miR signature with potential senescence regulatory function and ability to exert systemic effects using miR expression profiling in isolated endothelial cell extracts and plasma obtained from aged Prog-Tg and corresponding control animals. 68 and 51 differentially expressed (DE) miRs were found in ECs and plasma samples from Prog-Tg mice, respectively. Only 3 commonly shared deregulated miRs were found between Prog-Tg/WT and LA-Tg/WT lung ECs, indicating a progerin-specific effect on miR expression (Figure 5A, 5B and Supplementary Table 2). A comparative targetome KEGG pathway enrichment analysis of 41 significantly upregulated miRs conducted by miRSystem revealed the enrichment for the terms "cancer pathway" and "p53 signaling pathway" with deregulated miRs 124-3p, 206-3p, 485-5p, 31-5p, 34c-5p and 34a-5p (Figure 5C). This is conceivable since p53 signaling plays a key reciprocal role in cancer and senescence regulation [20]. The linkage of these miRs to the p53 pathway, together with previous findings on their upregulation during senescence [19, 37, 38] suggested that they fulfil features of senescence-associated (SA) miRs [12] and may thus represent an endothelial specific SA-miR signature.

We next overlapped the deregulated miRs in ECs with those in plasma of Prog-Tg mice. Only two miRs, miR34a-5p and miR31-5p were upregulated in ECs as well as in plasma of Prog-Tg mice but not in LA-Tg mice, and both were enriched within the p53-signaling cluster (Figure 5A, 5C, 5D). In further support of their potential involvement in systemic effects, miR34a-5p and miR31-5p were found significantly upregulated in whole lung tissue (Figure 5E) as well as in the non-EC lung populations depleted of ECs and in lung derived ECs (Figure 5F and Supplementary Figure 5D). Importantly, miR34a-5p but not miR31-5p was also found significantly upregulated in heart tissue (Figure 5E), implying the key importance of this miR in cardiac tissue and CVD pathology of Prog-Tg ECs. Finally, a strong trend towards increased expression of miR34a-5p and miR31-5p was observed in fibroblasts co-cultured in the presence of lung Prog-Tg ECs presumably due to either paracrine effects or direct secretion and uptake of these miRs (Supplementary Figure 5E). Overlapping analysis of putative miR34a-5p target mRNAs (using miR target prediction tool Targetscan), with all downregulated genes in Prog-Tg ECs (ranked list) revealed 307 commonly downregulated mRNAs, representing 53% of all known miR34-5p targets (Figure 5G). This suggested, in addition to the systemic also a cumulative effect of this miR on several targets in the Prog-Tg transcriptome.

miR34a-5p fine-tunes senescence in progerin-expressing ECs

Given the above observations implying a systemic relevance of miR34-5p and its potential involvement in CVD pathology in Prog-Tg mice, we next assessed whether the increased levels of miR34-5p affect the senescence phenotype of Prog-Tg ECs. For this, freshly isolated endothelial cell cultures were transfected either with antimiR neutralizing miR34a-5p or a control non-targeting antimiR. Specific antimiR treatment of Prog-Tg cells reduced the levels of miR34a-5p, as expected, and de-repressed the expression of its known direct targets, *Wnt7* and *Sirt1,* which were found significantly downregulated in Prog-Tg versus WT ECs, confirming the success of the antimiR treatment (Figure 6A and Supplementary Figure 6A, 6B). In WT cells, antimiR treatment did not affect the levels of miR34a-5p nor those of its target genes, probably due to the very low levels of miR34a-5p expressed in WT cells (Figure 6A and Supplementary Figure 6C). Importantly, miR34 inhibition downregulated p53 (*Trp53*) but also significantly repressed the late-stage senescence

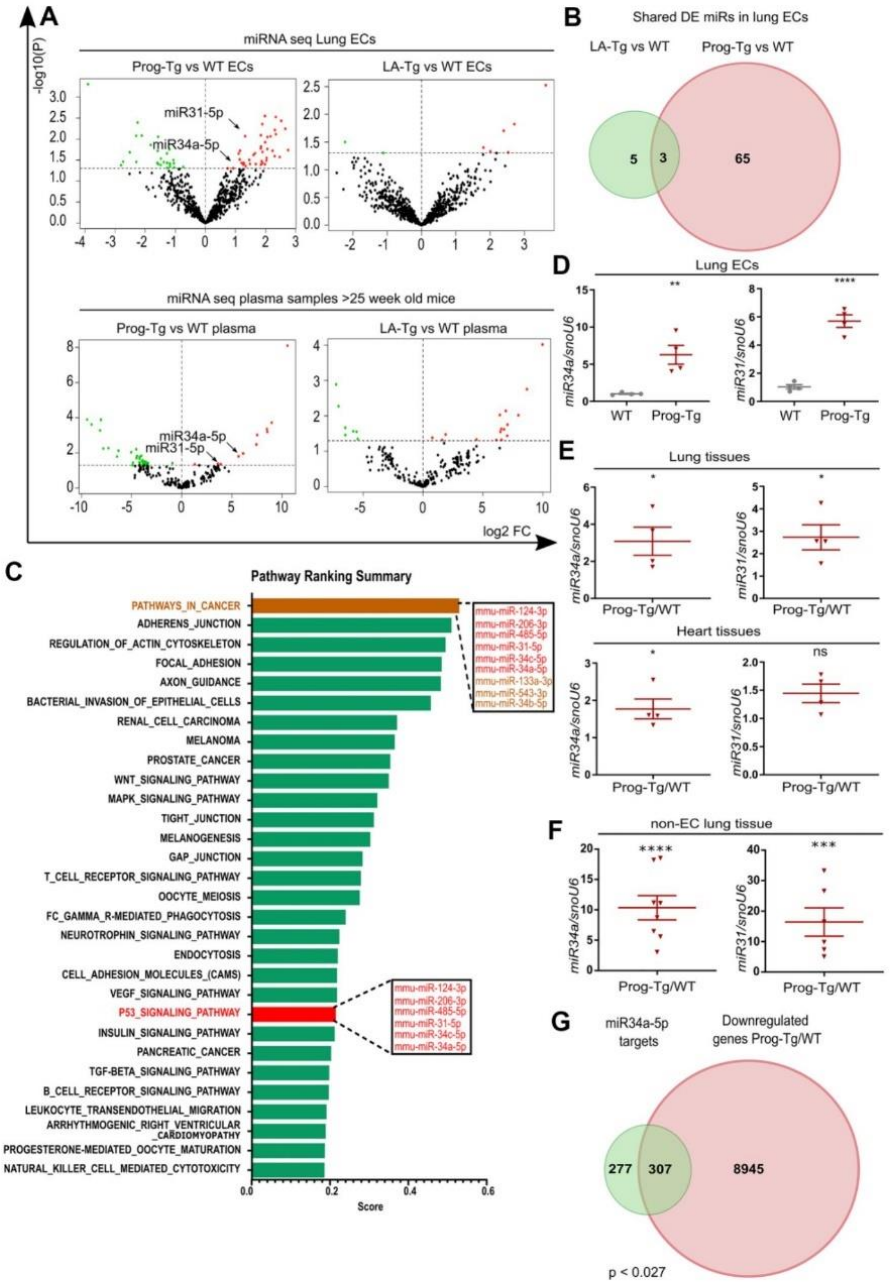

Figure 5. Senescent progerin-expressing ECs display a specific senescence-associated miR signature. (**A**) Volcano plots exhibiting differential expression (DE) analysis of miRs in Prog-Tg/WT and LA-Tg/WT lung ECs (upper panels) and in plasma samples of >25-week-old mice (lower panels) using threshold as depicted in Figure 1A (n=3). (**B**) Venn diagram showing overlap of DE miRs in Prog-Tg/WT and LA-Tg/WT lung ECs (topGO and GOstats packages in R/Bioconductor were used). (**C**) Bar graph representing the predicted top 30 pathways for the targetome of significantly DE miRs in Prog-Tg ECs with enriched term on the y-axis and ranking score on the x-axis. miRs linked to the "p53 signaling pathway" and "cancer pathway" are displayed in boxes (miRSystem version 20160513). (**D**) Expression levels analysed by qPCR of miR34a-5p (miR34) and miR31-5p (miR31) in cultured lung ECs normalized to small nuclear U6 RNA (snoU6). (**E**) Expression levels of miR34 and miR31 in the whole lung and heart tissues of Prog-Tg vs WT mice (>25 weeks) normalized to snoU6. (**F**) Expression levels of miR34a-5p and miR31-5p in non-EC populations from lung tissues of Prog-Tg vs WT mice normalized to snoU6. (**G**) Venn diagram displaying overlap between downregulated genes in Prog-Tg/WT lung ECs and miR34a-5p targets (Targetscan mouse) (Bioinformatics and Evolutionary Genomics). Hypergeometric test for the overlap showed a p-value of 0.027 and a representation factor of 1.1. For qPCRs n=4-8. The unpaired Students *t* test was used for *in vitro* experiments, paired Students *t* test for *in vivo* experiments using WT littermate controls. ns=non-significant, *p<0.05, **p<0.01, ***p<0.001, ****p<0.0001.

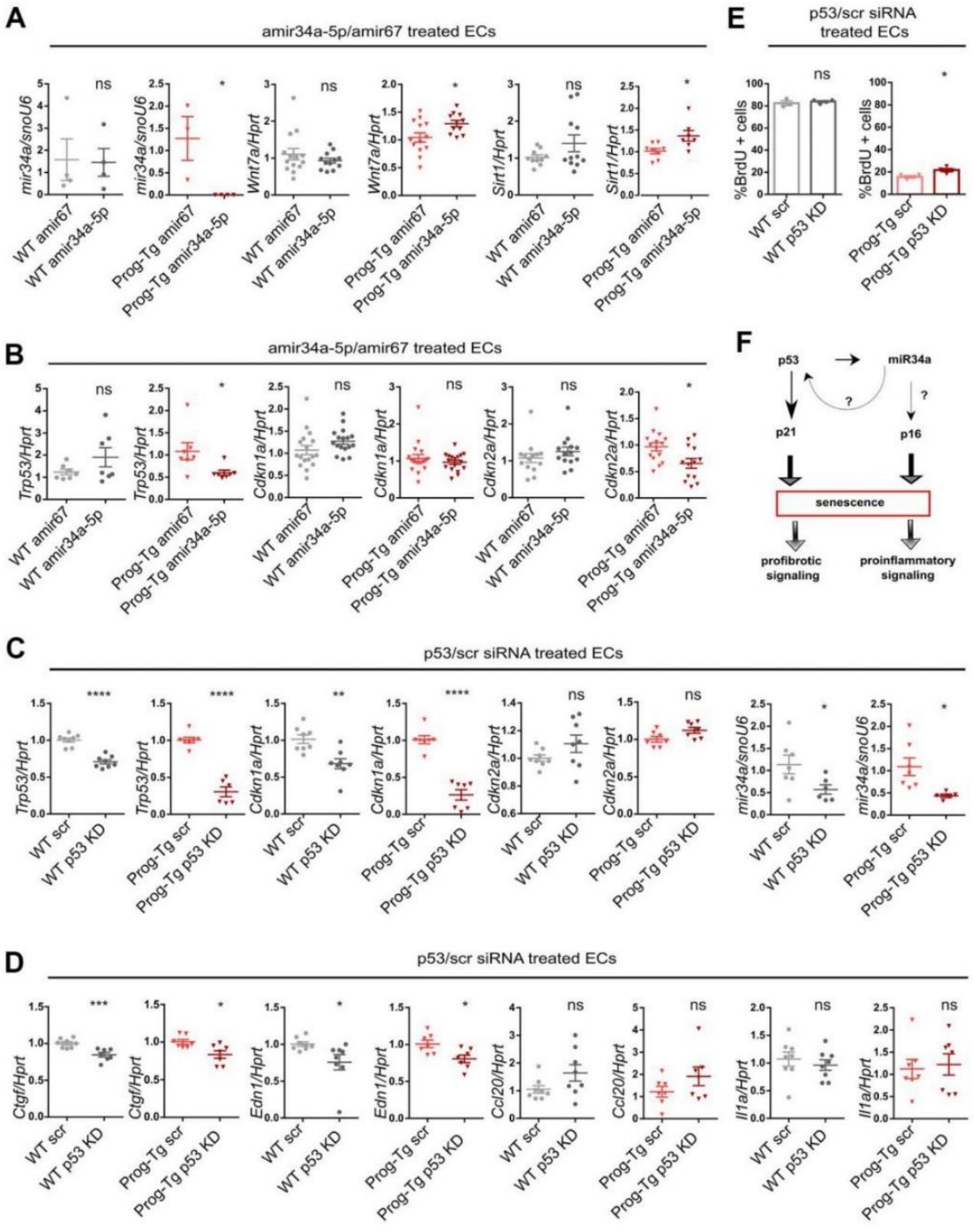

Figure 6. miR-34a-5p fine-tunes senescence in progerin-expressing ECs. WT and Prog-Tg lung ECs were transfected with antimiR34a-5p (amir34a-5p) or control antimir67 (amir67) and tested for (**A**) expression levels of miR34a-5p, and mir34 targets *Wnt7a* and *Sirt1* and (**B**) *Trp53*, *Cdkn1a* and *Cdkn2a*. WT and Prog-Tg lung ECs were transfected with p53 neutralizing siRNAs or scrambled siRNA (scr) and tested for (**C**) gene expression levels of senescence markers *Trp53*, *Cdkn1a, Cdkn2a* and miR34a-5p and (**D**) pro-fibrotic markers *Ctgf*, *Edn1* and pro-inflammatory markers (*Ccl20*, *Il1a*). (**E**) BrdU assay performed over 40 h. (**F**) Schematic representation of miR34a-5p acting on p53- and p16-branch regulating senescence pathways in Prog-Tg ECs. For qPCRs n≥3. Unpaired two-tailed Students *t* test, ns=non-significant *p<0.05, **p<0.01, ***p<0.001, ****p<0.0001.

regulator p16 (*Cdkn2*) (Figure 6B) in Prog-Tg, but not in WT cells, indicating its key role in maintaining the senescence phenotype in progerin-expressing ECs. In contrast, no effect was observed on early-stage senescence marker p21 *(Cdkn1)* and other SASP factors (Supplementary Figure 6D), suggesting the need for additional factors or more prolonged treatment for a fully resolved senescence phenotype. Since miR34a-5p was reported to act within the p53-signaling network [20], we next used p53 neutralizing siRNA to knockdown p53 to discern the p53 from the miR34a-5p-mediated effect on senescence and SASP. Compared to the scrambled siRNAs control, the p53-specific siRNA downregulated p53 (*Trp53*) levels by 70% in Prog-Tg ECs (Figure 6C). Similar to the results above, the p53-specific siRNA exerted only subtle effects in WT cells, presumably due to very low levels of *Trp53* in these cells (Figure 6C). In contrast to antimiR34a-5p treatment, p53 knockdown had no effect on p16 (*Cdkn2a*) but profoundly reduced the levels of its direct downstream targets, senescence marker p21 (*Cdkn1a*) and miR34a-5p, as expected and partially ameliorated the endothelial-specific SASP as evident by reduced levels of pro-fibrotic factors *Ctgf* and *Edn1* (Figure 6C, 6D), suggesting complementary effects of p53 and miR34a-5p in senescence regulation. Again, WT cells showed a similar but mostly reduced effect upon treatment (Figure 6C, 6D). The significant reduction in p53 and p21 levels in Prog-Tg cells correlated with a subtle but significant increase in proliferation as measured by BrdU incorporation assay (Figure 6E). Overall, these data suggest that miR34a-5p regulates senescence in endothelial cells by acting on two separate senescence signaling branches, a well-established p53- and, in addition a p16 pathway with presumably systemic effects on surrounding non-endothelial cell populations (Figure 6F).

Senescence and accumulation of miR-34a-5p at atheroprone aortic arch regions of Prog-Tg mice

Senescent cells have been shown to accumulate at atheroprone regions of impaired shear stress in aortic arch, thereby promoting the development of cardiovascular pathologies [39]. Given our previous findings of impaired shear stress in ECs- and aorta of Prog-Tg mice [24], we next examined if changes in senescence-associated miRs can be observed in different flow regions of aorta, which would have relevance to aging-linked cardiovascular pathology in these mice. For this, we dissected aorta from aged Prog-Tg and littermate mice and separated the upper region containing the aortic arch with disturbed blood flow patterns from that of descending aorta with laminar flow as previously reported [40] (Figure 7A). The distribution of senescence-associated miR34a-5p and miR31-5p between these aortic regions was then assessed by gene expression analysis of the corresponding tissue extracts. We found significant upregulation of miR34a-5p and a trend towards higher levels of miR31-5p in the aortic arch regions in comparison to those of descending aortas in Prog-Tg mice, but not in littermate controls, that correlated well with upregulation of p21 senescence marker (*Cdkn1*) (Figure 7B, 7C). These data indicate that mechanical stress, which is particularly high at regions of vessel curvatures such as in the aortic arch, leads to increased mechanical damage, senescence and increased expression of endothelial senescence associated miRs. Thus, particularly the circulating SA-miR34a-5p, which may putatively mediate systemic effects in non-endothelial surrounding cell populations, could be a potential target for clinical studies in the treatment of endothelial-rooted cardiovascular defects (Figure 7D).

DISCUSSION

microRNAs have recently gained immense attention in the treatment of various age-related cardiovascular pathologies [3]. However, precise miR-mediated treatments require the identification of specific cell type-mediated defects and elucidation of the accompanying miR signature and its functions. In this study, we identify an endothelial-specific miR-signature involved in p53-linked senescence with accompanying pro-inflammatory and pro-fibrotic systemic effects contributing to cardiovascular aging pathology in HGPS.

Cellular senescence has emerged as a primary driver of age-related pathologies, as senescent cells were shown to accumulate at regions of cellular insults such as atherosclerotic plaques particularly at vessel bifurcations. In line with this, the elimination of senescent cells reduced atherogenesis and cardiac aging [39, 41]. Similarly, a growing number of studies delineate the importance of endothelial senescence in developing age-related cardiovascular pathologies [1]. However, there is limited evidence on the specific-miRs and their role in endothelial senescence studied *in vivo* and to what extent these provoke tissue deterioration. To address these questions, we used a HGPS mouse model with endothelium-specific expression of progerin. Our previous findings showed that these mice recapitulate many aspects of cardiovascular pathology of HGPS patients such as perivascular and interstitial fibrosis and diastolic dysfunction [24]. Similar cardiovascular pathologies were observed later also in another endothelium-specific progerin-expressing mouse model generated via a different strategy, which, in addition, exhibited significantly compromised acetylcholine-regulated vasodilation of thoracic aorta [30]. Both reports strengthen the pivotal role of endothelial dysfunction in the cardiovascular pathology of HGPS.

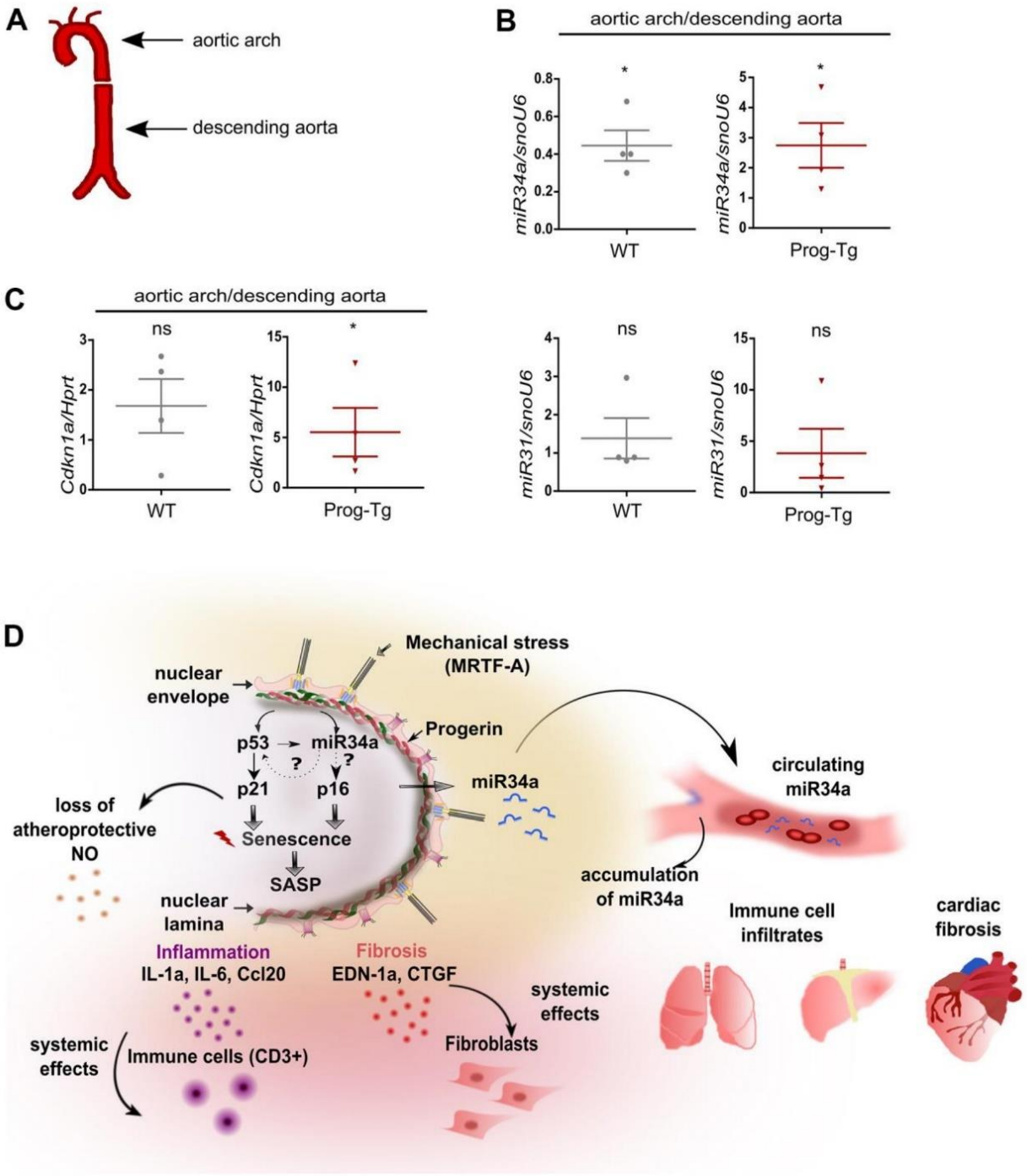

Figure 7. Analysis of circulatory SA-miRs at atheroprone aortic arch regions. (**A**) Schematic representation of aortic segment including aortic arch region and that of descending aorta. (**B**) Gene expression analysis of miR34a-5p (miR34a) and miR31-5p (miR31) and of (**C**) p21 (*Cdkn1a*) in WT and Prog-Tg aortic arch in comparison to descending aorta. n=4. Paired two-tailed Students *t* test, ns=non-significant *p<0.05. (**D**) Hypothetical model of intrinsic and extrinsic miR34-mediated senescence regulation in progerin-expressing endothelial cells. Mechanical stress particularly at vessel bifurcation leads to p53-linked senescence and miR34 upregulation. miR34 sustains senescence through positive feed-back mechanism acting on p53 but also separately by maintaining high levels of late senescence marker p16. Synergistic miR34-p53 action leads to elevation of SASP signaling and thus secretion of pro-inflammatory (Ccl20, IL-1a) and pro-fibrotic (CTGF, EDN-1a) factors with systemic effects on surrounding tissues leading to immune cell infiltrates and fibrosis in lung and liver and cardiac tissue. Systemic fibrosis and inflammation in tissues is further potentiated by increased release of miR34 in circulation.

In order to identify the endothelial specific miR profile with potential novel mechanistic insights into endothelial dysfunction in progeria, we applied mRNA and miR transcriptome analysis of primary progerin-expressing ECs and plasma of aged Prog-Tg animals coupled with qPCR and histological analysis. We found deregulation of a plethora of endothelial specific miRs with peculiar upregulation of senescence-associated miRs, miR206-3p, miR124-3p, miR485-5p, miR31-5p and miR34a-5p and miR34c-5p together with upregulation of a p53-linked senescence pathway and initiation of a SASP phenotype. Among these p53-linked miRs, circulatory miR34a-5p has the ability to exert systemic effects. Using antimiR34a-5p and p53 knockdown approaches, we demonstrate that a complementing and synergistic action of p53 and miR34a-5p fine-tunes senescence in progerin-expressing ECs. The involvement of the p53/p21 in HGPS has also been proposed in a previous study [42], showing that the p21 (*CDKN1A*) gene is upregulated by epigenetic pathways upon progerin-induced oxidative stress in HGPS patient fibroblasts. Thus, the induction of senescence signaling in HGPS may be regulated through various pathways and at different levels synergistically.

Previous studies on senescent hepatocytes reported beneficial but also deleterious systemic effects on the surrounding tissue through a cell non-autonomous mechanism causing "bystander senescence" in normal non-senescent surrounding cells [9]. However, similar studies with senescent endothelial cell populations studied in a specific, isolated fashion *in vivo,* and the extent and the mode of action of these cell non-autonomous effects are still missing. Here we show marked upregulation of senescence not only in isolated EC cultures but also in whole heart and lung tissues and in endothelial cell-depleted lung populations of Prog-Tg animals indicating systemic effects. We can demonstrate the direct adverse effects of these senescent progerin-expressing ECs on their non-endothelial neighbors transmitting senescence and fibrosis in a paracrine fashion using co-culture cell model systems. Importantly, similar pro-senescent and pro-fibrotic effects detected in co-culture using heart-derived progerin-expressing ECs highlight the relevance to cardiovascular pathology but also indicate that this is a general phenomenon applicable to endothelial cells originating from different vascular beds.

Pro-senescent effects of senescent cells may have beneficial tumor suppressive effects, but during aging they have deleterious effects inducing chronic damage [43]. The mediators of either paracrine senescence or apoptosis were shown to be pro-inflammatory factors such as interleukin Il1a that triggers secretion of a plethora of immune factors such as different CC chemokine ligands or tumor necrosis factor 1α [9, 44]. The expression of pro-inflammatory mediators in HGPS was shown to be elicited by NF-κB and STAT1-mediated inflammatory responses rooted in DNA damage [45, 46]. Accordingly, anti-inflammatory treatments have been very successful in the treatment of HGPS [45–47]. In line with these findings, we found the "immune response term" as one of the uppermost enriched gene ontology (GO) terms among the significantly differentially expressed genes in progerin-expressing ECs. The immune response term comprises 20 significantly deregulated pro-inflammatory mediators and represents a specific endothelium-specific inflammatory signature. Here we could validate the systemic inflammatory effects of endothelial cells *in vivo* by showing upregulation of top-most immune response candidates, *CCl20* and *Il1a* in the lung and heart tissues and corresponding ECs and also circulating in plasma, in line with dramatic immune cell infiltrates in the vicinity of blood vessels in lung and liver tissues of Prog-Tg mice. The latter observation is in accordance with the primary function of pro-inflammatory mediators in recruiting immune cells with an aim to initiate immune-mediated clearance of damaged cells [43]. Senescent cells, however, have developed mechanisms to evade immune-mediated clearance resulting in the persistence of immune cell infiltrates in the proximity of senescent cells [48]. Altogether our findings indicate that persistent senescence of ECs and the induced inflammatory response was sufficient to cause immune-cell tissue infiltration and accumulation in the vicinity of blood vessels.

In recent years miRs have gained attention as potent regulators of gene expression in accelerated aging disease and during physiological aging [16]. The miR interactome is very complex since each miR has the ability to affect hundreds of mRNA targets and thus have multifunctional effects [16]. Vice versa, a specific mRNA can be regulated by several miRs in a context-dependent manner. Senescence associated (SA) miRs, also called geromiRs, were found upregulated upon onset of cellular senescence, affecting predominantly genes involved directly or indirectly in cell cycle regulation [12, 19, 37]. SA-miRs seem to act predominantly through their effect on the p53/p21 or p16/Rb signaling axis [37]. Within the p53/p21 axis, activated p53 has the ability to either directly act on miR promoters or through modulation of the miR processing Drosha complex, which both lead to increased expression of several miRs with tumor suppressive function [49, 50]. Hence, p53 activation is typically associated with upregulation of SA-miRs. Here we found upregulation of SA-miRs, miR-206, miR-124, miR34a-5p, miR34c-5p and miR31-5p, linked

to p53 signaling but did not observe changes in miR-29 and miR-365, which were previously found deregulated in fibroblasts of Zmpste24-/- progeroid mice [17, 18]. Therefore, we conclude that these deregulated miRs resemble a unique endothelium-specific senescence-associated miR signature that will be a valuable tool for future clinical studies.

Among the upregulated SA-miRs, we focused on miR34a-5p, which was uniquely elevated in circulation as well as in lung and heart tissues of Prog-Tg mice. miR34a-5p was previously shown to be induced in human heart failure and animal models implicated in cardiovascular disease progression, and targeting the miR34a-5p has harnessed the therapeutic benefits in cardiac repair [21–23]. However, endothelial cell type specific miR34 effects in this context have not been investigated so far. Thus, these previous findings together with our observation of strong miR34a-5p accumulation at atheroprone regions of the aortic arch in Prog-Tg mice suggests that miR34a-5p is particularly relevant for cardiovascular pathology in HGPS and supposedly geriatric patients, with strong potential to be a novel predictive and therapeutic biomarker for CVD rooted in endothelial dysfunction. In addition to elevation in plasma and tissues, miR34a-5p levels were also dramatically upregulated in EC-depleted non-endothelial cell populations indicating potential systemic effects. miR34a-5p is a direct target of p53 and exerts tumor suppressive function via its repressive role on a plethora of targets involved in cell-cycle regulation. One study showed that it affects one quarter of mRNA targets within the p53 network [20, 49, 50]. One of the common miR34a-5p targets is NAD-dependent deacetylase silent information regulator 1 (*Sirt1*) that inhibits p53 through deacetylation and negatively affects cellular senescence [20]. We observed a modest decrease of *Sirt1* in Prog-Tg ECs, and *Sirt1* was significantly de-repressed upon anti-miR34 treatment. Another strongly downregulated miR34a-5p target in Prog-Tg/WT ECs, Wingless 7a (*Wnt7a*), was also de-repressed upon anti-miR34 treatment. The Wnt-pathway was previously found deregulated in HGPS and in physiological aging [51–53] and is one of the major pathways predicted to be affected by SA-miRs [16]. Here we show that de-repression of *Wnt7* and *Sirt1* correlates with a reduction of the late-senescence marker p16. Low to moderate grade damage usually leads to transient elevation of p21 to induce cell cycle arrest and, if the damage is repaired, is reverted to normal levels [10]. Consistent with this, we show that lowering p21 levels through siRNA mediated p53 knockdown could restore cell growth with no effect on p16 state. p16 is a late-stage senescence marker elevated upon increased persistent cellular stress, eventually causing permanent cell cycle arrest [10]. We hypothesize that increased miR34a-5p levels may contribute to persistent cellular stress through cumulative cell-cycle repression of *Sirt1* and *Wnt7* but also through the effects on many potential other targets, leading to permanent cell cycle arrest. The latter assumption is based on our Targetscan based prediction approach showing 50% of miR34a-5p targetome downregulated in Prog-Tg transcriptome. The novel finding that anti-miR34a-5p treatment is able to significantly lower p16-linked senescence in addition to p53-levels with minimal, non-significant reduction of p21 levels suggests that miR34a-5p mainly affects already cell-cycle arrested cells on their way to irreversible p16-mediated cell cycle arrest.

As for the underlying cause for the upregulation of miR34a-5p and the initiation of miR-linked p53 senescence we hypothesize that impaired shear stress and mechanical damage may be one of the triggering mechanisms (Figure 7B), because our previous findings revealed an impairment of the shear stress response and myocardin-related transcription factor A (MRTF-A) mechanosignaling pathway in progerin-expressing endothelial cells [24]. We addressed this potential model by testing miR34a-5p levels in curved regions of the aorta prone to disturbed blood flow and higher shear stress compared to the descending aorta exposed to laminar blood flow. In line with our hypothesis, we found accumulation of miR34a-5p and increased p21 levels particularly at the aortic arch region, in accordance with previous reports that disturbed flow, such as at aortic curvature, leads to activation of senescence signaling in endothelial cells [54, 55]. Thus, although our gene expression studies were performed in unstimulated cells without additional exposure to shear stress *in vitro*, the observed changes in gene expression in primary endothelial cells may still reflect the *in vivo* conditions of increased mechanical stress caused by progerin accumulation.

We found miR34a-5p levels also dramatically upregulated in plasma of Prog-Tg mice, indicating potential systemic effects. Therefore, progerin-expressing endothelial cells have the potential to affect a variety of tissues through secretion of miRs and other signaling molecules, such as adipose tissue [56]. Indeed, in Prog-Tg mice we observe loss of adipose tissue (our unpublished data) but mechanistic details remain to be explored in future studies.

Based on the novel findings in this study we propose the following hypothetical disease mechanism to explain EC-mediated cardiovascular pathology in HGPS (Figure 7D): Progerin induces persistent mechanical stress leading to the activation of the p53 pathway, and its target miRs, such as miR34-5p, rise particularly at

mechanosensitive atheroprone vessel bifurcations. Presumably through EC-mediated secretion, miR34a-5p reaches the circulation causing systemic cell cycle repressive effects on the neighboring non-endothelial cell populations. This pro-senescent miR34a-5p-mediated effect in turn exacerbates SASP-mediated inflammation in target tissue such as lung and liver, and fibrosis of cardiac tissue. Mechanistically, on both the extrinsic- and the intrinsic endothelial level, miR34a-5p has the ability to repress several positive cell cycle regulators causing a gradual increase in p16 levels. If the damage and miR34a-5p/p16 levels persist, cells enter a p16-mediated irreversible permanent cell cycle arrest. As a consequence, senescent cells switch to a pro-inflammatory and pro-fibrotic secretome resulting in immune cell attraction and fibroblast to myo-fibroblasts switch, respectively. Specifically, in endothelial cells SASP counteracts the effects of healthy atheroprotective nitric-oxide containing secretome consistent with previous findings of low nitric oxide levels in progerin-expressing endothelial cells [24, 31, 32] (Figure 7D). Collectively, our data demonstrate that presumably through its key strategic position, endothelial senescence exerts systemic tissue deterioration, and part of this systemic cell-cycle repressive effect involves SA-miRs, particularly miR34a-5p. Fine-tuned senescence-associated antimiR therapies targeting specifically ECs could be a beneficial strategy for the treatment of endothelial senescence in premature and pathophysiological aging and as a complementary intervention strategy during cancer therapy-induced senescence.

MATERIALS AND METHODS

Animals

Bi-transgenic LA-Tg and Prog-Tg mice were generated *de novo* by crossing tet operon-driven transgenic lamin A minigene wildtype (*tetop-LA^{Wt}*) or HGPS mutant (1824C>T; G608G; *tetop-LA^{G608G}*) mice [33] (see Supplementary Figure 1, C57BL/6J background) with transgenic mice expressing a tetracycline-responsive transcriptional activator under the control of the EC-specific VE-cadherin promoter (*Cdh5-tTA* mice, Jackson Laboratories, MGI: 4437711, *FVB* background). The VE-cadherin (*Cdh5*) promoter includes the full promoter region (-2226, +24) as described [34], and is active exclusively in the endothelial tissue from embryonic day 13.5 (E 13.5) on [57]. Mice were maintained at C57BL/6J background (N4 generation; ~94%) as previously described [24]. Animal studies were approved by the Regional Ethics Committee for Laboratory Animal Experiments at the Medical University of Vienna and the Austrian Ministry of Science Research and Economy (BMWFW-66.009/0321-WF/V/3b/2016 and BMWFW-66.009/0156-WF/V/3b/2017) according to Austrian Law BGBI. I Nr.114/2012 (TVG2012) and in accordance with the Guide for the Care and Use of Laboratory Animals published by the US National Institutes of Health (NIH Publication No. 85-23, revised 1996).

Primary endothelial cell isolation and culture

Primary endothelial cells were isolated from lungs and heart tissues of ~10-day old Prog-Tg and LA-Tg mice and corresponding WT littermate animals using ICAM-2 magnetic bead separation as described previously [24]. Briefly, lung tissue was isolated from mice, minced and digested in 200 U/ml collagenase type I (Gibco 17100-017) for 45 minutes at 37° C on an end over end rotor. For heart tissue, collagenase type II (Gibco 17101-015) was used. Thereafter, collagenase digested tissues were passed through an 18-gauge syringe needle 10-15 times and filtered through a 70µm Nylon cell strainer (Corning, REF: 431751). Cells were pelleted at 200 x g for 5 min and plated on 2% gelatin / 1 µg/ml fibronectin-coated plates. Cells were cultured in DMEM supplemented with 20% FCS, EC growth supplement (CellBiologics Catalog No 1166), 25 mM HEPES, 50 U/ml penicillin, 50 µg/ml streptomycin, 2 mM L-glutamine, 1 mM nonessential amino acids, 1 mM sodium pyruvate, and 139 µg/ml heparin (complete culture medium). Typically, after 48 hours, cells were incubated for 5 min at 37° C in a trypsin-EDTA solution (Sigma, T4049), resuspended in 1ml of cold medium and mixed with 10µl magnetic Dynabeads (Dynabeads Sheep Anti-Rat IgG Catalog No. 11035) coupled to ICAM-2 antibody (CD102 Rat anti-Mouse, Fisher Scientific REF: 553326). Cells were incubated for 45 min at 4° C and thereafter endothelial cells bound to the ICAM-2 coupled Dynabeads were separated from the rest of cells using a magnetic stand. Separated endothelial cells were cultured on a gelatin/fibronectin coated plate. Primary ECs were used for experiments at passage p2 or p3 after isolation.

Co-cultures

Co-cultures experiments were performed as described previously [24]. ECs at passage 2 were seeded on cell culture transwell filter inserts (Costar Corning Incorporated, 3460; pore size 0.4 µm) at a density of 3.6×10^4 cells/cm^2. WT fibroblasts, isolated from lung tissue of neonatal C57BL/6J mice [24], were seeded on the bottom of 12-well cell culture plates at a density of 2.4×10^4 cells/cm^2. Cells were cultured separate for 24 hours and thereafter co-cultured for 4 days prior to RNA isolation. Extrinsic effects of ECs on co-cultured fibroblasts were assessed by expression analysis of the known pro-fibrotic factors *Acta2*, senescence markers *Cdkn1a* and *Cdkn2a* and pro-inflammatory marker *Ccl20.*

AntimiR treatment

Primary lung ECs were transfected with an antimiR for miR34a-5p (miRIDIAN microRNA Hairpin Inhibitor assay from Dharmacon IH-310529-08-0005). Briefly, lung ECs of passage 2 were seeded on a 48-well cell culture plate at a density of 5×10^4 cells/cm^2 and cultured for 24 h in antibiotic free medium. Thereafter, cells were co-transfected with 100 nM antimiR34a-5p and 50 nM fluorescently labelled control antimiR (miRIDIAN microRNA Hairpin Inhibitor Transfection Control with Dy547 CP-004500-01-05) for 48 h using a lipofectamine-based transfection reagent (LipoFectMax transfection reagent ABP Biosciences FP310). As a negative control, the *C. elegans* Cel-miR-67 that has minimal sequence identity with mouse miRs was used (miRIDIAN microRNA Hairpin Negative Control #1 IN-001005-01-05). After transfection, cells were harvested, transfection efficiency was tested via flow cytometry, total RNA was extracted and used for subsequent expression analysis by qPCR. Efficient miR downregulation was assessed by measuring expression levels of miR34a-5p and direct miR targets in antimiR transfected cells.

p53 knockdown

For p53 knockdown in primary lung ECs, a pool of 4 siRNAs targeting the p53 mRNA (ON-TARGETplus Trp53 (22059) siRNA-SMARTpool L-040642-00-0005) was introduced into cells using a lipofectamine based-transfection reagent (LipoFectMax transfection reagent ABP Biosciences FP310). As a negative control, a pool of 4 scrambled siRNA (siGENOME Non-Targeting siRNA Pool #2, 20nmol D-001206-14-20) was tested side by side with the p53 siRNA pool. Briefly, lung ECs of passage 2 were seeded on a 48-well cell culture plate at a density of 5×10^4 cells/cm^2 and cultured for 24 h in antibiotic free medium. Thereafter, cells were co-transfected with 100 nM of the pool of 4 siRNAs targeting the p53 mRNA and 50 nM fluorescently labelled control antimiR (miRIDIAN microRNA Hairpin Inhibitor Transfection Control with Dy547 CP-004500-01-05) for 48 h. RNA was isolated 48 h after transfection and analysed via qPCR.

Total RNA isolation and gene expression analysis

Total RNA including miRs from tissues and cells was isolated using the miRNeasy Mini Kit (Qiagen 217084) and subsequently quantified using NanoDrop Technologies, ND-1000 spectrophotometer. Typically, RNA was isolated from 5×10^4 -1×10^6 cells. For gene expression analysis, cDNA was generated using RevertAid reverse transcriptase (Thermo Fisher Scientific). qPCR was performed using the primers listed in Table 1. All reactions were done in technical triplicates using Eppendorf RealPlex 2 Mastercycler with KAPA SYBR Green PCR master mix (Peqlab) and according to the manufacturer's instructions. Results were normalized to the expression of hypoxanthine-guanine phosphoribosyl-transferase (*Hprt)* and presented as a fold increase relative to *WT* littermate animals based on the ΔΔCt method. To detect intracellular miRs, miScript II RT Kit (Qiagen) and miScript Primer Assays (Qiagen) were used. Intracellular miRs were normalized to small nuclear U6 RNA (snoU6).

Analysis of EC- and non-EC populations from lung tissues

Lung tissues were dissected from mice >25 weeks, minced and treated with 200 U/ml collagenase type I (Gibco 17100-017) for 45 minutes at 37° C. Thereafter, tissues were triturated using a 19-gauge syringe and tissue homogenate was passed through a 70-µm cell strainer. After centrifugation, the cell pellet was resuspended in cold medium, 10 µl of rat anti-ICAM2 coupled magnetic beads were added and incubated for 30 min. Magnetic separation was used to isolate beads-coupled EC and free non-EC populations with subsequent RNA extraction, gene and miR expression analysis as described above.

Analysis of heart and lung preparations

For gene expression analysis in tissues, heart and lung extracts were prepared according to [24] and analysed by qPCR. For aortic preparations, aorta was dissected according to previous methods and the whole upper region containing aortic arch was separated from the lower parts of descending aorta [40]. Briefly, all tissues were dissected from >25 weeks old WT and Prog-Tg mice and immediately treated with an RNA stabilization reagent (RNAprotect Tissue Reagent 76106 Qiagen). Thereafter, tissues were transferred to Trizol and lysed using 2.8mm Precellys Zirconium oxide Ceramic beads (Kit CK28) and a Precellys 24 tissue homogenizer according to the manufacturer's protocols (Bertin Instruments). Lysed tissues were used for total RNA extraction as described above.

Generation of mRNA and miR libraries and NGS sequencing

RNA samples for intracellular mRNA-and miR sequencing were obtained from lung ECs isolated from ~10-day old mice. Briefly, lung cells were isolated and sorted twice using ICAM-2 magnetic beads to obtain pure ECs. At passage 3, when cells reached 90% confluence, total RNA and miR extracts were prepared and subsequently used for library generation and NGS

Table 1. List of primers used for real time PCR analyses.

Primer pair	Sequence
Hprt Forward	GCAGTCCCAGCGTCGTGATTA
Hprt Reverse	TGATGGCCTCCCATCTCCTTCA
Ccl20 Forward	TCCTTGCTTTGGCATGGGTA
Ccl20 Reverse	TCTTAGGCTGAGGAGGTTCACA
Ctgf Forward	CCTAGCTGCCTACCGACT
Ctgf Reverse	CTTGACAGGCTTGGCGATTT
IL-1 Forward	AGCTCGTCAGGCAGAAGTTT
IL-1 Reverse	TTCTGGCAACTCCTTCAGCAA
Edn1 Forward	ATCTGGGTCAACACTCCCGA
Edn1 Reverse	ACTTTGGGCCCTGAGTTCTT
Trp53 Forward	TCGAGCTCCCTCTGAGCC
Trp53 Reverse	TGGCAGGATATCTTCTGGAGG
p16 Forward	TCGTACCCCGATTCAGGTGATG
p16 Reverse	GCCGGATTTAGCTCTGCTCT
p21 Forward	TGCCAGCAGAATAAAAGGTG
p21 Reverse	TTGCTCCTGTGCGGAAC
Acta2 Forward	GTACCACCATGTACCCAGGC
Acta2 Reverse	GAAGGTAGACAGCGAAGCCA
Wnt7a Forward	CGCTGGGAGAGCGTACTG
Wnt7a Reverse	ATCGCATAGGTGAAGGCAGC
Sirt1 Forward	GATGACAGAACGTCACACGC
Sirt1 Reverse	ACAATCTGCCACAGCGTCAT
Forward HGPS (human specific)	ACTGCAGCAGCTCGGGG
Reverse 1 HGPS (human specific)	AGTTCTGGGGGCTCTGGGT
Reverse 2 HGPS (human specific)	TCTGGGGGCTCTGGGC

sequencing. 50 µl EDTA plasma was isolated from three Prog-Tg and WT littermate pairs of >25 weeks old mice. RNA isolation of plasma miRs was performed by TAmiRNA GmbH, Vienna with subsequent miR library preparation using CleanTag™ Small RNA Library Preparation Kit Catalog # L-3206. mRNA and intracellular miR library preparation and sequencing were performed at Vienna Biocenter NGS Facilities. For mRNA analysis, a polyA enrichment was performed from 100 ng total RNA using the NEBNext Poly(A) mRNA Magnetic Isolation Module according to the manufacturer's instructions. Library preparation of polyA+ enriched RNA was performed with the NEBNext UltraII Directional RNA library Kit from Illumina. Quality control of the libraries included a fragment analyser run and a qPCR to determine average size and concentration. The final equimolar pool was sequenced on the Illumina HiSeq2000 with a density of 18 pM and 1% PhiX. miR libraries were prepared from 100 ng total RNA with the QIAseq miRNA library Kit according to the manufacturer's instructions. Libraries were run on a fragment analyser and pooled equimolar by taking the smear concentration from 160-185 bp. The remaining adapter dimers were cleared from the pool by gel extraction on the Pippin Prep (3% agarose) with a tight cut from 155 bp to 190 bp. The concentration of the final pool was determined by qPCR using the KAPA library quant Kit and sequencing was performed on the Illumina HiSeq2000 with a density of 18 pM and 1 % PhiX. Bioinformatic analysis for all libraries was performed by the VBCF bioinformatics and scientific computing facility.

Bioinformatics analyses

The short sequencing reads were aligned against the *mus musculus* reference genome (GRCm38 release) [58] with STAR [59], version 2.5.1b using 2-pass alignment mode. For mRNA and intracellular miR libraries, roughly 30 million short reads per replicate were generated, of which ~80% and ~55-75%, respectively, could be mapped to the reference genome. For plasma miR libraries ~15-30 million short reads were generated with a mapping score

of 15% and 5%, respectively. Gencode v4 annotation was used in the alignment. After alignment, the short reads were associated with known genes, and the number of reads aligned within each gene was counted using HTSeq tool [60] version 0.5.4p3. The data was normalised to remove variation between samples caused by non-biological reasons and to make the values comparable across the sample set using the TMM normalisation method of the edgeR [61], R/Bioconductor package (R version 3.3.2, Bioconductor version 2.12). The method takes the variable number of total reads across samples into account by calculating specific scaling factors between the samples. For differential expression analyses, the data were further log transformed using the voom [62] approach, and the R package limma [63] was used to perform the statistical testing. Significance thresholds applied were a p-value<0.05 and a minimum expression fold change of 1.5 between the compared sample sets for mRNA data and a minimum fold change of 1 for miR data. For detection of functional enrichment in the differentially expressed gene lists (DE list enrichment) and for detection of functional enrichment towards the top of the list when all genes have been ranked according to the evidence for being differentially expressed (Ranked list enrichment), the GO [64, 65], KEGG [66] and Reactome [67] databases were used, together with topGO (Alexa A, Rahnenfuhrer J (2021). topGO: Enrichment Analysis for Gene Ontology. R package version 2.46.0.), Gostats [68], and GAGE [69] packages in R/Bioconductor. Heatmaps in Supplementary Figure 2C were generated with R. To generate the bar graph in Supplementary Figure 3A the top 200 GO terms from GAGE analysis were used for both datasets. The KEGG (Kyoto Encyclopedia of Genes and Genomes) pathway enrichment analysis of the differentially expressed miRs was conducted by the miRSystem (http://mirsystem.cgm.ntu.edu.tw/index.php) online database tool. To identify potentially enriched pathways, 41 significantly upregulated miRs and their fold changes were submitted to the miRSystem database and the pathway list was analysed by adjusting parameter settings of 50–500 genes in biological functions/ pathways, Hit ≥ 5.0, O:E ratios ≥ 2.0.

Immunofluorescence in tissues

For immunofluorescence analysis, lungs and hearts of >25 weeks aged mice were fixed overnight in 4% formaldehyde in PBS, dehydrated in xylene and embedded in paraffin. Serial 3-µm sections were deparaffinised, rehydrated followed by antigen retrieval using pressure cooker method performed for 30 min in Tris 0.01M, EDTA 0.001M. Then samples were quenched in 0.1% glycine in PBS, permeabilized and blocked in PBS with 2% BSA, 0.1% Tween for 1 h at RT and stained with the following primary antibodies: rabbit anti-CDKN2A/p19ARF 1:100 (ab80, Abcam), rabbit anti-PECAM-1/CD31 1:30 (LB-B4737, LifeSpan BioScience) and rat anti-CD3 1:400 (MCA1477, Bio-Rad). Next samples were incubated with secondary antibodies: goat anti-rabbit 488 (ThermoFisher), goat anti-rabbit 594 (ThermoFisher) and donkey anti-rat (SA5-10028, ThermoFisher) all diluted 1:200 and DAPI nucleic acid stain (1:500 in PBS) and mounted in Mowiol 4-88 (Sigma-Aldrich).

BrdU incorporation

Bromodeoxyuridine (BrdU) incorporation assay was performed using the APC BrdU Flow Kit (557892BD, Pharmingen). ECs at passage 2 were seeded in triplicates on 48-well plates at a density of 4×10^4 cells/cm^2 and cultured for 24 h prior to BrdU addition. Incorporation of BrdU was performed over 40 h and thereafter BrdU positive cells were measured by flow cytometry. The percentage of BrdU positive cells is calculated according to the total cell number measured by flow cytometry.

Plasma collection, conditioned media and enzyme-linked immunosorbent assay (ELISA)

Lung ECs at passage 2 were seeded at a density of 5 x 10^4 cells/cm^2 on a 24-well cell culture plate in phenol red-free complete culture medium (21063029, Gibco). After 48 h of incubation, the conditioned medium was collected, centrifuged at 5000 x g and filtered through a 0.2 µm filter. For negative control, the corresponding medium was incubated for the same period in the absence of cells. For plasma collection, blood from mice at the age >25 weeks were collected and spun down at 1900 x g followed by centrifugation at 16000 x g at 4° C for 10 min. Thereafter plasma was shock frozen in EDTA-overlaid tubes and stored at -80° C until used. ELISA assay was performed using Quantine ELISA Mouse CCL20/MIP-3α Immunoassay kit (MCC200, R&D Systems) and according to manufacturer's instructions. At least three biological replicates were used and each tested in technical duplicates. Two positive controls for ELISA were included: i) ECs treated with 20 µg/ml TNFα (PMC3014, ThermoFisher) and ii) ELISA kit provided control (892547, mouse Mip-3 α). Optical density was measured on a microplate reader at 450 nm and at 540 nm for wavelength correction.

SDS-PAGE, immunoblotting and antibodies

For direct lysis, cells were washed twice with PBS, and thereafter covered with 50 mM Tris-HCl, 100 mM DTT, 2% SDS, 0.1% bromophenol blue and 10% glycerol pH 6.8. Cell lysates were separated by SDS-PAGE, transferred onto nitrocellulose membranes, followed by a blocking step and incubation with primary antibodies as described previously [24]. To visualize protein bands, membranes were incubated with peroxidase-coupled secondary antibodies (Jackson Laboratories) for 1 h with subsequent detection using

the SuperSignal West Pico Plus Chemiluminescent Substrate (34580, Thermo Scientific). Protein bands were quantified using ChemiDoc MP Imaging System using Image Lab Software. Following primary antibodies were used: rabbit anti-PECAM1 (LS-B4737, LSBio), mouse monoclonal antibody (mAb) against human lamin A+C (Chemicon, clone JoL2, mab3211, Abcam) for detection of human lamins (including human progerin), mouse monoclonal Lamin A/C antibody E-1 (Santa Cruz sc-376248) for detection of mouse and human lamins, and mouse mAb against α-tubulin (clone B-5-1-2, T5168, MilliporeSigma).

Statistics

Data are presented as the mean ± SEM or median with minimum and maximum values. All experiments using WT and Prog-Tg ECs were performed at least 3 times using different primary cells isolated from corresponding littermate pairs. Statistical analyses were performed on dCT values using GraphPad Prism statistical software. The two groups were analysed using the unpaired two-sided Student's t-test and paired *t* test was used in experiments with littermate pairs. For evaluations of non-normally distributed data, a nonparametric Mann-Whitney rank-sum test was used. One-way ANOVA was used for multiple comparisons (Kruskal-Wallis test). Data were considered statistically significantly different if $p < 0.05$.

Study approval

Animal studies were approved by the Regional Ethics Committee for Laboratory Animal Experiments at the Medical University of Vienna and the Austrian Ministry of Science Research and Economy (BMWFW-66.009/0321-WF/V/3b/2016 and BMWFW-66.009/0156-WF/V/3b/2017).

AUTHOR CONTRIBUTIONS

Selma Osmanagic-Myers and Roland Foisner conceived the project. Selma Osmanagic-Myers and Roland Foisner together with Christina Manakanatas and Santosh Kumar Ghadge designed the experiments and wrote the manuscript. Christina Manakanatas, Santosh Kumar Ghadge and Azra Agic conducted the experiments and assembled the figures. Fatih Sarigol performed some bioinformatics analyses. Petra Fichtinger performed genotyping and helped with mouse handling. Irmgard Fischer helped with the analysis of histology data.

ACKNOWLEDGMENTS

We thank Maria Eriksson, Karolinska Institutet, Huddinge, Sweden for providing transgenic mice harboring the human lamin A wildtype and progeria minigenes. We acknowledge Johannes Grillari, Ludwig Boltzmann Institute, Austria for providing expertise in miR research. Furthermore, we thank TAmiRNA GmbH, Vienna, Austria for performing library miR preparation from plasma and data analysis; Vienna Biocenter Core Facilities (VBC, NGS Facilities) for mRNA and miR sequencing and Scientific Computing Facility (BioComp) for the analysis of mRNA and miR sequencing data. We also thank Max Perutz Labs BioOptics Light Microscopy facility (Josef Gotzmann, Thomas Peterbauer) and histology facility for providing expertise and training for analysis of tissue specimens.

CONFLICTS OF INTEREST

The authors declare that they have no conflicts of interest.

FUNDING

This work was supported by the Progeria Research Foundation (PRF 2016-64) to Roland Foisner (RF) and by the Austrian Science Fund (P 29668-B28 and P 32595-B) to Selma Osmanagic-Myers and (I 4694-B) to Roland Foisner, the latter under the frame of EJP RD, the European Joint Programme on Rare Diseases. In addition, this project has received funding from the European Union's Horizon 2020 research and innovation programme under the EJP RD COFUND-EJP N 825575. Christina Manakanatas is a recipient of a DOC Fellowship of the Austrian Academy of Sciences (ÖAW DOC 25619).

REFERENCES

1. North BJ, Sinclair DA. The intersection between aging and cardiovascular disease. Circ Res. 2012; 110:1097–108. https://doi.org/10.1161/CIRCRESAHA.111.246876 PMID:22499900

2. Boon RA, Iekushi K, Lechner S, Seeger T, Fischer A, Heydt S, Kaluza D, Tréguer K, Carmona G, Bonauer A, Horrevoets AJ, Didier N, Girmatsion Z, et al. MicroRNA-34a regulates cardiac ageing and function. Nature. 2013; 495:107–10. https://doi.org/10.1038/nature11919 PMID:23426265

3. Colpani O, Spinetti G. MicroRNAs orchestrating senescence of endothelial and vascular smooth muscle cells. Vasc Biol. 2019; 1:H75–81. https://doi.org/10.1530/VB-19-0017 PMID:32923957

4. Baker DJ, Wijshake T, Tchkonia T, LeBrasseur NK, Childs BG, van de Sluis B, Kirkland JL, van Deursen JM. Clearance of p16Ink4a-positive senescent cells delays ageing-associated disorders. Nature. 2011; 479:232–6.

https://doi.org/10.1038/nature10600 PMID:22048312

5. Yousefzadeh MJ, Zhao J, Bukata C, Wade EA, McGowan SJ, Angelini LA, Bank MP, Gurkar AU, McGuckian CA, Calubag MF, Kato JI, Burd CE, Robbins PD, Niedernhofer LJ. Tissue specificity of senescent cell accumulation during physiologic and accelerated aging of mice. Aging Cell. 2020; 19:e13094. https://doi.org/10.1111/acel.13094 PMID:31981461

6. Di Micco R, Krizhanovsky V, Baker D, d'Adda di Fagagna F. Cellular senescence in ageing: from mechanisms to therapeutic opportunities. Nat Rev Mol Cell Biol. 2021; 22:75–95. https://doi.org/10.1038/s41580-020-00314-w PMID:33328614

7. Wiley CD, Campisi J. From Ancient Pathways to Aging Cells-Connecting Metabolism and Cellular Senescence. Cell Metab. 2016; 23:1013–21. https://doi.org/10.1016/j.cmet.2016.05.010 PMID:27304503

8. Coppé JP, Desprez PY, Krtolica A, Campisi J. The senescence-associated secretory phenotype: the dark side of tumor suppression. Annu Rev Pathol. 2010; 5:99–118. https://doi.org/10.1146/annurev-pathol-121808-102144 PMID:20078217

9. Acosta JC, Banito A, Wuestefeld T, Georgilis A, Janich P, Morton JP, Athineos D, Kang TW, Lasitschka F, Andrulis M, Pascual G, Morris KJ, Khan S, et al. A complex secretory program orchestrated by the inflammasome controls paracrine senescence. Nat Cell Biol. 2013; 15:978–90. https://doi.org/10.1038/ncb2784 PMID:23770676

10. Childs BG, Baker DJ, Kirkland JL, Campisi J, van Deursen JM. Senescence and apoptosis: dueling or complementary cell fates? EMBO Rep. 2014; 15:1139–53. https://doi.org/10.15252/embr.201439245 PMID:25312810

11. Mijit M, Caracciolo V, Melillo A, Amicarelli F, Giordano A. Role of p53 in the Regulation of Cellular Senescence. Biomolecules. 2020; 10:420. https://doi.org/10.3390/biom10030420 PMID:32182711

12. Lafferty-Whyte K, Cairney CJ, Jamieson NB, Oien KA, Keith WN. Pathway analysis of senescence-associated miRNA targets reveals common processes to different senescence induction mechanisms. Biochim Biophys Acta. 2009; 1792:341–52. https://doi.org/10.1016/j.bbadis.2009.02.003 PMID:19419692

13. Terlecki-Zaniewicz L, Lämmermann I, Latreille J, Bobbili MR, Pils V, Schosserer M, Weinmüllner R, Dellago H, Skalicky S, Pum D, Almaraz JC, Scheideler M, Morizot F, et al. Small extracellular vesicles and their miRNA cargo are anti-apoptotic members of the senescence-associated secretory phenotype. Aging (Albany NY). 2018; 10:1103–32. https://doi.org/10.18632/aging.101452 PMID:29779019

14. Pasquinelli AE. MicroRNAs and their targets: recognition, regulation and an emerging reciprocal relationship. Nat Rev Genet. 2012; 13:271–82. https://doi.org/10.1038/nrg3162 PMID:22411466

15. Shenouda SK, Alahari SK. MicroRNA function in cancer: oncogene or a tumor suppressor? Cancer Metastasis Rev. 2009; 28:369–78. https://doi.org/10.1007/s10555-009-9188-5 PMID:20012925

16. Frankel D, Delecourt V, Harhouri K, De Sandre-Giovannoli A, Lévy N, Kaspi E, Roll P. MicroRNAs in hereditary and sporadic premature aging syndromes and other laminopathies. Aging Cell. 2018; 17:e12766. https://doi.org/10.1111/acel.12766 PMID:29696758

17. Ugalde AP, Ramsay AJ, de la Rosa J, Varela I, Mariño G, Cadiñanos J, Lu J, Freije JM, López-Otín C. Aging and chronic DNA damage response activate a regulatory pathway involving miR-29 and p53. EMBO J. 2011; 30:2219–32. https://doi.org/10.1038/emboj.2011.124 PMID:21522133

18. Xiong XD, Jung HJ, Gombar S, Park JY, Zhang CL, Zheng H, Ruan J, Li JB, Kaeberlein M, Kennedy BK, Zhou Z, Liu X, Suh Y. MicroRNA transcriptome analysis identifies miR-365 as a novel negative regulator of cell proliferation in Zmpste24-deficient mouse embryonic fibroblasts. Mutat Res. 2015; 777:69–78. https://doi.org/10.1016/j.mrfmmm.2015.04.010 PMID:25983189

19. Ugalde AP, Español Y, López-Otín C. Micromanaging aging with miRNAs: new messages from the nuclear envelope. Nucleus. 2011; 2:549–55. https://doi.org/10.4161/nucl.2.6.17986 PMID:22064465

20. Navarro F, Lieberman J. miR-34 and p53: New Insights into a Complex Functional Relationship. PLoS One. 2015; 10:e0132767. https://doi.org/10.1371/journal.pone.0132767 PMID:26177460

21. Bernardo BC, Gao XM, Winbanks CE, Boey EJ, Tham YK, Kiriazis H, Gregorevic P, Obad S, Kauppinen S, Du XJ, Lin RC, McMullen JR. Therapeutic inhibition of the miR-34 family attenuates pathological cardiac remodeling and

improves heart function. Proc Natl Acad Sci USA. 2012; 109:17615–20. https://doi.org/10.1073/pnas.1206432109 PMID:23047694

22. Iannolo G, Sciuto MR, Raffa GM, Pilato M, Conaldi PG. MiR34 inhibition induces human heart progenitor proliferation. Cell Death Dis. 2018; 9:368. https://doi.org/10.1038/s41419-018-0400-9 PMID:29511160

23. Ooi JY, Bernardo BC, Singla S, Patterson NL, Lin RC, McMullen JR. Identification of miR-34 regulatory networks in settings of disease and antimiR-therapy: Implications for treating cardiac pathology and other diseases. RNA Biol. 2017; 14:500–13. https://doi.org/10.1080/15476286.2016.1181251 PMID:27124358

24. Osmanagic-Myers S, Kiss A, Manakanatas C, Hamza O, Sedlmayer F, Szabo PL, Fischer I, Fichtinger P, Podesser BK, Eriksson M, Foisner R. Endothelial progerin expression causes cardiovascular pathology through an impaired mechanoresponse. J Clin Invest. 2019; 129:531–45. https://doi.org/10.1172/JCI121297 PMID:30422822

25. De Sandre-Giovannoli A, Bernard R, Cau P, Navarro C, Amiel J, Boccaccio I, Lyonnet S, Stewart CL, Munnich A, Le Merrer M, Lévy N. Lamin a truncation in Hutchinson-Gilford progeria. Science. 2003; 300:2055. https://doi.org/10.1126/science.1084125 PMID:12702809

26. Dorado B, Andrés V. A-type lamins and cardiovascular disease in premature aging syndromes. Curr Opin Cell Biol. 2017; 46:17–25. https://doi.org/10.1016/j.ceb.2016.12.005 PMID:28086161

27. Osmanagic-Myers S, Foisner R. The structural and gene expression hypotheses in laminopathic diseases-not so different after all. Mol Biol Cell. 2019; 30:1786–90. https://doi.org/10.1091/mbc.E18-10-0672 PMID:31306095

28. Kubben N, Misteli T. Shared molecular and cellular mechanisms of premature ageing and ageing-associated diseases. Nat Rev Mol Cell Biol. 2017; 18:595–609. https://doi.org/10.1038/nrm.2017.68 PMID:28792007

29. Hamczyk MR, Villa-Bellosta R, Gonzalo P, Andrés-Manzano MJ, Nogales P, Bentzon JF, López-Otín C, Andrés V. Vascular Smooth Muscle-Specific Progerin Expression Accelerates Atherosclerosis and Death in a Mouse Model of Hutchinson-Gilford Progeria Syndrome. Circulation. 2018; 138:266–82. https://doi.org/10.1161/CIRCULATIONAHA.117.030856 PMID:29490993

30. Sun S, Qin W, Tang X, Meng Y, Hu W, Zhang S, Qian M, Liu Z, Cao X, Pang Q, Zhao B, Wang Z, Zhou Z, Liu B. Vascular endothelium-targeted Sirt7 gene therapy rejuvenates blood vessels and extends life span in a Hutchinson-Gilford progeria model. Sci Adv. 2020; 6:eaay5556. https://doi.org/10.1126/sciadv.aay5556 PMID:32128409

31. Atchison L, Abutaleb NO, Snyder-Mounts E, Gete Y, Ladha A, Ribar T, Cao K, Truskey GA. iPSC-Derived Endothelial Cells Affect Vascular Function in a Tissue-Engineered Blood Vessel Model of Hutchinson-Gilford Progeria Syndrome. Stem Cell Reports. 2020; 14:325–37. https://doi.org/10.1016/j.stemcr.2020.01.005 PMID:32032552

32. Matrone G, Thandavarayan RA, Walther BK, Meng S, Mojiri A, Cooke JP. Dysfunction of iPSC-derived endothelial cells in human Hutchinson-Gilford progeria syndrome. Cell Cycle. 2019; 18:2495–508. https://doi.org/10.1080/15384101.2019.1651587 PMID:31411525

33. Sagelius H, Rosengardten Y, Hanif M, Erdos MR, Rozell B, Collins FS, Eriksson M. Targeted transgenic expression of the mutation causing Hutchinson-Gilford progeria syndrome leads to proliferative and degenerative epidermal disease. J Cell Sci. 2008; 121:969–78. https://doi.org/10.1242/jcs.022913 PMID:18334552

34. Gory S, Vernet M, Laurent M, Dejana E, Dalmon J, Huber P. The vascular endothelial-cadherin promoter directs endothelial-specific expression in transgenic mice. Blood. 1999; 93:184–92. https://doi.org/10.1182/blood.V93.1.184 PMID:9864160

35. Csoka AB, English SB, Simkevich CP, Ginzinger DG, Butte AJ, Schatten GP, Rothman FG, Sedivy JM. Genome-scale expression profiling of Hutchinson-Gilford progeria syndrome reveals widespread transcriptional misregulation leading to mesodermal/mesenchymal defects and accelerated atherosclerosis. Aging Cell. 2004; 3:235–43. https://doi.org/10.1111/j.1474-9728.2004.00105.x PMID:15268757

36. Ritschka B, Storer M, Mas A, Heinzmann F, Ortells MC, Morton JP, Sansom OJ, Zender L, Keyes WM. The senescence-associated secretory phenotype induces cellular plasticity and tissue regeneration. Genes Dev. 2017; 31:172–83. https://doi.org/10.1101/gad.290635.116 PMID:28143833

37. Suh N. MicroRNA controls of cellular senescence. BMB Rep. 2018; 51:493–9. https://doi.org/10.5483/BMBRep.2018.51.10.209 PMID:30269742

38. Weilner S, Schraml E, Wieser M, Messner P, Schneider K, Wassermann K, Micutkova L, Fortschegger K, Maier AB, Westendorp R, Resch H, Wolbank S, Redl H, et al. Secreted microvesicular miR-31 inhibits osteogenic differentiation of mesenchymal stem cells. Aging Cell. 2016; 15:744–54. https://doi.org/10.1111/acel.12484 PMID:27146333

39. Childs BG, Baker DJ, Wijshake T, Conover CA, Campisi J, van Deursen JM. Senescent intimal foam cells are deleterious at all stages of atherosclerosis. Science. 2016; 354:472–7. https://doi.org/10.1126/science.aaf6659 PMID:27789842

40. Osmanagic-Myers S, Rus S, Wolfram M, Brunner D, Goldmann WH, Bonakdar N, Fischer I, Reipert S, Zuzuarregui A, Walko G, Wiche G. Plectin reinforces vascular integrity by mediating crosstalk between the vimentin and the actin networks. J Cell Sci. 2015; 128:4138–50. https://doi.org/10.1242/jcs.172056 PMID:26519478

41. Baker DJ, Childs BG, Durik M, Wijers ME, Sieben CJ, Zhong J, Saltness RA, Jeganathan KB, Verzosa GC, Pezeshki A, Khazaie K, Miller JD, van Deursen JM. Naturally occurring p16(Ink4a)-positive cells shorten healthy lifespan. Nature. 2016; 530:184–9. https://doi.org/10.1038/nature16932 PMID:26840489

42. Mattioli E, Andrenacci D, Garofalo C, Prencipe S, Scotlandi K, Remondini D, Gentilini D, Di Blasio AM, Valente S, Scarano E, Cicchilitti L, Piaggio G, Mai A, Lattanzi G. Altered modulation of lamin A/C-HDAC2 interaction and p21 expression during oxidative stress response in HGPS. Aging Cell. 2018; 17:e12824. https://doi.org/10.1111/acel.12824 PMID:30109767

43. Malaquin N, Martinez A, Rodier F. Keeping the senescence secretome under control: Molecular reins on the senescence-associated secretory phenotype. Exp Gerontol. 2016; 82:39–49. https://doi.org/10.1016/j.exger.2016.05.010 PMID:27235851

44. Kim DE, Dollé ME, Vermeij WP, Gyenis A, Vogel K, Hoeijmakers JH, Wiley CD, Davalos AR, Hasty P, Desprez PY, Campisi J. Deficiency in the DNA repair protein ERCC1 triggers a link between senescence and apoptosis in human fibroblasts and mouse skin. Aging Cell. 2020; 19:e13072. https://doi.org/10.1111/acel.13072 PMID:31737985

45. Kreienkamp R, Graziano S, Coll-Bonfill N, Bedia-Diaz G, Cybulla E, Vindigni A, Dorsett D, Kubben N, Batista LF, Gonzalo S. A Cell-Intrinsic Interferon-like Response Links Replication Stress to Cellular Aging Caused by Progerin. Cell Rep. 2018; 22:2006–15. https://doi.org/10.1016/j.celrep.2018.01.090 PMID:29466729

46. Osorio FG, Bárcena C, Soria-Valles C, Ramsay AJ, de Carlos F, Cobo J, Fueyo A, Freije JM, López-Otín C. Nuclear lamina defects cause ATM-dependent NF-κB activation and link accelerated aging to a systemic inflammatory response. Genes Dev. 2012; 26:2311–24. https://doi.org/10.1101/gad.197954.112 PMID:23019125

47. Squarzoni S, Schena E, Sabatelli P, Mattioli E, Capanni C, Cenni V, D'Apice MR, Andrenacci D, Sarli G, Pellegrino V, Festa A, Baruffaldi F, Storci G, et al. Interleukin-6 neutralization ameliorates symptoms in prematurely aged mice. Aging Cell. 2021; 20:e13285. https://doi.org/10.1111/acel.13285 PMID:33393189

48. Pereira BI, Devine OP, Vukmanovic-Stejic M, Chambers ES, Subramanian P, Patel N, Virasami A, Sebire NJ, Kinsler V, Valdovinos A, LeSaux CJ, Passos JF, Antoniou A, et al. Senescent cells evade immune clearance via HLA-E-mediated NK and $CD8^+$ T cell inhibition. Nat Commun. 2019; 10:2387. https://doi.org/10.1038/s41467-019-10335-5 PMID:31160572

49. He L, He X, Lim LP, de Stanchina E, Xuan Z, Liang Y, Xue W, Zender L, Magnus J, Ridzon D, Jackson AL, Linsley PS, Chen C, et al. A microRNA component of the p53 tumour suppressor network. Nature. 2007; 447:1130–4. https://doi.org/10.1038/nature05939 PMID:17554337

50. Suzuki HI, Yamagata K, Sugimoto K, Iwamoto T, Kato S, Miyazono K. Modulation of microRNA processing by p53. Nature. 2009; 460:529–33. https://doi.org/10.1038/nature08199 PMID:19626115

51. Hernandez L, Roux KJ, Wong ES, Mounkes LC, Mutalif R, Navasankari R, Rai B, Cool S, Jeong JW, Wang H, Lee HS, Kozlov S, Grunert M, et al. Functional coupling between the extracellular matrix and nuclear lamina by Wnt signaling in progeria. Dev Cell. 2010; 19:413–25. https://doi.org/10.1016/j.devcel.2010.08.013 PMID:20833363

52. Schumacher B, van der Pluijm I, Moorhouse MJ, Kosteas T, Robinson AR, Suh Y, Breit TM, van Steeg H, Niedernhofer LJ, van Ijcken W, Bartke A, Spindler SR, Hoeijmakers JH, et al. Delayed and accelerated aging share common longevity assurance mechanisms. PLoS Genet. 2008; 4:e1000161. https://doi.org/10.1371/journal.pgen.1000161 PMID:18704162

53. Sola-Carvajal A, Revêchon G, Helgadottir HT, Whisenant D, Hagblom R, Döhla J, Katajisto P, Brodin D, Fagerström-Billai F, Viceconte N, Eriksson M. Accumulation of Progerin Affects the Symmetry of Cell Division and Is Associated with Impaired Wnt Signaling and the Mislocalization of Nuclear Envelope Proteins. J Invest Dermatol. 2019; 139:2272–80.e12. https://doi.org/10.1016/j.jid.2019.05.005 PMID:31128203

54. Dominic A, Banerjee P, Hamilton DJ, Le NT, Abe JI. Time-dependent replicative senescence vs. disturbed flow-induced pre-mature aging in atherosclerosis. Redox Biol. 2020; 37:101614. https://doi.org/10.1016/j.redox.2020.101614 PMID:32863187

55. Warboys CM, de Luca A, Amini N, Luong L, Duckles H, Hsiao S, White A, Biswas S, Khamis R, Chong CK, Cheung WM, Sherwin SJ, Bennett MR, et al. Disturbed flow promotes endothelial senescence via a p53-dependent pathway. Arterioscler Thromb Vasc Biol. 2014; 34:985–95. https://doi.org/10.1161/ATVBAHA.114.303415 PMID:24651677

56. Crewe C, Joffin N, Rutkowski JM, Kim M, Zhang F, Towler DA, Gordillo R, Scherer PE. An Endothelial-to-Adipocyte Extracellular Vesicle Axis Governed by Metabolic State. Cell. 2018; 175:695–708.e13. https://doi.org/10.1016/j.cell.2018.09.005 PMID:30293865

57. Sun JF, Phung T, Shiojima I, Felske T, Upalakalin JN, Feng D, Kornaga T, Dor T, Dvorak AM, Walsh K, Benjamin LE. Microvascular patterning is controlled by fine-tuning the Akt signal. Proc Natl Acad Sci USA. 2005; 102:128–33. https://doi.org/10.1073/pnas.0403198102 PMID:15611473

58. Zerbino DR, Achuthan P, Akanni W, Amode MR, Barrell D, Bhai J, Billis K, Cummins C, Gall A, Girón CG, Gil L, Gordon L, Haggerty L, et al. Ensembl 2018. Nucleic Acids Res. 2018; 46:D754–61. https://doi.org/10.1093/nar/gkx1098 PMID:29155950

59. Dobin A, Davis CA, Schlesinger F, Drenkow J, Zaleski C, Jha S, Batut P, Chaisson M, Gingeras TR. STAR: ultrafast universal RNA-seq aligner. Bioinformatics. 2013; 29:15–21. https://doi.org/10.1093/bioinformatics/bts635 PMID:23104886

60. Anders S, Pyl PT, Huber W. HTSeq--a Python framework to work with high-throughput sequencing data. Bioinformatics. 2015; 31:166–9. https://doi.org/10.1093/bioinformatics/btu638 PMID:25260700

61. Robinson MD, McCarthy DJ, Smyth GK. edgeR: a Bioconductor package for differential expression analysis of digital gene expression data. Bioinformatics. 2010; 26:139–40. https://doi.org/10.1093/bioinformatics/btp616 PMID:19910308

62. Law CW, Chen Y, Shi W, Smyth GK. voom: Precision weights unlock linear model analysis tools for RNA-seq read counts. Genome Biol. 2014; 15:R29. https://doi.org/10.1186/gb-2014-15-2-r29 PMID:24485249

63. Ritchie ME, Phipson B, Wu D, Hu Y, Law CW, Shi W, Smyth GK. limma powers differential expression analyses for RNA-sequencing and microarray studies. Nucleic Acids Res. 2015; 43:e47. https://doi.org/10.1093/nar/gkv007 PMID:25605792

64. Ashburner M, Ball CA, Blake JA, Botstein D, Butler H, Cherry JM, Davis AP, Dolinski K, Dwight SS, Eppig JT, Harris MA, Hill DP, Issel-Tarver L, et al. Gene ontology: tool for the unification of biology. The Gene Ontology Consortium. Nat Genet. 2000; 25:25–9. https://doi.org/10.1038/75556 PMID:10802651

65. Gene Ontology Consortium. The Gene Ontology resource: enriching a GOld mine. Nucleic Acids Res. 2021; 49:D325–34. https://doi.org/10.1093/nar/gkaa1113 PMID:33290552

66. Kanehisa M, Goto S. KEGG: kyoto encyclopedia of genes and genomes. Nucleic Acids Res. 2000; 28:27–30. https://doi.org/10.1093/nar/28.1.27 PMID:10592173

67. Griss J, Viteri G, Sidiropoulos K, Nguyen V, Fabregat A, Hermjakob H. ReactomeGSA - Efficient Multi-Omics Comparative Pathway Analysis. Mol Cell Proteomics. 2020; 19:2115–25. https://doi.org/10.1074/mcp.TIR120.002155 PMID:32907876

68. Falcon S, Gentleman R. Using GOstats to test gene lists for GO term association. Bioinformatics. 2007; 23:257–8. https://doi.org/10.1093/bioinformatics/btl567 PMID:17098774

69. Luo W, Friedman MS, Shedden K, Hankenson KD, Woolf PJ. GAGE: generally applicable gene set enrichment for pathway analysis. BMC Bioinformatics. 2009; 10:161. https://doi.org/10.1186/1471-2105-10-161 PMID:19473525

SUPPLEMENTARY MATERIALS

Supplementary Figures

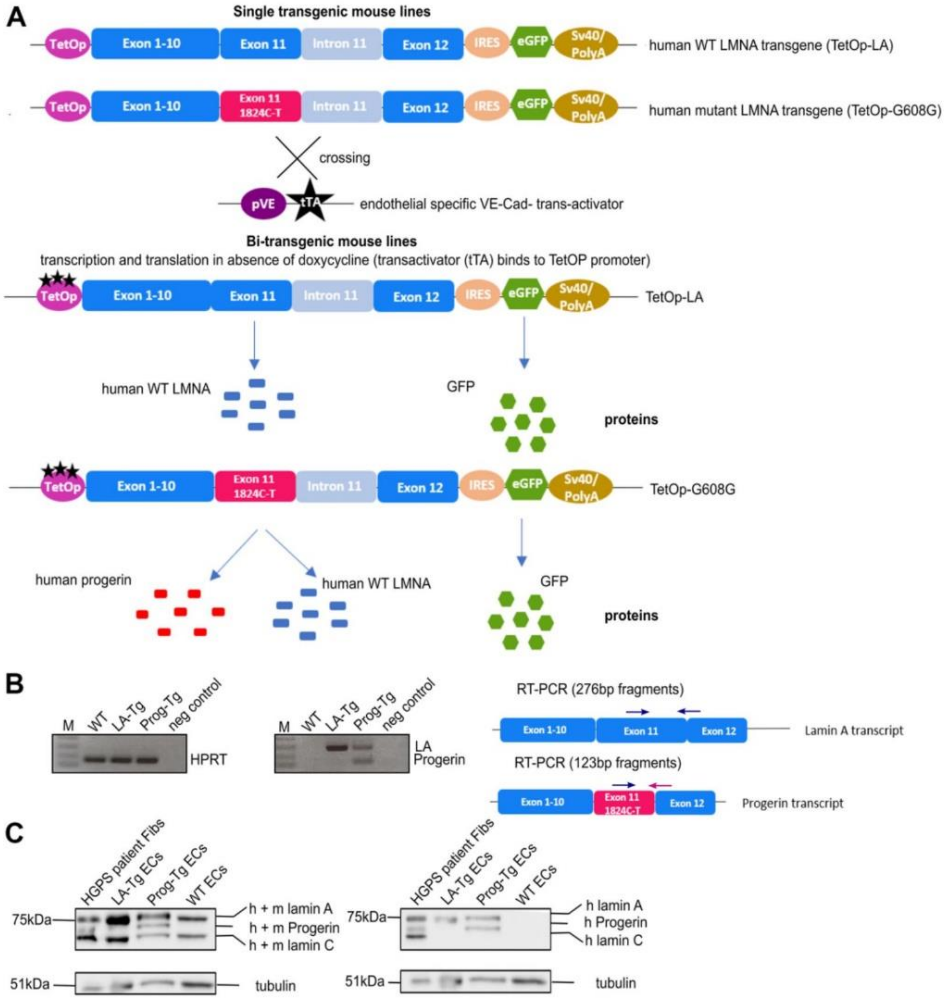

Supplementary Figure 1. Organization of the human wildtype and mutant lamin A minigenes and generated transcripts and proteins. (**A**) Schematic representation of the human wildtype (TetOp-LA) and mutant (TetOp-G608G) lamin A minigene carrying the most common HGPS mutation (1824C>T). Transgenic mice harboring these transgenes were crossed with mice expressing the transactivator under the endothelium-specific VE-Cad promoter (pVE-tTA) to generate bi-transgenic mice expressing the human wildtype or mutant (progerin) lamin A in the endothelium. Proteins encoded by these minigenes are indicated below. Human lamin A minigenes harbor complete exon 1-10, exon 11, with or without HGPS mutation (1824C>T), intron 11, exon 12, internal ribosomal entry site (IRES), coding region for eGFP and SV40 poly A site as indicated. TetOp indicates the tetracycline-responsive operator. pVE indicates the endothelial specific VE-cadherin (*Cdh5*) promoter and tTA (black stars) indicate the tetracycline trans-activator. (**B**) RT-PCR analyses of transcripts in WT, LA-Tg and Prog-Tg lung endothelial cells, using primers from [33] that specifically amplify human *LMNA* sequences (right panel), show one band of expected 276 bp size for the WT human *LMNA* (LA) and one band of expected 123 bp size for human progerin and no bands in control WT samples and negative controls. RT-PCR analysis using mouse *Hprt* specific primers shows expected band size of 172 bp. Right panel shows a schematic representation of the triple RT-PCR and primer binding sites in *LMNA* minigene. (**C**) Immunoblot analyses of cell extracts of mouse WT, LA-Tg and Prog-Tg endothelial cells and of human HGPS patient fibroblasts as control, using lamin A/C antibody E-1, (Santa Cruz sc-376248) detecting endogenous mouse lamin A/C and ectopic human lamin A and progerin (left panel) and monoclonal antibody clone JoL2 (Chemicon, mab3211, Abcam) detecting exclusively human lamin A/C and progerin. Tubulin was used as loading control. Note that the TetOp-G608G transgene generates both wildtype and mutant lamin A transcripts and proteins, while the TetOp-LA transgene produces exclusively wildtype lamin A.

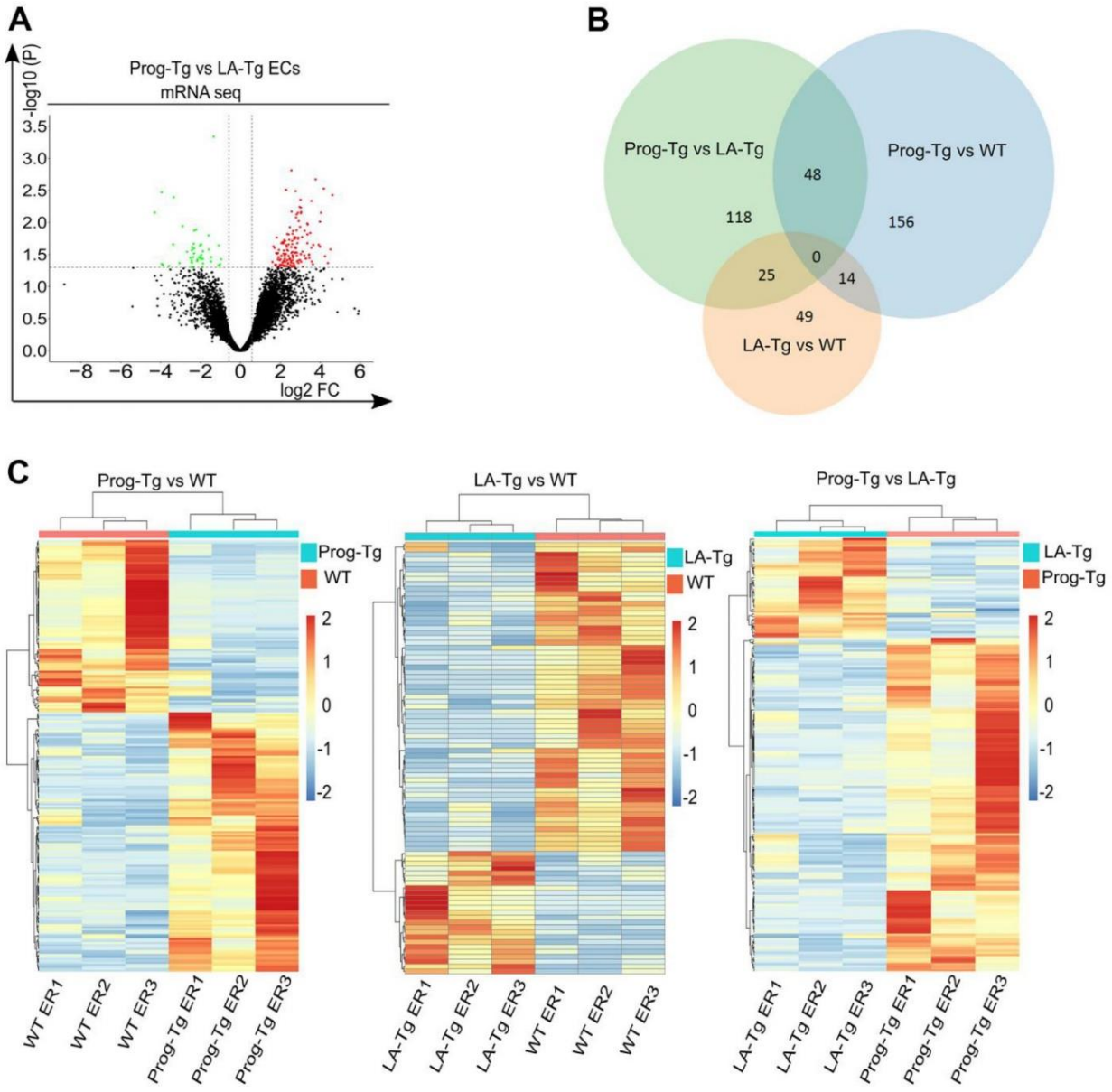

Supplementary Figure 2. Differential gene expression analyses of Prog-Tg and LA-Tg endothelial cells. (**A**) Volcano plot depicting differential expression (DE) analysis of genes in Prog-Tg/LA-Tg lung endothelial cells. Red, upregulated, green, downregulated genes; X-axis, log_2 values of fold change (FC>1,5 and <-1.5) and y-axis, $-log_{10}$ values of p-value ($p<0.05$, n=3). (**B**) Analysis of shared DE genes between Prog-Tg/WT, LA-Tg/WT and Prog-Tg/LA-Tg depicted by a 3-way Venn diagram. (**C**) Heatmaps showing clustering of the differentially expressed genes in Prog-Tg vs WT and LA-Tg vs WT (associated with Figure 1A) and of Prog-Tg vs LA-Tg (associated with Supplementary Figure 2B).

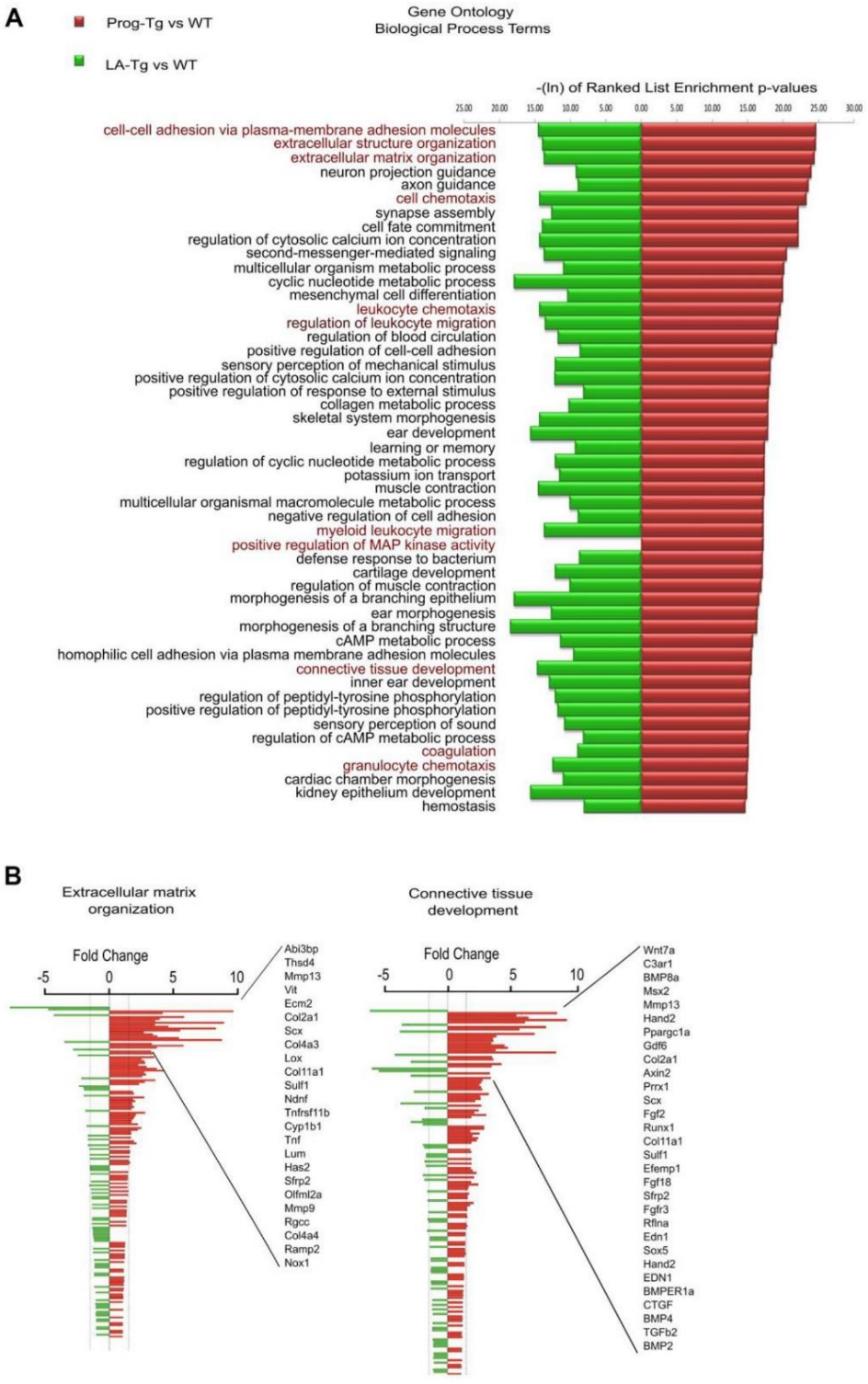

Supplementary Figure 3. Gene ontology analyses of differentially expressed genes. (**A**) Depiction of the top 50 gene ontology biological process terms as found in the ranked list enrichment analysis of Prog-Tg/WT compared to LA-Tg/WT DE genes. The x-axis represents -ln of ranked list enrichment p-values. (**B**) Ranked-list enrichment gene ontology analysis in Prog-Tg/WT lung ECs showing deregulated genes in terms "extracellular matrix organization" and "connective tissue development".

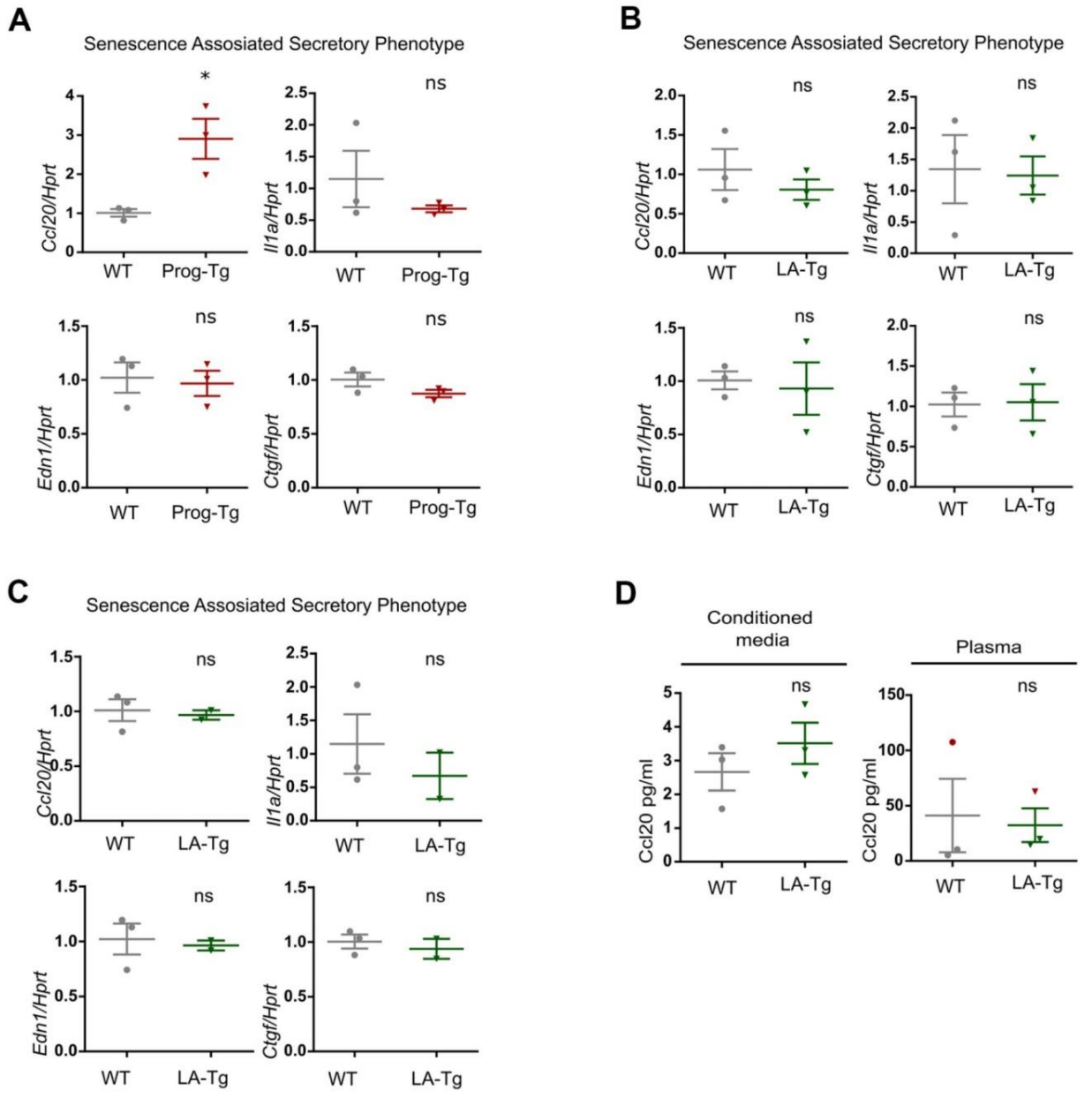

Supplementary Figure 4. Expression analyses of senescence and SASP markers in endothelial cells, conditioned media and plasma. (**A**) Gene expression analysis of pro-inflammatory markers *Ccl20* and *Il-1a* and pro-fibrotic markers *Edn1* and *Ctgf* in WT and Prog-Tg ECs derived from heart tissue. (**B**, **C**) Gene expression analysis in WT and LA-Tg lung derived ECs (**B**) and heart derived ECs (**C**). (**D**) ELISA assay for detection of Ccl20 in cell culture supernatant samples of lung ECs and in plasma samples of >25 week-old WT and LA-Tg mice, respectively. Red sphere and rectangle in the left panel represent two littermate mice with unusually high levels of Ccl20. Paired two-tailed Students *t* test was applied for *in vivo* experiments with littermate pairs and unpaired two-tailed Students *t* test for *in vitro* co-culture experiments. ns=non-significant, *p<0.05.

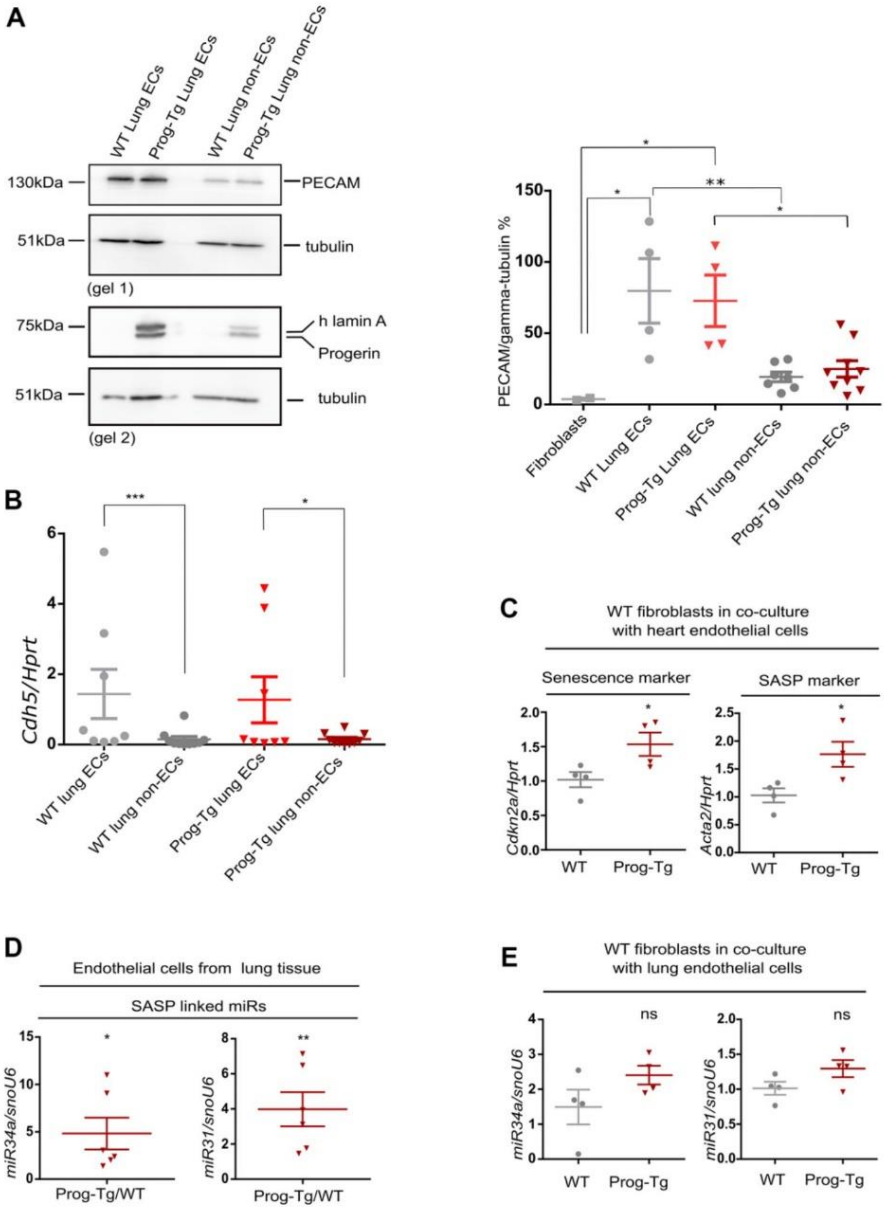

Supplementary Figure 5. Expression analyses of SASP and senescence markers in endothelial and non-endothelial cells from tissue and in co-cultures of fibroblasts and endothelial cells. (**A**) Endothelial cell- and non-endothelial cell populations obtained from lung homogenates using ICAM-2 magnetic bead separation were tested for purity using immunoblotting with endothelial cell marker PECAM-1 (gel 1), anti-human lamin A to detect progerin (gel 2) and respective gamma-tubulin loading controls. Quantification of PECAM-1/gamma-tubulin protein band intensities in EC and non-EC populations (right panel). Immortalized fibroblasts (not shown on representative blot) were used as a negative control. Note that the low PECAM-1 levels in non-EC populations indicate the removal of the majority of ECs. For EC and non-EC populations n=4-9. PECAM-1-negative fibroblasts were used as negative control (n=2). For statistical evaluation, one-way ANOVA was used (Sidak's multiple comparisons test). (**B**) EC and non-EC populations in (**A**) were tested for gene expression levels of EC marker VE-cadherin (*Cdh5*) by qPCR. (**C**) WT fibroblasts were co-cultured with ECs derived from hearts of WT and Prog-Tg mice, respectively, and tested for gene expression of senescence marker *Cdkn2a* and pro-fibrotic marker *Acta2* by qPCR. (**D**) Expression of SA-miRs, miR34a-5p and miR31-5p were tested in EC populations of Prog-Tg versus WT mice (>25 weeks, n≥3). (**E**) Expression of miR-34a-5p (miR-34a) and miR-31-5p (miR-31) in WT fibroblasts co-cultured with either WT or Prog-Tg lung ECs. For qPCRs n=4-6. Paired two-tailed Students *t* test was used for *in vivo* experiments and an unpaired two tailed Students *t* test for *in vitro* co-culture experiments. ns=non-significant, *p<0.05, **p<0.01, ***p<0.001.

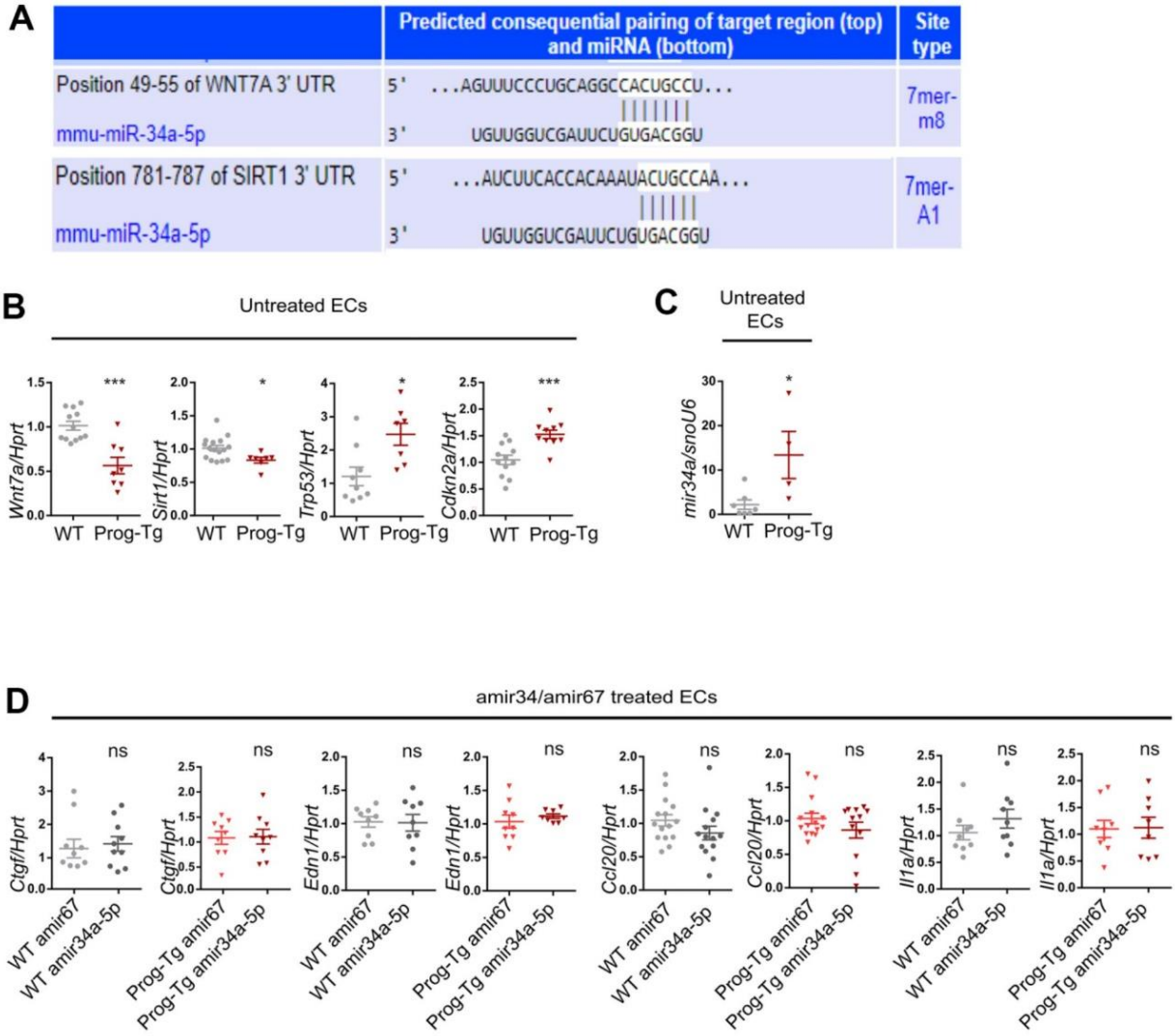

Supplementary Figure 6. Anti-miR34 treatment of endothelial cells. (**A**) Image showing binding sites of miR34a-5p in 3´ UTR of *Wnt7a* and *Sirt1* (TargetScanMouse version 7.2). (**B**) Gene expression analysis of depicted targets in untreated WT and Prog-Tg lung ECs. (**C**) Gene expression analysis of miR34a-5p in untreated lung ECs used for antimiR34 transfection experiments. (**D**) Gene expression analysis of depicted genes in antimiR34a-5p versus control antimiR67 transfected WT and Prog-Tg lung ECs. For qPCR n≥3, statistics were performed using unpaired two-tailed Students *t* test, ns=non-significant, *p<0.05, ***p<0.001.

Supplementary Tables

Please browse Full Text version to see the data of Supplementary Tables 1, 2.

Supplementary Table 1. Lists differentially expressed mRNAs in Prog-Tg/WT, LA-Tg/WT and Prog-Tg/LA-Tg endothelial cells (associated with Figure 1A, 1B).

Supplementary Table 2. Lists differentially expressed miRs in Prog-Tg/WT and LA-Tg/WT endothelial cells and plasma, associated with Figure 4A–4C.

6. Analysis of Prog-Tg EC secretome (Unpublished data)

Current state of Research

Cell to cell communication over long distances can be established by secretion of extracellular vesicles (EVs). Secreted by most cell types, EVs are membrane bound vesicles that differ in their biogenesis pathway, size and biological content and include apoptotic bodies, microvesicles and exosomes, the last two being grouped together in many studies [63] [64]. Exosomes and small microvesicles are typically termed small extracellular vesicles (sEV). The first observations of sEV as a means for sharing biological information goes back more than twenty years when it was observed that immune cells present antigens via EV secretion [64]. A few years later it was shown that miRs and mRNA carried by secreted exosomes can be taken up by recipient cells and deliver biological information. Since those findings there has been an increasing number of studies showing that all eukaryotic cells share biological information like proteins, nucleic acids and lipids by secretion of a range of membrane bound vesicles that differ in size and content [64].

Typically, exosomes are considered as a subgroup of microvesicles 30-150nm in diameter [65], but differ from bigger microvesicles in their way of biogenesis and biological content [64]. Exosomes are generated by inward budding of the membrane of multivesicular bodies (MVBs) forming intraluminal vesicles (ILVs). Upon maturation MVB can follow two distinct fates, the one being fusion with lysosomes or autophagosomes for cargo degradation and the other one fusion with the plasma membrane. Upon fusion with the plasma membrane MVBs release the ILVs into the extracellular space. Those ILVs are then referred to as exosomes [66]. Several mechanisms of biogenesis of MVBs have been described with the best-described one being the pathway utilizing the endosomal sorting complex required for transport (ESCRT) machinery. This pathway is responsive for sorting ubiquitinated proteins into ILVs [67]. Whether MVBs formed by the ESCRT pathway are destined to degrade or to fuse with the plasma membrane and generate exosomes is still unclear [68] . Along with the ESCRT machinery also other pathways of MVB generation exist, namely the ceramide-sphingomyelin pathway, in which ceramide is generated from sphingomyelin hydrolysis by neutral sphingomyelinase 2 (nSMSase2) leading to formation of ILVs [69], and an ubiquitination independent ESCRT-III pathway utilizing heparin sulfate proteoglycan syndecan [70]. The existence of different biogenesis pathways of MVB and therefore of exosomes inevitably raises the question whether these different pathways determine the specific cargo of exosomes or whether different vesicles subpopulations carrying a different content exist [66]. Although the exact process of exosome release remains unclear, it is generally accepted that Rab GTPases, soluble N-ethylmaleimide-sensitive factor attachment protein receptors (SNAREs) and the cytoskeleton are involved in this process, which shows that exosome release is an active process requiring energy [65].

In contrast to exosomes, microvesicles can directly bud from the plasma membrane [66]. They are extremely heterogeneous in size, starting from exosome like microvesicles with a diameter as small as 50nm, to very large microvesicles with a diameter of 1um. Microvesicles can be generated by different mechanism, such as the ESCRT machinery, which produces very small microvesicles highly resembling exosomes [71], the nSMase2 pathway [72] and the actin cytoskeleton rearrangement pathway [73]. Like exosomes, microvesicles are also actively secreted by cells [65].

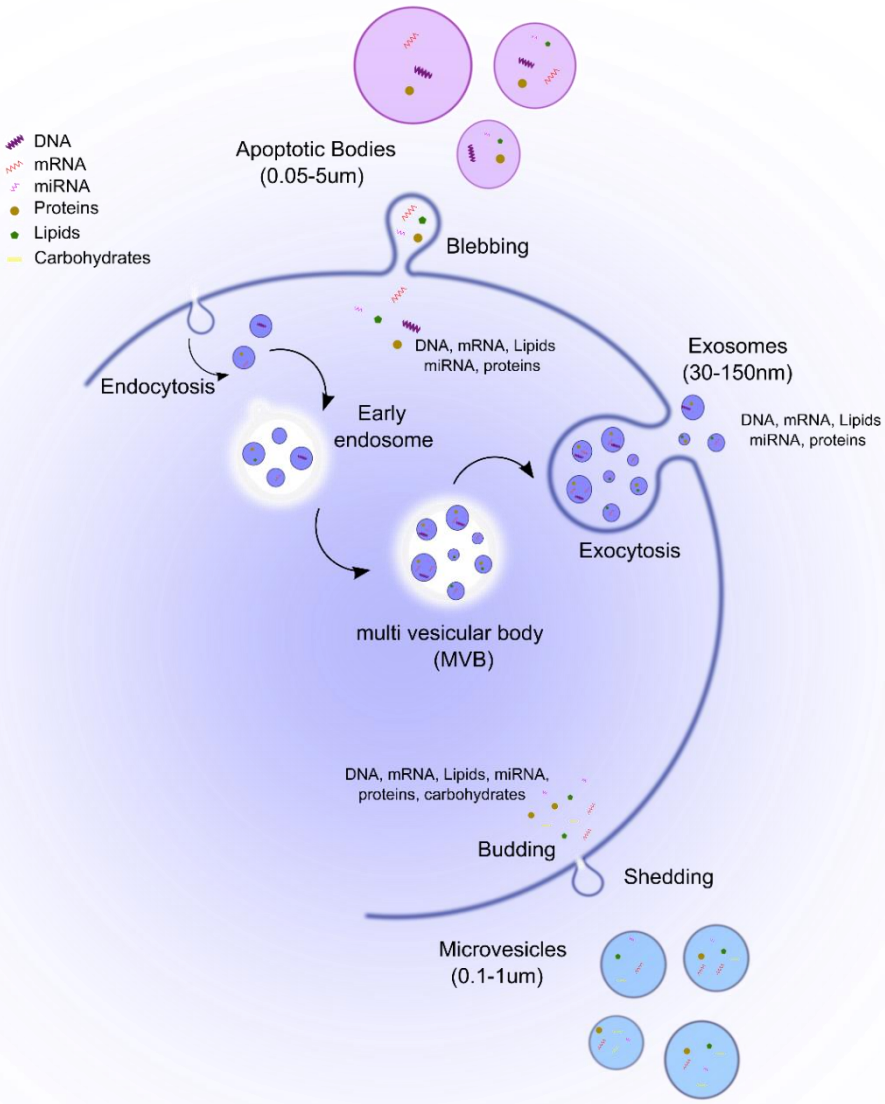

Figure 1: Biogenesis and content of different extracellular vesicles: Exosomes are mainly generated by formation of intraluminal multi vesicular bodies (MVB). MVB then fuse with the plasma membrane and release their content into the extracellular space. Exosomes can carry DNA, mRNA, miRNA, proteins and lipids. Their size varies from 30-150nm in diameter, Microvesicles are generated by budding of the plasma membrane and their cargo involves DNA, mRNA, miRNA, lipids, proteins as well as carbohydrates. Their size is between 0.1-1um, Apoptotic bodies are generated by blebbing of apoptotic cells, which occurs due to reorganization of actin. Their cargo includes DNA, mRNA, miRNA, proteins and lipids and they can be very heterogeneous in size varying from 0.05-5um.

sEV can carry different cargos, including protein cargo, DNA cargo and RNA cargo [66]. Protein cargo has been shown to be incorporated in sEV by either binding to components of their biogenesis machinery [74] or in the case of membrane proteins, by direct interaction with sEV membrane proteins like tetraspanins [75]. Moreover, several studies have suggested that fragmented genomic DNA (gDNA) [76], mitochondrial DNA (mtDNA) [77] and parasitic DNA [78] can be present in sEV derived from plasma samples and cell culture medium. The physiological role of sEV transferred DNA is yet to be established, but recent studies have shown that it might play a role in cellular homeostasis during cancer. Upon DNA damage fragmented DNA is exported into the cytoplasm where it triggers cytoplasmic DNA sensors inducing senescence and apoptosis [79]. By inclusion of DNA fragments in sEV activation of the cytoplasmic DNA sensors is prevented. The discovery of horizontal mRNA transfer between cells by sEV [80] and evidence that sEV-transferred mRNA can be translated into functional proteins in the recipient cell [79] opened the pathway for extensive studies of sEV-transferred RNAs. Apart from mRNA, sEV, in particular exosomes, are highly enriched in miRs indicating that exosomes might fulfill their signaling role through gene regulation [81]. Different biological processes, involving cell development, growth and repair, cell migration, immunomodulation but also senescence and aging, among others, have been reported to be mediated by exosome derived miRs [82]. miRs have been described as small, approximately 22nt long non-coding RNAs which regulate gene expression by binding to the 3′ untranslated region (3′ UTR) of their target mRNA resulting in either translational repression or mRNA degradation [13].

The first reported exosome-transferred miRs were shown to play an important role in the pathology of cancer [83], but since then exosome-linked miRs were found to play an integral role in tissue aging and longevity [82]. Several well-known aging linked exosome-enclosed miRs, such as miR34, miR21 and miR29, have been described to modulate tissue functionality by regulating regenerative pathways but also by affecting life expectancy [82]. Age related exosome-enclosed miRs, termed exosome associated gero-miRs by some authors, are expressed at different levels in many body fluids, such as blood, plasma and serum, depending on age and the progression of age-related diseases [82]. These exosome-enclosed gero-miRs may be associated with aging mechanisms, as they often target genes involved in human longevity and regeneration [82].

One of the initiating events during human aging is the accumulation of senescent cells which leads to tissue degeneration and aging associated inflammation, termed inflammaging. Interestingly, senescent cells, especially senescent ECs, were shown to release more exosomes than normal cells [19]. Moreover, the composition of those senescent cell-associated exosomes was different in comparison to the exosomes released by young healthy cells [20]. A nice example showing the difference in composition of exosomes origination from young and aged donors is a study that revealed that exosomes from plasma samples of young individuals have proliferative effects and promote osteogenic differentiation and maturation of mesenchymal stem cells (MSCs). This was not the case for exosomes originating from plasma samples of aged individuals [84]. Interestingly, many miRs are up- or down-regulated in senescent cells, including intracellular miRs as well as secreted exosome-associated miRs. In particular, up- and down-regulated miRs in or originating from senescent cells were shown to regulate genes associated with pathways of senescence, such as the p53-p21 and the p16 pathways [85] [86] [87] [88]. Moreover, intracellular as well as secreted exosome-associated miRs are bona fide members of the senescence associated secretory phenotype (SASP) characteristic for senescent cells [14] [12]. These data indicate that a cellular transcriptional program is activated upon senescence whereby both the number and the composition of exosomes is changed, contributing directly to the SASP [82] [89].

One of the most deadly age-related diseases is cardiovascular disease (CVD) [1], and a key initiating event in CVD development is endothelial cell senescence, as mentioned above [4] [9]. A major mechanism linking endothelial cell senescence and progression of CVD is the altered production of sEV, in particular exosomes, by senescent endothelial cells [20]. In accordance to that, sEV produced by young and healthy endothelial cells promote protective signals to their microenvironment [90]. Taking these data into consideration, an increasing number of studies suggest quantification and characterization of endothelial senescent cell-released exosomes as a useful prognostic tool for CVD. Moreover, characterization of endothelial cell-released exosomes might pave the path for future therapeutic targets for these large group of diseases [20].

The production and the content of sEV represents a 'snapshot' of the physiological state of a tissue or cell, distinguishing between a young, healthy state and a senescent cell state. This holds true also for endothelial cells. For instance, in vitro simulated ischaemic preconditioning was shown to affect the rates and content of sEV production by endothelial cells [90]. In this study, a co-culture of primary rat cardiomyocytes with normoxic (20-21% oxygen) human umbilical vein endothelial cells (HUVECs) led to an up to 30% reduction in the percentage of cardiomyocyte death after simulated ischaemia and reperfusion (sIR). This protective function of HUVECs on cardiomyocytes was attributed to HUVEC-produced sEV, since removal of those from the conditioned media of HUVECs abolished their protective mode of action. Thus, this study clearly demonstrated the protective mode of action of young, non-senescent endothelial cells (HUVECs) on cardiomyocytes. In contrast, other studies showed the deteriorating and harmful effect of senescent endothelial cells on their microenvironment [91]. For instance, exosomes isolated from conditioned media of senescent HUVECs and added to young endothelial cells led to repression of adherens junction protein expression like vascular endothelial-cadherin (VE-cadherin), as well as to a decrease in cell growth and an impaired endothelial migration capacity in young endothelial cells [91].

Taken into consideration the current knowledge on endothelial cell-produced sEV and, in particular, their importance in aging related CVDs [92], we sought to investigate the role and composition of sEV produced by progerin-expressing endothelial cells (Prog-Tg ECs) originating from Prog-Tg mice (see above). As expression of progerin specifically in the endothelium leads to activation of a p53 linked senescence signalling and initiation of a senescence associated secretory phenotype (SASP) as shown above [49], and since EC-secreted sEV may be part of a pathway linking EC senescence and progression of CVD, we decided to analyse the Prog-Tg EC-released sEV. Moreover, we focused on so called secreted gero-miRs, which have been characterized as novel members of the SASP [12] [14] and as important mediators of organismal and cellular aging [93]. For that, we incubated Prog-Tg ECs for 48 hours with a conditioned cell culture media which had been depleted of all vesicles (vesicle free media) and subsequently isolated sEV produced by endothelial cells utilizing differential ultracentrifugation. We focused specifically on the sEV fraction with a diameter of up to 200nm, including mainly exosomes and small microvesicles, since those vesicles are known to be secreted actively from cells [65]. In this way one can identify primarily the active senescence-induced secretion mechanisms of Prog-Tg ECs rather than the passive leakage of apoptotic bodies. Another reason was that these sEV have emerged as very potent non-invasive biomarkers for the prognosis, detection and therapeutics of a wide spectrum of diseases, including CVD [94].

Summary of unpublished data

In our **unpublished study** we performed sequencing of exosome-enclosed miRs secreted within 48h into the conditioned media (vesicle free media) of ECs. Isolation of sEV, in the range of 30-150nm (mainly including exosomes), was performed by differential ultracentrifugation as described in many previous studies [92] [95]. These isolated exosome fractions were characterized by different methods prior to miR isolation to ensure purity. Standard techniques for the characterization of sEV include optical methods, mainly electron microscopy (EM), detection of fluorescently labelled exosomes by flow cytometry and nanoparticle tracking analysis (NTA), as well as non-optical methods such as immunoblotting for exosome specific markers, such as tetraspanins [92] [96]. Tetraspanins are typically described as membrane-spanning proteins with a highly conserved structure and mainly function as membrane protein organizers [97]. In our study I primarily used the optical nanoparticle tracking analysis method (NTA), which showed a high concentration of sEV with an average diameter of approximately 150nm. Moreover, we tried to identify exosomes by electron microscopy (EM). These results were not as conclusive but still revealed the existence of sEV with a diameter of up to approximately 200nm.

Sequencing of exosome enclosed miRs from 48 h conditioned media of Prog-Tg ECs revealed only three miRs significantly upregulated, namely miR133a-3p, miR21a-3p and miR582-5p, and nine significantly downregulated ones. Exosomes originating from the control LA-Tg ECs (see above) did not show any significantly upregulated miRs, while 13 significantly downregulated miRs were detected. Even though the number of upregulated miRs in exosomes originating from Prog-Tg ECs is low it is of great interest since they are specific for Prog-Tg EC and may thus be physiologically relevant for our disease model.

miR133a-3p has been characterized as a muscle-specific miR which mediates an anti-hypertrophic effect by regulating targets involved in calcium signalling, cell growth and cellular developmental pathways [58]. In regard to CVD, overexpression of miR133a-3p has a cardioprotective effect by inhibiting apoptosis and led to a reduction of cardiac hypertrophy in vivo and in vitro [58] [59]. In accordance with these findings, myocadiac intracellular levels of miR133a-3p were decreased in hypertrophic cardiomyopathy (HCM) [59]. Since in our system exosome-associated miR133a-3p was found upregulated in the secretome of Prog-Tg ECs we hypothesize that Prog-Tg ECs of the Prog-Tg mice, which show a CVD phenotype with left ventricular hypertrophy [38], secret increased levels of the cardioprotective miR133a-3p as a “warning” signal to their surrounding tissues.

Moreover, miR133a-3p is expressed in a tissue specific manner with an abundant prominent expression in the myocardium and plays a key role in promoting cardiogenesis, [60]. Since miR133a-3p expression is elevated in serum of patients with acute myocardial infarction (AMI), it has also been used as a diagnostic biomarker of AMI [60]. Interestingly, several clinical studies show that serum miR133a-3p levels are highly increased in critical inflammatory illnesses and that its expression levels correlate with the severity of the disease [60]. Therefore, miR133a-3p might act as a pro-inflammatory agent, this being in accordance with our model, since we found upregulation of inflammatory signalling in the endothelium-specific mice (see above). Altogether, miR133a-3p is involved in normal heart function as well as heart pathology.

A recent and highly interesting study, which focussed on the pro-senescent effects mediated by senescent endothelial cells via sEV-associated miR secretion, revealed that senescent HUVECs release a significantly higher number of sEV compared to control non-senescent HUVECs. When examined for their cargo, those sEV were highly enriched in miR21 and miR217, which are known to target the anti-aging genes DNMT1 and SIRT1 [19]. Interestingly, DNMT1 was also found slightly decreased in Prog-

Tg ECs [49]. When control non-senescent HUVECs were treated with sEV originating from senescent HUVECs, a miR21/miR217-related impairment in the expression levels of their target genes DNMT1 and SIRT1 was noticed. Moreover, the treated non-senescent HUVECs showed a reduction of proliferative markers and a partial senescent phenotype. Interestingly, also a partial demethylation of the genetic locus encoding miR21 was induced by sEV originating from senescent HUVECs [19]. Overall, those findings suggest that sEV-enclosed miR21 and miR217 originating from senescent HUVECs are mediators of a pro-senescence effect affecting cell viability and replication in neighbouring cells [19].

In contrast to the current knowledge on miR133a-3p and miR21 in endothelial cell-mediated paracrine effects, not much is known about miR582-5p. A recent study showed that miR-582-5p acts as a tumour suppressor in a non-small lung cancer cell model by targeting the survival pathway Hippo-Yap/Taz [61]. Another recent study reported that miR582-5p functions as an anti-carcinogenic agent by regulating cell proliferation and apoptosis in human endometrial carcinoma [62]. Anti-cancerogenic pathways typically act by suppressing pro-survival signals and therefore often convey a pro-senescence effect. In Prog-Tg ECs, miR582-5p may therefore be a pro-senescent candidate which mediates paracrine senescence to the surrounding microenvironment contributing to a systemic Prog-Tg EC mediated effect.

In order to prove that sEV enclosed miRs originating from ECs can indeed be taken up by neighbouring ECs and therefore contribute to the cell-to-cell communication, we also performed an in vitro study utilizing primary mouse ECs. For this, we transfected ECs with a stably fluorescently labelled miR (Dy-547 labelled *c. elegans* miR-67) and collected the cell supernatant after 48h from which we subsequently isolated by ultracentrifugation the exosome (sEV)-containing fraction of EVs. Subsequently, we applied those exosomes on recipient ECs, which had not been transfected with the fluorescently labelled miR. After 48h the recipient ECs were found to contain the fluorescent signal by flow cytometry. These results clearly indicate that cell to cell communication via exosome-enclosed miRs can occur between ECs in our system. Thus, acquiring specific knowledge of the cargo of sEV secreted by Prog-Tg ECs can prove to be a strong diagnostic tool for CVD and further on may also reveal novel therapeutic targets for treatment of CVD and atherosclerosis, not only in aged individuals but also in HGPS patients.

Results

Characterization of endothelial cell-secreted small extracellular vesicle (sEV)

Due to the recently acquired knowledge on the importance of small extracellular vesicles (sEV) secreted by endothelial cells (ECs) in the development of aging-related CVD [20] [92], we sought to investigate the secretome of Prog-Tg ECs in culture. We decided to focus specifically on sEV, enriching for exosomes, since this fraction of sEV was shown to be an important mediator of cell-to-cell communication. In order to characterize the sEV fraction secreted by Prog-Tg ECs and by the control LA-Tg and WT ECs (see above) we grew primary mouse cells for 48h in media depleted of all extracellular vesicles (vesicle free media). Subsequently we isolated sEV, enriching for exosomes, from the 48h-conditioned cell culture media by ultracentrifugation. The isolated sEV fraction of vesicles was characterized by optical methods. Nanoparticle tracking analyzer (NTA) was used in order to check the concentration and size of the isolated sEV fraction. In contrast to previous studies, reporting that senescent ECs secrete a significant higher number of sEV [19] than healthy cells, senescent Prog-Tg ECs did not reveal higher numbers of secreted sEV compared to the control LA-Tg ECs and WT ECs (Figure 2). Instead, WT and LA-Tg EC-derived conditioned media contained a higher number of secreted sEV ($4,5E^7$ particles/ml for WT ECs and $3,8^7$ particles/ml for LA-Tg ECs particles/ml) in comparison to the Prog-Tg ECs ($1,8E^7$ particles/ml). One of the reasons for this discrepancy between published and our data may be that Prog-Tg cells are more sensitive to stress and a large fraction may die during the incubation time in the in vitro culture. According to the NTA analysis, the median size of the isolated sEV was approximately the same for Prog-Tg, LA-Tg and WT ECs, confirming the enrichment for exosomes (30-200nm in diameter) in the sEV fraction (Figure 2). For each genotype three biological replicates were used.

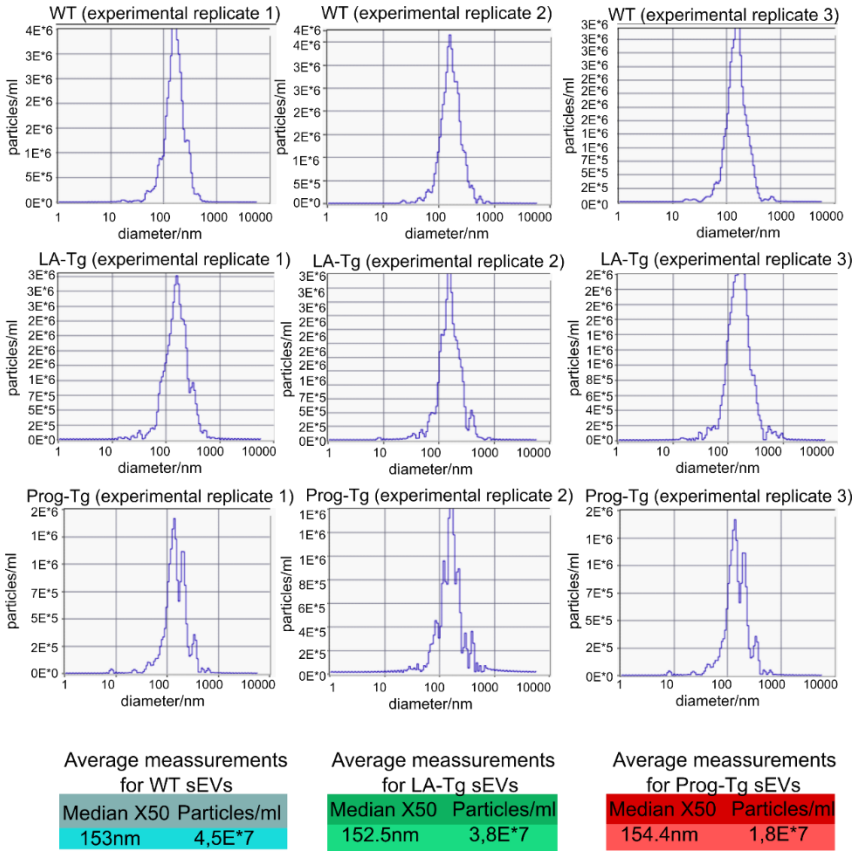

Figure 2: Nanoparticle tracking analysis (NTA) of sEV fraction enriched for exosomes. Three biological replicates for each genotype (WT, LA-Tg and Prog-Tg) were analyzed by NTA to check concentration and size distribution of sEVs isolated from the 48h-incubated cell culture media of ECs by ultracentrifugation. Isolated EVs had a size range characteristic for exosomes in all three genotypes (median X50 around 150nm). The concentration though of secreted sEVs was higher for WT ($4,5E^7$ particles/ml) and LA-Tg ($3,8E^7$ particles/ml) than for Prog-Tg ECs ($1,8E^7$ particles/ml).

Furthermore, we characterized EC-secreted sEV by electron microscopy (EM). The results were not as conclusive, since only a limited number of vesicles could be detected, but still they revealed exosome-type structures up to 200nmm in diameter in media from Prog-Tg and WT ECs in three biological replicates (Figure 3). In comparison, the control vesicle-free media used for the incubation of ECs did not show these structures (Figure 3). Overall, these results showed that primary ECs in culture secrete sEV and that we are able to isolate exosome-enriched fractions of the secreted sEV.

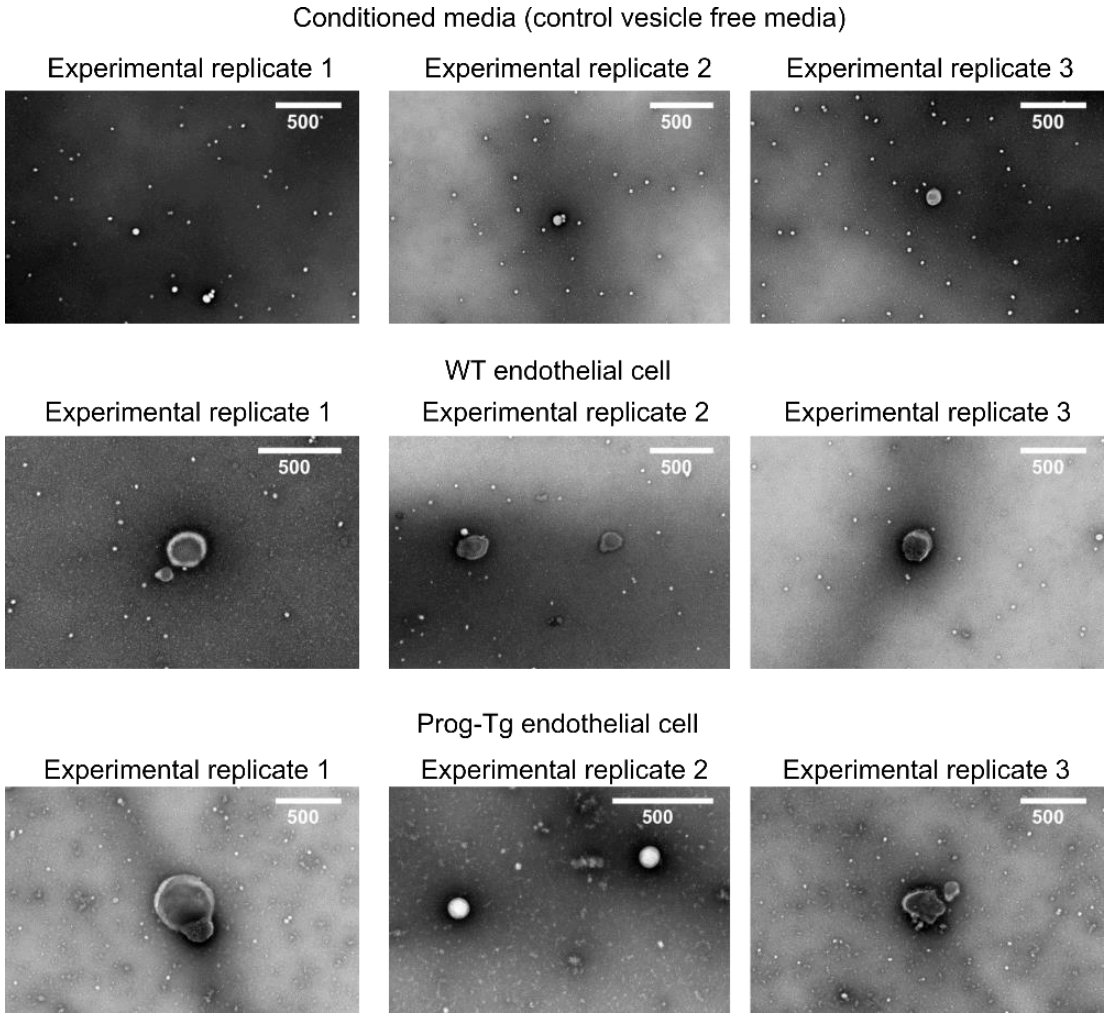

Figure 3: Representative electron microscopy (EM) images of sEV fractions enriched for exosomes. Representative negative-staining EM images of three biological replicates for sEVs obtained from WT and Prog-Tg ECs revealed exosome-like structures, with a diameter around 100-200nm. As a control, conditioned media (vesicle free media) was used which showed no sEVs.

miRNA-sequencing of endothelial cell-secreted small extracellular vesicle-bound miRNAs

Based on the emerging role of sEV-associated miRs in the development of aging-related CVD and senescence [82], we sought to investigate their potential role in progerin-mediated CVD. In order to tackle this question, we isolated exosome-bound miRs from the secretome of ECs in culture. We collected and tested the exosome-enriched fractions of EC-secreted sEV as shown above, and isolated secreted miRs from Prog-Tg, LA-Tg and WT samples in three biological replicates. These exosome-bound miRs were subjected to miR-sequencing (miR-seq). In order to identify differentially expressed miRs (DE-miRs) we first compared exosome-bound miRs of Prog-Tg ECs to those of WT ECs (Prog-

Tg/WT) and exosome-bound miRs of control LA-Tg ECs to those of WT ECs (LA-Tg/WT). Eventually, in order to pinpoint a progerin-specific effect we compared DE miRs in Prog-Tg/WT and LA-Tg/WT.
Prog-Tg ECs showed only three miRs significantly upregulated and 9 significantly down regulated (Table 1, Table 2). In direct comparison the control LA-Tg ECs showed no miR significantly upregulated, but 13 significantly downregulated (Table 3). Among the 9 significantly downregulated miRs in the secretome of Prog-Tg ECs and the 13 significantly downregulated miRs in the secretome of the control LA-Tg ECs, only 5 miRs were found commonly downregulated (miR-455-3p, miR-344-3p, miR-350-5p, miR-877-3p, miR-30c-1-3p). This overlap, although not insignificant, was not further investigated since these miRs have until now, to the best of our knowledge, not been well described in literature (Figure 4).
Although only three miRs were significantly upregulated in the secretome of Prog-Tg ECs, namely miR133a-3p, miR21a-3p and miR582-5p, these results are highly interesting. Firstly, they are progerin-specific, and secondly, they have potential physiological relevance in our disease model. In particular, miR133a-3p has been linked to normal and pathological heart function and was shown to be elevated in serum of patients with acute myocardial infarction [60]. miR21a-3p in sEV originating from senescent ECs was shown to promote pro-senescence effects [19] and miR582-5p is known to be an anti-tumorigenic miRs, therefore mediating pro-senescent effects [61] [62].

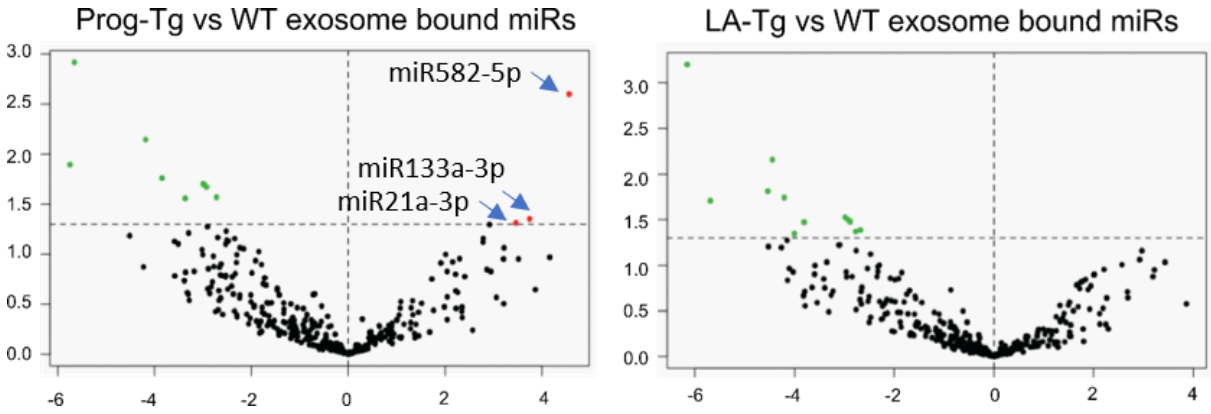

Figure 4: miR-sequencing of secreted sEV-associated miRs. Sequencing of miRs in sEV fractions, enriched for exosomes, derived from WT, LA-Tg and Prog-Tg ECs in three biological replicates revealed three miRs significantly up and 9 significantly down-regulated in Prog-Tg/WT secretome. The control EC secretome LA-Tg/WT showed no significantly up and 13 significantly downregulated miRs. X axis represents the log2 FC, Y axis represents the log10 pvalue, significantly differentially expressed miRs (DE miRs) had a FC >= 1.5 or <= -1.5 and a pvalue <= 0.05.

In vitro communication between endothelial cells through transfer of miRs enclosed in endothelial cell-secreted small extracellular vesicle enclosed

In order to test whether cell to cell communication via sEV can occur in our ECs system, we performed the following in vitro experiment utilizing primary WT ECs (donor ECs). WT ECs were transfected for 48h with fluorescently labelled miRs (Dy547 labeled *c. elegans* miR-67) using three different concentrations, 0 pmol miR Dy547 miR-67 as a control, 200 pmol and 400 pmol. Thereafter, secreted exosomes were isolated from the cell culture media of the donor ECs by ultracentrifugation and added to the cell culture media of fresh untreated WT ECs (recipient ECs) (Figure 5A). After 24h of incubation with the exosome-containing fractions derived from the donor ECs, untransfected recipient ECs were

monitored by flow cytometry (FACS). This analysis clearly revealed the presence of the fluorescent signal Dy547 in recipient cells (Figure 5B). The percentage of recipient ECs expressing the Dy547 fluorescent signal was proportional to the concentration of DY547 labelled miR-67 used for transfection of the donor ECs (Figure 5C). These data nicely demonstrated that transfer of miRs can be mediated by sEV, mainly exosomes, and that EC secreted- miRs may in this way contribute to the cell-to-cell communication in the endothelium. Moreover, progerin expressing senescent ECs could establish a pro-senescence signaling network and influence their surrounding cells and microenvironment, thereby contributing to the CVD pathology observed in Prog-Tg mice [38].

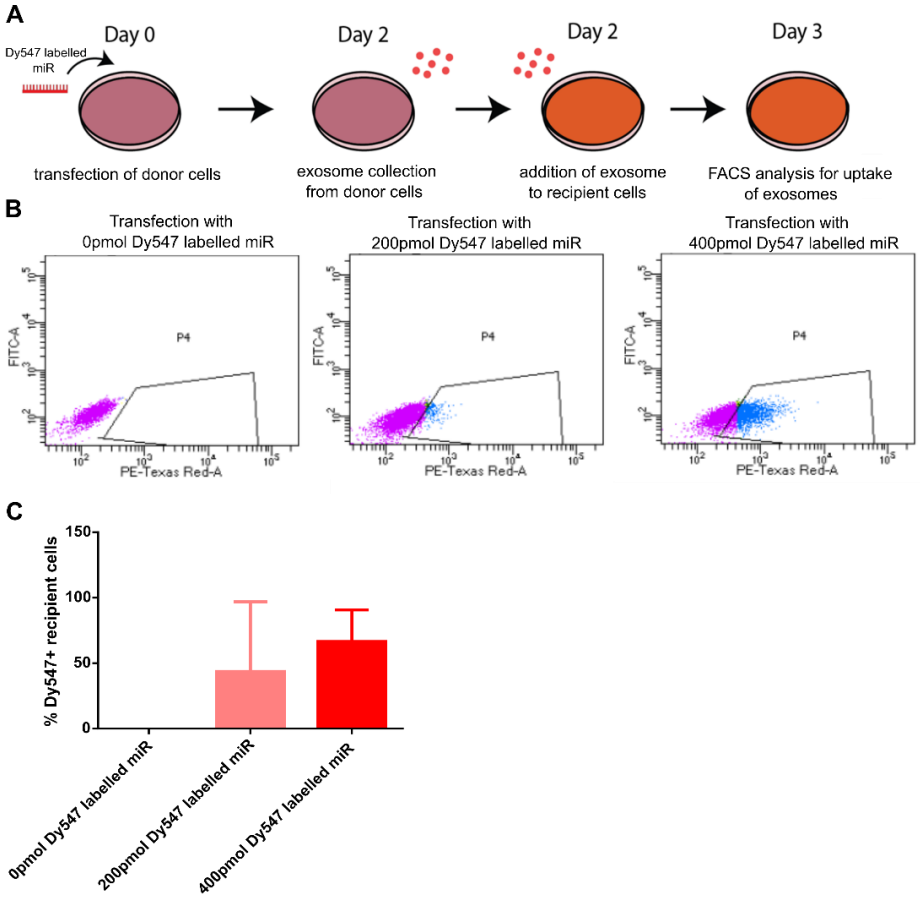

Figure 5: in vitro sEV-associated miR transfer between ECs: (A) Schematic representation of experimental design used for proving in vitro sEV-mediated miR transfer between ECs, (B) Representative images obtained by flow cytometry (FACS) showing percentage of recipient ECs expressing Dy547 fluorescence signal, (C) Bar diagram showing percentage of Dy547 positive recipient ECs, N=2

Materials and Methods

Isolation and culture of primary endothelial cells (ECs)

Isolation and culture of primary ECs was performed as described in our two previous publications [38] [49]. Typically, lung ECs at passage 2 were used.

Isolation of small extracellular vesicle fraction (sEV) from cell culture media by ultracentrifugation

To prepare sEV-free culture media, complete culture media (CCM) [38] was subjected to ultracentrifugation at 100000rcf overnight. For isolation of small extracellular vesicles (sEV) a minimum of 5ml culture media, originating from a confluent 6cm cell culture plate, was used. Cells were grown in sEV-free media and left to secret for 48h prior to isolation of sEV. Cell culture supernatant was subjected to sequential centrifugations, starting with 500g for 15min at 4^0C. Subsequently, supernatant from previous step was centrifuged at 14000g for 15min at 4^0C. Thereafter, supernatant from previous step was transferred to ultracentrifugation tubes (quick seal polypropylene tubes, Beckman Coulter REF: 342412, tube was filled up until completely full) and subjected to ultracentrifugation at 100,000g for 1.5h at 4^0C using a Beckman ultracentrifuge and a Ti70 rotor. Tubes were carefully opened with a scalpel and supernatant was removed completely. Pellet containing the sEV fraction, enriched for exosomes, was resuspended in 20ul PBS and incubated with RNase A (final concentration 0.5mg/ml) for 20 minutes at 37^0 C to degrade unprotected RNA. Thereafter, isolated exosomes were resuspended in a maximum volume of 200ul of Trizol in case sEV were subsequently use for miR isolation, or in 200ul PBS for sEV analysis by EM or NTA. Isolated sEV were stored at -80^0C over several months.

Preparation of sEV samples for electron microscopy (EM)

sEV isolated from 5ml of cell culture media and resuspended in 50ul PBS were used for preparation of EM samples. Briefly, 8ul of dissolved isolated sEV were applied to glow-discharged formvar-carbon type B coated electron microscopy grids for 3 minutes. Subsequently, excess liquid was carefully removed with a Whatman paper and the grid was carefully washed 1x with 2% PTA **(**Phosphotungstic acid**)** stain for 30 seconds. Grids were air-dried for 2 minutes and images were taken with 44.000x magnification at the EM-facility of the Vienna Biocenter Campus Facilities (https://www.viennabiocenter.org/vbcf/electron-microscopy/).

Isolation of sEV bound miRs and miR-sequencing

For sEV-associated miR isolation miRNeasy Mini Kit from Qiagen was used (Cat: 217004). Briefly, isolated sEV were dissolved in 700ul Qiazol, vortexed vigorously for 30 seconds and incubated for 10 minutes at room temperature (RT). RNA spike-in control (*c. elegans* miR-39-3p spike in control, Qiagen REF: 203202) was added at this step. Thereafter, 140ul chloroform were added and sample was centrifuged at 12,000g for 15min at 4^0C. Upper RNA containing aqueous phase was transferred to a new 2ml tube and glycogen was added to sample to a final concentration of 50ug/ml. Rest of the procedure was performed as described in the protocol of the Mini Kit from Qiagen. Isolated miR can be stored at -80^0C.

Experimental design for in vitro sEV-associated miR transfer between ECs

Briefly, 35000 primary ECs (donor ECs) cultured on a 6cm cell culture plate in penicillin/streptavidin free media at passage 2 were transfected with the fluorescently labelled Dy547 *c. elegans* miR-67, using a lipofection protocol, at day 0 (Day 0). Transfection was performed as follows: 2ul lipofectamine (LipoFectMax ABP Bioscience) were mixed with 30ul serum reduced media (Optimem, Gibco REF: 31985-062) (mixture 1) and the correct volume of Dy547-miR-67 for achieving a final concentration of either 200pmol or 400pmol in cell culture media of cells to be transfected was mixed with another 30ul serum-reduced media (mixture 2). Mixture 1 and mixture 2 were mixed and after an incubation time of 20 minutes at room temperature the final mixture was added to the cell culture media of donor ECs. After 24 hours cell culture media was removed and donor ECs were washed 4 times with PBS to get rid of any Dy547-miR leftover in the cell culture media. Transfection was allowed to occur for 48 hours (D2). Subsequently, sEV enriched for exosomes were collected from culture supernatants by differential ultracentrifugation (see above). Isolated sEV were dissolved in 200ul of vesicle-free cell culture media (conditioned media) and added to cell culture media of recipient ECs, also at passage 2. After 24h (D3) recipient ECs were trypsinized and analyzed my flow cytometry (FACS). Percentage of Dy547 positive cells was determined by using the Texas Red channel.

Table 1 (Prog-Tg secretome vs WT secretome significantly Upregulated miRs)

ID	mean_Pr_sn	mean_WT_sn	sd_Pr_sn	sd_WT_sn	FC	logFC	P.Value	adj.P.Val	avgRank
mmu-miR-582-5p	28,45490818	0,904899047	18,71744385	1,567331126	23,6068413	4,561133111	0,00251116	0,5072546	3
mmu-miR-133a-3p	17012,4717	4128,443623	13604,77861	6619,44728	13,3946235	3,743582129	0,04431581	0,998719186	7
mmu-miR-21a-3p	55,55451836	6,786696267	43,64750779	5,916513188	10,9909888	3,458249283	0,04862038	0,998719186	8

Table 2 (Prog-Tg secretome vs WT secretome significantly Downregulated miRs)

ID	mean_Pr_sn	mean_WT_sn	sd_Pr_sn	sd_WT_sn	FC	logFC	P.Value	adj.P.Val	avgRank
mmu-miR-3057-5p	0	44,47819215	0	10,64228437	-50,38062552	-5,654797129	0,001207242	0,487725802	1
mmu-miR-455-3p	0	65,09156872	0	44,94234266	-53,6138326	-5,744533365	0,012728842	0,998719186	2
mmu-miR-214-3p	0	25,95079245	0	21,6076254	-18,15776301	-4,182514572	0,007159019	0,964081177	4
mmu-miR-6540-5p	0	53,53928571	0	59,24117291	-14,37132643	-3,845121319	0,017359855	0,998719186	5
mmu-miR-27a-5p	0	29,71068123	0	27,5077422	-10,31970748	-3,367330171	0,027632459	0,998719186	9
mmu-miR-344-3p	0	19,90768992	0	20,82737273	-7,987915059	-2,997818992	0,019863775	0,998719186	11
mmu-miR-350-5p	0	20,86808922	0	18,07277164	-7,834663769	-2,969871362	0,02020596	0,998719186	13
mmu-miR-877-3p	0	17,11754165	0	14,87633372	-7,611366999	-2,928155585	0,021200317	0,998719186	15
mmu-miR-30c-1-3p	0	13,57339253	0	11,83302638	-6,577774331	-2,717599513	0,026937817	0,998719186	23

Table 3 (LA-Tg secretome vs WT secretome significantly Downregulated miRs)

ID	mean_LaTr_sn	mean_WT_sn	sd_LaTr_sn	sd_WT_sn	FC	logFC	P.Value	adj.P.Val	avgRank
mmu-miR-132-3p	0	118,7503724	0	81,0608921	-71,1928649	-6,153660753	0,000627705	0,253592948	1
mmu-miR-34b-3p	15,82875824	81,02248962	27,41621349	26,42362301	-23,204341	-4,536322821	0,015394143	0,999384498	2
mmu-miR-467c-5p	0	29,68677016	0	13,19676862	-21,794794	-4,445911663	0,00694087	0,999384498	3
mmu-miR-455-3p	0	65,09156872	0	44,94234266	-51,6047262	-5,689431296	0,019592115	0,999384498	4
mmu-miR-301b-3p	0	23,22251934	0	13,55291899	-18,4852967	-4,208306293	0,018088101	0,999384498	5
mmu-miR-374c-3p	0	23,12644125	0	6,802037116	-16,0724386	-4,006516936	0,045029944	0,999384498	8
mmu-miR-195a-3p	0	46,90339043	0	57,35558257	-14,007232	-3,808099984	0,033594284	0,999384498	10
mmu-miR-374b-5p	0	19,97283563	0	5,8744866	-16,0724386	-4,006516936	0,045029944	0,999384498	11
mmu-miR-344-3p	0	19,90768992	0	20,82737273	-7,9237193	-2,986177774	0,029710926	0,999384498	13
mmu-miR-350-5p	0	20,86808922	0	18,07277164	-7,63320494	-2,932288925	0,031511032	0,999384498	14
mmu-miR-877-3p	0	17,11754165	0	14,87633372	-7,39549427	-2,886646572	0,033157639	0,999384498	19
mmu-miR-1981-3p	0	20,53970695	0	24,97974602	-6,84230415	-2,774482236	0,04270468	0,999384498	22
mmu-miR-30c-1-3p	0	13,57339253	0	11,83302638	-6,40902978	-2,680105973	0,041100016	0,999384498	24

7. Discussion

As people live longer, aging-linked diseases have become a scourge of modern society, with cardiovascular disease (CVD) holding a central position in age-related diseases. CVD has been defined as an umbrella term as it includes a wide range of conditions that affect the heart, the blood vessels or both. Even though very heterogeneous, one of the first and foremost events in the development of most CVD is a dysfunctional endothelium [5]. The endothelium, comprised of a single cell layer of endothelial cells (ECs), coats the inside of all blood vessels, the inner walls of the heart chambers and the lymphatic vessels [2]. Its main functions involve regulating the vascular tone, forming a barrier between blood and tissue as well as acting as a signal transducer for circulating factors that can influence the vessel wall phenotype [3]. Accumulation of dysfunctional vascular ECs can be triggered by a wide range of internal and external insults, including hypertension, diabetes, increased LDL cholesterol, smoking [5] and, in particular also aging itself, which can act independently of the other risk factors [98] [99]. Patients suffering from the premature aging disease HGPS develop accelerated atherosclerosis and CVD at an early age, but all of the usual extrinsic risk factors leading to the development of a dysfunctional endothelium and subsequently CVD in aged people are absent in HGPS patients. This suggests that CVD development in HGPS is promoted by the aging process itself in absence of all the extrinsic influences, initiated by the production of the mutant lamin variant progerin.

Until recently, only the role of the observed loss of smooth muscle cells (SMCs) in HGPS patients had been extensively studied in the context of the development of atherosclerosis and CVD [24] [26] [27]. In particular, it has been shown that mouse models with a ubiquitous or specific expression of progerin in SMCs exhibit a premature aging phenotype and develop a severe vascular pathology, including severe loss of vascular SMCs, this being one of the main hallmarks of atherosclerosis in HGPS patients [26]. Taking into consideration the strategically important position of the endothelium for the development of atherosclerosis and CVD, the pivotal role of endothelial cell dysfunction in the initiation of CVD and the fact that progerin accumulates at atherosclerotic plaque regions in HGPS patients [100], but also in plaques of healthy aged individuals [101], more attention should be put in delineating the specific role of progerin expression in ECs and its contribution to EC dysfunction and the development of CVD. In order to address this unanswered question we were the first ones to generate a mouse model that express progerin specifically in the endothelium (Prog-Tg mice) [38].

In our **first publication** we show that Prog-Tg mice develop a CVD phenotype highly similar to the one observed in HGPS patients. In particular, we observed interstitial and perivascular fibrosis along with left ventricular diastolic dysfunction accompanied by left ventricular hypertrophy. Moreover, Prog-Tg mice were observed to die prematurely, with 40% of Prog-Tg mice dying at around 25 weeks of age. Prog-Tg mice as well as cultured Prog-Tg ECs showed loss of atheroprotective *eNOS* (endothelial nitric oxide synthase) and subsequently also of NO (nitric oxide) levels. This result was highly interesting since NO in the endothelium is known to mediate vasodilation [102] and to protect surrounding tissues from fibrosis by mediating an antifibrotic paracrine effect [103]. According to that, loss of NO secretion has been described as a hallmark of aging-related changes in the endothelium [5] [104] and thus our results indicate aging related changes also in the endothelium of the Prog-Tg mouse model. In line with the observed phenotype of perivascular fibrosis in Prog-Tg mice, a co-culture model showed that Prog-Tg ECs mediate a strong profibrotic paracrine signal to co-cultured fibroblasts also in vitro. We did though not observe loss of SMC in the Prog-Tg mouse model, as it has extensively

been described in literature in HGPS patient and mice [26]. We assume that VSMC loss is a cell intrinsic effect of progerin expression in the tunica media and SMCs, leading to atherosclerosis, while EC dysfunction contributes to fibrosis and heart defects, all hallmarks of HGPS.

One of the key physiological functions of the endothelium is to respond to shear stress, which is the frictional stress caused by the constant blood flow [5]. A healthy endothelium can respond to changes in shear stress by aligning the ECs to the direction of the blood flow, whereas a dysfunctional endothelium does not have that ability. Shear stress response occurs through changes in cytoskeletal arrangements and nucleo-cytoskeletal coupling that subsequently lead to changes in gene expression, in turn activating atheroprotective and anti-fibrotic signaling pathways [105]. In our study we showed a defective shear stress response of the aortic endothelium in vivo and of Prog-Tg ECs in vitro, as cells were unable to align their actin cytoskeleton. This correlated nicely with the observed reduced *eNOS* and NO levels in vivo and in vitro since it is known that *eNOS* harbors a shear stress response element in its promoter region[44] [105]. An impaired shear stress response of progerin expressing cells has previously been reported in vitro [106] [107], but the novelty and physiological relevance that our study offers is the finding that a shear stress response impairment is detected in vivo, in particular in the endothelium of the atheroprone aorta.

Based on the observed impaired shear stress response in vivo and in vitro we sought to find out how this effect is mediated on a mechanistic level. Since shear stress impairment is rooted in dysfunctional cytoskeletal rearrangements and nucleo-cytoskeletal coupling, we decided to check expression levels and localization of actin and LINC family members, proteins well known to be involved in this process. To this end, emerin, a stress-responsive protein at the nuclear envelope was found severely aggregated and SUN1/2, a protein of the LINC complex physically linking actin and lamin networks, was upregulated at the nuclear rim of Prog-Tg ECs. Since emerin is known to regulated actin polymerization, we checked F/G actin levels and observed an increase in F-actin in Prog-Tg ECs accompanied by an increase in expression levels of *Actb* both in Prog-Tg ECs as well as in tissues of Prog-Tg animals. These findings were in line with previous reports in fibroblasts, showing that mechanical force, such as shear stress, can lead to an increase of emerin at the nuclear envelope which subsequently leads to an increase of the F/G actin ratio [108].

Since changes in actin polymerization are known to lead to changes in gene expression via actin-regulated transcription factors, we sought to investigate how these changes were mediated on a mechanistic level. We focused on the transcription factor MRTF-A since it is known that MRTF-A is mechanosensitive, emerin-regulated and F-actin-sensitive. MRTF-A is bound to G-actin and kept inactive in the cytoplasm but liberated upon polymerization of G actin to F-actin and transported into the nucleus. Moreover, MRTF-A is implicated in transcriptional regulation of many cytoskeletal genes [109]. Interestingly, MRTF-A was found mislocalized in Prog-Tg ECs. Furthermore, we were able to show that pharmacological inhibition of MRTF-A abolished the paracrine pro-fibrotic effect of Prog-Tg ECs in the in vitro co-culture model and led to an increase of *eNOS* levels in Prog-Tg ECs. Moreover, we demonstrated by Chip-qPCR that MRTF-A binds directly to the promoter region of *Nos3* and therefore presumably leads to inhibition of its transcription. This was in accordance with previous studies showing the negative regulation of MRTF-A on transcription of *Nos3* [44] [110].

According to the findings of our first publication we propose a model in which progerin accumulation at the nuclear rim of ECs leads to formation of a rigid, stiff lamina, which in turn causes aggregation of emerin, SUN1/2 increase and subsequently leads to a more rigid less dynamic nucleocytoskeletal coupling and an increase of filamentous F-actin in the cytoplasm. Mechanistically, we propose that a constantly progerin-mediated increase of mechanical stress at the nuclear envelope leads to an

emerin and F-actin-regulated mis-localization of the mechanoresponsive transcription factor MRTF-A in Prog-Tg ECs. We hypothesize that this leads among other transcriptional changes to the inhibition of atheroprotective *eNOS* expression levels, resulting in downregulation of NO secretion by Prog-Tg ECs. As a result of the impaired MRTF-A/eNOS signalling axis and the decreased NO levels, we propose the promotion of a paracrine pro-fibrotic effect mediated by Prog-Tg ECs to fibroblasts in vitro and surrounding tissues in vivo. This study is of great importance since it underpins for the first time the pivotal part of endothelial cell dysfunction in the development of CVD in HGPS. Moreover, it provides for the first time a mechanistic explanation of progerin induced pro-fibrotic changes in the endothelium leading to the development of a CVD phenotype in Prog-Tg mice. Therefore, those findings open a new avenue for future therapeutic approaches for treatment not only of HGPS patients, but also of normally aged individuals in regard to CVDs. An impairment of endothelial function in HGPS was subsequently also shown in another endothelial specific progerin expressing mouse model [111] and in ECs derived from induced pluripotent cells developed from HGPS patients [112] [113].

As a logical continuation to the findings of our first publication, in our **second publication** we focussed on delineating how progerin expression in the endothelium leads to a CVD phenotype and a paracrine pro-fibrotic effect on a mechanistic and molecular level. In particular, we wanted to investigate which specific signalling and disease pathways are affected by progerin expression in the endothelium and how they are linked to the mechanosignalling defects observed earlier. Moreover, we wanted to pinpoint how the paracrine pro-fibrotic effect, and possibly other paracrine effects, are mediated and which molecules are implicated in this process. In order to address these questions, we performed mRNA as well as miRNA-sequencing in progerin-expressing ECs (Prog-Tg) (Table 4, Table 5, Table 8, Table 9) and as a control in wild type lamin A-expressing ECs (LA-Tg) (Table 6, Table 7, Table 10, Table 11). We also included miRs in our transcriptomic analyses as there is increasing evidence in the past years that they are involved in CVD [114], but the molecular mechanisms remain elusive. Moreover, we also sequenced miRs in the plasma of mice and in the EC culture media, as miRs have also been shown as major mediators of paracrine effects (Table 12-15).
Both mRNA and miR sequencing revealed upregulation of mediators of a senescence phenotype and senescence-linked pathways in Prog-Tg ECs. Moreover, this upregulation of senescence pathways was highly specific for Prog-Tg ECs, as revealed by overlapping deregulated genes and miRs in Prog-Tg versus WT ECs and in the control LA-Tg versus WT ECs revealed. This was an important finding, since it indicated that the observed phenotype is not just an artefact induced by overexpression of human lamin A in the endothelium per se, but is dependent on the HGPS mutant lamin variant. mRNA sequencing showed upregulation of a p53-linked senescence pathway and of pro-inflammatory and pro-fibrotic mediators, revealing a senescence-associated secretory phenotype (SASP) in Prog-Tg ECs. In particular, GO analysis showed the pro-inflammatory pathway to be the upmost deregulated one in Prog-Tg ECs, with deregulation of many interleukins and chemokines. The implication of p53/p21 signaling in HGPS has been previously proposed by a study, which revealed an epigenetic regulation of p21 upon progerin induced oxidative stress in HGPS fibroblasts [115]. In accordance with these findings, senescence and SASP were also detected in vivo in lung as well as in heart tissue of Prog-Tg mice, indicating physiological relevance for CVD. Moreover, immunohistological analysis of lung and liver tissue of Prog-Tg mice showed increased infiltration of immune cells, providing further proof of an in vivo paracrine pro-inflammatory effect. The observation of increased infiltration of immune cells in liver tissue can be explained by its key role as an immunological defense organ in mammals.

Additionally, stainings of lung tissues with senescence marker p19 (Cdkn2d) functioning upstream of p53 [116] revealed senescence in the tissue in vivo. In accordance to that, in an experimental setup where we separated EC- from non-EC population ex vivo and then detected expression of senescence and SASP markers also in non-EC populations, we could further confirm in vivo paracrine pro-senescence and SASP effects mediated by Prog-Tg ECs to surrounding tissues. Altogether, our results show that progerin expression in the endothelium activates an intracellular senescence signaling program which is accompanied by a paracrine senescent and SASP effect mediated by Prog-Tg ECs to surrounding tissues.

In our first publication we have already shown that Prog-Tg ECs in co-culture with fibroblast mediate a paracrine pro-fibrotic effect in vitro[38]. To further study the Prog-Tg EC mediated paracrine pro-senescent and SASP effect in vitro, we used the same co-culture system of ECs with fibroblasts and tested expression of several markers in fibroblasts. These experiments demonstrated that indeed Prog-Tg ECs mediate not only a pro-fibrotic, but also a pro-senescent and pro-inflammatory effect to their co-cultured fibroblasts. The finding that pro-senescent effects are mediated by Prog-Tg ECs reveals a ``bystander senescence`` effect, as it has previously been described [117] [118]. The fact that paracrine pro-senescence, but also pro-fibrotic effects were mediated not only by lung-derived Prog-Tg ECs but also by heart Prog-Tg ECs is consistent with a physiological relevance of these pathways to CVD in HGPS. In particular, upregulation of the pro-fibrotic marker *Acta2* suggested that progerin expression in the microvasculature of the cardiac tissue might contribute to the observed fibrosis in the heart of HGPS patients.

Thus, endothelial cell senescence is the root for the development of CVD in HGPS. It is broadly accepted that cellular senescence is one of the main causes of age-related diseases [119]. Moreover, it has been shown that clearance of senescent cells, for instance by senolytic agents, can lead to a delayed onset or attenuation of age-related symptoms in young and aged individuals respectively [7] [120]. Cellular senescence can be characterized as a two-dimensional phenomenon, leading to expression of senescence associated mediators and pathways intracellularly and influencing surrounding tissues in a paracrine manner by the senescence associated secretory phenotype (SASP) [121]. SASP can have beneficial and deleterious effects depending on a developmental and tissue specific context. In the context of an aging tissue SASP has been reported to cause tissue dysfunction, chronical inflammation (inflammaging) and age-related diseases, including CVD [121]. Apart from the well-established SASP markers which include pro-inflammatory and pro-fibrotic mediators, proteases and extracellular matrix (ECM) components, also miRs have recently been proven as highly potent SASP components [12].

In recent years, miRs have emerged as potent mediators of SASP. Our miR-sequencing data of Prog-Tg ECs revealed a highly interesting EC-specific senescence associated miR signature, with upregulation of a plethora of senescence associated miRs (SA-miRs) including miR206-3p, miR124-3p, miR485-5p, miR31-5p, miR34a-5p and miR34c-5p. KEGG pathway analysis of upregulated miRs in Prog-Tg ECs showed a strong association with the p53-senescence linked pathway, mirroring the situation observed by mRNA-sequencing analyses. These data suggested that gene and miR expression collaborate so as to activate and maintain senescence and SASP signaling, induced by progerin expression in the endothelium.

Further on, in order to reveal any systemic effects, we performed miR-sequencing also of plasma samples of Prog-Tg mice. miR34a-5p and miR31-5p were suspects of mediating a systemic effect, since they were found highly upregulated also in plasma samples of Prog-Tg mice. Reassuringly, both miRs were found significantly upregulated also in lung and heart tissue, providing evidence for an in vivo

function, and in non-EC tissues further indicating their potential role as paracrine mediators. The finding that miR34a-5p is upregulated both in Prog-Tg ECs as well as in plasma samples of Prog-Tg mice was highly interesting in the context of CVD, since miR34a-5p is both a well-established biomarker and mediator of CVD [52] [53] [54] and a recently established senescence-associated miR (SA-miR) [15] [51]. Reassuringly, an overlap of all known miR34a-5p mRNA targets (according to targetscan online target prediction tool) and of all downregulated genes in Prog-Tg ECs revealed that more than 50% of all known miR34a-5p targets were found in the list of downregulated genes in Prog-Tg ECs. These results indicated a significant intracellular but also systemic role of miR34a-5p in the pro-senescence effect mediated by progerin expression in the endothelium.

To delineate the specific senescence signaling program activated by progerin expression in the endothelium functionally, we used miR34a-5p and p53 neutralizing approaches. More specifically, p53 knockdown caused a reduced expression of its immediate downstream target and early senescence marker *Cdkn1a* (p21) but not of the deep senescence marker *Cdkn2a* (p16), usually upregulated in the permanently senescent cell state. Certain pro-inflammatory SASP markers were also affected by p53 knockdown, while pro-fibrotic markers were not altered upon reduction of p53 expression levels. Moreover, p53 was shown to directly regulate expression levels of miR34a-5p, which in turn affected expression of p53 in a positive feedback loop. This is in accordance with previous reports showing that p53 regulates the expression of miR34a by direct binding to its promoter, and miR34a subsequently increases the stability and activity of p53 by inhibiting negative regulators of p53, such as SIRT1 [86]. On the other hand, miR34a-5p inactivation by specific antagomiRs affected expression levels of *Cdkn2a* but did not influence *Cdkn1a* or SASP markers. Interestingly, inhibition of p53 but not of miR34a-5p led to a slight but significant increase of survival of Prog-Tg ECs. This limited effect may be explained by increasing levels of miR34a-5p resulting in upregulation of p16 which presumably leads to a non-reversible cell-cycle arrest. Overall, those experiments revealed that p53 and miR34a-5p act in a complementary and synergistic mode in order to establish and maintain senescence signaling in Prog-Tg ECs.

To provide physiological relevance to CVD and in order to establish a possible connection between the previously observed mechanosignalling defects in Prog-Tg ECs with the p53 and miR-linked senescence pathways [38], we checked expression levels of senescence markers and SA-miRs in the atheroprone aortic arch regions. Blood flow around the aortic arch is known to switch from a laminar flow to a disturbed flow, increasing locally shear stress response [122]. Since we have previously shown that Prog-Tg ECs exhibit a disturbed shear stress response, we wanted to test whether there is a connection to increased expression of senescence and SASP markers in atheroprone regions. Indeed, expression levels of the senescence markers *Cdkn1a* and of the SA-miR34a-5p and SA-miR31-5p were significantly increased specifically in the aortic arche of Prog-Tg mice.

As mentioned above extracellular vesicles (EVs) have been shown to play an integral role in cell to cell communication, but also in the pathogenesis of several diseases, such as cancer development, neurodegenerative diseases and importantly cardiovascular disease (CVD) [123] [124]. EVs, especially small extracellular (sEV), are important for physiological and pathological functions in the cardiovascular system [124]. Physiological cardiac function depends to a great extent on the communication and the coordinate interplay between cardiomyocytes and other cell types present in the heart muscle, such as endothelial cells (ECs), fibroblasts and immune cells (non-cardiomyocytes). sEVs participate in intercellular communication by enclosing and transporting various bioactive molecules, such as miRs and proteins to recipient cells. In the CVD context, sEVs can be released by many cell types present in the heart, including EC [124]. As discussed above, progerin-expressing

senescent ECs establish a SASP-linked ‘’communication network ‘’ with their surrounding microenvironment, through which pro-senescent signals are transmitted to neighboring cells. sEV-enclosed miRs constitute a novel member of the SASP [12]. Interestingly a previous study suggested that endothelial cell senescence and progression of CVD is associated with the production of altered sEVs by senescent endothelial cells [20]. Therefore, characterization of endothelial cell released sEV and of their content poses an innovative diagnostic tool as well as a therapeutic approach for CVD.

We have shown that Prog-Tg ECs develop a senescence and SASP phenotype and that intracellular but also secreted miRs are an integral part of this process [12] [20]. Therefore, we analyzed the sEV-enclosed miR secretome of Prog-Tg ECs in the culture media. We show that Prog-Tg ECs as well as the control LA-Tg and WT ECs release sEV in the size range of exosomes (30-150um). Surprisingly, we did not see an increased concentration of sEV in media of senescent Prog-Tg ECs versus LA-Tg or WT ECs, which is in contrast to previous studies showing that senescent ECs release a significantly higher number of sEV than control cells [19]. One possible explanation for this might be that in our study we used primary ECs which are highly susceptible to oxidative stress, especially in case of Prog-Tg ECs. Therefore, senescent, Prog-Tg ECs may die in culture much earlier than WT cells and thus secrete less sEV. Another explanation might be that at the time point of collection of the cell culture media used for isolation of sEV, Prog-Tg ECs were only 70% confluent in comparison to the 100% confluent LA-Tg and WT ECs. This was the case because, although the same number of ECs were plated initially for all genotypes, Prog-Tg ECs in culture proliferate much slower that LA-Tg and WT ECs. Although we normalized the volume of the cell culture media of LA-Tg and WT ECs to cell numbers, this may not be as accurate and biased through a high number of dead cells. Further studies are needed to investigate this issue in more detail.

miR-sequencing revealed three sEV-enclosed miRs significantly upregulated in the secretome of Prog-Tg ECs. These results were highly interesting since they proved to be progerin-specific, with the control LA-Tg ECs not showing any significantly upregulated sEV-enclosed miRs. Moreover, all three upregulated miRs have a high physiological relevance in the context of our mouse disease model. In particular, miR133a-3p has been extensively described as a cardioprotective factor which inhibits apoptosis and leads to reduction of cardiac hypertrophy in vivo and in vitro [58] [59]. We hypothesize that in our Prog-Tg mice senescent Prog-Tg ECs in the heart, and potentially in other tissues, secret significantly higher levels of sEV-enclosed miR133a-3p as a “protective” warning signal. By doing so they might inform surrounding ECs and non-ECs to activate a cardioprotective, anti-hypertrophic signal and thereby prevent spreading of EC dysfunction. Interestingly, several clinical studies have shown that miR133a-3p levels are significantly increased in serum of patients with critical inflammatory illnesses, with its expression levels correlating with the severity of the disease [60]. Since we showed that Prog-Tg ECs upregulate pro-inflammatory signals, such as cytokines, chemokines and interleukins, miR133a-3p may act as an additional pro-inflammatory agent mediating SASP signals to surrounding cells. According to the above-mentioned roles of miR133a-3p in paracrine signaling, its specific functions in CVD appear to be highly complex. Nevertheless, it poses an interesting candidate for further investigations to pinpoint its specific mode of action in the context of Prog-Tg ECs paracrine signaling.

The second sEV-enclosed miR which was found significantly upregulated in the secretome of Prog-Tg ECs was miR21a-3p. This was of high interest, as a recent study revealed miR21 to be a specific senescent EC-derived paracrine signaling agent. In particular, this study showed that senescent ECs change their sEV cargo and that one miR that is highly upregulated in those sEV is miR21 [19]. miR21

has been characterized as a senescence associated miR (SA-miR) known to fulfill its function by targeting pro-survival genes, including DNMT1 and SIRT1. Interestingly, our mRNA-seq data revealed that DNMT1 was downregulated in Prog-Tg ECs [49]. According to this study, miR21 might be one additional SASP member secreted by Prog-Tg ECs enclosed in sEV and mediating progerin induced pro-senescence effects. Another recent study showed that serum-derived sEV enriched in miR21 significantly reduce cardiomyocyte apoptosis in cellular as well as mouse models for acute myocardial infarction (AMI) and attenuated to a great extent the infarct size in mouse hearts after AMI [125]. The protective effect of serum derived sEV was reduced upon inhibition of miR21. According to this study, upregulation of sEV-enclosed miR21 in the secretome of Prog-Tg ECs might mediate an anti-apoptotic signal to protect neighboring cells from programmed cell death.
miR582-5p was the third sEV-enclosed miR to be found significantly enriched in the secretome of Prog-Tg ECs. Although less is known about the specific function of this miR, it has been described as an anti-tumorigenic miR [61] [62]. miRs that act as tumor suppressors typically inhibit pro-survival signals and therefore function as pro-senescence mediators. In the case of miR582-5p we hypothesize that Prog-Tg ECs may upregulate miR582-5p in their secretome in order to strengthen their paracrine pro-senescence signaling. Therefore, miR582-5p might be part of the well-orchestrated Prog-Tg EC specific SASP signaling.

Overall, based on the novel findings of our studies but also of our unpublished data, we propose a hypothetical disease model of progerin-induced ``mechanosenescence`` (Figure 6): Progerin-induced mechanical stress leads to activation of the p53-senescence linked pathway and other senescence-mediating agents, importantly including SA-miRs. Because of the proposed link between mechanical defects and senescence, upregulation of senescence and SASP mediators is higher at atheroprone regions, such as the atheroprone aortic arch. Due to the for CVD strategically relevant function of ECs, secretion of miR34a-5p and other SA miRs by progerin-expressing ECs along with other SASP molecules, such as Ccl20, by ECs results in a pro-inflammatory, and a pro-fibrotic SASP phenotype in target tissues. This in turn may represent major pathways facilitating CVD in HGPS. More specifically, pro-inflammatory effects are not only observed in the cardiovascular tissue but also in lung and liver tissues. In addition, also the pro-fibrotic changes in the cardiac tissue in HGPS may be caused by the paracrine effect of progerin-expressing ECs. Mechanistically we propose that miR34a-5p leads to an intracellular increase of the deep senescence marker p16, which if persistent leads to an irreversible cell cycle arrest with systemic pro-inflammatory and pro-fibrotic paracrine consequences. Therefore, while healthy ECs secret atheroprotective NO, the Prog-Tg ECs-specific SASP counteracts this effect by upregulation of several SASP markers and SA-miRs leading to a systemic tissue deterioration mediated by progerin expression in ECs. Our study is of particular importance since it provides novel aspects for antimiR based therapeutic interventions that could prove particularly beneficial for treating EC senescence and the associated CVD in premature but also pathophysiological aging.
Recently, a lot of attention has been paid to the sEV-enclosed miRs in the context of therapeutic and prognostic approaches. The secretome of a cell can be described as its distinct extracellular signature, which is very specific according to cell type, developmental and the cellular state and disease condition. To this end, analysis of a cell´s secretome can reveal important information on its role in a pathological condition. Regarding cellular senescence and CVD, characterization of the secretome has revealed a lot of potential disease mediators and therapeutic targets. Therefore, analyzing the Prog-Tg EC specific secretome, specifically in terms of sEV-enclosed miRs, may reveal novel mediators of progerin-induced but also normal geriatric CVD. In this regard, miRs pose a very powerful tool due to

their ability to pleiotropically target hundreds or in many cases thousands of genes [126]. Consequently, this opens the possibility of one single miR being able to modulate entire biological pathways that might be pathogenically disrupted in a patient. One concern that comes up though due to the pleiotropic nature of miRs are their off-target biological effects. Nevertheless, similar unspecific responses have also been noticed with traditional therapeutics that target single protein coding genes [126]. Collectively, miRs pose a very powerful new therapeutic tool for treatment of many multi-dimensional diseases, such as CVD.

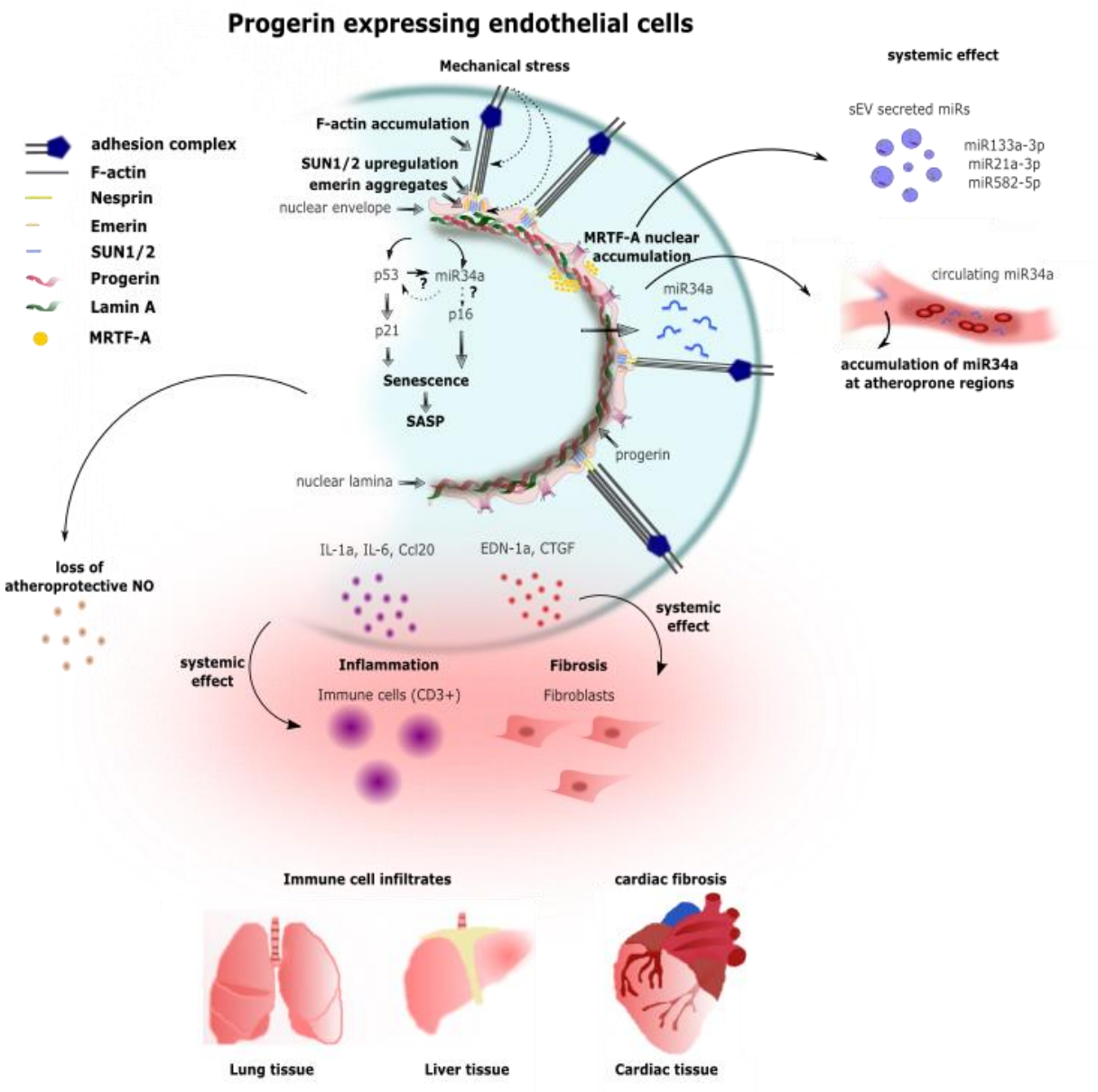

Figure 6: Working model: In progerin expressing endothelial cells progerin expression at the nuclear rim leads to increased mechanical stress by causing emerin aggregation, SUN1/2 upregulation and an upregulation of F-actin stress fibers. These changes in turn lead to nuclear accumulation of MRTF-A which results in upregulation of paracrine pro-fibrotic signaling and loss of atheroprotective NO signaling. We hypothesize that the increased mechanical stress might initiate senescence signaling (mechanosenescence) by causing increased expression of the p53 signaling pathway and the SA miR34a-5p. p53 and miR34a-5p work synergistically in order to establish and maintain senescence signaling. Senescent ECs cause a systemic effect and influence their surrounding cells and microenvironment, but also tissues, by secretion of SASP factors, such as pro-inflammatory and pro-fibrotic factors and SA-miRs. The systemic paracrine effects are manifested by immune cell infiltration in lung and liver tissues, cardiac tissue fibrosis and secretion of small extracellular vesicle enclosed SA-miRs, such as miR133a-3p, miR21a-3p and miR582-5p. Accumulation of SA miRs, such as miR34a-5p at atheroprone aortic arch regions, provides a link to mechanosenescence. Overall, we propose that progerin accumulation at the nuclear rim of Prog-Tg ECs leads to mechanosignaling defects and ``mechanosenescence``, resulting in an increase of p53 senescence and SASP signaling and subsequently in paracrine senescence.

8. Appendix

Table 4- Upregulated genes Prog-Tg vs WT ECs

ID	FC	Log2FC	P.Value	adj.P.Val	MGI_symbol
ENSMUSG00000103135	22,294172	4,478595	0,004024	0,999997	Gm37979
ENSMUSG00000044162	27,808089	4,797433	0,01051	0,999997	Tnip3
ENSMUSG00000055561	12,408825	3,633295	0,002434	0,999997	Spink5
ENSMUSG00000031289	20,566398	4,362217	0,018074	0,999997	Il13ra2
ENSMUSG00000026343	17,058046	4,092381	0,014403	0,999997	Gpr39
ENSMUSG00000027022	14,980397	3,905004	0,013162	0,999997	Xirp2
ENSMUSG00000050397	10,92638	3,449744	0,004471	0,999997	Foxl2
ENSMUSG00000032496	13,610236	3,76662	0,013135	0,999997	Ltf
ENSMUSG00000029695	10,751641	3,426485	0,007059	0,999997	Aass
ENSMUSG00000096960	9,7100709	3,279482	0,001885	0,999997	A230028O05Rik
ENSMUSG00000037086	21,454098	4,423181	0,02622	0,999997	Prr32
ENSMUSG00000021750	12,65267	3,66137	0,01675	0,999997	Fam107a
ENSMUSG00000027919	27,769556	4,795432	0,03072	0,999997	Lce1g
ENSMUSG00000071550	12,036115	3,589298	0,019014	0,999997	Cfap44
ENSMUSG00000043773	9,4136934	3,234761	0,007798	0,999997	1700048O20Rik
ENSMUSG00000037977	9,4970918	3,247486	0,00823	0,999997	6430571L13Rik
ENSMUSG00000026166	15,26131	3,931807	0,026985	0,999997	Ccl20
ENSMUSG00000044313	9,1687197	3,19672	0,007642	0,999997	Mab21l3
ENSMUSG00000026678	9,644475	3,269703	0,012279	0,999997	Rgs5
ENSMUSG00000030187	8,8575195	3,146903	0,003888	0,999997	Klra2
ENSMUSG00000021728	8,6741008	3,116714	0,008554	0,999997	Emb
ENSMUSG00000050395	18,915194	4,241474	0,03386	0,999997	Tnfsf15
ENSMUSG00000012350	9,4106268	3,234291	0,018945	0,999997	Ehf
ENSMUSG00000047746	9,102686	3,186292	0,016515	0,999997	Fbxo40
ENSMUSG00000084984	8,1719227	3,030676	0,003948	0,999997	Far1os
ENSMUSG00000045201	26,454817	4,725459	0,039724	0,999997	Lrrc3b
ENSMUSG00000056054	9,3559092	3,225878	0,020976	0,999997	S100a8
ENSMUSG00000086531	8,1512183	3,027016	0,006119	0,999997	Gm11351
ENSMUSG00000043333	17,455562	4,125615	0,034913	0,999997	Rhbdl2
ENSMUSG00000022123	19,032875	4,250422	0,038245	0,999997	Scel
ENSMUSG00000028528	7,7529527	2,954746	0,005321	0,999997	Dnajc6
ENSMUSG00000027261	8,7085807	3,122438	0,023201	0,999997	Hao1
ENSMUSG00000029378	8,2674504	3,047442	0,019094	0,999997	Areg
ENSMUSG00000024905	7,1952209	2,847039	0,004823	0,999997	Mtl5
ENSMUSG00000090216	8,2030674	3,036163	0,019484	0,999997	Gm16549
ENSMUSG00000068859	7,63278	2,932209	0,012331	0,999997	Sp9
ENSMUSG00000058427	12,843495	3,682966	0,038601	0,999997	Cxcl2
ENSMUSG00000017868	7,8065639	2,964688	0,017508	0,999997	Sgk2
ENSMUSG00000097981	6,9491269	2,796832	0,009764	0,999997	Gm7583
ENSMUSG00000030468	8,3382342	3,059742	0,030357	0,999997	Siglecg

ENSMUSG00000039742	6,8305459	2,772001	0,010588	0,999997	Fam71f1
ENSMUSG00000050663	7,0673177	2,821163	0,013217	0,999997	Trhde
ENSMUSG00000008658	8,9852002	3,167551	0,034795	0,999997	Rbfox1
ENSMUSG00000027599	6,4820497	2,69645	0,007142	0,999997	Armc1
ENSMUSG00000090602	6,3945496	2,676843	0,011577	0,999997	Gm5611
ENSMUSG00000020963	6,8786183	2,782119	0,022816	0,999997	Tshr
ENSMUSG00000029134	6,287897	2,652578	0,012332	0,999997	Plb1
ENSMUSG00000031497	7,0228138	2,812049	0,030213	0,999997	Tnfsf13b
ENSMUSG00000079138	6,5093984	2,702524	0,021812	0,999997	Gm8818
ENSMUSG00000002565	8,3153925	3,055784	0,043633	0,999997	Scin
ENSMUSG00000106746	8,2066355	3,036791	0,041329	0,999997	2900064F13Rik
ENSMUSG00000085766	6,862782	2,778794	0,030468	0,999997	2810430I11Rik
ENSMUSG00000073805	5,8568892	2,550135	0,007552	0,999997	Fam196a
ENSMUSG00000045104	6,6474302	2,732797	0,032799	0,999997	Gm5514
ENSMUSG00000015354	6,3707138	2,671455	0,028679	0,999997	Pcolce2
ENSMUSG00000042717	7,4830925	2,903635	0,044346	0,999997	Ppp1r3a
ENSMUSG00000035775	7,6989361	2,944659	0,046088	0,999997	Krt20
ENSMUSG00000022148	5,8526649	2,549094	0,01694	0,999997	Fyb
ENSMUSG00000086898	6,11285	2,611845	0,025012	0,999997	Itpr3os
ENSMUSG00000027399	6,297266	2,654726	0,030378	0,999997	Il1a
ENSMUSG00000091712	7,211671	2,850334	0,045007	0,999997	Sec14l5
ENSMUSG00000022805	5,555733	2,473977	0,012258	0,999997	Maats1
ENSMUSG00000029380	7,448965	2,89704	0,048241	0,999997	Cxcl1
ENSMUSG00000070732	5,4724951	2,452199	0,011239	0,999997	Rbm44
ENSMUSG00000087659	5,4723565	2,452162	0,011063	0,999997	Gm12606
ENSMUSG00000032726	5,4918954	2,457304	0,014722	0,999997	Bmp8a
ENSMUSG00000047507	5,5272813	2,46657	0,020986	0,999997	Baiap3
ENSMUSG00000033837	6,9531545	2,797668	0,049629	0,999997	Foxh1
ENSMUSG00000017754	6,1849981	2,628773	0,035186	0,999997	Pltp
ENSMUSG00000092344	6,2318266	2,639655	0,038592	0,999997	Hspe1-ps3
ENSMUSG00000030510	5,8699597	2,553351	0,031472	0,999997	Cers3
ENSMUSG00000039543	5,8568561	2,550126	0,032372	0,999997	Cfap70
ENSMUSG00000002257	5,4378329	2,443032	0,024196	0,999997	Def6
ENSMUSG00000086976	5,1898236	2,375686	0,01203	0,999997	Gm12316
ENSMUSG00000042078	5,7524176	2,524168	0,034613	0,999997	Svop
ENSMUSG00000047344	5,9072277	2,562481	0,041025	0,999997	Lancl3
ENSMUSG00000028033	6,1009532	2,609035	0,045194	0,999997	Kcnq5
ENSMUSG00000007122	5,3250933	2,412807	0,027399	0,999997	Casq1
ENSMUSG00000021390	5,1984367	2,378078	0,021562	0,999997	Ogn
ENSMUSG00000074796	5,1291037	2,358707	0,021457	0,999997	Slc4a11
ENSMUSG00000034634	5,1797258	2,372876	0,024275	0,999997	Ly6d
ENSMUSG00000106696	5,2051962	2,379953	0,025507	0,999997	Gm42729
ENSMUSG00000034813	5,9264291	2,567163	0,048663	0,999997	Grip1

ENSMUSG00000022947	5,8224567	2,541628	0,047052	0,999997	Cbr3
ENSMUSG00000031877	4,9431239	2,305423	0,017902	0,999997	Ces2g
ENSMUSG00000100334	5,5318971	2,467774	0,044745	0,999997	C230024C17Rik
ENSMUSG00000084094	5,2394334	2,389411	0,034632	0,999997	Gm13961
ENSMUSG00000039252	5,4293612	2,440782	0,04271	0,999997	Lgi2
ENSMUSG00000064109	4,9433246	2,305482	0,02796	0,999997	Hcst
ENSMUSG00000085033	5,4326697	2,441661	0,045388	0,999997	Gm11646
ENSMUSG00000030074	4,9858622	2,317843	0,03192	0,999997	Gxylt2
ENSMUSG00000067085	5,0276517	2,329885	0,034548	0,999997	Gm10197
ENSMUSG00000107168	4,9205863	2,29883	0,032445	0,999997	Gm42507
ENSMUSG00000063415	5,3912665	2,430624	0,04921	0,999997	Cyp26b1
ENSMUSG00000020080	4,5643745	2,190417	0,024291	0,999997	Hkdc1
ENSMUSG00000006411	4,7410803	2,245216	0,037619	0,999997	Nectin4
ENSMUSG00000086578	4,4629192	2,157988	0,022071	0,999997	Gm13583
ENSMUSG00000020875	4,7071646	2,234858	0,037968	0,999997	Hoxb9
ENSMUSG00000060093	4,8077851	2,265372	0,045223	0,999997	Hist1h4a
ENSMUSG00000101942	4,7898884	2,259992	0,045429	0,999997	Gm19582
ENSMUSG00000055313	4,4488719	2,15344	0,028431	0,999997	Pgbd1
ENSMUSG00000027202	4,5650997	2,190646	0,035393	0,999997	Slc12a1
ENSMUSG00000052485	4,6859197	2,228332	0,045643	0,999997	Tmem171
ENSMUSG00000107355	4,5201447	2,176369	0,036298	0,999997	AI839979
ENSMUSG00000110234	4,6213268	2,208307	0,045728	0,999997	Gm45799
ENSMUSG00000027208	4,5360878	2,181449	0,042661	0,999997	Fgf7
ENSMUSG00000085731	4,4829113	2,164436	0,040825	0,999997	Gm16229
ENSMUSG00000014329	4,4354822	2,149091	0,039411	0,999997	Bicc1
ENSMUSG00000107035	4,2065471	2,072636	0,028063	0,999997	Ybx1-ps2
ENSMUSG00000097626	4,4281491	2,146704	0,046066	0,999997	4921504A21Rik
ENSMUSG00000091744	4,2450405	2,085778	0,038107	0,999997	Gm17732
ENSMUSG00000085166	4,1365355	2,048423	0,031397	0,999997	Gm15522
ENSMUSG00000073486	4,2375014	2,083214	0,039221	0,999997	Gm10518
ENSMUSG00000022054	4,0848952	2,030299	0,029751	0,999997	Nefm
ENSMUSG00000033644	4,0607177	2,021735	0,030765	0,999997	Piwil2
ENSMUSG00000109438	3,9440021	1,97966	0,032714	0,999997	Gm45073
ENSMUSG00000107667	3,9388454	1,977773	0,032257	0,999997	C530044C16Rik
ENSMUSG00000026831	4,1283332	2,045559	0,047712	0,999997	1700007K13Rik
ENSMUSG00000074121	4,0912039	2,032525	0,047965	0,999997	Ntf5
ENSMUSG00000031298	4,0929901	2,033155	0,048904	0,999997	Adgrg2
ENSMUSG00000040003	3,8363047	1,939717	0,030983	0,999997	Magi2
ENSMUSG00000037014	3,5815093	1,840568	0,027181	0,999997	Sstr4
ENSMUSG00000011008	3,5141422	1,813173	0,019338	0,999997	Mcoln2
ENSMUSG00000046908	3,6300724	1,859998	0,036191	0,999997	Ltb4r1
ENSMUSG00000047712	3,6907365	1,883909	0,046876	0,999997	Ust
ENSMUSG00000068417	3,3088006	1,726308	0,019644	0,999997	Pnp2

ENSMUSG00000020135	3,38675	1,759901	0,047509	0,999997	Apc2
ENSMUSG00000021260	3,3041922	1,724298	0,047818	0,999997	Hhipl1
ENSMUSG00000056220	3,1212171	1,642109	0,049519	0,999997	Pla2g4a
ENSMUSG00000073739	3,0727197	1,619516	0,046239	0,999997	Gm16287
ENSMUSG00000042942	3,0802571	1,623051	0,048776	0,999997	Greb1l

Table 5-Downregulated genes Prog-Tg vs WT ECs

ID	FC	Log2FC	P.Value	adj.P.Val	MGI_symbol
ENSMUSG00000021613	-26,11972597	-4,707067856	0,00928538	0,9999972	Hapln1
ENSMUSG00000085925	-18,14903983	-4,18182132	0,00989237	0,9999972	Rtl1
ENSMUSG00000061171	-71,68128198	-6,163524534	0,02639667	0,9999972	Slc38a11
ENSMUSG00000096938	-20,92999385	-4,387499982	0,02463516	0,9999972	9530052E02Rik
ENSMUSG00000020734	-25,68976328	-4,683121691	0,03035114	0,9999972	Grin2c
ENSMUSG00000028716	-13,46512317	-3,751155522	0,02074302	0,9999972	Pdzk1ip1
ENSMUSG00000097083	-19,55941309	-4,289791175	0,02932112	0,9999972	D930019O06Rik
ENSMUSG00000108255	-11,61404998	-3,537799243	0,02319649	0,9999972	Gm16499
ENSMUSG00000059412	-19,1214731	-4,257121766	0,03394926	0,9999972	Fxyd2
ENSMUSG00000033740	-14,96975725	-3,903978922	0,03112051	0,9999972	St18
ENSMUSG00000094686	-30,10513162	-4,91193752	0,03853544	0,9999972	Ccl21a
ENSMUSG00000021763	-8,514346947	-3,089895879	0,00839322	0,9999972	BC067074
ENSMUSG00000043496	-14,91000715	-3,898209044	0,0320939	0,9999972	Tril
ENSMUSG00000096549	-21,28535919	-4,411789531	0,04248414	0,9999972	Prickle4
ENSMUSG00000050105	-9,62815486	-3,267259346	0,02979325	0,9999972	Grrp1
ENSMUSG00000040694	-13,22423133	-3,725111961	0,03730367	0,9999972	Apobec2
ENSMUSG00000023987	-25,31286429	-4,661798861	0,04739801	0,9999972	Pgc
ENSMUSG00000061524	-7,756399182	-2,955387054	0,01407911	0,9999972	Zic2
ENSMUSG00000087100	-8,943401304	-3,160823613	0,03205892	0,9999972	Gm14641
ENSMUSG00000019312	-13,91731043	-3,798808527	0,04696204	0,9999972	Grb7
ENSMUSG00000028072	-12,23046344	-3,612407167	0,04488567	0,9999972	Ntrk1
ENSMUSG00000072875	-9,09603784	-3,185238256	0,03435049	0,9999972	Gpr27
ENSMUSG00000027863	-8,084585575	-3,015173821	0,028906	0,9999972	Cd2
ENSMUSG00000083495	-8,965380338	-3,164364788	0,03498103	0,9999972	Gm13877
ENSMUSG00000107966	-8,384128893	-3,067660896	0,0363146	0,9999972	Gm44001
ENSMUSG00000105048	-6,447952053	-2,688841016	0,01158717	0,9999972	Gm42966
ENSMUSG00000033174	-9,91698374	-3,30990139	0,04688179	0,9999972	Mgll
ENSMUSG00000104632	-7,292875078	-2,866487682	0,0296526	0,9999972	Gm42909
ENSMUSG00000030093	-7,664198803	-2,938134984	0,03221605	0,9999972	Wnt7a
ENSMUSG00000032946	-7,432520179	-2,893851475	0,0356621	0,9999972	Rasgrp2
ENSMUSG00000043458	-7,802767171	-2,963985852	0,04061454	0,9999972	Pcdhb12
ENSMUSG00000048349	-6,551631241	-2,711854157	0,0271116	0,9999972	Pou4f1
ENSMUSG00000026327	-7,611835182	-2,928244324	0,0386552	0,9999972	Serpinb11
ENSMUSG00000031129	-5,737313641	-2,520375388	0,02009555	0,9999972	Slc9a9
ENSMUSG00000047793	-6,796479784	-2,7647877	0,04413405	0,9999972	Sned1

ENSMUSG00000017417	-6,035017602	-2,593357979	0,03042788	0,9999972	Plxdc1
ENSMUSG00000102549	-7,162809018	-2,840525476	0,0489415	0,9999972	Gm38137
ENSMUSG00000066705	-5,842104152	-2,546488078	0,03053822	0,9999972	Fxyd6
ENSMUSG00000090637	-6,271545099	-2,648820919	0,04079051	0,9999972	Gm6189
ENSMUSG00000096870	-6,14789905	-2,620093476	0,04236731	0,9999972	Gm21816
ENSMUSG00000037989	-5,124610494	-2,357442354	0,00829363	0,9999972	Wnk2
ENSMUSG00000084985	-5,690771063	-2,508624142	0,03320672	0,9999972	Gm16135
ENSMUSG00000110986	-5,304691854	-2,407268948	0,01889295	0,9999972	AC153970.1
ENSMUSG00000024935	-5,899777091	-2,560660447	0,03978312	0,9999972	Slc1a1
ENSMUSG00000107835	-5,656446963	-2,499896124	0,03352114	0,9999972	Gm43999
ENSMUSG00000077309	-5,504841827	-2,460701111	0,03285932	0,9999972	n-R5s8
ENSMUSG00000107173	-5,336576445	-2,415914512	0,02512979	0,9999972	Gm43266
ENSMUSG00000106603	-6,018059967	-2,589298482	0,04829386	0,9999972	Gm43509
ENSMUSG00000027544	-5,775852035	-2,530033784	0,04375665	0,9999972	Nfatc2
ENSMUSG00000033981	-5,095124721	-2,349117462	0,02216538	0,9999972	Gria2
ENSMUSG00000034227	-5,504004665	-2,460481693	0,04072266	0,9999972	Foxj1
ENSMUSG00000037358	-5,462806058	-2,449642205	0,03886163	0,9999972	4930578C19Rik
ENSMUSG00000045287	-5,250488652	-2,392451698	0,03405825	0,9999972	Rtn4rl1
ENSMUSG00000047394	-4,851712933	-2,278494191	0,02541381	0,9999972	Odf3b
ENSMUSG00000104990	-4,506680313	-2,172065114	0,0057253	0,9999972	Gm43504
ENSMUSG00000032289	-4,713167018	-2,236696806	0,0282514	0,9999972	Thsd4
ENSMUSG00000111131	-4,522940285	-2,177260949	0,0179054	0,9999972	AC115297.1
ENSMUSG00000111197	-4,747242535	-2,247089758	0,03312972	0,9999972	AC055818.1
ENSMUSG00000103805	-4,518114277	-2,175720761	0,0205507	0,9999972	Gm37063
ENSMUSG00000044556	-4,375708628	-2,129516675	0,01404438	0,9999972	Tex38
ENSMUSG00000030317	-4,617896335	-2,207235787	0,03390661	0,9999972	Timp4
ENSMUSG00000034413	-4,295315673	-2,102764162	0,02468775	0,9999972	Neurl1b
ENSMUSG00000089281	-4,196723189	-2,069263308	0,02107059	0,9999972	Scarna6
ENSMUSG00000105553	-4,644079076	-2,215392538	0,04966363	0,9999972	Gm42514
ENSMUSG00000036411	-4,110433649	-2,039290606	0,01652844	0,9999972	9530077C05Rik
ENSMUSG00000091587	-4,086703979	-2,030937745	0,02134835	0,9999972	Gm17191
ENSMUSG00000031028	-4,116209998	-2,041316587	0,03379756	0,9999972	Tub
ENSMUSG00000034872	-4,144972157	-2,051362411	0,04859515	0,9999972	Gipc3
ENSMUSG00000029167	-3,648582627	-1,867336126	0,01305773	0,9999972	Ppargc1a
ENSMUSG00000105217	-3,917080325	-1,969778713	0,04744034	0,9999972	Gm42873
ENSMUSG00000084644	-3,812566681	-1,93076257	0,04416445	0,9999972	Gm24379
ENSMUSG00000105041	-3,799080609	-1,925650323	0,04353359	0,9999972	Gm42676
ENSMUSG00000108291	-3,503776056	-1,808910568	0,02970005	0,9999972	Gm44292
ENSMUSG00000068601	-3,547806076	-1,826927154	0,03449719	0,9999972	Gm10244
ENSMUSG00000049690	-3,224910335	-1,689259048	0,01780558	0,9999972	Nckap5
ENSMUSG00000032186	-3,286234816	-1,716435571	0,02831358	0,9999972	Tmod2
ENSMUSG00000018740	-3,335154852	-1,737753748	0,03847816	0,9999972	Slc25a35
ENSMUSG00000104436	-3,313242888	-1,728243969	0,03706176	0,9999972	Gm37423

ENSMUSG00000040254	-3,301915474	-1,723303189	0,04106283	0,9999972	Sema3d
ENSMUSG00000037736	-3,228068819	-1,690671336	0,04345391	0,9999972	Limch1
ENSMUSG00000077202	-3,249576241	-1,700251596	0,04724927	0,9999972	Gm25612
ENSMUSG00000039115	-3,200922232	-1,678487626	0,04453706	0,9999972	Itga9
ENSMUSG00000020193	-2,954188522	-1,562761895	0,02408444	0,9999972	Zpbp
ENSMUSG00000006784	-2,754787482	-1,461941026	0,04226665	0,9999972	Ttc25
ENSMUSG00000021187	-2,558015954	-1,355025262	0,024658	0,9999972	Tc2n
ENSMUSG00000097440	-2,514888683	-1,330494543	0,04342494	0,9999972	Gm6277
ENSMUSG00000105408	-2,480328295	-1,310531088	0,0449923	0,9999972	Gm7285

Table 6-Upregulated genes LA-Tg vs WT ECs

ID	FC	Log2FC	P.Value	adj.P.Val	MGI_symbol
ENSMUSG00000086976	6,394999465	2,676944238	0,005743	0,999998047	Gm12316
ENSMUSG00000070732	6,373148536	2,672006285	0,006693	0,999998047	Rbm44
ENSMUSG00000044976	7,664427319	2,938177999	0,022768	0,999998047	Wdr72
ENSMUSG00000106702	7,608934342	2,927694413	0,025179	0,999998047	Gm42846
ENSMUSG00000036353	6,539837398	2,709254766	0,023767	0,999998047	P2ry12
ENSMUSG00000076928	6,358447368	2,668674525	0,028017	0,999998047	Trac
ENSMUSG00000096960	5,469154677	2,451317865	0,01568	0,999998047	A230028O05Rik
ENSMUSG00000030187	5,546990503	2,471705255	0,01923	0,999998047	Klra2
ENSMUSG00000078139	5,075721621	2,343612946	0,038051	0,999998047	AK157302
ENSMUSG00000055653	4,752322378	2,248632706	0,031761	0,999998047	Gpc3
ENSMUSG00000017868	5,548677128	2,472143857	0,048053	0,999998047	Sgk2
ENSMUSG00000043773	5,282380716	2,401188284	0,044661	0,999998047	1700048O20Rik
ENSMUSG00000044550	4,762001114	2,251567958	0,03637	0,999998047	Tceal3
ENSMUSG00000094344	4,625999069	2,209764976	0,026017	0,999998047	Gm11942
ENSMUSG00000108126	4,848514969	2,277542938	0,046497	0,999998047	Gm43909
ENSMUSG00000097626	4,672201846	2,224102602	0,040404	0,999998047	4921504A21Rik
ENSMUSG00000073486	4,504033592	2,171217587	0,033653	0,999998047	Gm10518
ENSMUSG00000002076	4,158524517	2,056071738	0,013994	0,999998047	Hsf2bp
ENSMUSG00000064109	4,444535006	2,15203249	0,04136	0,999998047	Hcst
ENSMUSG00000024905	3,945151674	1,980080767	0,045822	0,999998047	Mtl5
ENSMUSG00000093798	3,582647014	1,841025907	0,039351	0,999998047	Gm8355
ENSMUSG00000082901	3,516876402	1,814294633	0,046713	0,999998047	Gm14323
ENSMUSG00000052572	3,306900851	1,725479791	0,022228	0,999998047	Dlg2
ENSMUSG00000084304	3,364246396	1,750283372	0,042254	0,999998047	Gm6142
ENSMUSG00000083064	3,311877962	1,727649512	0,039179	0,999998047	Gm7785

Table 7-Downregulated genes LA-Tg vs WT ECs

ID	FC	logFC	P.Value	adj.P.Val	MGI_symbol
ENSMUSG00000113288	-10,4719102	-3,388452723	0,000800156	0,999998047	AC164164.1
ENSMUSG00000021763	-11,2334498	-3,489729142	0,009344815	0,999998047	BC067074
ENSMUSG00000109317	-8,70749394	-3,122257564	0,006975968	0,999998047	Gm45041

ENSMUSG00000067356	-9,51570979	-3,250311274	0,011442297	0,999998047	B430203G13Rik
ENSMUSG00000102989	-7,77199366	-2,958284725	0,007640371	0,999998047	Gm38318
ENSMUSG00000049202	-8,45964832	-3,080597689	0,010829579	0,999998047	4930515G13Rik
ENSMUSG00000042589	-7,53794563	-2,91417139	0,013504011	0,999998047	Cux2
ENSMUSG00000097178	-7,34417405	-2,876600249	0,013038891	0,999998047	2310002F09Rik
ENSMUSG00000054256	-7,2695859	-2,861873186	0,01429315	0,999998047	Msi1
ENSMUSG00000104060	-7,63378356	-2,932398283	0,017835661	0,999998047	Gm37954
ENSMUSG00000099230	-6,46292067	-2,692186284	0,010065201	0,999998047	Mir6989
ENSMUSG00000105217	-6,33202011	-2,662665838	0,015373447	0,999998047	Gm42873
ENSMUSG00000084701	-6,6616257	-2,735874295	0,024938559	0,999998047	n-R5s87
ENSMUSG00000104910	-9,39838959	-3,232413573	0,035754334	0,999998047	Gm43331
ENSMUSG00000024186	-6,6847799	-2,740880059	0,026608705	0,999998047	Rgs11
ENSMUSG00000085925	-8,64110283	-3,111215449	0,035982338	0,999998047	Rtl1
ENSMUSG00000103146	-6,10113914	-2,609078631	0,017565095	0,999998047	Gm37745
ENSMUSG00000102383	-6,65324191	-2,73405749	0,029111859	0,999998047	Gm38142
ENSMUSG00000064796	-5,80961404	-2,538442322	0,020192773	0,999998047	Terc
ENSMUSG00000083340	-6,01178711	-2,58779392	0,023345577	0,999998047	Gm13156
ENSMUSG00000098199	-5,65930147	-2,500623991	0,018633394	0,999998047	Gm9358
ENSMUSG00000102782	-5,69596146	-2,509939384	0,020468196	0,999998047	Gm37625
ENSMUSG00000021974	-6,63177573	-2,729395218	0,035643629	0,999998047	Fgf9
ENSMUSG00000113065	-6,36186725	-2,669450267	0,032210119	0,999998047	AC131743.1
ENSMUSG00000086701	-5,13712582	-2,360961409	0,017439218	0,999998047	Gm13595
ENSMUSG00000107966	-7,79877595	-2,963247705	0,048367049	0,999998047	Gm44001
ENSMUSG00000112637	-6,18840283	-2,629567112	0,038670906	0,999998047	AC124346.3
ENSMUSG00000045912	-4,76033418	-2,251062854	0,014980108	0,999998047	C2cd4c
ENSMUSG00000104400	-6,52720555	-2,706465472	0,045772241	0,999998047	Gm38010
ENSMUSG00000105842	-5,16302855	-2,368217575	0,028122999	0,999998047	Gm43329
ENSMUSG00000101059	-6,38074471	-2,673724814	0,044900544	0,999998047	Gm4017
ENSMUSG00000046854	-5,7930064	-2,534312259	0,039950661	0,999998047	Pip5kl1
ENSMUSG00000089789	-4,93517978	-2,303102642	0,026131314	0,999998047	Rdh1
ENSMUSG00000039238	-5,6579169	-2,500270988	0,040014748	0,999998047	Zfp750
ENSMUSG00000106432	-6,2266466	-2,6384554	0,046420755	0,999998047	Gm43259
ENSMUSG00000102380	-5,01636188	-2,326641427	0,040268243	0,999998047	Gm38140
ENSMUSG00000104479	-5,33315843	-2,414990185	0,044108768	0,999998047	Gm10305
ENSMUSG00000044122	-4,7325407	-2,242614912	0,031704032	0,999998047	Proca1
ENSMUSG00000040140	-4,55521124	-2,187517959	0,020201939	0,999998047	Tdrd6
ENSMUSG00000097399	-4,73590915	-2,243641405	0,035108106	0,999998047	Gm26555
ENSMUSG00000109435	-4,72248741	-2,239546949	0,035347526	0,999998047	Gm7067
ENSMUSG00000037541	-4,72356329	-2,239875589	0,035971427	0,999998047	Shank2
ENSMUSG00000104821	-4,99609815	-2,320801821	0,049090122	0,999998047	Gm42481
ENSMUSG00000043794	-4,51259701	-2,173957946	0,03089445	0,999998047	D830025C05Rik
ENSMUSG00000110558	-4,42887749	-2,14694109	0,02730924	0,999998047	Gm45779
ENSMUSG00000113557	-4,70135816	-2,233077591	0,042898959	0,999998047	AC153143.2

ENSMUSG00000044574	-4,37486707	-2,129239182	0,03257854	0,999998047	5031434C07Rik
ENSMUSG00000053693	-4,45704075	-2,15608615	0,042669888	0,999998047	Mast1
ENSMUSG00000104571	-4,15348714	-2,054323088	0,024850807	0,999998047	Gm43010
ENSMUSG00000102533	-4,20888545	-2,073438244	0,034670119	0,999998047	Gm37226
ENSMUSG00000109008	-4,27914068	-2,097321111	0,040843183	0,999998047	Gm44899
ENSMUSG00000103818	-4,12470627	-2,044291384	0,029675818	0,999998047	Gm38009
ENSMUSG00000104292	-3,93575492	-1,976640385	0,016929041	0,999998047	Gm38042
ENSMUSG00000087790	-4,08865371	-2,031625878	0,030238292	0,999998047	Gm25970
ENSMUSG00000024027	-4,1823046	-2,064298139	0,042058566	0,999998047	Glp1r
ENSMUSG00000106468	-4,10839603	-2,038575259	0,0414138	0,999998047	AC122844.1
ENSMUSG00000100394	-3,83740817	-1,940132229	0,028513269	0,999998047	Gm28791
ENSMUSG00000108693	-3,81267003	-1,930801676	0,040885063	0,999998047	Gm45153
ENSMUSG00000074824	-3,5503597	-1,827965196	0,017530012	0,999998047	Rslcan18
ENSMUSG00000003271	-3,39079025	-1,761621542	0,031452021	0,999998047	Sult2b1
ENSMUSG00000104293	-3,5004496	-1,807540234	0,046139265	0,999998047	Gm38043
ENSMUSG00000030693	-2,84913164	-1,510522279	0,024928472	0,999998047	Klk10
ENSMUSG00000010342	-2,86746596	-1,51977636	0,049589444	0,999998047	Tex14

Table 8-Upregulated miRNAs Prog-Tg vs WT ECs

ID	FC	logFC	P.Value	adj.P.Val
mmu-miR-124-3p	5,739758082	2,520989932	0,003661838	0,428187056
mmu-miR-692	6,296966737	2,654657046	0,005676254	0,428187056
mmu-miR-669a-3-3p	5,062498711	2,339849636	0,002966651	0,428187056
mmu-miR-133a-3p	5,070892996	2,342239832	0,007652383	0,428187056
mmu-miR-7224-3p	4,952840033	2,308256025	0,006056889	0,428187056
mmu-miR-206-3p	6,711503196	2,746635927	0,018250929	0,526960334
mmu-miR-6950-3p	3,94278709	1,979215807	0,002814865	0,428187056
mmu-miR-409-5p	4,490055414	2,16673325	0,008583334	0,428187056
mmu-miR-185-3p	4,171439119	2,06054519	0,008920564	0,428187056
mmu-miR-6921-3p	3,713754802	1,892878565	0,004401645	0,428187056
mmu-miR-184-3p	3,963316815	1,986708297	0,011877024	0,526960334
mmu-miR-873a-5p	4,703647471	2,233779937	0,018963909	0,526960334
mmu-miR-465c-5p	5,542644046	2,470574359	0,026696728	0,526960334
mmu-miR-193b-5p	4,155563895	2,055044259	0,017195977	0,526960334
mmu-miR-470-5p	4,930418128	2,301710001	0,025531813	0,526960334
mmu-miR-6399	3,588535648	1,843395252	0,008082891	0,428187056
mmu-miR-6539	3,602879382	1,849150354	0,015090942	0,526960334
mmu-miR-485-5p	3,586801292	1,842697822	0,0165788	0,526960334
mmu-miR-6240	3,724181004	1,896923193	0,020163641	0,526960334
mmu-miR-543-3p	4,101101235	2,036011357	0,02799338	0,526960334
mmu-miR-127-5p	4,083861058	2,029933783	0,032555035	0,526960334
mmu-miR-487b-3p	3,655327086	1,870000507	0,033648008	0,526960334
mmu-miR-1931	3,140044255	1,650784892	0,021765086	0,526960334

mmu-miR-493-5p	3,726141507	1,897682464	0,037097836	0,526960334
mmu-miR-7035-3p	3,94564626	1,980261619	0,03973994	0,526960334
mmu-miR-147-3p	3,03142312	1,599995235	0,02391806	0,526960334
mmu-miR-31-5p	2,496809598	1,320085808	0,008495764	0,428187056
mmu-miR-329-5p	3,596611771	1,846638439	0,04061823	0,526960334
mmu-miR-7033-5p	3,19724504	1,676829318	0,03927645	0,526960334
mmu-miR-7213-3p	2,750906681	1,4599072	0,031292442	0,526960334
mmu-miR-3058-3p	2,797708122	1,484245458	0,039088831	0,526960334
mmu-miR-147-5p	2,420611501	1,275371551	0,036925291	0,526960334
mmu-miR-7090-5p	2,534594162	1,341754762	0,044112499	0,546425794
mmu-miR-466f-5p	2,431892372	1,282079381	0,039125579	0,526960334
mmu-miR-125b-1-3p	2,220160118	1,150663728	0,018892473	0,526960334
mmu-miR-7048-3p	2,389184646	1,256518355	0,040459115	0,526960334
mmu-miR-653-5p	2,29950412	1,201322782	0,036827511	0,526960334
mmu-miR-34b-5p	2,207239693	1,142243306	0,030592981	0,526960334
mmu-miR-34c-5p	2,154711603	1,107494785	0,022161099	0,526960334
mmu-miR-34a-5p	1,899154076	0,925356954	0,049643492	0,55934863
mmu-miR-1983	1,672786555	0,742253371	0,049896065	0,55934863

Table 9-Downregulated miRNAs Prog-Tg vs WT ECs

ID	FC	logFC	P.Value	adj.P.Val
mmu-miR-190a-3p	-14,91374776	-3,898570941	0,000491833	0,377728027
mmu-miR-6971-3p	-4,76661778	-2,252965945	0,004032167	0,428187056
mmu-miR-150-5p	-4,92853695	-2,301159442	0,00835692	0,428187056
mmu-miR-24-2-5p	-4,326860365	-2,113320563	0,008272327	0,428187056
mmu-miR-6902-5p	-5,706859477	-2,512697039	0,020560018	0,526960334
mmu-miR-190a-5p	-6,651040791	-2,733580119	0,03446878	0,526960334
mmu-miR-7054-5p	-3,523460147	-1,816992896	0,013773553	0,526960334
mmu-miR-129-1-3p	-4,906485759	-2,294690073	0,035050002	0,526960334
mmu-miR-150-3p	-6,966238557	-2,800379878	0,041854922	0,526960334
mmu-miR-212-5p	-2,963635523	-1,567368031	0,008830653	0,428187056
mmu-miR-3064-3p	-3,000194588	-1,585056075	0,019066035	0,526960334
mmu-miR-6900-3p	-2,782050361	-1,476148536	0,029216318	0,526960334
mmu-miR-3084-5p	-3,026270647	-1,597541017	0,036975439	0,526960334
mmu-miR-132-3p	-2,945915202	-1,558715903	0,039502851	0,526960334
mmu-miR-148a-3p	-2,605965739	-1,381818117	0,035424092	0,526960334
mmu-miR-132-5p	-2,423863205	-1,27730828	0,022011747	0,526960334
mmu-miR-30c-5p	-2,787628797	-1,479038464	0,041626863	0,526960334
mmu-miR-138-1-3p	-2,283139733	-1,191019158	0,017567187	0,526960334
mmu-miR-182-5p	-2,42069683	-1,275422406	0,036866287	0,526960334
mmu-miR-7030-3p	-2,410188242	-1,269145829	0,048642925	0,55934863
mmu-miR-181c-3p	-2,27345902	-1,184888999	0,03821883	0,526960334
mmu-miR-7235-3p	-2,254884091	-1,173053276	0,03871593	0,526960334

mmu-miR-26a-1-3p	-2,258099373	-1,175108977	0,044862458	0,546894721
mmu-miR-192-5p	-2,087645371	-1,061876662	0,031576391	0,526960334
mmu-miR-582-3p	-2,062863285	-1,044648211	0,037802013	0,526960334
mmu-miR-194-5p	-2,046367285	-1,033065105	0,047362727	0,55934863
mmu-miR-10a-3p	-1,663114581	-0,733887567	0,04616086	0,553930314

Table 10-Upregulated miRNAs LA-Tg vs WT ECs

ID	FC	logFC	P.Value	adj.P.Val
mmu-miR-7224-3p	12,26398771	3,616356251	0,002981259	0,989345488
mmu-miR-6981-5p	6,4945274	2,699224546	0,015038779	0,989345488
mmu-miR-466q	5,245745448	2,391147802	0,019771629	0,989345488
mmu-miR-692	5,731846636	2,519000009	0,048689305	0,989345488
mmu-miR-5132-5p	4,01807436	2,006504263	0,046601548	0,989345488
mmu-miR-7048-3p	3,487102413	1,802028735	0,039903088	0,989345488

Table 11-Downregulated miRNAs LA-Tg vs WT ECs

ID	FC	logFC	P.Value	adj.P.Val
mmu-miR-466k	-4,700339213	-2,232764877	0,031647838	0,989345488
mmu-miR-181c-5p	-2,166476975	-1,115350904	0,049684018	0,989345488

Table 12-Upregulated miRNAs Prog-Tg vs WT plasma

ID	FC	logFC	P.Value	adj.P.Val
mmu-miR-148b-3p	1484,035262	10,53530966	7,93E-09	3,20E-06
mmu-miR-151-5p	497,3459304	8,958105861	0,000187896	0,015182008
mmu-miR-652-3p	358,6348832	8,486372011	0,000439898	0,025388391
mmu-miR-28a-5p	367,5588232	8,521831344	0,000633364	0,028430995
mmu-miR-484	183,4112697	7,518938478	0,000950824	0,03841327
mmu-miR-3535	173,658624	7,440110247	0,003308918	0,121527542
mmu-miR-30e-3p	69,45289828	6,117962994	0,010769965	0,241725878
mmu-miR-30f	69,45289828	6,117962994	0,010738212	0,241725878
mmu-miR-34a-5p	50,77641907	5,66608675	0,015671773	0,293390812
mmu-miR-298-5p	14,79237556	3,886781854	0,043255122	0,379438803
mmu-miR-532-5p	12,06012435	3,592172878	0,041396915	0,379438803
mmu-miR-31-5p	12,28706954	3,619068969	0,047592109	0,379438803
mmu-miR-26b-5p	2,450916082	1,293321088	0,044028573	0,379438803

Table 13-Downregulated miRNAs Prog-Tg vs WT plasma

ID	FC	logFC	P.Value	adj.P.Val
mmu-miR-451a	-689,036193	-9,428435955	0,000126445	0,013034082
mmu-miR-152-3p	-505,644059	-8,981978367	0,000239527	0,016128158
mmu-miR-24-1-5p	-264,5037937	-8,047144604	0,00012905	0,013034082
mmu-miR-3074-1-3p	-264,5037937	-8,047144604	0,00012905	0,013034082

mmu-miR-181a-2-3p	-282,7503773	-8,143385139	0,000520047	0,026262381
mmu-miR-574-3p	-224,894219	-7,813102766	0,005630893	0,174990826
mmu-miR-421-3p	-157,7046912	-7,301081766	0,005290754	0,174990826
mmu-miR-30a-3p	-78,5808883	-6,296106571	0,007481046	0,201489514
mmu-miR-181a-5p	-32,48086913	-5,021518332	0,009087894	0,229469324
mmu-miR-140-3p	-87,17383759	-6,445823316	0,015985553	0,293390812
mmu-let-7d-5p	-23,12181284	-4,53118261	0,006166306	0,177941971
mmu-miR-7663-3p	-21,92279292	-4,454359701	0,015095143	0,293390812
mmu-miR-379-5p	-22,73634991	-4,506928758	0,019801402	0,333323597
mmu-miR-23a-3p	-28,72347704	-4,844158496	0,035783003	0,379438803
mmu-miR-361-5p	-18,3249574	-4,19573794	0,021138006	0,341590184
mmu-miR-7043-3p	-18,08703925	-4,176884361	0,016702942	0,293390812
mmu-miR-423-3p	-16,11545069	-4,010372631	0,014469017	0,293390812
mmu-miR-299b-5p	-18,2802744	-4,192215822	0,033827758	0,379438803
mmu-miR-299a-3p	-18,2802744	-4,192215822	0,033827758	0,379438803
mmu-miR-221-3p	-29,747387	-4,894691043	0,049764897	0,379438803
mmu-miR-490-3p	-15,56360623	-3,96010448	0,028750598	0,379438803
mmu-miR-429-3p	-15,00643969	-3,90750983	0,0257994	0,379438803
mmu-miR-1843a-5p	-18,24550891	-4,189469487	0,040949154	0,379438803
mmu-miR-673-3p	-13,14026787	-3,71592278	0,030954477	0,379438803
mmu-miR-136-3p	-14,61807855	-3,869681786	0,037566458	0,379438803
mmu-miR-3071-5p	-14,61807855	-3,869681786	0,037566458	0,379438803
mmu-miR-15b-5p	-13,42797609	-3,747169968	0,03640011	0,379438803
mmu-miR-135a-1-3p	-11,68189491	-3,546202406	0,032517712	0,379438803
mmu-miR-322-3p	-15,17596495	-3,923716347	0,048939191	0,379438803
mmu-miR-6538	-12,50650446	-3,644606711	0,048455756	0,379438803
mmu-miR-676-5p	-11,59811247	-3,535818129	0,047337623	0,379438803
mmu-miR-1843b-3p	-11,24383886	-3,491062778	0,042143593	0,379438803
mmu-miR-3065-5p	-10,16867568	-3,346059896	0,037897633	0,379438803
mmu-miR-338-3p	-10,16867568	-3,346059896	0,037897633	0,379438803
mmu-miR-486b-5p	-1,904406323	-0,929341324	0,038564782	0,379438803
mmu-miR-486a-5p	-1,904207304	-0,929190548	0,038550857	0,379438803
mmu-miR-486b-3p	-1,904207304	-0,929190548	0,038550857	0,379438803
mmu-miR-486a-3p	-1,904406323	-0,929341324	0,038564782	0,379438803

Table 14-Upregulated miRNAs LA-Tg vs WT plasma

ID	FC	logFC	P.Value	adj.P.Val
mmu-miR-106b-3p	1009,765773	9,979804967	9,59E-05	0,038738309
mmu-miR-150-5p	411,1384323	8,683480428	0,001759455	0,177704959
mmu-miR-127-3p	249,7429286	7,964300019	0,009519033	0,480711173
mmu-miR-148b-3p	120,5992828	6,914077518	0,007213504	0,480711173
mmu-miR-484	132,9105859	7,054312205	0,01770174	0,758826521
mmu-miR-195a-5p	109,6191566	6,776356129	0,024029833	0,758826521

mmu-miR-541-5p	93,11337324	6,540916482	0,023463614	0,758826521
mmu-miR-144-5p	86,11130617	6,428130767	0,009415615	0,480711173
mmu-miR-181c-5p	130,9459904	7,032828074	0,036507335	0,807942134
mmu-miR-409-3p	89,11647857	6,477620321	0,028174252	0,758826521
mmu-miR-151-5p	94,5632358	6,563207498	0,047455198	0,807942134
mmu-miR-1941-5p	69,68247888	6,122724042	0,0479357	0,807942134
mmu-let-7f-2-3p	22,21406304	4,473401386	0,046545983	0,807942134
mmu-miR-320-3p	3,715672319	1,893623278	0,033380766	0,807942134
mmu-miR-30c-5p	3,052151013	1,609826345	0,047996562	0,807942134
mmu-miR-26a-5p	1,718444027	0,781102861	0,041447609	0,807942134

Table 15-Downregulated miRNAs Prog-Tg vs WT plasma

ID	FC	logFC	P.Value	adj.P.Val
mmu-miR-24-1-5p	-153,4005966	-7,261160283	0,001288428	0,173508242
mmu-miR-3074-1-3p	-153,4005966	-7,261160283	0,001288428	0,173508242
mmu-miR-92b-3p	-132,4267775	-7,049051063	0,005321801	0,430001493
mmu-miR-328-3p	-90,59528136	-6,501364005	0,021630218	0,758826521
mmu-miR-23b-3p	-90,33854128	-6,497269713	0,034718413	0,807942134
mmu-miR-181a-2-3p	-56,43350028	-5,81847993	0,027159055	0,758826521
mmu-miR-15a-5p	-46,86121322	-5,5503224	0,027973108	0,758826521
mmu-miR-375-3p	-43,86442992	-5,454979614	0,044706174	0,807942134

9. Bibliography

[1] B. J. North and D. A. Sinclair, “The intersection between aging and cardiovascular disease,” *Circulation Research*. 2012, doi: 10.1161/CIRCRESAHA.111.246876.

[2] A. Milutinović, D. Šuput, and R. Zorc-Milutinović A, Šuput D, Zorc-Pleskovič R. 2020. Pathogenesis of atherosclerosis in the tunica intima, media, and adventitia of coronary arteries: An updated review. Bosnian Journal of Basic Medical Sciences. 20(1):21–30.doi:10.17305/bjbms.2019.4320.P, “Pathogenesis of atherosclerosis in the tunica intima, media, and adventitia of coronary arteries: An updatedMilutinović A, Šuput D, Zorc-Milutinović A, Šuput D, Zorc-Pleskovič R. 2020. Pathogenesis of atherosclerosis in the tunica intima, media, and adven,” *Bosn. J. Basic Med. Sci.*, vol. 20, no. 1, pp. 21–30, 2020.

[3] J. E. Deanfield, J. P. Halcox, and T. J. Rabelink, “Endothelial function and dysfunction: Testing and clinical relevance,” *Circulation*, vol. 115, no. 10, pp. 1285–1295, 2007, doi: 10.1161/CIRCULATIONAHA.106.652859.

[4] H. Matsushita, E. Chang, A. J. Glassford, J. P. Cooke, C. P. Chiu, and P. S. Tsao, “eNOS activity is reduced in senescent human endothelial cells: Preservation by hTERT immortalization,” *Circ. Res.*, vol. 89, no. 9, pp. 793–798, 2001, doi: 10.1161/hh2101.098443.

[5] C. Collins and E. Tzima, “Hemodynamic forces in endothelial dysfunction and vascular aging,” *Exp. Gerontol.*, vol. 46, no. 2–3, pp. 185–188, 2011, doi: 10.1016/j.exger.2010.09.010.

[6] J. C. Kohn, M. C. Lampi, and C. A. Reinhart-King, “Age-related vascular stiffening: Causes and consequences,” *Frontiers in Genetics*, vol. 6, no. MAR. 2015, doi: 10.3389/fgene.2015.00112.

[7] D. J. Baker *et al.*, “Clearance of p16 Ink4a-positive senescent cells delays ageing-associated disorders,” *Nature*, 2011, doi: 10.1038/nature10600.

[8] M. J. Yousefzadeh *et al.*, “Tissue specificity of senescent cell accumulation during physiologic and accelerated aging of mice,” *Aging Cell*, 2020, doi: 10.1111/acel.13094.

[9] A. B. Gevaert *et al.*, “Endothelial Senescence Contributes to Heart Failure with Preserved Ejection Fraction in an Aging Mouse Model,” *Circ. Hear. Fail.*, vol. 10, no. 6, 2017, doi: 10.1161/CIRCHEARTFAILURE.116.003806.

[10] J.-P. Coppé, P.-Y. Desprez, A. Krtolica, and J. Campisi, “The Senescence-Associated Secretory Phenotype: The Dark Side of Tumor Suppression,” *Annu. Rev. Pathol. Mech. Dis.*, 2010, doi: 10.1146/annurev-pathol-121808-102144.

[11] C. D. Wiley and J. Campisi, “From Ancient Pathways to Aging Cells - Connecting Metabolism and Cellular Senescence,” *Cell Metabolism*. 2016, doi: 10.1016/j.cmet.2016.05.010.

[12] L. Terlecki-Zaniewicz *et al.*, “Small extracellular vesicles and their miRNA cargo are anti-apoptotic members of the senescence-associated secretory phenotype,” *Aging (Albany. NY).*, vol. 10, no. 5, pp. 1103–1132, 2018, doi: 10.18632/aging.101452.

[13] A. E. Pasquinelli, “Non-coding RNA: MicroRNAs and their targets: recognition, regulation and an emerging reciprocal relationship,” *Nat. Publ. Gr.*, 2012, doi: 10.1038/nrg3162.

[14] K. Lafferty-Whyte, C. J. Cairney, N. B. Jamieson, K. A. Oien, and W. N. Keith, “Pathway analysis of senescence-associated miRNA targets reveals common processes to different senescence induction mechanisms,” *Biochim. Biophys. Acta - Mol. Basis Dis.*, vol. 1792, no. 4, pp. 341–352, 2009, doi: 10.1016/j.bbadis.2009.02.003.

[15] A. P. Ugalde, Y. Español, and C. López-Otín, “Micromanaging aging with miRNAs: New messages from the nuclear envelope,” *Nucleus*, vol. 2, no. 6, pp. 549–555, 2011, doi: 10.4161/nucl.2.6.17986.

[16] J. O’Brien, H. Hayder, Y. Zayed, and C. Peng, “Overview of microRNA biogenesis, mechanisms of actions, and circulation,” *Front. Endocrinol. (Lausanne).*, vol. 9, no. AUG, pp. 1–12, 2018, doi: 10.3389/fendo.2018.00402.

[17] M. Tkach and C. Théry, “Communication by Extracellular Vesicles: Where We Are and Where We Need to Go,” *Cell*, vol. 164, no. 6, pp. 1226–1232, 2016, doi: 10.1016/j.cell.2016.01.043.

[18] F. Teng and M. Fussenegger, “Shedding Light on Extracellular Vesicle Biogenesis and Bioengineering,” *Adv. Sci.*, vol. 8, no. 1, pp. 1–17, 2021, doi: 10.1002/advs.202003505.

[19] E. Mensà *et al.*, “Small extracellular vesicles deliver miR-21 and miR-217 as pro-senescence effectors to endothelial cells,” *J. Extracell. Vesicles*, vol. 9, no. 1, 2020, doi: 10.1080/20013078.2020.1725285.

[20] B. G. and R. R. Carracedo Julia *, Alique Matilde, Ramírez-Carracedo Rafael, “Endothelial Extracellular Vesicles Produced by Senescent Cells: Pathophysiological Role in the Cardiovascular Disease Associated with all Types of Diabetes Mellitus,” *Curr. Vasc. Pharmacol.*, 2019.

[21] F. L. DeBusk, “The Hutchinson-Gilford progeria syndrome. Report of 4 cases and review of the literature,” *J. Pediatr.*, vol. 80, no. 4 PART 2, pp. 697–724, 1972, doi: 10.1016/S0022-3476(72)80229-4.

[22] L. B. Gordon, W. T. Brown, and F. S. Collins, *Hutchinson-Gilford Progeria Syndrome*. 1993.

[23] L. B. Gordon, K. Cao, and F. S. Collins, “Progeria: Translational insights from cell biology,” *J. Cell Biol.*, vol. 199, no. 1, pp. 9–13, 2012, doi: 10.1083/jcb.201207072.

[24] M. Olive *et al.*, “Cardiovascular pathology in Hutchinson-Gilford progeria: Correlation with the vascular pathology of aging,” *Arterioscler. Thromb. Vasc. Biol.*, vol. 30, no. 11, pp. 2301–2309, 2010, doi: 10.1161/ATVBAHA.110.209460.

[25] A. Prakash *et al.*, “Cardiac Abnormalities in Patients With Hutchinson-Gilford Progeria Syndrome,” 2018, doi: 10.1001/jamacardio.2017.5235.

[26] M. R. Hamczyk *et al.*, “Vascular smooth muscle–specific progerin expression accelerates atherosclerosis and death in a mouse model of Hutchinson-Gilford progeria syndrome,” *Circulation*, 2018, doi:

10.1161/CIRCULATIONAHA.117.030856.

[27] W. E. Stehbens, B. Delahunt, T. Shozawa, and E. Gilbert-Barness, “Smooth muscle cell depletion and collagen types in progeric arteries,” *Cardiovasc. Pathol.*, vol. 10, no. 3, pp. 133–136, 2001, doi: 10.1016/S1054-8807(01)00069-2.

[28] A. Harvey, A. C. Montezano, R. A. Lopes, F. Rios, and R. M. Touyz, “Vascular Fibrosis in Aging and Hypertension: Molecular Mechanisms and Clinical Implications,” *Can. J. Cardiol.*, vol. 32, no. 5, pp. 659–668, 2016, doi: 10.1016/j.cjca.2016.02.070.

[29] P. Scaffidi, L. Gordon, and T. Misteli, “The cell nucleus and aging: Tantalizing clues and hopeful promises: Recent evidence links structural proteins in the cell nucleus with aging,” *PLoS Biol.*, vol. 3, no. 11, pp. 1855–1859, 2005, doi: 10.1371/journal.pbio.0030395.

[30] S. Osmanagic-Myers and R. Foisner, “The structural and gene expression hypotheses in laminopathic diseases - Not so different after all,” *Mol. Biol. Cell*, vol. 30, no. 15, pp. 1786–1790, 2019, doi: 10.1091/mbc.E18-10-0672.

[31] Y. Gruenbaum and R. Foisner, “Lamins: Nuclear intermediate filament proteins with fundamental functions in nuclear mechanics and genome regulation,” *Annu. Rev. Biochem.*, vol. 84, pp. 131–164, 2015, doi: 10.1146/annurev-biochem-060614-034115.

[32] A. De Sandre-Giovannoli *et al.*, “Lamin A truncation in Hutchinson-Gilford progeria,” *Science (80-.).*, vol. 300, no. 5628, p. 2055, 2003, doi: 10.1126/science.1084125.

[33] B. Dorado and V. Andrés, “A-type lamins and cardiovascular disease in premature aging syndromes,” *Curr. Opin. Cell Biol.*, vol. 46, no. 2, pp. 17–25, 2017, doi: 10.1016/j.ceb.2016.12.005.

[34] W. E. Stehbens, S. J. Wakefield, E. Gilbert-Barness, R. E. Olson, and J. Ackerman, “Histological and ultrastructural features of atherosclerosis in progeria,” *Cardiovasc. Pathol.*, vol. 8, no. 1, pp. 29–39, 1999, doi: 10.1016/S1054-8807(98)00023-4.

[35] F. G. Osorio *et al.*, “Hutchinson-Gilford progeria: Splicing-directed therapy in a new mouse model of human accelerated aging,” *Sci. Transl. Med.*, vol. 3, no. 106, pp. 1–12, 2011, doi: 10.1126/scitranslmed.3002847.

[36] R. Varga *et al.*, “Progressive vascular smooth muscle cell defects in a mouse model of Hutchinson-Gilford progeria syndrome,” *Proc. Natl. Acad. Sci. U. S. A.*, vol. 103, no. 9, pp. 3250–3255, 2006, doi: 10.1073/pnas.0600012103.

[37] E. Cells, G. Bidault, M. Garcia, J. Capeau, R. Morichon, and C. Vigouroux, “Progerin Expression Induces Inflammation ,” pp. 1–16.

[38] S. Osmanagic-Myers *et al.*, “Endothelial progerin expression causes cardiovascular pathology through an impaired mechanoresponse,” *J. Clin. Invest.*, 2019, doi: 10.1172/JCI121297.

[39] Z.-J. Chen *et al.*, “Dysregulated interactions between lamin A and SUN1 induce abnormalities in the nuclear envelope and endoplasmic reticulum in progeric laminopathies,” *J. Cell Sci.*, vol. 127, no. 8, pp. 1792–1804, 2014, doi: 10.1242/jcs.139683.

[40] C. M. Hale *et al.*, “Dysfunctional connections between the nucleus and the actin and microtubule networks in laminopathic models,” *Biophys. J.*, vol. 95, no. 11, pp. 5462–5475, 2008, doi: 10.1529/biophysj.108.139428.

[41] M. Zwerger *et al.*, “Myopathic lamin mutations impair nuclear stability in cells and tissue and disrupt nucleo-cytoskeletal coupling,” *Hum. Mol. Genet.*, vol. 22, no. 12, pp. 2335–2349, 2013, doi: 10.1093/hmg/ddt079.

[42] M. Gurusaran and O. R. Davies, “A molecular mechanism for LINC complex branching by structurally diverse SUN-KASH 6:6 assemblies,” *Elife*, vol. 10, pp. 1–25, 2021, doi: 10.7554/ELIFE.60175.

[43] C. Guilluy *et al.*, “Isolated nuclei adapt to force and reveal a mechanotransduction pathway in the nucleus,” *Nat. Cell Biol.*, vol. 16, no. 4, pp. 376–381, 2014, doi: 10.1038/ncb2927.

[44] F. Fang *et al.*, “Myocardin-related transcription factor a mediates OxLDL-induced endothelial injury,” *Circ. Res.*, vol. 108, no. 7, pp. 797–807, 2011, doi: 10.1161/CIRCRESAHA.111.240655.

[45] X. Weng *et al.*, “Endothelial MRTF-A mediates angiotensin II induced cardiac hypertrophy,” *J. Mol. Cell. Cardiol.*, vol. 80, pp. 23–33, 2015, doi: 10.1016/j.yjmcc.2014.11.009.

[46] E. N. Olson and A. Nordheim, “Linking actin dynamics and gene transcription to drive cellular motile functions,” *Nature Reviews Molecular Cell Biology*, vol. 11, no. 5. pp. 353–365, 2010, doi: 10.1038/nrm2890.

[47] L. L. Luchsinger, C. A. Patenaude, B. D. Smith, and M. D. Layne, “Myocardin-related transcription factor-A complexes activate type I collagen expression in lung fibroblasts,” *J. Biol. Chem.*, vol. 286, no. 51, pp. 44116–44125, 2011, doi: 10.1074/jbc.M111.276931.

[48] K. Kuwahara *et al.*, “Myocardin-Related Transcription Factor A Is a Common Mediator of Mechanical Stress- and Neurohumoral Stimulation-Induced Cardiac Hypertrophic Signaling Leading to Activation of Brain Natriuretic Peptide Gene Expression,” *Mol. Cell. Biol.*, vol. 30, no. 17, pp. 4134–4148, 2010, doi: 10.1128/MCB.00154-10.

[49] C. Manakanatas *et al.*, “Endothelial and systemic upregulation of miR-34a-5p fine-tunes senescence in progeria,” *Aging (Albany. NY).*, vol. 14, no. 1, pp. 195–224, 2022, doi: 10.18632/aging.203820.

[50] T. Ozaki and A. Nakagawara, “Role of p53 in cell death and human cancers,” *Cancers (Basel).*, vol. 3, no. 1, pp. 994–1013, 2011, doi: 10.3390/cancers3010994.

[51] F. Navarro and J. Lieberman, “miR-34 and p53: New insights into a complex functional relationship,” *PLoS One*, vol. 10, no. 7, pp. 1–23, 2015, doi: 10.1371/journal.pone.0132767.

[52] B. C. Bernardo *et al.*, “Therapeutic inhibition of the miR-34 family attenuates pathological cardiac remodeling and improves heart function,” *Proc. Natl. Acad. Sci.*, vol. 109, no. 43, pp. 17615–17620, 2012, doi: 10.1073/pnas.1206432109.

[53] G. Iannolo, M. R. Sciuto, G. M. Raffa, M. Pilato, and P. G. Conaldi, “MiR34 inhibition induces human heart progenitor proliferation article,” *Cell Death Dis.*, vol. 9, no. 3, 2018, doi: 10.1038/s41419-018-0400-9.

[54] J. Y. Y. Ooi, B. C. Bernardo, S. Singla, N. L. Patterson, R. C. Y. Lin, and J. R. McMullen, "Identification of miR-34 regulatory networks in settings of disease and antimiR-therapy: Implications for treating cardiac pathology and other diseases," *RNA Biol.*, vol. 14, no. 5, pp. 500–513, 2017, doi: 10.1080/15476286.2016.1181251.

[55] A. Mathiesen, T. Hamilton, N. Carter, M. Brown, W. McPheat, and A. Dobrian, "Endothelial extracellular vesicles: From keepers of health to messengers of disease," *Int. J. Mol. Sci.*, vol. 22, no. 9, 2021, doi: 10.3390/ijms22094640.

[56] E. Hergenreider *et al.*, "Atheroprotective communication between endothelial cells and smooth muscle cells through miRNAs," *Nat. Cell Biol.*, vol. 14, no. 3, pp. 249–256, 2012, doi: 10.1038/ncb2441.

[57] F. Jansen, Q. Li, A. Pfeifer, and N. Werner, "Endothelial- and Immune Cell-Derived Extracellular Vesicles in the Regulation of Cardiovascular Health and Disease," *JACC Basic to Transl. Sci.*, vol. 2, no. 6, pp. 790–807, 2017, doi: 10.1016/j.jacbts.2017.08.004.

[58] N. Wehbe, S. A. Nasser, G. Pintus, A. Badran, A. H. Eid, and E. Baydoun, "MicroRNAs in Cardiac Hypertrophy," *Int. J. Mol. Sci.*, vol. 20, no. 19, 2019, doi: 10.3390/ijms20194714.

[59] E. L. Vegter, P. Van Der Meer, L. J. De Windt, Y. M. Pinto, and A. A. Voors, "MicroRNAs in heart failure: From biomarker to target for therapy," *Eur. J. Heart Fail.*, vol. 18, no. 5, pp. 457–468, 2016, doi: 10.1002/ejhf.495.

[60] Y. Xiao, J. Zhao, J. P. Tuazon, C. V. Borlongan, and G. Yu, "MicroRNA-133a and Myocardial Infarction," *Cell Transplant.*, vol. 28, no. 7, pp. 831–838, 2019, doi: 10.1177/0963689719843806.

[61] B. Zhu *et al.*, "MiR-582-5p is a tumor suppressor microRNA targeting the Hippo-YAP/TAZ signaling pathway in non-small cell lung cancer," *Cancers (Basel).*, vol. 13, no. 4, pp. 1–21, 2021, doi: 10.3390/cancers13040756.

[62] L. Li and L. Ma, "Upregulation of miR-582-5p regulates cell proliferation and apoptosis by targeting AKT3 in human endometrial carcinoma," *Saudi J. Biol. Sci.*, vol. 25, no. 5, pp. 965–970, 2018, doi: 10.1016/j.sjbs.2018.03.007.

[63] X. T. T. Dang, J. M. Kavishka, and D. X. Zhang, "Extracellular Vesicles as an E ffi cient and Versatile," *Cells*, vol. 9, p. 2191, 2020.

[64] G. Raposo and P. D. Stahl, "Extracellular vesicles: a new communication paradigm?," *Nat. Rev. Mol. Cell Biol.*, vol. 20, no. 9, pp. 509–510, 2019, doi: 10.1038/s41580-019-0158-7.

[65] M. Guo, Z. Yin, F. Chen, and P. Lei, "Mesenchymal stem cell-derived exosome: A promising alternative in the therapy of Alzheimer's disease," *Alzheimer's Res. Ther.*, vol. 12, no. 1, pp. 1–15, 2020, doi: 10.1186/s13195-020-00670-x.

[66] M. P. Bebelman, M. J. Smit, D. M. Pegtel, and S. R. Baglio, "Biogenesis and function of extracellular vesicles in cancer," *Pharmacol. Ther.*, vol. 188, pp. 1–11, 2018, doi: 10.1016/j.pharmthera.2018.02.013.

[67] W. M. Henne, N. J. Buchkovich, and S. D. Emr, "The ESCRT Pathway," *Dev. Cell*, vol. 21, no. 1, pp. 77–91, 2011, doi: 10.1016/j.devcel.2011.05.015.

[68] J. H. Hurley, "Reverse Topology Membrane Scission by the ESCRTs," *Biophys. J.*, vol. 116, no. 3, p. 461a, 2019, doi: 10.1016/j.bpj.2018.11.2488.

[69] K. Trajkovic, "Ceramide triggers budding of exosome vesicles into multivesicular endosomes (Science (1244))," *Science (80-.).*, vol. 320, no. 5873, p. 179, 2008, doi: 10.1126/science.320.5873.179.

[70] M. F. Baietti *et al.*, "Syndecan-syntenin-ALIX regulates the biogenesis of exosomes," *Nat. Cell Biol.*, vol. 14, no. 7, pp. 677–685, 2012, doi: 10.1038/ncb2502.

[71] Q. Wang and Q. Lu, "Plasma membrane-derived extracellular microvesicles mediate non-canonical intercellular NOTCH signaling," *Nat. Commun.*, vol. 8, no. 1, pp. 1–8, 2017, doi: 10.1038/s41467-017-00767-2.

[72] F. Bianco *et al.*, "Acid sphingomyelinase activity triggers microparticle release from glial cells," *EMBO J.*, vol. 28, no. 8, pp. 1043–1054, 2009, doi: 10.1038/emboj.2009.45.

[73] A. E. Sedgwick, J. W. Clancy, M. Olivia Balmert, and C. D'Souza-Schorey, "Extracellular microvesicles and invadopodia mediate non-overlapping modes of tumor cell invasion," *Sci. Rep.*, vol. 5, no. September, pp. 1–14, 2015, doi: 10.1038/srep14748.

[74] F. X. Guix *et al.*, "Tetraspanin 6: A pivotal protein of the multiple vesicular body determining exosome release and lysosomal degradation of amyloid precursor protein fragments," *Mol. Neurodegener.*, vol. 12, no. 1, pp. 1–21, 2017, doi: 10.1186/s13024-017-0165-0.

[75] D. Perez-Hernandez *et al.*, "The intracellular interactome of tetraspanin-enriched microdomains reveals their function as sorting machineries toward exosomes," *J. Biol. Chem.*, vol. 288, no. 17, pp. 11649–11661, 2013, doi: 10.1074/jbc.M112.445304.

[76] B. K. Thakur *et al.*, "Double-stranded DNA in exosomes: A novel biomarker in cancer detection," *Cell Res.*, vol. 24, no. 6, pp. 766–769, 2014, doi: 10.1038/cr.2014.44.

[77] P. Sansone *et al.*, "Packaging and transfer of mitochondrial DNA via exosomes regulate escape from dormancy in hormonal therapy-resistant breast cancer," *Proc. Natl. Acad. Sci. U. S. A.*, vol. 114, no. 43, pp. E9066–E9075, 2017, doi: 10.1073/pnas.1704862114.

[78] X. Sisquella *et al.*, "Malaria parasite DNA-harbouring vesicles activate cytosolic immune sensors," *Nat. Commun.*, vol. 8, no. 1, 2017, doi: 10.1038/s41467-017-02083-1.

[79] M. A. A. S. C. M. J. and; S. J. Sollott, "乳鼠心肌提取 HHS Public Access," *Physiol. Behav.*, vol. 176, no. 3, pp. 139–148, 2017, doi: 10.1038/ncb1800.Glioblastoma.

[80] J. Ratajczak, M. Wysoczynski, F. Hayek, A. Janowska-Wieczorek, and M. Z. Ratajczak, "Membrane-derived microvesicles: Important and underappreciated mediators of cell-to-cell communication," *Leukemia*, vol. 20, no. 9, pp. 1487–1495, 2006, doi: 10.1038/sj.leu.2404296.

[81] S. R. Baglio *et al.*, "Human bone marrow- and adipose-mesenchymal stem cells secrete exosomes enriched in distinctive miRNA and tRNA species," *Stem Cell Res. Ther.*, vol. 6, no. 1, pp. 1–20, 2015, doi: 10.1186/s13287-015-

0116-z.

[82] Y. Hamdan, L. Mazini, and G. Malka, “Exosomes and micro-rnas in aging process,” *Biomedicines*, vol. 9, no. 8, 2021, doi: 10.3390/biomedicines9080968.

[83] J. Mills, M. Capece, E. Cocucci, A. Tessari, and D. Palmieri, “Cancer-derived extracellular vesicle-associated microRNAs in intercellular communication: One cell’s trash is another cell’s treasure,” *Int. J. Mol. Sci.*, vol. 20, no. 24, 2019, doi: 10.3390/ijms20246109.

[84] S. Weilner *et al.*, “Vesicular Galectin-3 levels decrease with donor age and contribute to the reduced osteo-inductive potential of human plasma derived extracellular vesicles,” *Aging (Albany. NY).*, vol. 8, no. 1, pp. 16–33, 2016, doi: 10.18632/aging.100865.

[85] S. Fulzele *et al.*, “Muscle-derived miR-34a increases with age in circulating extracellular vesicles and induces senescence of bone marrow stem cells,” *Aging (Albany. NY).*, vol. 11, no. 6, pp. 1791–1803, 2019, doi: 10.18632/aging.101874.

[86] M. Yamakuchi and C. J. Lowenstein, “MiR-34, SIRT1 and p53: The feedback loop,” *Cell Cycle*, vol. 8, no. 5, pp. 712–715, 2009, doi: 10.4161/cc.8.5.7753.

[87] and P. J. B. Jonathan R. Baker, Chaitanya Vuppusetty, Thomas Colley, Shyreen Hassibi, Peter S. Fenwick, Louise E. Donnelly, Kazuhiro Ito, “MicroRNA-570 is a novel regulator of cellularsenescence and inflammaging,” *FASEB J.*, 2019.

[88] C. J. Proctor and K. Goljanek-Whysall, “Using computer simulation models to investigate the most promising microRNAs to improve muscle regeneration during ageing,” *Sci. Rep.*, vol. 7, no. 1, pp. 1–12, 2017, doi: 10.1038/s41598-017-12538-6.

[89] J. Boulestreau, M. Maumus, P. Rozier, C. Jorgensen, and D. Noël, “Mesenchymal Stem Cell Derived Extracellular Vesicles in Aging,” *Front. Cell Dev. Biol.*, vol. 8, no. February, pp. 1–9, 2020, doi: 10.3389/fcell.2020.00107.

[90] S. M. Davidson, J. A. Riquelme, Y. Zheng, J. M. Vicencio, S. Lavandero, and D. M. Yellon, “Endothelial cells release cardioprotective exosomes that may contribute to ischaemic preconditioning,” *Sci. Rep.*, vol. 8, no. 1, pp. 1–9, 2018, doi: 10.1038/s41598-018-34357-z.

[91] P. F. Wong, K. L. Tong, J. Jamal, E. S. Khor, S. L. Lai, and M. R. Mustafa, “Senescent HUVECs-secreted exosomes trigger endothelial barrier dysfunction in young endothelial cells,” *EXCLI J.*, vol. 18, pp. 764–776, 2019, doi: 10.17179/excli2019-1505.

[92] C. Hromada, S. Mühleder, J. Grillari, H. Redl, and W. Holnthoner, “Endothelial extracellular vesicles-promises and challenges,” *Front. Physiol.*, vol. 8, no. MAY, 2017, doi: 10.3389/fphys.2017.00275.

[93] S. Weilner, E. Schraml, H. Redl, R. Grillari-Voglauer, and J. Grillari, “Secretion of microvesicular miRNAs in cellular and organismal aging,” *Exp. Gerontol.*, vol. 48, no. 7, pp. 626–633, 2013, doi: 10.1016/j.exger.2012.11.017.

[94] M. I. Mosquera-Heredia *et al.*, “Exosomes: Potential disease biomarkers and new therapeutic targets,” *Biomedicines*, vol. 9, no. 8, pp. 1–48, 2021, doi: 10.3390/biomedicines9081061.

[95] P. Chhoy, C. W. Brown, J. J. Amante, and A. M. Mercurio, “Protocol for the separation of extracellular vesicles by ultracentrifugation from in vitro cell culture models,” *STAR Protoc.*, vol. 2, no. 1, p. 100303, 2021, doi: 10.1016/j.xpro.2021.100303.

[96] Z. Andreu and M. Yáñez-Mó, “Tetraspanins in extracellular vesicle formation and function,” *Front. Immunol.*, vol. 5, no. SEP, pp. 1–12, 2014, doi: 10.3389/fimmu.2014.00442.

[97] C. M. Termini and J. M. Gillette, “Tetraspanins function as regulators of cellular signaling,” *Front. Cell Dev. Biol.*, vol. 5, no. APR, pp. 1–14, 2017, doi: 10.3389/fcell.2017.00034.

[98] E. G. Lakatta and D. Levy, “Arterial and cardiac aging: Major shareholders in cardiovascular disease enterprises: Part I: Aging arteries: A ‘set up’ for vascular disease,” *Circulation*, vol. 107, no. 1, pp. 139–146, 2003, doi: 10.1161/01.CIR.0000048892.83521.58.

[99] J. C. Wang and M. Bennett, “Aging and atherosclerosis: Mechanisms, functional consequences, and potential therapeutics for cellular senescence,” *Circulation Research*, vol. 111, no. 2. pp. 245–259, 2012, doi: 10.1161/CIRCRESAHA.111.261388.

[100] M. I. Miyamoto, K. Djabali, and L. B. Gordon, “Atherosclerosis in ancient humans, accelerated aging syndromes and normal aging: Is lamin a protein a common link?,” *Glob. Heart*, vol. 9, no. 2, pp. 211–218, 2014, doi: 10.1016/j.gheart.2014.04.001.

[101] I. A. H. A. H. O. O. N. W. N. Wight, “Chapter 16. Vascular Disease in Hutchinson Gilford Progeria Syndrome and Aging.”

[102] J. Davignon and P. Ganz, “Role of endothelial dysfunction in atherosclerosis,” *Circulation*, vol. 109, no. 23 SUPPL., 2004, doi: 10.1161/01.cir.0000131515.03336.f8.

[103] R. N. El Accaoui *et al.*, “Aortic valve sclerosis in mice deficient in endothelial nitric oxide synthase,” *Am. J. Physiol. - Hear. Circ. Physiol.*, vol. 306, no. 9, pp. 1302–1313, 2014, doi: 10.1152/ajpheart.00392.2013.

[104] A. Harvey, A. C. Montezano, and R. M. Touyz, “Vascular biology of ageing-Implications in hypertension,” *J. Mol. Cell. Cardiol.*, vol. 83, pp. 112–121, 2015, doi: 10.1016/j.yjmcc.2015.04.011.

[105] J. L. Balligand, O. Feron, and C. Dessy, “eNOS activation by physical forces: From short-term regulation of contraction to chronic remodeling of cardiovascular tissues,” *Physiol. Rev.*, vol. 89, no. 2, pp. 481–534, 2009, doi: 10.1152/physrev.00042.2007.

[106] a T. A. A. and K. N. D. Elizabeth A. Booth,‡a Stephen T. Spagnol, “Nuclear stiffening and chromatin softening with progerin expression leads to an attenuated nuclear response to force,” *Soft Matter*, 2015.

[107] b Julia T. Philipa, Kris Noel Dahla, “Nuclear mechanotransduction: Response of the lamina to extracellular stresswith

implications in aging," *J. Biomech.*, 2008.
[108] H. Q. Le *et al.*, "Mechanical regulation of transcription controls Polycomb-mediated gene silencing during lineage commitment," *Nat. Cell Biol.*, vol. 18, no. 8, pp. 864–875, 2016, doi: 10.1038/ncb3387.
[109] C. Esnault *et al.*, "Rho-actin signaling to the MRTF coactivators dominates the immediate transcriptional response to serum in fibroblasts," *Genes Dev.*, vol. 28, no. 9, pp. 943–958, 2014, doi: 10.1101/gad.239327.114.
[110] X. W. 1 *et al.*, "A crosstalk between chromatin remodeling and histone H3K4 methyltransferase complexes in endothelial cells regulates angiotensin II-induced cardiac hypertrophy."
[111] S. Sun *et al.*, "Vascular endothelium–targeted Sirt7 gene therapy rejuvenates blood vessels and extends life span in a Hutchinson-Gilford progeria model," *Sci. Adv.*, vol. 6, no. 8, 2020, doi: 10.1126/sciadv.aay5556.
[112] L. Atchison *et al.*, "iPSC-Derived Endothelial Cells Affect Vascular Function in a Tissue-Engineered Blood Vessel Model of Hutchinson-Gilford Progeria Syndrome," *Stem Cell Reports*, vol. 14, no. 2, pp. 325–337, 2020, doi: 10.1016/j.stemcr.2020.01.005.
[113] G. Matrone, R. A. Thandavarayan, B. K. Walther, S. Meng, A. Mojiri, and J. P. Cooke, "Dysfunction of iPSC-derived endothelial cells in human Hutchinson–Gilford progeria syndrome," *Cell Cycle*, vol. 18, no. 19, pp. 2495–2508, 2019, doi: 10.1080/15384101.2019.1651587.
[114] S. S. Zhou *et al.*, "MiRNAS in cardiovascular diseases: Potential biomarkers, therapeutic targets and challenges review-article," *Acta Pharmacologica Sinica*. 2018, doi: 10.1038/aps.2018.30.
[115] E. Mattioli *et al.*, "Altered modulation of lamin A/C-HDAC2 interaction and p21 expression during oxidative stress response in HGPS," *Aging Cell*, vol. 17, no. 5, pp. 1–16, 2018, doi: 10.1111/acel.12824.
[116] B. Ritschka *et al.*, "The senescence-associated secretory phenotype induces cellular plasticity and tissue regeneration," *Genes Dev.*, 2017, doi: 10.1101/gad.290635.116.
[117] S. Hubackova, K. Krejcikova, J. Bartek, and Z. Hodny, "IL1-and TGFβ-Nox4 signaling, oxidative stress and DNA damage response are shared features of replicative, oncogene-induced, and drug-induced paracrine 'Bystander senescence,'" *Aging (Albany. NY).*, 2012, doi: 10.18632/aging.100520.
[118] J. C. Acosta *et al.*, "A complex secretory program orchestrated by the inflammasome controls paracrine senescence," *Nat. Cell Biol.*, vol. 15, no. 8, pp. 978–990, 2013, doi: 10.1038/ncb2784.
[119] N. Bhatia-Dey, R. R. Kanherkar, S. E. Stair, E. O. Makarev, and A. B. Csoka, "Cellular senescence as the causal nexus of aging," *Front. Genet.*, vol. 7, no. FEB, pp. 1–14, 2016, doi: 10.3389/fgene.2016.00013.
[120] Y. Zhu *et al.*, "The achilles' heel of senescent cells: From transcriptome to senolytic drugs," *Aging Cell*, vol. 14, no. 4, pp. 644–658, 2015, doi: 10.1111/acel.12344.
[121] N. Malaquin, A. Martinez, and F. Rodier, "Keeping the senescence secretome under control: Molecular reins on the senescence-associated secretory phenotype," *Exp. Gerontol.*, vol. 82, pp. 39–49, 2016, doi: 10.1016/j.exger.2016.05.010.
[122] M. A. Van Doormaal *et al.*, "Haemodynamics in the mouse aortic arch computed from MRI-derived velocities at the aortic root," *J. R. Soc. Interface*, vol. 9, no. 76, pp. 2834–2844, 2012, doi: 10.1098/rsif.2012.0295.
[123] M. Vidal, "Exosomes: Revisiting their role as 'garbage bags,'" *Traffic*, vol. 20, no. 11, pp. 815–828, 2019, doi: 10.1111/tra.12687.
[124] S. Fu, Y. Zhang, Y. Li, L. Luo, Y. Zhao, and Y. Yao, "Extracellular vesicles in cardiovascular diseases," *Cell Death Discov.*, vol. 6, no. 1, 2020, doi: 10.1038/s41420-020-00305-y.
[125] H. Gu *et al.*, "Serum-derived extracellular vesicles protect against acute myocardial infarction by regulating miR-21/PDCD4 signaling pathway," *Front. Physiol.*, vol. 9, no. APR, 2018, doi: 10.3389/fphys.2018.00348.
[126] J. Hanna, G. S. Hossain, and J. Kocerha, "The potential for microRNA therapeutics and clinical research," *Front. Genet.*, vol. 10, no. MAY, 2019, doi: 10.3389/fgene.2019.00478.